RP TU Rheinland-Pfälzische Technische Universität Kaiserslautern Landau

APEX1 as a novel component of the ultrafine anaphase bridge resolution machinery

vom Fachbereich Biologie

der Rheinland-Pfälzischen Technischen Universität Kaiserslautern-Landau

zur Verleihung des akademischen Grades Dr. rer. nat. genehmigte

Dissertation

von

Farbod Mohseni, M.Sc., geb. in Kermanshah

Mündliche Prüfung: 30.10.2026

Dekan:	Prof. Dr. Stefan Kins
Promotionskommissionsvorsitzender:	Prof. Dr. Stefan Kins
Berichterstattende:	Prof. Dr. Zuzana Storchová
	Prof. Dr. Jörg Fahrer

D 386

Darlegung des Eigenanteils

Farbod Mohseni
APEX1 as a novel component of the ultrafine anaphase bridge resolution machinery

Im Folgenden ist aufgeführt, welchen Anteil Dritte an den in der Dissertation enthaltenen Arbeiten hatten. Arbeiten, die von Dritten oder in Zusammenarbeit mit Dritten durchgeführt wurden, sind in den jeweiligen Abbildungslegenden entsprechend gekennzeichnet.

Konzeption/Planung	Prof. Dr. Zuzana Storchová und Dr. Markus Räschle (in Teilen)
Literaturrecherche	
Versuchsdesign	Prof. Dr. Zuzana Storchová, Dr. Markus Räschle (in Teilen)
Methodenentwicklung	Prof. Dr. Zuzana Storchová und Dr. Markus Räschle (in Teilen)
Datenerhebung	Die betreuten Studierenden Nikita Kvasov, Amr Abdrbo und Katharina Gauch, sowie Kruno Kuscovi und das Labor von Prof. Dr. Iva Tolic (Live-Cell Imaging) führten einzelne Experimente in Teilen durch, wie in den entsprechenden Abbildungslegenden angegeben.
Datenanalyse	Die betreuten Studierenden Nikita Kvasov, Amr Abdrbo und Katharina Gauch führten erste Analysen der von ihnen erhobenen Daten in Teilen durch. Statistische Analyse der Experimente von Studneten sowie der eigenen wurde von Farbod Mohseni durchgeführt. Dr. Markus Räschle und Erik Heller führten die Protemoik-Datenanalyse in Teilen durch. Erik Marcel Heller führte die initiale Prozessierung der proteomischen Daten durch. Erik Marcel Heller und Dr. Markus Räschle führten die statisitsche Analyse der Proteomik-Daten in Teilen durch.
Programmierung	Erik Heller und Dr. Markus Räschle (R-data), in Teilen
Interpretation und Diskussion der Ergebnisse	Prof. Dr. Zuzana Storchová und Dr. Markus Räschle, in Teilen
Schreiben der Dissertation	

Die vorliegende Einschätzung über die erbrachten Leistungen Dritter wurde mit den genannten Personen einvernehmlich abgestimmt.

06.08.2026 Farbod Mohseni
_____
Datum, Unterschrift Doktorand/in

06.08.2026 Prof. Dr. Zuzana Storchová
_____
Datum, Unterschrift Betreuer/in

Darlegung aller benutzten Hilfsmittel und Hilfestellungen

Farbod Mohseni
APEX1 as a novel component of the ultrafine anaphase bridge resolution machinery

Alle zur Auswertung in Anspruch genommenen Programme sind in Tabelle 2.15 dargelegt. Weiterhin habe ich KI-Systeme zur sprachlichen Verbesserung sowie für die Zusammenfassung in die deutsche Sprache verwendet. Die verwendeten Quellen und Hilfsmittel (auch generative KI-Systeme) sind kenntlich gemacht und vollständig (d.h. mit Angabe von Version und Nutzungszweck) aufgeführt. Sofern der Einsatz von KI-Systemen über eine reine Grammatikprüfung und Stilverbesserung hinausgeht, ist der Einsatz nachvollziehbar kenntlich gemacht. Für Fehler, auch bei Übernahme aus generativen KI-Systemen, bin ich verantwortlich.

Dr. Markus Räschle und Erik Marcel Heller haben mich bei der statistischen Beurteilung der Daten untertstützt.

Die Datenerhebung mit “Live-Cell Imaging” wurde von Kruno Kuscovi und dem Labor von Prof. Dr. Iva Tolic (Ruder Boskovic Institute, Zagreb, Croatia) übernommen (siehe Kapitel 3.11.6 Live-Cell Imaging, sowie entsprechende Abbildungslegenden). Metaanalyse von der Proteomik-Daten wurde von Erik Marcel Heller durchgeführt (siehe Kapitel 3.9.7.1, sowie entsprechende Abbildungslegenden).

06.08.2026 Farbod Mohseni

Datum, Unterschrift Doktorand/in

Eidesstattliche Erklärung

Ich erkläre hiermit, dass die Dissertation von mir, Farbod Mohseni, selbstständig unter der Betreuung von Prof. Dr. Zuzana Storchová angefertigt wurde. Alle benutzten Quellen, Hilfsmittel und Hilfestellungen wurden angegeben. Die Beiträge beteiligter Studierender, Mitarbeiterinnen und Mitarbeiter sowie anderer Personen wurden klar gekennzeichnet.

Die Dissertation dient der Erlangung des akademischen Grades Doktor der Naturwissenschaften (Dr. rer. nat.) an der Rheinland-Pfälzischen Technischen Universität Kaiserslautern-Landau. Die Dissertation oder Teile daraus wurden weder als Prüfungsarbeit für eine staatliche oder andere wissenschaftliche Prüfung eingereicht, noch wurde die gleiche oder eine in wesentlichen Teilen vergleichbare Arbeit bei einem anderen Fachbereich oder einer anderen Universität als Dissertation eingereicht.

Die Promotionsordnung des Fachbereichs Biologie der Rheinland-Pfälzischen Technischen Universität Kaiserslautern-Landau ist mir in ihrer derzeit gültigen Fassung bekannt.

06.08.2026 Farbod Mohseni
_____

Datum, Unterschrift Doktorand/in

Table of Contents

I. Summary 10

II. Zusammenfassung 11

1 Introduction 13

1.1 The eukaryotic cell cycle checkpoints and their role in genome integrity 13

1.1.1 Cell cycle regulation by cyclin-CDK complexes 14

1.2 Replication stress: sources, cellular responses, and consequences 16

1.2.1 Coordinated protein activity ensures faithful DNA replication 16

1.2.2 Replication stress is a hallmark of cancer 17

1.2.3 R-loops and genome stability 19

1.2.4 Consequences of Replication Stress and the Cellular DNA Repair Response 21

1.2.5 Consequences of replication stress in mitosis 23

1.3 Anaphase bridges and their resolution 24

1.3.1 Chromatin bridges 24

1.3.2 Ultrafine anaphase bridges 25

1.3.3 Bloom syndrome helicase: from homologous recombination to UFB resolution 30

1.3.4 FANCD2 and FANCI in replication stress, common fragile site maintenance, and FS-UFB resolution 31

1.3.5 PICH as an early bridge-recognition factor in UFB resolution 32

1.3.6 TOP3A in homologous recombination, replication stress, and mitotic UFB resolution 33

1.3.7 RPA1–3 in Replication Stress and Ultrafine Bridge Biology 34

1.4 Candidate proteins and experimental strategy 34

1.4.1 Overview of APEX1 functions in genome maintenance. 35

1.4.2 ALYREF in mRNA export and transcription-replication conflict regulation 36

1.4.3 The HCT116 F9 cell line as a model for studying UFB resolution 38

1.4.4 Cell-cycle synchronization for the analysis of replication stress and mitosis 39

1.4.5 ChIP–MS as a strategy to identify chromatin-associated UFB-resolution factors 41

1.5 Aim of the study 43

2 Materials 44

2.1 Equipment 44

2.2 Chemicals 47

2.3 Buffers and Solutions 49

2.4 Molecular biology 51

2.5 Plasmids and siRNA 52

2.6 Immunoprecipitation reagents 53
2.7 Bacteria culture 53
2.8 Cell culture 53
2.9 SDS-PAGE and Western blotting 55
2.10 Microscopy 56
2.11 Flow cytometry 56
2.12 Mass spectrometry 56
2.13 List of antibodies 57
2.14 Kits 59
2.15 Software 59
3 Methods 61
3.1 Cell culture techniques 61
3.1.1 Freezing of human cell lines 61
3.1.2 Thawing of human cell lines 61
3.1.3 Cell counting 62
3.2 Generation of APEX1 knockout and rescue cell lines 62
3.2.1 CRISPR–Cas9-mediated APEX1 knockout 62
3.2.2 Single-cell clone selection of APEX1 knockout cells 62
3.2.3 Molecular cloning and verification of APEX1 rescue constructs 63
3.2.4 Transfection and lentiviral transduction 64
3.3 Thymidine cell cycle synchronization 65
3.4 Cell cycle-specific depletion of BLM 66
3.5 Cell cycle-specific expression of APEX1 66
3.6 Colony formation assay 66
3.7 Protein detection 67
3.7.1 Sample preparation for Western blotting 67
3.7.2 Protein concentration determination 67
3.7.3 SDS–PAGE and immunoblotting 67
3.8 ChIP–WB 68
3.8.1 Protein isolation 68
3.8.2 Immunoprecipitation 69
3.9 ChIP-MS sample preparation and mass spectrometry analysis 69
3.9.1 Crosslinking and harvesting 69
3.9.2 Chromatin preparation by sonication 69

3.9.3 Determination of chromatin fragmentation 70
3.9.4 ChIP-MS with GFP and RFP nanobody beads 70
3.9.5 LC–MS/MS analysis 71
3.9.6 Analysis of proteome data for individual ChIP-MS experiments 71
3.9.7 Processing proteomics data for meta-analysis 71
3.9.8 Pathway enrichment analysis 73
3.10 Flow cytometric cell cycle analysis 73
3.10.1 Immunostaining for flow cytometry analysis 74
3.11 Fluorescence microscopy 74
3.11.1 DAPI staining for fluorescence microscopy 74
3.11.2 Microscopic detection of mitotic aberrations 74
3.11.3 Staining and visualization of UFBs with interacting proteins 75
3.11.4 Metaphase spread analysis by microscopy 76
3.11.5 Microscopy setup and image analysis 77
3.11.6 Live-cell microscopy using the Lattice Lightsheet 7 77
3.11.7 Proximity ligation assay (PLA) 77
3.12 Statistical analysis 78
3.13 Data visualization 78
4 Results 79
4.1 Proteomic screening for candidate UFB-resolution proteins 79
4.1.1 BLM ChIP-MS identifies replication stress-associated interactors 79
4.1.2 TOP3A ChIP-MS detects R-loop factors under mild replication stress 82
4.1.3 FANCD2 ChIP-MS supports the replication stress-dependent recruitment of APEX1 85
4.1.4 FANCI ChIP-MS reveals RNA-processing factors under mild replication stress 87
4.1.5 Meta-analysis of UFB marker proteins highlights APEX1 89
4.1.6 RNAseH1 overexpression impairs APEX1 recruitment 92
4.2 Validation of APEX1 and ALYREF association with UFB marker proteins 95
4.2.1 Reciprocal APEX1 ChIP-MS supports an association with UFB marker proteins 95
4.2.2 ALYREF ChIP-MS reveals enrichment of R-loop factors 98
4.2.3 Stress-dependent association of BLM with APEX1 and ALYREF 101
4.2.4 APEX1–BLM–FANCD2 interactions occur independently of RNA or DNA 102
4.2.5 ALYREF–BLM interactions occur independently of RNA or DNA 103
4.2.6 APEX1 co-localizes with BLM on ultra-fine anaphase bridges more frequently under mild replication stress 105

4.2.7 ALYREF association with UFBs shows no significant change under APH treatment 106
4.2.8 ALYREF knockdown does not affect UFBs formation 107
4.2.9 Proximity ligation assay reveals APEX1 co-localization with ultra-fine bridges 108
4.3 Consequences of APEX1 loss and BLM depletion on genome stability 111
4.3.1 CRISPR/Cas9-mediated knockout of APEX1 in F9 HCT116 cells 111
4.3.2 Ultra-fine bridges arise more frequently in APEX1-deficient cells with replication stress 112
4.3.3 Mitotic aberration arises more frequently in APEX1-deficient cells 115
4.3.4 Loss of APEX1 increases post-mitotic genome instability 116
4.3.5 Double strand DNA breaks arise frequently in APEX1-deficient cells 118
4.3.6 Effects of APEX1 and BLM co-depletion on long-term cell survival 122
4.3.7 APEX1 loss and BLM depletion show non-additive effects on genome instability 123
4.3.8 APEX1 and BLM loss reveal two correlated routes to genome instability 126
4.3.9 APEX1 loss increases the persistence of wavy UFBs during mitosis 128
4.4 Characterization of APEX1 function in UFB resolution 131
4.4.1 APEX1 rescue in the HCT116 F9AK cell line 131
4.4.2 APEX1 re-expression suppresses UFB formation 132
4.4.3 Time-dependent induction of APEX1 following doxycycline treatment 134
4.4.4 APEX1 re-expression after replication restores proper UFB resolution 135
4.4.5 Catalytically active APEX1 is required for efficient resolution of fragile site ultrafine anaphase bridges (FS-UFBs) 138
4.4.6 APEX1 is not required for the resolution of centromeric UFBs 141
4.4.7 Lagging chromatin after APEX1 loss primarily reflects acentric DNA fragments 144
4.4.8 APEX1 is required for efficient resolution of fragile site- ultra fine bridges (FS-UFBs) . 145
5 Discussion 148
5.1 Meta-analysis of mitotic chromatin interaction partners of UFB marker proteins 148
5.2 Molecular characterization of candidate proteins 149
5.2.1 APEX1 associates with UFB under replication stress 149
5.2.2 ALYREF associates with UFB markers without a clear role in UFB resolution 151
5.3 APEX1 and BLM have overlapping and distinct roles in genome stability 152
5.4 Evidence for a specific role of APEX1 in the resolution of FS-UFBs 154
5.5 Proposed models for APEX1-dependent FS-UFB resolution 155
5.5.1 Current model of FS-UFB resolution 155
5.5.2 Two possible sites of APEX1 incision during FS-UFB resolution 156

Model 1: APEX1 cleavage within the DNA strand of an R-loop-associated FS-UFB intermediate 156
Model 2: APEX1 cleavage at an ssDNA/dsDNA junction within a stalled fork-derived FS-UFB intermediate 157
6 Conclusion 159
7 Supplementary information 160
7.1 Supplementary Figure 160
7.2 Supplementary Data 169
7.3 List of figures 174
7.4 List of supplementary figures 175
7.5 List of supplementary Movies 175
7.6 List of tables 176
7.7 List of abbreviations 176
7.8 Acknowledgement 179
7.9 Curriculum Vitae 180
8 References 183

I. Summary

Replication stress is an important source of chromosomal instability and tumorigenesis because it interferes with faithful DNA synthesis. However, how replication stress affects mitotic chromosome segregation remains incompletely understood, particularly in relation to the formation and resolution of persistent sister chromatid connections such as ultrafine anaphase bridges (UFBs). UFBs are thin, histone-free DNA structures that connect sister chromatids during anaphase. While their exact origin and nature remain poorly characterized, they likely arise from under replicated DNA or from unresolved recombination intermediates. The UFBs can be visualized only through the recruitment of specific UFB-associated proteins, including Bloom syndrome helicase (BLM), the PLK1-interacting checkpoint translocase PICH, and Fanconi anemia proteins such as FANCD2 and FANCI. Although these proteins have been implicated in UFB resolution, the complete molecular mechanism and the identity of additional cofactors remain unclear.

In this study, chromatin immunoprecipitation of know UFB-associated proteins coupled to mass spectrometry (ChIP-MS) was used to systematically identify novel proteins associated with UFB-resolution factors that arise from mild replication stress. This screen identified several proteins that have not been associated with this type of damage, among them also APEX1, as a potential UFB-associated protein. APEX1 is a multifunctional DNA repair and redox regulatory protein best known for its role in base excision repair and has also been identified as an R-loop-associated factor. However, its function in mitotic genome stability has not been well characterized.

Functional analysis revealed increased UFB formation, chromatin bridges, and Binucleation in APEX1 knockout cells, suggesting that APEX1 contributes to accurate chromosome segregation during mitosis. Importantly, simultaneous depletion of BLM did not further increase these phenotypes, indicating a possible functional interaction between APEX1 and BLM in the prevention or resolution of persistent sister chromatid linkages. Together, these findings identify APEX1 as a novel factor involved in UFB resolution and suggest that APEX1 contributes to genome stability beyond its canonical role in DNA repair. Overall, this work supports a role for APEX1 in resolving replication stress–induced UFBs and limiting the persistence of fragile site–associated DNA intermediates into mitosis. By potentially cooperating with BLM-dependent processing pathways, APEX1 may help reduce mitotic and post-mitotic defects, including, micronuclei, binucleation, and polyploidy.

II. Zusammenfassung

Replikationsstress ist eine wichtige Ursache chromosomaler Instabilität und Tumorentstehung, da er die fehlerfreie DNA-Synthese beeinträchtigt. Wie sich Replikationsstress auf die mitotische Chromosomensegregation auswirkt, ist jedoch noch nicht vollständig verstanden. Dies gilt insbesondere für die Entstehung und Auflösung persistierender Verbindungen zwischen Schwesterchromatiden, wie ultrafeinen Anaphasebrücken (ultrafine anaphase bridges, UFBs). UFBs sind dünne, histonfreie DNA-Strukturen, die Schwesterchromatiden während der Anaphase miteinander verbinden. Obwohl ihr genauer Ursprung und ihre molekulare Beschaffenheit bislang nur unzureichend charakterisiert sind, entstehen sie vermutlich aus unterreplizierter DNA oder nicht aufgelösten Rekombinationsintermediaten. UFBs können ausschließlich durch die Rekrutierung spezifischer UFB-assoziierter Proteine sichtbar gemacht werden. Dazu gehören die Bloom-Syndrom-Helikase BLM, die PLK1-interagierende Checkpoint-Translokase PICH sowie Fanconi-Anämie-Proteine wie FANCD2 und FANCI. Obwohl diese Proteine mit der Auflösung von UFBs in Verbindung gebracht wurden, sind der vollständige molekulare Mechanismus und die Identität weiterer beteiligter Kofaktoren weiterhin unklar.

In dieser Studie wurde die Chromatin-Immunpräzipitation bekannter UFB-assoziierter Proteine in Kombination mit Massenspektrometrie (ChIP-MS) eingesetzt, um systematisch neue Proteine zu identifizieren, die unter mildem Replikationsstress mit Faktoren der UFB-Auflösung assoziiert sind. Dieser Ansatz identifizierte mehrere Proteine, die bisher nicht mit dieser Art von DNA-Schäden in Verbindung gebracht worden waren. Dazu gehörte auch APEX1, das als potenziell UFB-assoziiertes Protein identifiziert wurde. APEX1 ist ein multifunktionales DNA-Reparatur- und Redox-regulierendes Protein, das vor allem für seine Funktion in der Basenexzisionsreparatur bekannt ist und zudem als R-Loop-assoziierter Faktor beschrieben wurde. Seine Funktion bei der Aufrechterhaltung der mitotischen Genomstabilität ist jedoch bislang nur unzureichend charakterisiert.

Die funktionelle Analyse zeigte eine erhöhte Bildung von UFBs und Chromatinbrücken sowie eine verstärkte Binukleation in APEX1-Knockout-Zellen. Dies deutet darauf hin, dass APEX1 zu einer korrekten Chromosomensegregation während der Mitose beiträgt. Bemerkenswerterweise führte die gleichzeitige Depletion von BLM zu keiner weiteren Zunahme dieser Phänotypen. Dies weist auf eine mögliche funktionelle Zusammenarbeit zwischen APEX1 und BLM bei der Vermeidung oder Auflösung persistierender Verbindungen zwischen Schwesterchromatiden hin.

Zusammenfassend identifizieren diese Ergebnisse APEX1 als einen neuen Faktor, der an der Auflösung von UFBs beteiligt ist, und deuten darauf hin, dass APEX1 über seine kanonische Funktion in der DNA-

Reparatur hinaus zur Genomstabilität beiträgt. Insgesamt unterstützen die Ergebnisse eine Funktion von APEX1 bei der Auflösung replikationsstressinduzierter UFBs und bei der Begrenzung der Persistenz von mit fragilen Stellen (fragile sites) assoziierten DNA-Intermediaten bis in die Mitose. Durch eine mögliche funktionelle Zusammenarbeit mit BLM-abhängigen Prozessierungswegen könnte APEX1 dazu beitragen, mitotische und postmitotische Defekte wie Mikronukleusbildung, Binukleation und Polyploidie zu reduzieren.

1 Introduction

The human genome contains more than three billion base pairs and is highly conserved, as it contains the complete blueprint for the development, function, and maintenance of the organism. The growth of a human body is allowed through repeated cycles of cell division, differentiation, and proliferation, transforming a single cell into billions of specialized cells [1]. This process relies on the eukaryotic cell cycle, a tightly regulated and highly conserved mechanism that ensures accurate duplication and faithful segregation of genetic material into daughter cells [2]. By preserving genome integrity, the cell cycle safeguards cellular viability and organismal health throughout life and across generations. Thus, the fate of each cell, and ultimately of the organism, depends on the precise coordination of molecular events that govern each round of cell division [3].

1.1 The eukaryotic cell cycle checkpoints and their role in genome integrity

The human cell cycle is divided into four sequential phases: G_1, S, G_2, and mitosis, with G_1, S, and G_2 collectively referred to as interphase, during which the cell prepares for division [4]. Cells can also exit the active cycle and enter a reversible quiescent state known as G_0, where proliferation is temporarily halted (Figure 1.1). During the G1 phase, cells undergo extensive growth, accumulate metabolic resources, and duplicate cellular components required for division, except for DNA. This phase is critical for determining whether a cell commits to another round of replication. Entry into S phase marks the initiation of DNA synthesis, during which the genome is duplicated in a semi-conservative manner, and sister chromatid cohesion is established to ensure proper chromosome segregation later in mitosis [5]. Following DNA replication, cells progress into G2 phase, which serves as a final preparatory stage for mitosis. In G2, cells continue to grow, synthesize proteins essential for chromosome segregation and cell division, and repair any DNA damage that may have occurred during replication [6].

Mitosis is the phase of the cell cycle in which duplicated chromosomes are equally distributed into two daughter nuclei, thereby preserving genetic material during cell divisions. This process is classically divided into four consecutive stages: prophase, metaphase, anaphase, and telophase [7] (Figure 1.1). During prophase, chromosomes undergo condensation into compact structures, while centrosomes mature and migrate toward opposite poles of the cell. Prometaphase is initiated by nuclear envelope breakdown (NEBD), allowing spindle microtubules to access and attach to kinetochores on the chromosomes, leading to the establishment of a bipolar mitotic spindle [6]. In metaphase, chromosomes are positioned at the spindle equator, forming the metaphase plate, which ensures that sister chromatids are properly attached to microtubules stretched from opposite spindle poles. Anaphase is triggered by the separation of sister chromatids, which are then pulled toward opposite poles, securing the equal segregation of the genome [8]. Finally, during telophase, the mitotic spindle disassembles, and

nuclear envelopes re-form around each set of chromosomes, giving rise to two genetically identical nuclei [9]. Subsequently, Cytokinesis is the final step of cell division, during which the cytoplasm is physically separated to generate two daughter cells. This process requires cleavage the inward constriction of the cell membrane to form a dividing groove followed by abscission, which severs the intercellular bridge connecting the daughter cells [10]. Defects in chromosome segregation, persistent chromatin bridges, or unresolved DNA structures can delay or disrupt cytokinesis. If cytokinesis fails, cells may become binucleated or tetraploid [11]. The precise coordination of these mitotic events is critical for maintaining genomic integrity. Defects in chromosome alignment, segregation, or spindle function can result in aneuploidy and genome instability, which are key features of many pathological conditions, including cancer [12].

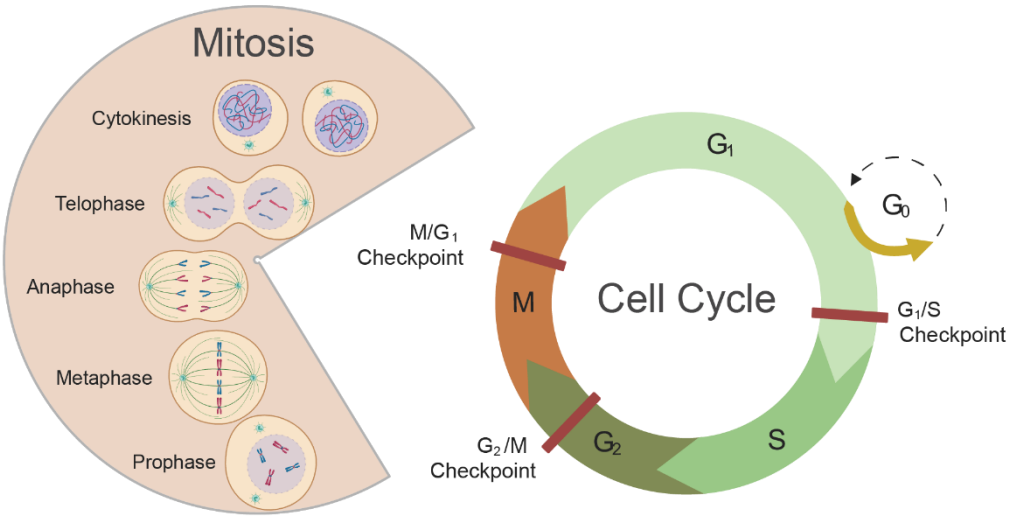


Figure 1.1 | Overview of the eukaryotic cell cycle and mitotic progression.
Schematic representation of cell cycle phases. The cell cycle comprises interphase (G1, S, and G2), during which cells grow and replicate their genome, and M phase, in which duplicated chromosomes are segregated and cell division is completed by cytokinesis. Cells may also exit the cycle into a quiescent G0 state and re-enter upon mitogenic stimulation. Mitosis proceeds through prophase, prometaphase, metaphase, anaphase, and telophase, encompassing chromosome condensation, nuclear envelope breakdown, spindle attachment, metaphase alignment, sister chromatid separation, and reformation of daughter nuclei, ultimately generating two genetically identical cells. Image modified using BioRender.com

1.1.1 Cell cycle regulation by cyclin-CDK complexes

Progression through the cell cycle is tightly controlled by checkpoint mechanisms and regulatory proteins that preserve cell cycle fidelity and ensure the correct order of cellular events. These checkpoints act as surveillance systems that first detect problems such as DNA damage, incomplete DNA replication, or chromosome attachment defects. Once these defects are recognized, checkpoint signalling pathways are activated to delay or arrest cell cycle progression, mainly by regulating phase-specific cyclin–CDK complexes (Figure 1.2). This allows cells time to repair DNA damage, complete DNA replication, or correct chromosome segregation errors before entering the next cell cycle phase [13]. In G1 phase, Cyclin D–CDK4/6 promotes phosphorylation of RB, leading to release of the activator E2F

transcription factors, mainly E2F1, E2F2, and E2F3. These factors induce the expression of genes required for S-phase entry, including Cyclin E, which forms the Cyclin E–CDK2 complex. This complex further enhances E2F activity in a positive feedback loop and commits the cell to DNA replication. The activity of these complexes is negatively regulated by CDK inhibitors. Members of the INK4 family, such as p16, inhibit Cyclin D–CDK4/6, whereas CIP/KIP proteins, including p21 and p27, inhibit Cyclin E/A–CDK2 complexes. Together, these inhibitors prevent premature or uncontrolled cell cycle progression [14].

The first major checkpoint, the G1/S checkpoint, integrates signals related to DNA integrity, growth factor availability, and cellular energy status, and determines whether cells commit to DNA synthesis. When conditions are unfavourable, such as in the presence of DNA damage or insufficient mitogenic signals, cells arrest in G1 or exit the cycle into the quiescent G0 state. Upon successful passage through this checkpoint, cells enter S phase, where CDK2 switches its partner from Cyclin E to Cyclin A. The Cyclin A–CDK2 complex drives DNA replication and maintains E2F activity, ensuring proper progression through S phase [15].

Following DNA replication, cells progress into G2 phase, during which the G2/M checkpoint ensures that replication is complete, and any DNA damage has been repaired. This transition is mainly controlled by the accumulation of Cyclin B and formation of the Cyclin B–CDK1 complex. CDK1 is activated by the phosphatase CD25, which removes inhibitory phosphorylation, thereby preparing the cell for mitotic entry. Active Cyclin B–CDK1 initiates key mitotic events, including chromosome condensation, nuclear envelope breakdown, and spindle assembly [16].

The third major checkpoint, the spindle assembly checkpoint (SAC), operates during metaphase and safeguards accurate chromosome segregation by monitoring proper kinetochore–microtubule attachment and biorientation of all chromosomes on the mitotic spindle [17]. The third major checkpoint, the spindle assembly checkpoint (SAC), operates during metaphase and safeguards accurate chromosome segregation by monitoring proper kinetochore–microtubule attachment and biorientation of all chromosomes on the mitotic spindle [18].

Together, these checkpoint mechanisms and the precisely timed activation and inactivation of cyclin–CDK complexes ensure orderly cell cycle progression and maintenance of genomic stability. In response to severe or persistent DNA damage, cells may permanently withdraw from the cell cycle by entering

senescence or undergo programmed cell death through apoptosis, thereby preventing the propagation of genomic instability [19].

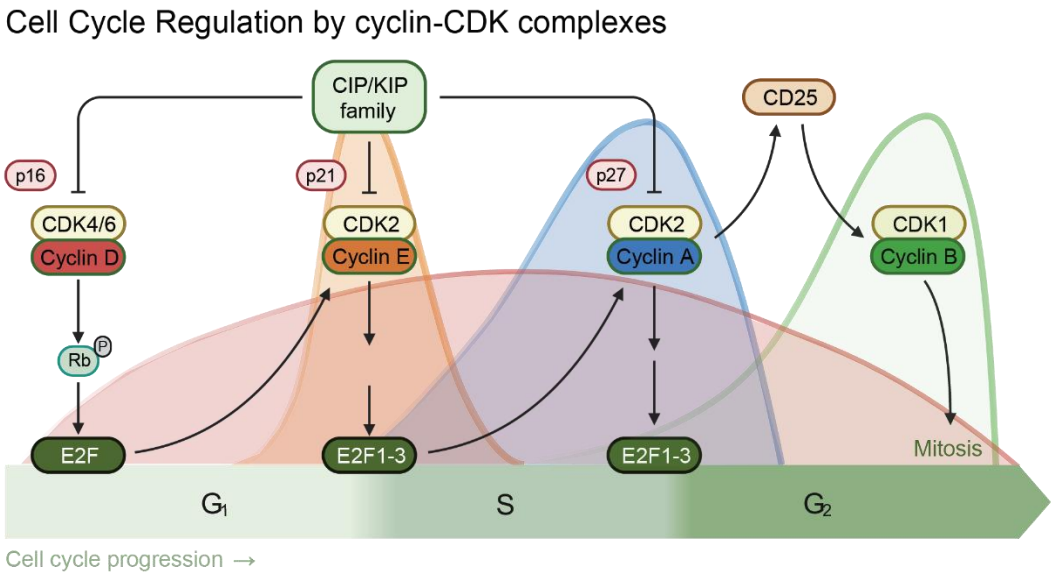


Figure 1.2 | representation of the sequential activation of cyclin–CDK complexes that drive cell cycle transitions. Cyclin E–CDK2 and cyclin A–CDK2 complexes regulate commitment to S phase by promoting E2F-dependent transcription required for DNA replication. Increasing activity of cyclin, A/B–CDK1 provides a second regulatory decision point that promotes entry into mitosis. Activation of cyclin D–CDK4/6 is essential for progression through G1 and re-entry into interphase for a new round of the cell cycle. Image adapted from Matthews et al., 2022 and modified using BioRender.com.

1.2 Replication stress: sources, cellular responses, and consequences

1.2.1 Coordinated protein activity ensures faithful DNA replication

The S phase of the cell cycle is a highly regulated process that ensures faithful duplication of the genome. It relies on the coordinated action of numerous molecular factors to achieve accurate DNA synthesis and maintain genomic integrity. DNA replication initiates at defined origins of replication, where the pre-replication complex assembled during G1 becomes activated and recruits the MCM helicase [20]. The helicase unwinds the DNA double helix, generating two single-stranded templates and forming a replication fork. Single-stranded DNA-binding proteins (SSBs) stabilize the exposed DNA, while topoisomerases relieve the torsional stress that accumulates ahead of the advancing fork. PCNA functions as a sliding clamp that anchors DNA polymerases to the DNA, thereby ensuring high processivity and efficient synthesis [21]. DNA polymerases δ and ε both synthesize DNA in the 5'→3' direction, but they mainly act on different strands at the replication fork. Polymerase ε primarily performs continuous leading-strand synthesis, whereas polymerase δ mainly performs discontinuous lagging-strand synthesis by extending Okazaki fragments [22]. Together, these polymerases convert the parental DNA strands into newly synthesized daughter strands (Figure 1.3).

Replication proceeds bidirectionally from each origin. In each direction, the leading strand is synthesized continuously toward the replication fork, whereas the lagging strand is synthesized discontinuously as short Okazaki fragments that are subsequently processed and ligated into a continuous strand [23]. RNA primers initiate the formation of each Okazaki fragment, after which DNA polymerases extend them. The coordinated activity of the DNA helicase, polymerases, PCNA, topoisomerases, and additional supporting proteins that assist in replication ensures efficient bidirectional replication and accurate duplication of the entire genome [24]. This coordination is essential because even small defects in replication fork progression can leave DNA incompletely replicated or damaged, creating replication stress that threatens chromosome segregation and genome stability.

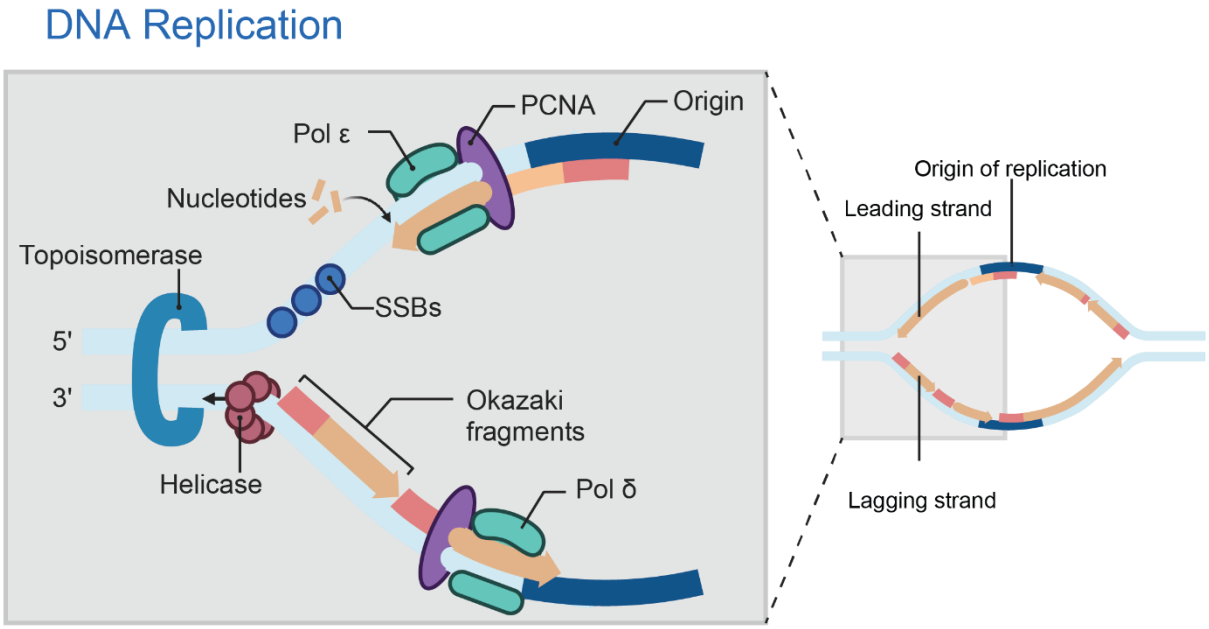


Figure 1.3 | Schematic overview of DNA replication during S phase.
Replication initiates at defined origins where the MCM helicase unwinds the DNA to form replication forks. Single-stranded DNA is stabilized by SSBs, while topoisomerases relieve torsional stress ahead of the fork. PCNA acts as a sliding clamp to ensure processive DNA synthesis by polymerases δ and ε. DNA synthesis proceeds bidirectionally, with continuous synthesis on the leading strand and discontinuous synthesis on the lagging strand through the formation of Okazaki fragments. Image modified using BioRender.com.

1.2.2 Replication stress is a hallmark of cancer

DNA replication is challenged by a variety of endogenous and exogenous obstacles that can slow or block replication fork progression and give rise to replication stress [25]. One common source is the formation of DNA secondary structures, such as G-quadruplexes or hairpins, which can arise at repetitive or G-rich sequences and physically obstruct the replication machinery [26]. Replication can also be impaired by transcription–replication conflicts, which occur when the replication fork encounters active RNA polymerases, transcription complexes, or RNA hybrids known as R-loops [27,28]. These structures can act as barriers to fork movement and increase the risk of fork stalling or collapse.

Replication stress can also result from an imbalance in nucleotide pools, which limits the availability of building blocks required for DNA synthesis and reduces polymerase efficiency. In addition, ssDNA gaps may form when DNA synthesis is interrupted or repriming occurs downstream of a lesion, leaving unreplicated regions behind the fork [29]. Different types of DNA damage further challenge replication. Abasic sites and oxidized or alkylated bases can block replicative polymerases, whereas DNA–protein crosslinks create bulky obstacles on the DNA template. Mis incorporated ribonucleotides can distort DNA structure and interfere with replication, while intra-strand and inter-strand crosslinks prevent normal strand separation or polymerase progression [30]. Together, these obstacles disrupt faithful DNA synthesis and, if not properly resolved, can leave genomic regions under-replicated or damaged before mitosis [31,32] (Figure 1.4).

To ensure completion of DNA replication under these conditions, cells activate a set of DNA damage tolerance pathways that allow replication forks to bypass obstacles without immediate lesion removal. Four major mechanisms operate in this context. Translesion synthesis (TLS) is initiated by RAD18-dependent monoubiquitination of PCNA, which promotes the recruitment of specialized TLS polymerases capable of synthesizing DNA directly across damaged templates [33]. Although efficient, this process is often error prone. In contrast, template switching provides an error-free bypass strategy. RAD18 and UBC13 mediate polyubiquitination of PCNA, enabling the use of the newly synthesized sister chromatid as a template for DNA synthesis, a process that requires RAD51, BLM, and NBS1.

Another important response is fork-reversal, in which the replication fork is remodelled into a four-way junction structure. This reaction, mediated by RAD51 together with fork remodelling enzymes such as SMARCAL1, ZRANB3, HLTF, and FBH1, stabilizes stalled forks and facilitates subsequent repair or template switching [34]. Finally, repriming provides a rapid means to restart DNA synthesis downstream of a lesion. This pathway depends on PRIMPOL, which generates a new primer beyond the obstacle, leaving behind ssDNA gaps that are filled in post-replicatively, and is regulated by ATR–CHK1 signalling [35] (Figure 1.4). Together, these pathways illustrate that cells use multiple coordinated strategies to cope with replication stress. Rather than relying on a single mechanism, translesion synthesis, template switching, fork reversal, and repriming act together to maintain DNA synthesis and preserve genome stability when replication forks encounter blocking lesions [36].

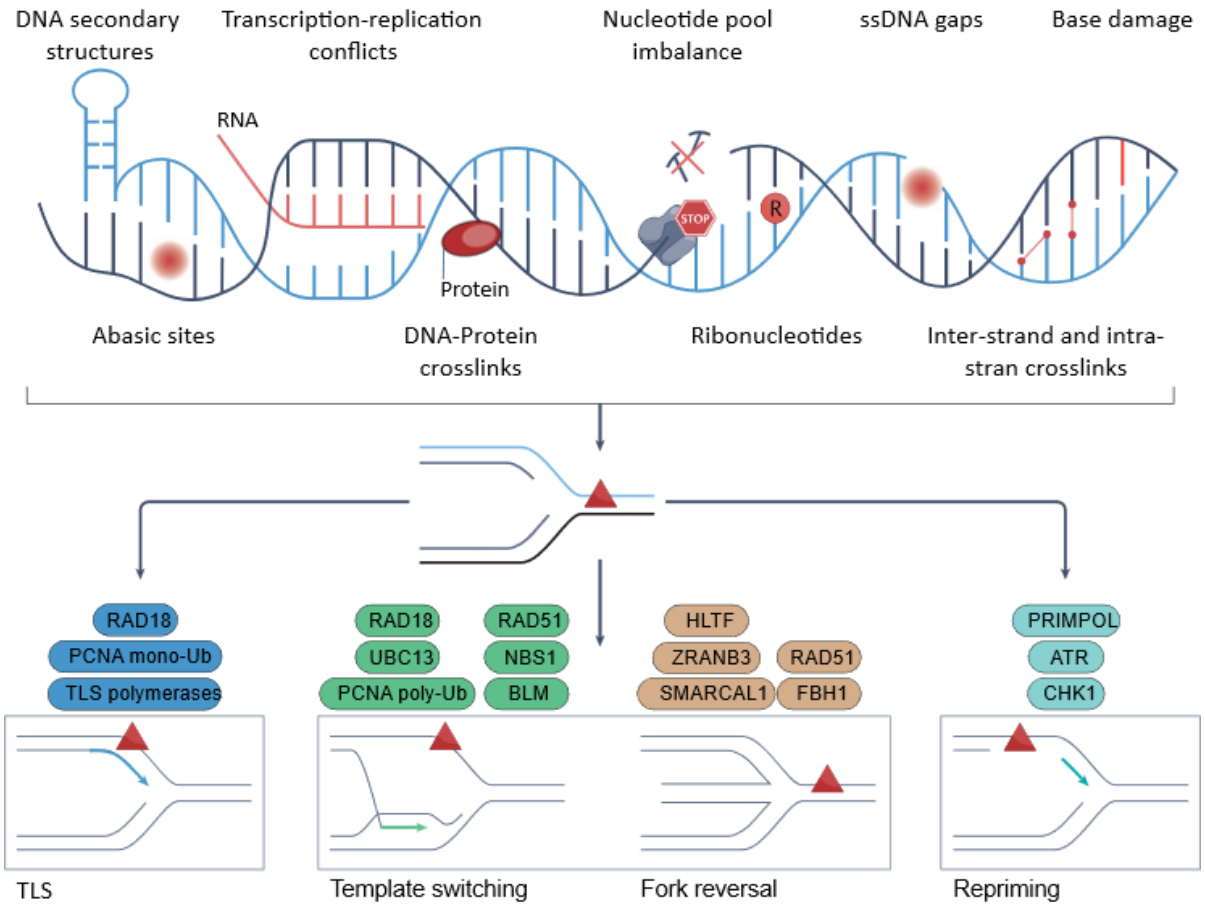


Figure 1.4 | Major pathways and mediators of the replication stress response.
Replication stress arises from endogenous obstacles such as abasic sites, transcription–replication conflicts, ribonucleotide incorporation into DNA, protein–DNA crosslinks, secondary DNA structures, single-stranded DNA gaps or breaks, and nucleotide pool imbalances that stall replicative polymerases. Exogenous sources include DNA inter- and intra-strand crosslinks generated by crosslinking agents and base damage. When replication forks encounter these DNA lesions or roadblocks (indicated by red triangles), DNA damage tolerance mechanisms are activated to ensure fork progression and genome stability. Translesion synthesis (TLS) is initiated by RAD18-dependent monoubiquitination of PCNA, which promotes the recruitment of specialized TLS polymerases to bypass DNA lesions. Template switching is triggered by RAD18- and UBC13-mediated polyubiquitination of PCNA and involves downstream factors such as RAD51, BLM, and NBS1, enabling the use of the undamaged sister chromatid as a template. Fork reversal, a related pathway, remodels stalled forks into four-way junctions through the coordinated action of RAD51, SMARCAL1, ZRANB3, HLTF, and FBH1. In addition, repriming by PRIMPOL allows DNA synthesis to resume downstream of lesions, leaving ssDNA gaps that are filled post-replicatively. PRIMPOL activity is regulated by the ATR–CHK1 signaling pathway. Image source: Adapted from Cybulla and Vindigni 2023.

1.2.3 R-loops and genome stability

R-loops are three-stranded nucleic acid structures composed of an RNA: DNA hybrid and a displaced single-stranded DNA strand [37]. They commonly form during transcription when the nascent RNA transcript anneals back to the complementary DNA template behind RNA polymerase [37,38]. Although R-loops were initially considered rare by-products of transcription, they are now recognized as widespread genomic structures with important physiological roles in transcriptional regulation, DNA repair, replication, and chromatin organization [39]. However, when R-loops accumulate excessively or form at particularly vulnerable genomic regions, such as common fragile sites, highly transcribed loci, or repetitive sequences, they can become a major threat to genome stability.

One important source of R-loop-associated genome instability is the transcription–replication conflict. This occurs when the replication machinery encounters actively transcribing RNA polymerases or transcription-associated nucleic acid structures [40]. In this context, R-loops can act as physical barriers to replication fork progression, increasing the risk of fork stalling, fork collapse, and DNA damage. These conflicts can occur in either co-directional or head-on orientation, with head-on collisions generally creating a stronger obstacle to replication fork movement. Persistent R-loops are therefore particularly harmful at difficult-to-replicate regions, including common fragile sites, highly transcribed loci, such as ribosomal DNA regions, and repetitive sequences [41,42] (Figure 1.5).

To prevent harmful R-loop accumulation, cells rely on several regulatory mechanisms. RNA-processing and RNA-export factors reduce the likelihood that nascent transcripts re-anneal to the DNA template, while RNase H enzymes remove RNA: DNA hybrids by degrading the RNA strand [39,43]. In addition, several helicases and DNA repair proteins help remodel R-loop-containing structures or repair the DNA damage that arises when these structures persist. Defects in these pathways can lead to replication stress, chromosome fragility, and mitotic abnormalities [44].

BLM has recently been linked to the regulation of R-loop-associated genome instability. BLM-depleted human cells and fibroblasts derived from Bloom syndrome patients show increased R-loop-associated genome instability. Moreover, BLM localizes near R-loops in cells and can resolve R-loop structures in vitro with an efficiency comparable to its activity on D-loop substrates. These findings suggest that BLM contributes to genome stability not only through its established roles in homologous recombination and replication fork recovery, but also by limiting harmful R-loop accumulation and reducing transcription–replication conflicts [45].

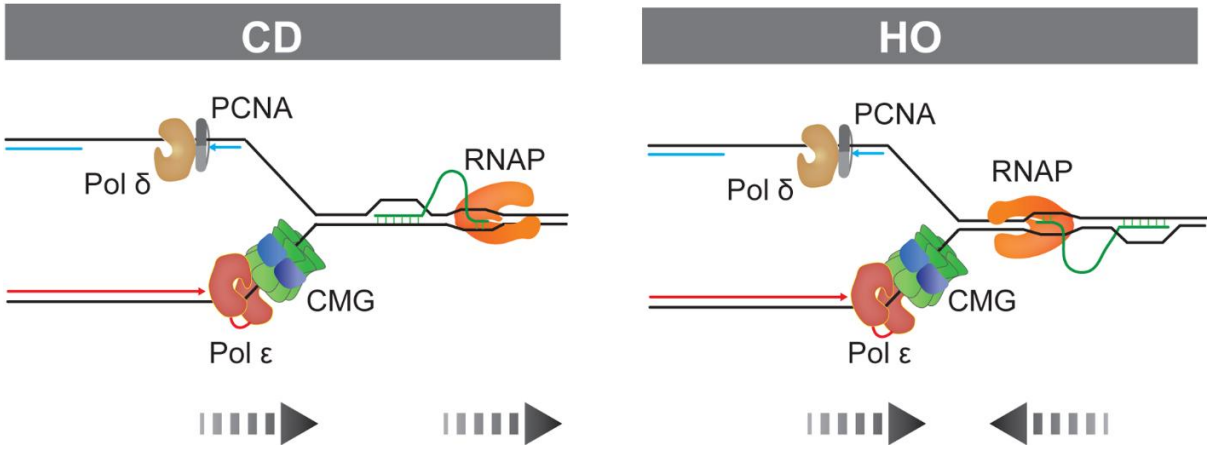


Figure 1.5 | Co-directional (CD) and head-on (HO) collisions between replisomes and co-transcriptional R-loops in eukaryotes.
Parental DNA strands are indicated in black, nascent leading and lagging strands are in red and blue, respectively. Dashed arrows represent directions of replication and transcription (Kumar and Remus, 2023).

1.2.4 Consequences of Replication Stress and the Cellular DNA Repair Response

So far, DNA replication and the cellular response to replication stress have been introduced. However, replication stress is not only a problem during S phase. If stalled forks or damaged replication intermediates are not properly processed, they can persist into G2 and mitosis and threaten faithful chromosome segregation. Therefore, cells depend on several repair and damage-tolerance pathways to stabilize stalled forks, complete DNA synthesis, and prevent damaged or under-replicated DNA from being transmitted to daughter cells [24]. One of the earliest consequences of replication fork stalling is the accumulation of single-stranded DNA (ssDNA) (Figure 1.6). This occurs when helicase activity continues while DNA polymerase progression is slowed or blocked. The exposed ssDNA is rapidly coated by RPA, which protects the DNA and promotes activation of the ATR–CHK1 checkpoint pathway. This checkpoint stabilizes stalled forks, slows cell-cycle progression, and allows time for repair or replication restart [46,47].

Replication can also continue past blocking lesions through repriming downstream of the damage. This process is mediated in part by PRIMPOL and allows DNA synthesis to restart without prolonged fork arrest [29]. However, repriming leaves behind post-replicative ssDNA gaps opposite the lesion (Figure 1.6). These gaps must later be filled to complete DNA replication. Gap filling can occur through RAD51-dependent homologous recombination-mediated repair, template switching, or translesion synthesis. Homologous recombination and template switching use the sister chromatid or newly synthesized strand as a template and are therefore generally accurate. In contrast, translesion synthesis polymerases can synthesize across damaged bases but have lower fidelity than replicative polymerases, making this pathway more mutagenic [48–50].

If replication-associated lesions are not bypassed or repaired, stalled forks can collapse and generate double-strand breaks (DSBs) (Figure 1.6). DSBs are among the most cytotoxic DNA lesions and are repaired mainly by homologous recombination (HR) or non-homologous end joining (NHEJ). HR is mainly active in S and G2 phases and uses the sister chromatid as an intact template, making it largely error-free. In contrast, NHEJ directly ligates broken DNA ends without using a homologous template and can therefore introduce small insertions or deletions at the break site. Thus, the repair pathway used after fork collapse strongly influences whether genome integrity is restored accurately or whether mutations and chromosome rearrangements are introduced [51,52].

Post-replicative ssDNA gaps must be repaired after fork passage to restore complete DNA synthesis. Several pathways can contribute to this process. In homologous recombination-mediated gap repair, RAD51-dependent strand invasion can use the newly synthesized sister chromatid as a template to fill the missing DNA. Template switching provides a related error-free mechanism, in which the undamaged sister strand is used to bypass the lesion and complete DNA synthesis. In some cases, translesion synthesis polymerases can also fill gaps by synthesizing across damaged bases, although this pathway is more error-prone because these polymerases have lower fidelity than replicative polymerases. Therefore, the pathway used to fill ssDNA gaps influences both replication completion and mutation risk [53].

Replication stress can also be caused by bulky lesions such as DNA–protein crosslinks (DPCs), which physically block DNA polymerases and can also interfere with transcription. DPC repair often requires proteolytic processing of the protein adduct by specialized proteases such as SPRTN, followed by removal of the remaining DNA damage and gap filling by DNA synthesis. Nucleotide excision repair-related mechanisms and other repair factors can also contribute depending on the type and context of the lesion [54].

Together, these pathways show that replication stress is handled in a stepwise manner. First, cells stabilize stalled forks and activate checkpoint signalling. Second, they bypass blocking lesions or restart DNA synthesis downstream of them. Third, the resulting gaps, breaks, or damaged intermediates are repaired by appropriate DNA repair pathways. If these processes fail, under-replicated DNA and unresolved repair intermediates can persist into mitosis. These structures may appear as ultrafine anaphase bridges or chromatin bridges and can break during anaphase or cytokinesis, leading to chromosome breaks, mis segregation of chromosomal fragments, micronucleus formation, and

aneuploidy. In this way, replication stress directly links defective DNA synthesis to chromosomal instability, tumorigenesis, aging, and cellular dysfunction [24].

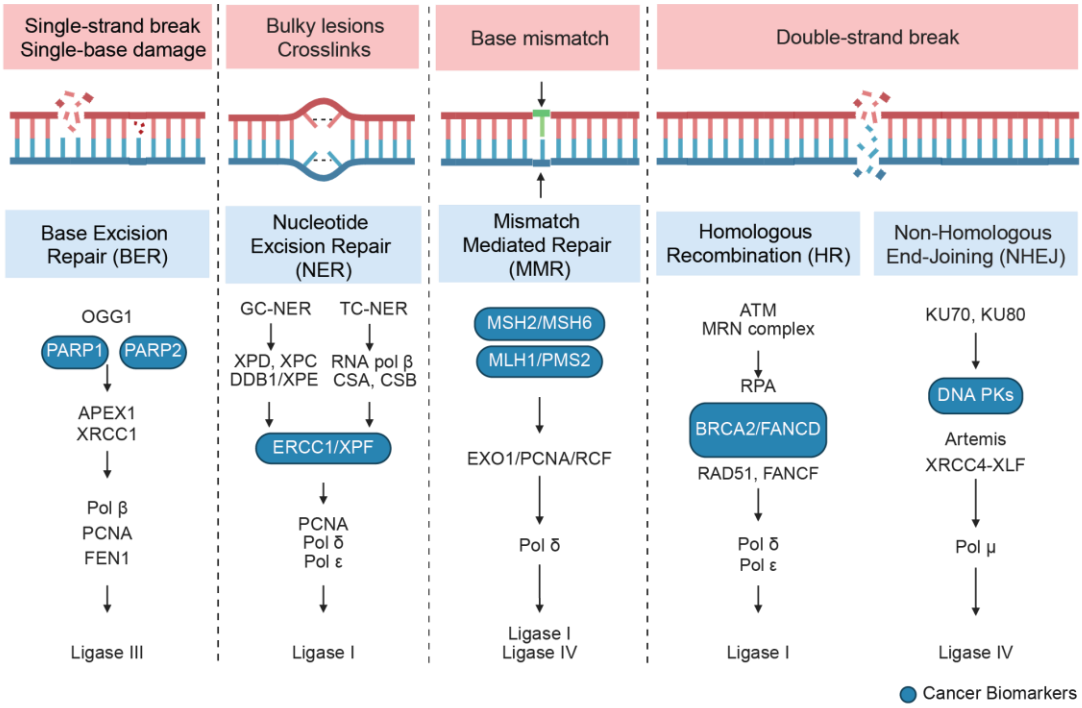


Figure 1.6 | DNA damage types induced by replication stress and their corresponding repair pathways.
Major DNA damage types include single-stranded DNA (ssDNA), single-strand breaks (SSBs), double-strand breaks (DSBs), base mismatches, bulky adducts, DNA crosslinks, and oxidative base damage. These lesions are resolved by specialized DNA repair mechanisms. Base excision repair (BER) removes small base lesions and SSBs. Mismatch repair (MMR) corrects replication errors using the MSH2–MSH6 and MLH1–PMS2 complexes together with EXO1, PCNA, Pol δ/ε, and Ligase I. Nucleotide excision repair (NER), including global genome NER (GG-NER) and transcription-coupled NER (TC-NER), eliminates bulky DNA lesions. DSBs are repaired either by non-homologous end joining (NHEJ) or by homologous recombination (HR). Together, the figure illustrates how replication stress–induced DNA damage is detected and processed by multiple, highly coordinated repair pathways to maintain genome integrity. Image modified using BioRender.com.

1.2.5 Consequences of replication stress in mitosis

In eukaryotes, replication stress often results in under-replicated DNA (UR-DNA) and unresolved replication intermediates that persist into mitotic entry, where they interfere with faithful chromosome segregation [55]. This can lead to several mitotic abnormalities that compromise genome stability and promote chromosomal instability. One major outcome is the formation of lagging chromatin, in which chromosome fragments or entire chromosomes fail to segregate properly during anaphase and remain trapped between the two daughter nuclei. These lagging structures can subsequently give rise to micronuclei, small extranuclear bodies that contain mis segregated DNA [56]. Replication stress can also generate persistent DNA connections between sister chromatids, leading to anaphase bridges that physically link the separating chromosome masses and can impair cytokinesis, resulting in binucleation [57]. In addition, replication stress increases the risk of whole chromosome mis segregation, causing aneuploidy, where daughter cells inherit an abnormal number of chromosomes

[58]. Together, these mitotic defects represent key mechanisms by which replication stress promotes genomic instability and contributes to disease development, including cancer (Figure 1.7).

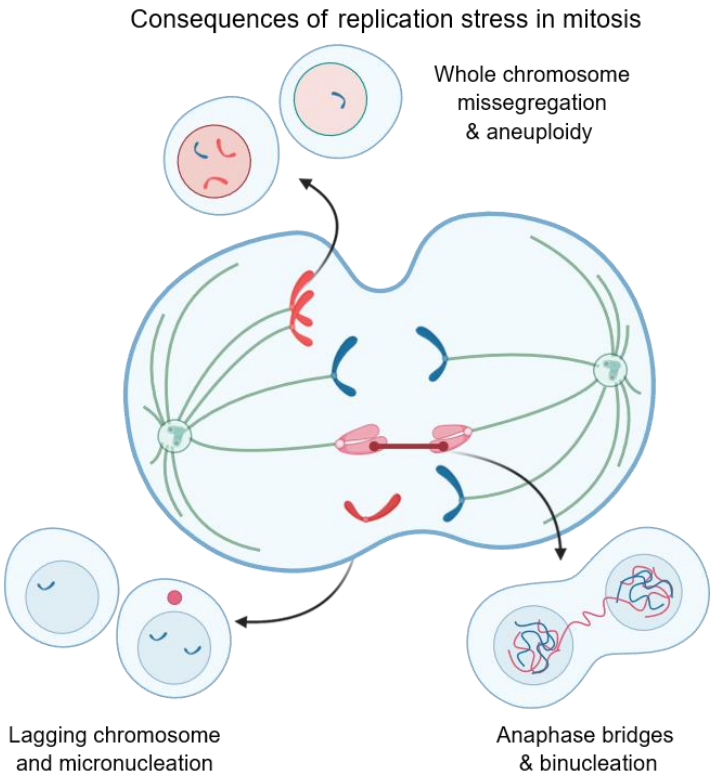


Figure 1.7 | Consequences of replication stress in mitosis and chromosome mis-segregation.
Replication stress can impair faithful chromosome segregation, resulting in mitotic abnormalities such as lagging chromatin and micronucleation, anaphase bridges associated with cytokinesis failure and binucleation, and whole chromosome mis segregation leading to aneuploidy. These defects promote chromosomal instability and contribute to tumor development. Image adapted from van Jaarsveld and Kops (2016) and modified using BioRender.com.

1.3 Anaphase bridges and their resolution

During anaphase, sister chromatids can segregate accurately only if all DNA connections between them have been removed. However, unresolved DNA intermediates can persist into mitosis and form anaphase bridges. As illustrated in Figure 1.8, these structures can be broadly classified into chromatin bridges and ultra-fine DNA bridges (UFBs)[57,59]. These two classes differ in their molecular composition, origin, detection, and consequences for genome stability.

1.3.1 Chromatin bridges

Chromatin bridges contain DNA structures with nucleosomes and other chromatin components, making them detectable by conventional DNA staining [60]. Chromatin bridges can arise through several mechanisms. One major source is the formation of dicentric chromosomes, which contain two centromeres and are often generated by telomere dysfunction, telomere shortening, or telomere–telomere fusions. During anaphase, the two centromeres of a dicentric chromosome can be pulled toward opposite spindle poles, creating a visible chromatin bridge between the separating

chromosome masses. Chromatin bridges can also arise when sister chromatids remain physically linked because of unresolved DNA catenanes or defects in the removal of cohesion before chromosome segregation. In these cases, the bridge reflects a failure to fully separate replicated chromatids before [61]. The mechanical force generated during anaphase can stretch these bridges and eventually cause chromosome breakage. Broken chromosome ends may then be incorrectly rejoined, producing new fusion chromosomes that can enter another round of breakage during the next mitosis. This process, known as the breakage–fusion–bridge cycle, can drive repeated chromosome breakage, amplifications, deletions, and complex rearrangements. Therefore, chromatin bridges are not only markers of segregation failure, but also active drivers of chromosomal instability and genome rearrangement [62,63].

1.3.2 Ultrafine anaphase bridges

UFBs were first discovered in 2007. They are present in all species and are more abundant than chromatin bridges [64]. UFBs can originate from distinct genomic regions and arise from persistent DNA intertwining structures between sister chromatids, including incompletely replicated DNA, Holliday junction (HJ)-like recombination intermediates, and double-stranded DNA (dsDNA) catenates [65]. UFB formation is closely linked to replication errors and replication stress [57], and their frequency can be enhanced by replication-perturbing agents such as thymidine, aphidicolin, mitomycin C, and hydroxyurea [66]. UFBs are categorized into several subtypes: centromeric UFBs (C-UFBs), telomeric UFBs (T-UFBs), fragile site UFBs (FS-UFBs), homologous recombination-associated UFBs (HR-UFBs), and ribosomal UFBs (r-UFBs) [67,68]. Although UFBs arise from different genomic regions, they are often marked by a common set of proteins involved in their detection and resolution. PICH (PLK1-interacting checkpoint helicase) is an early UFB marker that binds stretched DNA. In mammalian cells, UFBs are frequently coated by the helicases PICH, BLM, and FANCM [69]. The presence of multiple UFB subtypes highlights the complexity of mitotic chromosome processing and may provide insight into mechanisms that drive chromosome rearrangements during tumour evolution.

Centromeric UFBs (C-UFBs)

Centromeric ultrafine anaphase bridges (C-UFBs) represent one of the most frequently observed classes of UFBs and can be detected even in unperturbed mitotic cells. Unlike common fragile site–associated UFBs, which are strongly linked to replication stress and Fanconi anaemia (FA) pathway activity, C-UFBs are generally considered non-FA-associated UFBs [70]. They originate from centromeric regions, which are highly specialized heterochromatic domains that maintain sister chromatid cohesion until metaphase and are among the last genomic regions to complete topological resolution before chromosome segregation (REF). Because sister centromeres remain closely paired until

anaphase onset, centromeric DNA is particularly susceptible to the persistence of unresolved double-stranded DNA catenanes. C-UFBs are therefore thought to mainly consist of fully replicated but still interlinked double-stranded DNA molecules that arise when sister chromatids fail to decatenate completely before anaphase [71]. Their resolution depends strongly on topoisomerase IIα (TOP2α), which removes DNA catenanes by passing one double-stranded DNA segment through another. Consistent with this role, C-UFBs are rapidly resolved during anaphase under normal conditions, whereas their frequency increases when TOP2α activity is inhibited, for example by ICRF-193 [72]. C-UFBs can be distinguished from other UFB classes by their colocalization with centromere-associated markers such as CENP-A at the bridge termini [73].

Fragile sites UFBs (FS-UFBs)

Common fragile sites (CFSs) are genomic loci that are difficult to replicate because they often replicate late in S phase, contain a low density of replication origins, and are enriched in sequences that can form secondary DNA structures. As a result, replication forks passing through CFSs are particularly susceptible to slowing or stalling under mild replication stress. This can leave segments of DNA under-replicated when cells enter mitosis and thereby promote the formation of fragile site ultrafine anaphase bridges (FS-UFBs) [74].

Unlike C-UFBs, which are frequently seen in healthy or unstressed cells, FS-associated UFBs are rare [75]. As an alternative several treatments can be used to induce replication stress, including hydroxyurea, cisplatin, mitomycin C, and aphidicolin. However, low-dose aphidicolin is particularly relevant for the study of CFS-associated replication stress because it partially inhibits replicative DNA polymerases and slows DNA synthesis without completely blocking cell-cycle progression. Under these conditions, difficult-to-replicate regions such as CFSs are more likely to remain incompletely replicated when cells enter mitosis [50,76,77].

Fanconi anaemia proteins FANCD2 and FANCI localize to CFSs during late S phase and G2. If replication or repair at these regions is not completed before mitosis, the unresolved intermediates can persist into anaphase and appear as FS-UFBs. These bridges are often flanked by FANCD2- and FANCI-positive sister foci at both ends, indicating that they originate from fragile site-associated replication intermediates [78]. Unlike many centromeric UFBs, FS-UFBs can also contain regions coated by the single-stranded DNA-binding protein complex RPA, suggesting that they include single-stranded DNA generated during the processing of under-replicated intermediates.

Several pathways help prevent CFS-derived intermediates from persisting into anaphase. FANCD2 and FANCI support efficient replication and repair at CFSs by stabilizing stalled forks and recruiting DNA repair factors. They have also been linked to the processing of transcription–replication conflicts,

including R-loop-associated structures, for example through the recruitment of RNA-processing factors such as DDX47 to sites of conflict [79].

In early mitosis, cells can still complete DNA replication at CFS regions through a process known as mitotic DNA synthesis (MiDAS). This process often involves the nuclease MUS81, which introduces controlled DNA cuts at under-replicated regions. These cuts allow the DNA to be processed and extended through a repair mechanism similar to break-induced replication. If MUS81 activity or MiDAS is impaired, these regions remain under-replicated, leading to increased FS-UFB formation. This indicates that MUS81-mediated processing and late-stage DNA synthesis are important for completing replication before chromosomes segregate during mitosis [55]. If CFS-associated lesions are not fully repaired or resolved during mitosis, they can be transmitted into daughter cells. In the following G1 phase, these unresolved lesions are often marked by 53BP1 nuclear bodies, which are thought to protect inherited DNA damage until repair can be completed. Thus, FS-UFBs represent a visible mitotic consequence of incomplete CFS replication. Their persistence can promote chromosome breakage, micronucleus formation, and chromosomal instability, linking replication stress at fragile sites to genome instability and chromosome rearrangements [80].

Telomeric UFBs (T-UFBs)

Telomeric ultra-fine anaphase bridges (T-UFBs) originate from telomeric regions located at the ends of linear chromosomes. Telomeres are specialized nucleoprotein structures composed of G-rich tandem repeat sequences that are recognized by specialize proteins and together form protective caps, preventing chromosome ends from being recognized as DNA breaks and from undergoing end-to-end fusion [81]. A key structural feature of telomeres is the T-loop, in which the telomeric DNA folds back on itself to shield the chromosome terminus. These regions are inherently difficult to replicate due to their repetitive sequence composition and complex DNA architecture, making them particularly susceptible to replication perturbations [82].

T-UFBs form when telomere replication is delayed or perturbed, making them conceptually similar to FS-UFBs [83]. Telomeres are protected by the shelterin complex, which includes proteins such as TRF1, TRF2, POT1, TIN2, TPP1, and RAP1. This complex prevents chromosome ends from being recognized as DNA breaks and supports proper replication of telomeric repeats. When shelterin function is disturbed, for example by altered TRF2 activity or expression of defective TRF2 variants, telomere structure and protection can be impaired. As a result, telomeres may become difficult to replicate or remain physically linked between sister chromatids. These unresolved telomeric connections can persist into anaphase and appear as telomeric UFBs [84].

BLM helicase plays an important role in telomere replication and in the resolution of T-UFBs. Under conditions of replication stress, such as aphidicolin treatment, BLM is frequently detected on telomeric UFBs, where it is recruited by the shelterin component TRF1 [85]. This recruitment suggests that BLM promotes replication through telomeric regions. In addition, inhibition of topoisomerase IIα with ICRF-193 can induce T-UFBs, and TRF1 has been shown to recruit TOP2α to telomeres, indicating that some T-UFBs represent fully replicated but catenated telomeric DNA that requires TOP2α-mediated decatenation for resolution during mitosis [86]. Together, these findings indicate that telomeres require both BLM-dependent replication support and TOP2α-dependent decatenation to prevent unresolved telomeric DNA links from persisting into anaphase.

Homologous Recombination UFBs (HR-UFBs)

Homologous recombination (HR), while essential for the accurate repair of DNA double-strand breaks and interstrand crosslinks, can itself generate persistent DNA entanglements that give rise to a distinct subtype of ultra-fine anaphase bridges known as HR-UFBs [32,87,88]. These bridges arise when homologous recombination intermediates fail to be fully resolved before cells enter mitosis. During anaphase, HR-UFBs are typically marked by the helicases PICH and BLM, and they are subsequently converted into single-stranded DNA bridges coated by the replication protein RPA [57].

Unlike fragile site–associated UFBs, HR-UFBs are not generally linked to FANCD2 foci, highlighting their distinct origin. Consistent with this, inhibition of key HR factors such as RAD51 or BRCA2 leads to a reduction in FANCD2-negative UFBs, supporting the view that HR activity directly contributes to their formation. In contrast, loss of 53BP1, a protein involved in DNA double-strand break recognition and repair, results in an increase in HR-UFBs, suggesting that imbalances in DNA repair pathway choice can influence their frequency [89]. Thus, HR-UFBs represent a cytological manifestation of unresolved recombination intermediates and highlight the importance of completing HR before chromosome segregation.

Ribosomal ultra-fine anaphase bridges (R-UFBs)

Ribosomal UFBs arise from ribosomal DNA (rDNA) loci, which are highly repetitive genomic regions that pose challenges for chromosome replication, repair, and segregation. These loci remain transcriptionally active even in early mitosis [90]. Ongoing transcription can interfere with chromosome condensation and DNA decatenation, increasing the likelihood of bridge formation [91]. The most specific protein marker for R-UFBs is the presence of the protein UBF (Upstream Binding Factor), creating UBF-positive signals at their termini, and indicating that the bridge originates from rDNA regions [92]. R-UFBs are primarily composed of unresolved double-stranded DNA catenanes and are typically recognized by the proteins PICH and TOP2α, which facilitate their processing and resolution. Consistent with this,

inhibition of TOP2α with ICRF-193 or depletion of PICH leads to a marked increase in R-UFB frequency, underscoring the importance of proper decatenation for rDNA segregation [90]. In addition to catenation-based mechanisms, R-UFBs can also originate from unresolved homologous recombination intermediates or RNA–DNA hybrid structures formed during active rDNA transcription, reflecting the multiple molecular pathways that contribute to their formation [93].

While UFBs can arise from different genomic regions, many of them appear to be processed by shared DNA-processing factors. Several core UFB-associated factors, including the DNA translocase PICH, the BLM helicase, and replication protein A (RPA), have been consistently detected on multiple UFBs' subtypes [89]. Among these factors, PICH is proposed to act as one of the earliest responders to UFB formation. This may reflect its ability to recognize histone-free DNA structures or DNA under mechanical tension during mitosis [94]. In line with this idea, PICH has been observed to coat mitotic chromatin after nuclear envelope breakdown, particularly during prometaphase and at kinetochore-associated regions [95].

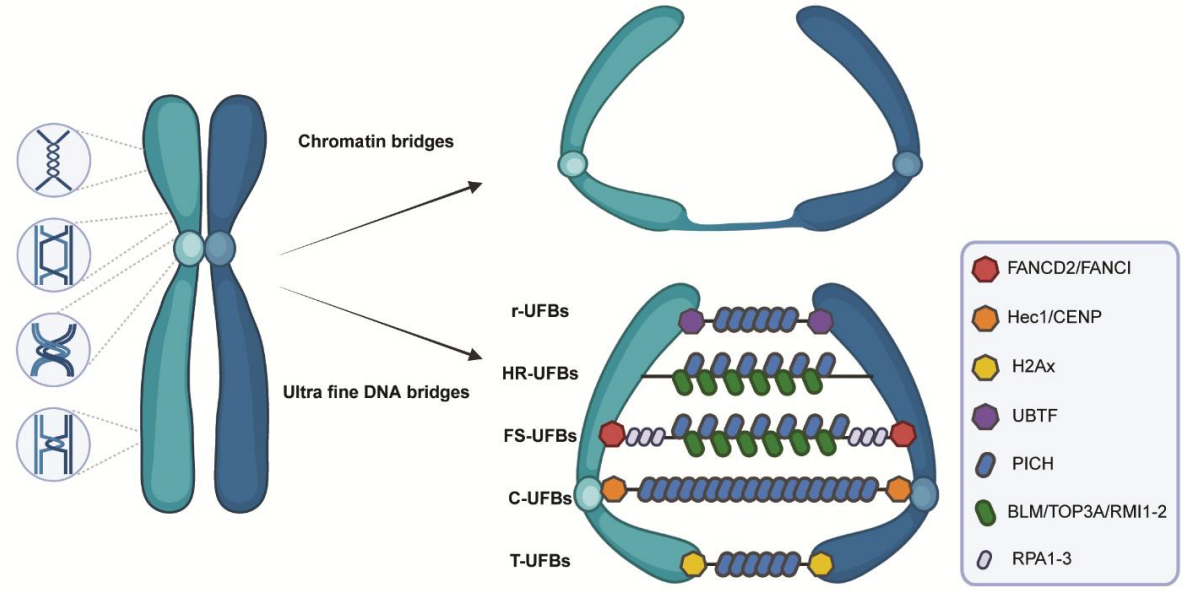


Figure 1.8 | DNA anaphase bridges and major classes of ultra-fine anaphase bridges (UFBs).
Anaphase bridges represent DNA connections between segregating sister chromatids and can be broadly classified into chromatin bridges and ultra-fine anaphase bridges (UFBs). UFBs are currently grouped into five major categories based on their origin: centromeric UFBs (C-UFBs), which arise at centromeres and mainly consist of dsDNA catenates; ribosomal UFBs (r-UFBs), which originate from rDNA loci; fragile site UFBs (FS-UFBs), which result from unresolved replication intermediates at common fragile sites; homologous recombination-associated UFBs (HR-UFBs), which form from unresolved recombination intermediates; and telomeric UFBs (T-UFBs), which arise at telomeres due to replication defects or telomere dysfunction, including altered shelter in regulation and end-to-end chromosome fusions. Image created/modified using BioRender.com.

1.3.3 Bloom syndrome helicase: from homologous recombination to UFB resolution

Bloom syndrome helicase (BLM) is a conserved member of the RecQ family of DNA helicases and plays an important role in maintaining genome stability. BLM is particularly important during homologous recombination (HR)-mediated DNA repair and during replication stress, where it contributes to the stabilization, restart, and repair of stalled or collapsed replication forks [96] (Figure 1.9). In vitro, BLM can act on a wide range of DNA and nucleic acid substrates, including Holliday junctions, D-loops, G-quadruplexes, RNA: DNA hybrids, and single-stranded DNA overhangs. Loss of BLM function causes Bloom syndrome, a rare genetic disorder characterized by elevated sister chromatid exchanges, chromosomal instability, and increased cancer predisposition [97].

During HR repair, DNA lesions such as double strand breaks or interstrand crosslinks can generate recombination intermediates, including double Holliday junctions (dHJs), which physically connect sister chromatids. These intermediates must be resolved before chromosome segregation to prevent the formation of persistent DNA linkages. BLM functions together with TOP3A, RMI1, and RMI2 in the so-called BTRR complex. This complex promotes dHJ dissolution by catalysing branch migration and decatenation, thereby generating non-crossover products and limiting potentially harmful chromosomal rearrangements [98].

In contrast to structure-specific nucleases such as MUS81 and GEN1, which resolve recombination intermediates by cleavage and can generate both crossover and non-crossover products, the BTRR complex mainly promotes dissolution without DNA breakage [99]. This makes BLM-dependent dissolution an important mechanism for preserving genome integrity during DNA repair. Consistent with this role, BLM-deficient cells show elevated levels of sister chromatid exchanges and defects in the processing of complex DNA structures [100]. BLM has also been implicated in the resolution of ultrafine anaphase bridges (UFBs). BLM localizes to UFBs together with PICH and contributes to their processing during anaphase [64]. PICH is thought to recruit or stabilize BLM-containing complexes on UFBs, where the BTRR complex may help disentangle unresolved DNA intermediates [101]. In several UFB classes, BLM-dependent processing is associated with the generation of single-stranded DNA regions that become coated by replication protein A (RPA) [57]. However, the precise molecular mechanism by which BLM and the BTRR complex promote UFB resolution remains incompletely understood.

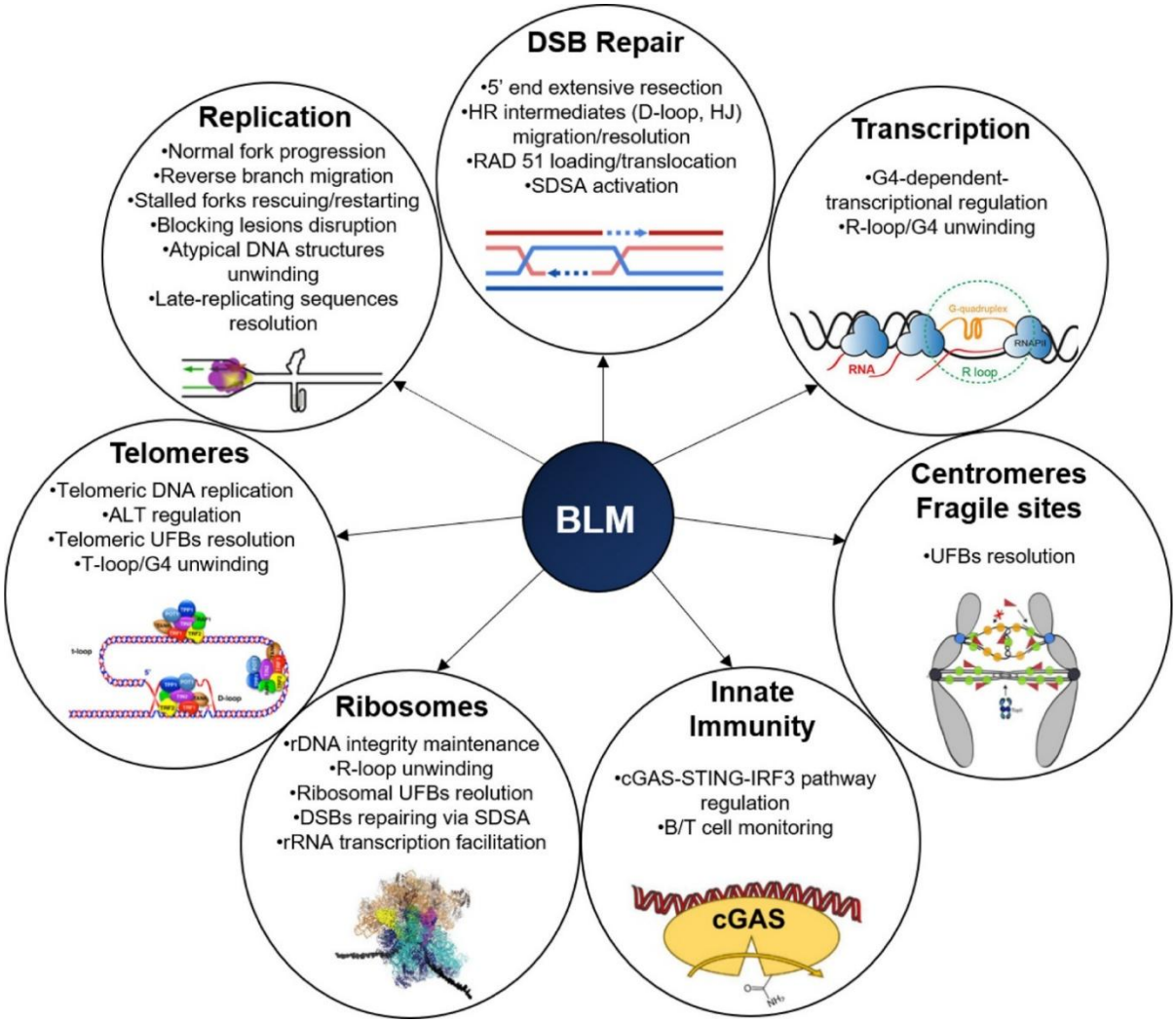


Figure 1.9 | Overview of BLM functions in genome maintenance.
Schematic representation of the diverse roles of BLM across cellular compartments and DNA metabolic pathways. During DNA replication, BLM promotes replication fork progression, restart, and reverse branch migration, while facilitating the resolution of DNA structures that impede fork movement. BLM also unwinds secondary nucleic acid structures, including G-quadruplexes (G4s) and R-loops, thereby supporting efficient DNA replication and transcription. In homologous recombination (HR), BLM processes recombination intermediates, such as displacement loops (D-loops) and Holliday junctions to ensure accurate DNA repair. Additional functions include the maintenance of telomere integrity, particularly in alternative lengthening of telomeres (ALT)-positive cells, and the preservation of ribosomal DNA (rDNA) stability. BLM is further implicated in the resolution of ultrafine anaphase bridges (UFBs) arising from centromeric DNA, under-replicated regions, recombination intermediates, telomeres, and rDNA loci. Emerging evidence also suggests a role for BLM in regulating innate immune signaling through the cGAS–STING–IRF3 pathway. Adopted from (Ababou et al. 2021).

1.3.4 FANCD2 and FANCI in replication stress, common fragile site maintenance, and FS-UFB resolution

FANCD2 and FANCI are central components of the Fanconi anaemia pathway and function together as the FANCI-FANCD2, or known as ID2, complex [102]. In response to DNA damage and replication stress, the FA core complex monoubiquitinates FANCD2 and FANCI, allowing the complex to accumulate on damaged or difficult-to-replicate DNA together with BRCA1, BRCA2, and other repair factors [103]. Structural studies showed that FANCD2 and FANCI form a DNA-binding heterodimer, and more recent

work suggested that monoubiquitination stabilizes the ID2 complex on DNA as a clamp-like scaffold [104,105]. Therefore, FANCD2 and FANCI are best understood as DNA-associated organizers of the replication stress response rather than enzymes that directly cut or unwind DNA.

The function of ID2 complex is particularly important at common fragile sites (CFSs). CFSs often replicate late, contain few replication origins, and are frequently located within large genes [106]. FANCD2 and FANCI localize to fragile regions during late S phase and G2, where they help stabilize stalled forks, protect replication intermediates, and recruit downstream repair factors. One important downstream factor is FAN1, which is recruited by ubiquitinated FANCD2 and helps regulate fork progression and reduce chromosome abnormalities under replication stress [107,108].

The role of FANCD2 and FANCI at CFSs is closely linked to mitotic DNA synthesis (MiDAS). When replication remains incomplete at CFSs, cells can still perform late DNA synthesis in early mitosis. This process depends on factors such as MUS81 and POLD3 and helps complete replication before chromosome segregation. FANCD2-positive twin foci are commonly observed at CFS-associated regions in prometaphase and anaphase, marking loci that require late processing [108,109].

FANCD2 and FANCI have also been linked to transcription-replication conflicts. Many CFSs overlap with large actively transcribed genes, where transcription can interfere with replication fork progression. FANCD2 has further been associated with R-loop processing and RNA-processing factors such as DDX47 under mild replication stress, suggesting that the ID2 complex helps protect difficult-to-replicate genomic regions from transcription-associated replication stress [79].

FS-UFBs therefore represent a visible mitotic consequence of incomplete CFS replication. These bridges often arise between FANCD2- and FANCI-positive sister foci and can contain regions coated by RPA, indicating the presence of single-strand DNA generated during processing of under-replicated or damaged replication intermediates. This supports a model in which FANCD2 and FANCI contribute to FS-UFB resolution indirectly [110]. Their main role in FS-UFB biology is likely to mark, stabilize, and coordinate the processing of fragile site-associated replication intermediates so that these structures can be resolved before they cause chromosome breakage, micronucleus formation, or chromosomal instability.

1.3.5 PICH as an early bridge-recognition factor in UFB resolution

PICH, also known as ERCC6L, is a mitotic SNF2-family ATPase and DNA translocase that plays a central role in the detection and processing of UFBs [111,112]. Unlike many chromatin-associated ATPases, PICH is largely excluded from the nucleus during interphase and associates with chromosomes only after nuclear envelope breakdown[111]. During mitosis, PICH binds to stretched DNA structures and is one of

the earliest and most used markers of UFBs[64,112]. Its localization to these structures suggests that PICH recognizes physical or topological features of stretched DNA rather than a specific DNA sequence[112]. Once bound, PICH can remodel DNA and promote the recruitment or stabilization of other UFB marker proteins, including BLM, TOP3A, TOP2A, and RIF1[59,94,113]. More recent studies further showed that PICH function is regulated by SUMOylation and SUMO-interacting motifs, indicating that its activity on mitotic bridges is controlled not only by DNA topology but also by post-translational modification pathways[114].

Together, these findings support a model in which PICH acts as an early bridge-recognition and bridge-remodelling factor. Rather than resolving UFBs alone, PICH likely creates a platform that allows other processing enzymes, including the BTRR complex and topoisomerase-dependent pathways, to bind and resolve UFBs.

1.3.6 TOP3A in homologous recombination, replication stress, and mitotic UFB resolution

Topoisomerase IIIα (TOP3A) is the type IA topoisomerase of the BTRR complex, which consists of BLM, TOP3A, RMI1, and RMI2[115]. TOP3A functions as a specialized topological enzyme during both interphase and mitosis. Biochemically, TOP3A cleaves single-stranded DNA, forms a 5′-phosphotyrosyl intermediate, opens a protein-mediated ssDNA gate, allows passage of a second DNA strand, and then re-ligates the broken strand[116]. Classical biochemical work showed that purified human TOP3A relaxes negatively supercoiled DNA in a magnesium-dependent manner and forms a covalent intermediate with ssDNA[117]. More recent optical-tweezers studies of human TOP3A-RMI1-RMI2 directly visualized gate opening and showed that the open gate can capture either an ssDNA or a dsDNA transported strand. These findings support the view that TOP3A is specialized for hemicatenane removal and topological simplification of complex DNA intermediates[118].

In interphase, TOP3A functions mainly within homologous recombination (HR) DNA repair and replication pathways. During homologous recombination, the BTRR complex dissolves double Holliday junctions to generate non-crossover products[119]. TOP3A-RMI1/2 also influences how BLM processes D-loops and cooperates with MRN and DNA2 during long-range DNA-end resection[120].

In mitosis, TOP3A is part of the UFB-processing machinery. Previous Study showed that TOP3A colocalizes with BLM and RMI1 on UFBs, placing TOP3A in a mitotic chromosome-disjunction pathway[87]. Reconstitution experiments further showed that PICH coats stretched double-stranded bridge DNA, recruits BTRR to dsDNA segments, and enables TOP3A-containing complexes to simplify topological linkages. In contrast, RPA excludes BTRR from ssDNA-rich bridge regions. This distinction is important for FS-UFBs and HR-associated UFBs, which can contain both dsDNA and processed ssDNA.

Therefore, TOP3A is unlikely to coat the entire bridge uniformly. Instead, it probably acts on bridge regions that retain DNA structures compatible with type IA strand-passage activity[101].

1.3.7 RPA1–3 in Replication Stress and Ultrafine Bridge Biology

Replication protein A (RPA) is a heterotrimeric ssDNA-binding complex composed of RPA1, RPA2, and RPA3[121,122]. During interphase, RPA binds exposed ssDNA that forms during DNA replication, replication stress, or DNA-end resection. By coating ssDNA, RPA protects it from degradation and prevents the formation of secondary structures[122]. RPA-coated ssDNA also provides a binding platform for ATRIP-ATR and TopBP1, leading to activation of the ATR-Chk1 checkpoint pathway and promoting replication stress signalling and DNA repair[123,124].

RPA is also involved in homologous recombination. After DNA-end resection, RPA first binds the newly generated ssDNA. It is then replaced or remodelled by recombination factors such as BRCA2, RAD52, and RAD51, allowing RAD51 filament formation and repair by homologous recombination[125]. Single-molecule studies showed that RPA can bind ssDNA stably, but it can also exchange with free RPA molecules and move along ssDNA. This dynamic behaviour explains how RPA can protect ssDNA while still allowing access to repair and replication factors[126].

During mitosis, RPA primarily marks single-stranded DNA regions rather than all UFBs. This is important because UFBs can contain different DNA structures. PICH and the BTRR complex mainly act on stretched double-stranded DNA regions, whereas RPA accumulates on single-stranded regions generated during bridge processing[101]. RPA-coated UFBs have been observed in HR-associated UFBs and FS-UFBs, where they likely reflect processed or under-replicated DNA[57]. Therefore, RPA is best understood as a marker and protector of single-stranded DNA on UFBs rather than as a general UFB marker.

1.4 Candidate proteins and experimental strategy

Preliminary analysis from my master's thesis identified apurinic/apyrimidinic endo deoxyribonuclease 1 (APEX1) and Aly/REF export factor (ALYREF) as potential candidate proteins associated with UFB-related protein complexes[127]. ChIP-MS analysis of FANCD2 and BLM experiments showed enrichment of APEX1 and ALYREF after aphidicolin treatment. Immunofluorescence experiments further suggested that both candidate proteins colocalized more frequently with UFBs under replication stress. Together, these findings supported a more detailed analysis of APEX1 and ALYREF in UFB-associated genome stability pathways.

1.4.1 Overview of APEX1 functions in genome maintenance.

Human apurinic/apyrimidinic endonuclease 1 (APEX1), also known as APE1 or redox factor 1 (Ref-1), is a ubiquitously expressed multifunctional protein of approximately 36.5 kDa. APEX1 plays a central role in the cellular response to oxidative stress through two main activities (Figure 1.10A). First, it acts as the major endonuclease in the base excision repair (BER) pathway, where it cleaves DNA at apurinic/apyrimidinic sites to initiate repair of damaged bases (Figure 1.10C). Second, APEX1 functions as a redox co-activator of several transcription factors, including Egr-1, p53, HIF-1α, CREB, AP-1, NF-κB, and Pax proteins[128] (Figure 1.10B). These functions are supported by distinct regions of the protein: the N-terminal domain contains regulatory motifs important for redox activity and nuclear localization, whereas the C-terminal catalytic domain mediates AP endonuclease activity[129]. In addition to its canonical roles in DNA repair and redox regulation, APEX1 has been linked to RNA metabolism and nucleolar stress responses. APEX1 interacts with the RNase III enzyme DROSHA and contributes to the processing of selected microRNAs[130]. It has also been associated with nucleophosmin (NPM1), a nucleolar protein involved in ribosomal RNA biogenesis. More recently, APEX1 was shown to co-localize with NPM1 in the nucleolus and to promote biomolecular condensate formation that supports ATR–CHK1 DNA damage signalling[131].

APEX1 has recently been linked to R-loop metabolism through a non-canonical role in processing RNA abasic sites. R-loops can promote the formation of abasic sites in the DNA strand of R-loop hybrids, partly through the activity of the glycosylase MPG. APEX1 can be recruited to these RNA abasic sites and cleaves the DNA strand within the R-loop hybrid, providing a potential mechanism for R-loop resolution. This suggests that APEX1 may contribute to genome stability not only through its canonical function in base excision repair, but also by regulating persistent R-loop structures that could otherwise interfere with transcription and replication[132].

Because of these diverse activities, APEX1 has gained increasing attention in cancer biology. Elevated APEX1 expression has been reported in several tumour types, where it can contribute to tumour progression and chemoresistance, partly through redox-mediated regulation of gene expression. APEX1 can also be secreted and detected in serum, suggesting its potential use as a prognostic or non-invasive biomarker. Together, these findings establish APEX1 as a multifunctional protein involved in genome maintenance, transcriptional regulation, RNA metabolism, and cancer-associated stress responses[133].

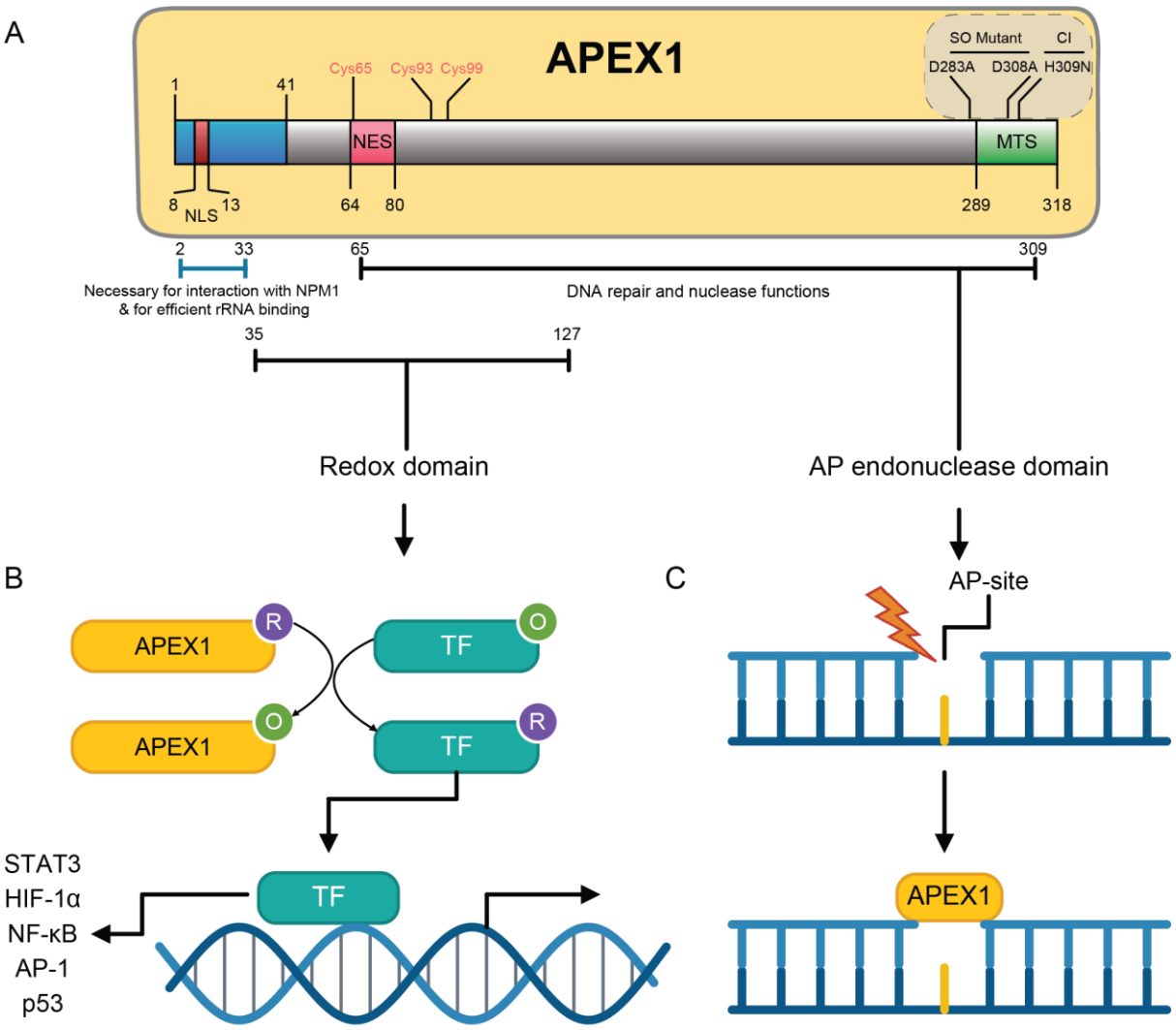


Figure 1.10 | Structural and functional organization of APE1/Ref-1.
(A) Structural organization of the APE1/Ref-1 protein, showing the nuclear localization signal (NLS), nuclear export signal (NES), mitochondrial targeting sequence (MTS), and the C-terminal endonuclease domain responsible for DNA repair. The positions of the catalytically inactive SO and CI mutants used for APEX1 re-expression experiments are indicated. (B) Model illustrating the redox regulatory function of APE1/Ref-1. Through thiol–disulfide exchange reactions involving cysteine residues, APE1/Ref-1 reduces transcription factors to their active state while becoming oxidized itself. Oxidized; R, reduced. (C) Schematic illustration of the DNA repair function of APE1/Ref-1 during base excision repair (BER). APE1/Ref-1 binds to DNA, scans for apurinic/apyrimidinic (AP) sites, and cleaves the phosphodiester backbone to initiate repair. The schematic was adapted from Siqueira et al. (2024)[134] and Yang and Sun (2024)[135].

1.4.2 ALYREF in mRNA export and transcription-replication conflict regulation

ALYREF, also known as Aly/REF export factor or THOC4, is a 32 kDa protein encoded by a gene located on chromosome 17q25.3[134]. ALYREF is a conserved RNA-binding protein and an important component of the transcription-export (TREX) complex, which links mRNA processing to nuclear export. The core TREX complex contains the THO complex together with the RNA helicase UAP56/DDX39B, ALYREF, and additional export adaptor proteins[135]. During transcription and mRNA maturation, the THO complex associates with nascent transcripts and helps package newly synthesized RNA into export-competent messenger ribonucleoprotein[136]. ALYREF participates in this process in an ATP-dependent manner and

can be loaded onto intronless transcripts by UAP56 through its N- and C-terminal UAP56/DDX39B-binding motifs (UBMs). ALYREF acts as an export adaptor by binding both mRNA through its RNA recognition motif (RRM), while its RGG-like regions contribute to nucleic acid and export receptor interactions NXF1-NXT1[137]. Once recruited, NXF1-NXT1 mediates the passage of mRNA through the nuclear pore complex into the cytoplasm. Through this function, ALYREF contributes to efficient mRNA export and helps prevent the accumulation of improperly processed or retained nuclear transcripts (Figure 1.11).

ALYREF has also recently been linked to genome stability. UAP56/DDX39B was previously shown to reduce harmful RNA-DNA hybrids across the genome, thereby limiting transcription-replication conflicts[137,138]. The 2024 study by Bhandari and colleagues extended this concept directly to ALYREF, showing that ALYREF binds R-loops, promotes UAP56-mediated R-loop dissociation, and limits R-loop-dependent replication stress and genome instability[137]. This shows that ALYREF is not only involved in packaging nascent RNA and transferring it through mRNP assembly steps but also helps prevent the same RNA from reannealing to the template DNA.

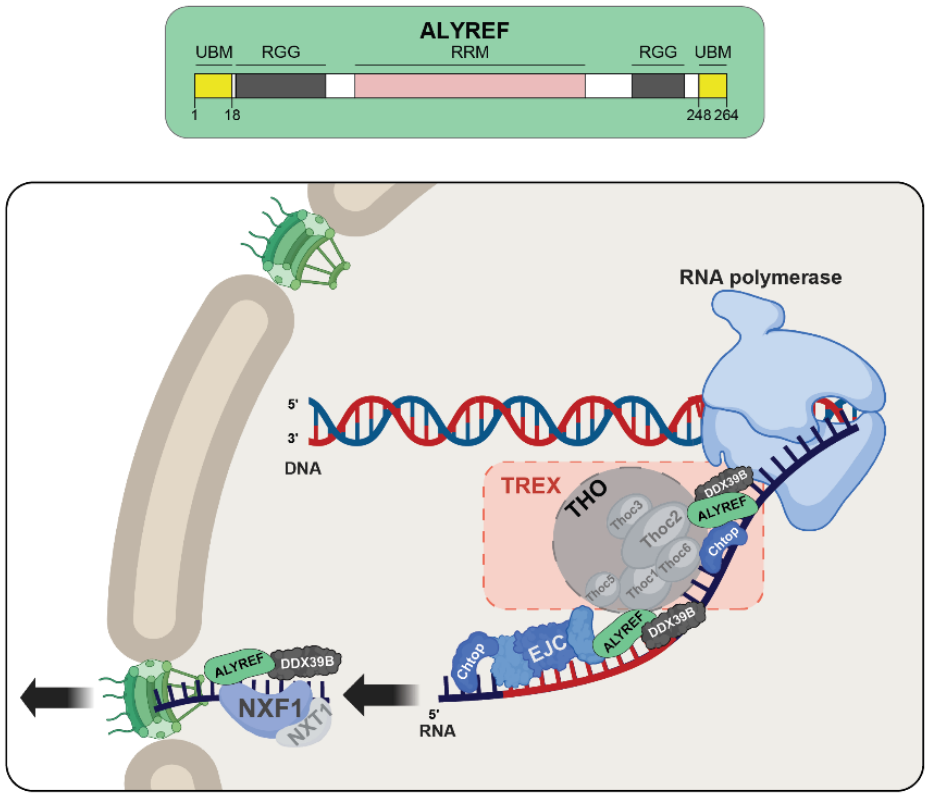


Figure 1.11 | Domain organization and proposed co-transcriptional function of ALYREF.
(A) Schematic representation of the human ALYREF protein. The N- and C-terminal UAP56/DDX39B-binding motifs (UBMs), two arginine-glycine-glycine-rich (RGG) motifs, and the central RNA recognition motif (RRM) are indicated. Numbers denote amino acid positions. (B) Schematic overview of the proposed role of ALYREF in transcription-coupled mRNA processing and export. ALYREF is recruited co-transcriptionally as part of the TREX complex, where it interacts with DDX39B/UAP56, the THO complex, and additional RNA-processing factors to promote messenger ribonucleoprotein (mRNP) assembly. During mRNP maturation, UAP56 is replaced by the NXF1–NXT1 export receptor, generating an export-competent mRNP that is transported through the nuclear pore complex. Adapted from Stewart (2010) and Pühringer et al. (2020).

1.4.3 The HCT116 F9 cell line as a model for studying UFB resolution

The development of novel model cell lines is essential to obtain reliable and controlled platforms for dissecting cellular mechanisms. To investigate the formation and resolution of ultrafine anaphase bridges (UFBs), we engineered HCT116 colorectal carcinoma cell line. The parental HCT116 cell line has been derived from an adult male with colorectal carcinoma and carries an activating mutation in codon 13 of the RAS proto-oncogene. These cells are nearly diploid and commonly display a modal chromosome number of 45, largely due to frequent loss of the Y chromosome. Their relatively stable karyotype and suitability for genome editing have made HCT116 cell line a useful model for studying chromosome segregation, DNA repair, and genome stability[139].

In this study, we used a genetically modified HCT116 Tet-OsTIR1 BLM-AID-eGFP cell line (HCT116 B1), hereafter referred to as the BLM-AID-eGFP cell line, to monitor endogenous BLM dynamics and to examine the role of BLM in UFB resolution. In this cell line, the endogenous BLM protein was C-terminally fused to an auxin-inducible degron (AID) tag, allowing rapid depletion of BLM after auxin treatment. In addition, eGFP was included in the tag to enable visualization of endogenous BLM in live and fixed cells. Previous characterization showed that treatment of asynchronous cells with auxin for 24 h reduced AID-tagged BLM to approximately 10%. Importantly, the BLM-AID-eGFP fusion protein was shown to be functional, as it efficiently suppressed the accumulation of recombination intermediates that give rise to sister chromatid exchanges[140].

To enable simultaneous visualization of UFB-associated factors, we additionally used a double-tagged HCT116 B1-derived cell line expressing PICH-mCherry together with BLM-AID-eGFP (HCT116 F9) (Figure 1.12A). Validation of the mCherry-tagged PICH protein confirmed homozygous tagging in the double-tagged cell line (Figure 1.12B). Consistent with the known mitotic localization pattern of PICH, the PICH-mCherry signal was diffuse in the cytoplasm during interphase and rapidly re-localized to chromatin after nuclear envelope breakdown. This dual-tagged system therefore allowed visualization of both BLM and PICH dynamics during mitosis, while simultaneously enabling inducible BLM depletion. This unique combination provided a suitable model to study the formation, persistence, and resolution of UFBs, as well as the contribution of candidate proteins to these processes (Figure 1.12C)[140].

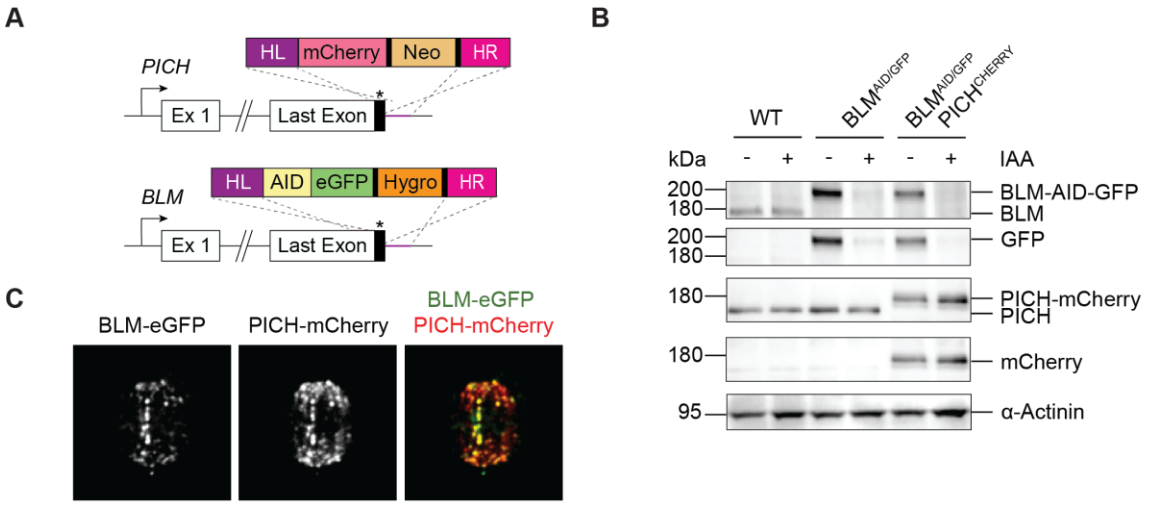


Figure 1.12 | Characterization of the HCT116 F9 cell line for visualization of ultrafine DNA bridges (UFBs).
(A) Schematic illustration of the gene-editing strategy used to generate the HCT116 F9 cell line expressing BLM helicase–AID–eGFP and PICH–mCherry fusion proteins. (B) Detection of endogenous and tagged BLM and PICH proteins in parental HCT116 cells, BLM–AID–eGFP cells, and BLM–AID–eGFP/PICH–mCherry cells by western blot analysis. Membranes were probed with antibodies against BLM, GFP, PICH, mCherry, and α-actinin. α-Actinin served as a loading control. (C) Experimental scheme for live-cell microscopy analysis of UFB formation and resolution. (D) Representative image of a fixed anaphase cell showing UFB visualization in the HCT116 F9 cell line. BLM was detected via the eGFP tag, whereas PICH was visualized either by immunofluorescence staining or direct mCherry fluorescence. DNA was counterstained with DAPI. The image was adapted from our previous study "Mitotic BLM functions are required to maintain genomic stability (Hamman et al., 2026).

1.4.4 Cell-cycle synchronization for the analysis of replication stress and mitosis

Because many cellular processes are tightly coupled to specific stages of the cell cycle, studying cell cycle–dependent events require experimental strategies that allow the enrichment of cells at defined phases. This need has led to the development of numerous protocols for cell cycle synchronization (Figure 1.13), enabling the investigation of the molecular and structural mechanisms governing cell cycle progression. In general, two main approaches are used to obtain cell populations enriched in specific cell-cycle phases. Cells can be isolated physically, for example by collecting mitotic cells through shake-off or by sorting cells based on DNA content or cell-cycle markers. Alternatively, asynchronous cell populations can be treated with chemical agents that arrest cells at defined cell-cycle stages. Physical isolation methods are usually gentler because they do not directly block cell-cycle regulators, but they often provide fewer synchronized cells and may require modified cells for marker-based sorting. Chemical synchronization is usually more efficient and easier to scale up; however, it can affect cell metabolism and genome stability, especially when DNA replication is directly inhibited[141]. Agents such as hydroxyurea and aphidicolin, commonly used to enrich cells at the G1/S boundary, inhibit DNA synthesis and activate cell cycle checkpoints; however, at high concentrations, they can also induce DNA damage and trigger the DNA damage response, potentially confounding experimental outcomes[142]. For this reason, effective synchronization methods must be both reversible and minimally cytotoxic.

Thymidine-based synchronization represents a comparatively mild approach, as it induces a transient arrest at the G1/S boundary by creating an imbalance in the nucleotide pool without causing extensive DNA damage[141]. Although double-thymidine block is often used to achieve stronger synchronization, preliminary comparison showed no major difference between single- and double-thymidine synchronization in our experimental system. Therefore, a single-thymidine block was used in this study to reduce the total time cells were arrested at the G1/S boundary and to minimize synchronization-associated stress. Upon release, cells progressed through S phase, G2, and into mitosis in a sufficiently synchronized manner for the analysis of mitotic phenotypes. More recently, Palbociclib has emerged as a non-toxic and reversible alternative for G1 synchronization. By selectively inhibiting CDK4/6, Palbociclib prevents RB phosphorylation, suppresses E2F-dependent transcription, and blocks entry into S phase, resulting in an efficient and controlled G1 arrest[143]. In contrast, synchronization in mitosis remains particularly challenging. Once cells pass metaphase, progression through the remaining stages of mitosis is rapid and largely irreversible. Classical agents such as nocodazole and colchicine, which disrupt microtubule dynamics and activate the spindle assembly checkpoint, have been widely used to arrest cells in metaphase[18]. However, these drugs are inherently cytotoxic and can induce DNA damage and stress responses, limiting their suitability for sensitive mechanistic studies[144]. Thus, while a wide range of synchronization strategies is available, each method presents inherent advantages and limitations. Careful selection of synchronization approaches is therefore essential when investigating cell cycle–dependent functions of proteins, particularly in studies aiming to preserve physiological relevance and genomic integrity.

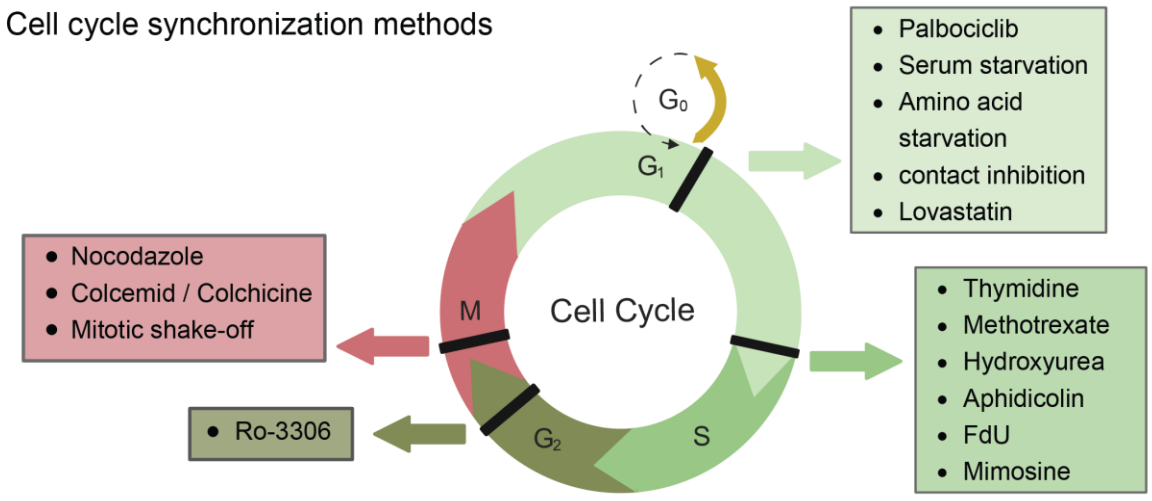


Figure 1.13 | Cell cycle synchronization methods.
Overview of the most common cell cycle synchronization approaches. Cells can be synchronized either by mechanical methods that isolate cells at a specific phase (e.g., mitotic shake-off) or by chemical treatments that arrest cells at defined stages of the cell cycle. Image adapted from Ligasová and Koberna, 2021, and modified using BioRender.com.

1.4.5 ChIP–MS as a strategy to identify chromatin-associated UFB-resolution factors

Identification of proteins involved in UFB resolution is technically challenging due to the low abundance of anaphase cells with UFBs, as well as low abundance of the proteins associated with them. MS-based proteomics can identify proteins within cellular complexes, and ChIP-MS is particularly suitable because UFBs arise from unresolved chromatin structures[145]. Chromatin immunoprecipitation coupled with mass spectrometry (ChIP-MS) combines classical chromatin immunoprecipitation with proteomic analysis to identify proteins associated with chromatin-bound factors in vivo. Similar to conventional ChIP, cells are crosslinked with formaldehyde and chromatin sheared by sonication and the protein of interest is immunoprecipitated. In contrast to ChIP-qPCR or ChIP-seq, which mainly identify DNA regions bound by a protein, ChIP-MS identifies proteins associated with the immunoprecipitated chromatin complex[145].

Previous work has demonstrated the value of ChIP-MS for studying replication stress-associated chromatin complexes. For example, FANCD2-based ChIP-MS was used to identify proteins recruited to common fragile sites under mild replication stress, revealing several DNA repair factors, including ATRX, BLM and components of the BTR complex[146]. This supports the use of ChIP-MS as a powerful strategy to investigate chromatin-associated protein networks involved in fragile site maintenance, replication stress responses, and UFB resolution.

In this study, I established a series of chromatin immunoprecipitation–mass spectrometry experiments to identify mitotic chromatin-associated interaction partners involved in DNA repair and UFB resolution. The scale and specificity of this experimental design provided a unique opportunity to study these processes under conditions that closely resemble replication stress-induced mitotic DNA structures. A key feature of this approach was thymidine block synchronization because it allowed cells to be arrested at the G1/S boundary and then released to progress through one synchronized cell cycle[147]. This enabled APH-induced replication stress to be applied during a defined replication window, followed by analysis of mitotic chromatin and UFB-associated phenotypes at an optimized mitotic time point[148]. Compared with mitotic arrest methods such as nocodazole or STLC treatment, this approach is less directly disruptive to spindle function and anaphase progression, which is important for studying chromosome segregation and UFB resolution[149].

To date, interactome studies of UFB-associated marker proteins remain limited. Although proteins such as BLM and FANCD2 are used to visualize fragile site-associated UFBs and replication stress-induced mitotic DNA structures[110], their mitotic interaction networks under mild replication stress have not been systematically characterized in detail. Previous studies have identified interaction partners of UFB and replication stress-associated proteins using targeted co-immunoprecipitation,

affinity purification, proximity labelling, and mass spectrometry approaches. For example, Pladevall-Morera et al. used SILAC-based FANCD2 ChIP-MS to identify proteins associated with FANCD2-marked common fragile sites after mild replication stress[146]. In a study, Martin et al. applied cell-cycle-stage-specific TOPBP1 Co-IP–LC–MS, followed by label-free and TMT-based quantitative proteomics, to define mitosis-enriched TOPBP1 interaction networks[150]. More recently, proximity proteomics has also been used to map the BLM–TOP3A–RMI1–RMI2 proximal proteome[151]. Together, these studies demonstrate that chromatin- and interaction-focused mass spectrometry can reveal protein networks involved in replication stress responses and mitotic DNA repair. However, the present study extended this approach by performing systematic chromatin-focused IP–MS analyses of several UFB-associated and mitotic DNA repair factors, including FANCD2, FANCI, BLM, TOP3A, and PICH, in mitotic cells under APH-induced replication stress. This experimental design allowed the comparison of multiple UFB-associated protein networks under the same replication stress conditions and provided a more integrated view of the proteins recruited to mitotic chromatin.

1.5 Aim of the study

Accurate chromosome replication and segregation are essential for genome stability. Replication stress can stall or collapse replication forks, leaving genomic regions incompletely replicated or damaged. If these unresolved DNA structures persist into mitosis, sister chromatids may fail to separate properly and form chromatin bridges or ultrafine anaphase bridges (UFBs) during anaphase. UFBs are marked by several known proteins, including PICH, BLM, FANCD2, FANCI, and TOP3A, which coat or process different bridge subtypes. However, the mechanisms that resolve UFBs remain incompletely understood. It is still unclear whether all required factors have been identified and whether distinct UFB classes depend on more than one resolution pathway.

The main aim of this study was to **identify new proteins involved in preventing and resolving persistent sister chromatid linkages** under mild replication stress induced by aphidicolin. Chromatin immunoprecipitation followed by mass spectrometry was used on known UFB-associated factors, including PICH, BLM, FANCD2, FANCI, and TOP3A, to identify candidate proteins involved in UFB resolution. Particular attention was given to APEX1 and ALYREF, which were identified as candidate interactors in the ChIP-MS analysis and selected for further validation.

APEX1 is of particular interest because it participates in several DNA repair and genome maintenance pathways. However, because APEX1 has multiple functions, it remains difficult to determine which activity contributes to specific cellular processes. To address this, this study used CRISPR/Cas9-generated APEX1 knockout cells together with rescue experiments using wild-type and mutant APEX1 constructs. This approach allowed to analyze the different functions of APEX1 to be examined separately and helped determine **how APEX1 activity at specific cell-cycle stages contributes to the resolution of ultrafine bridges**.

Another aim of this study was to understand **how APEX1 cooperates with BLM in UFB resolution** and in the maintenance of genome stability under replication stress. Various mitotic and post-mitotic phenotypes were studied in cells with altered levels of APEX1 and BLM after mild replication stress. This allowed us to assess whether APEX1 and BLM act in the same pathway or in parallel pathways to prevent chromosome segregation errors and genome instability.

2 Materials

2.1 Equipment

Table 1 | List of equipment

Equipment	Manufacturer
Agarose gel documentation system	Intas Science Imaging Instruments GmbH, Göttingen, Germany
Agarose gel electrophoresis system	Nippon genetics EUROPE GmbH, Düren, Germany
Automated microscope stage MS-2000 XYZ	Applied Scientific Instrumentation, Eugene, USA
Azure c300 system	Azure Biosystems, Dublin, USA
Blotting paper Whatman 3 mm	A. Hartenstein GmbH, Würzburg, Germany
C18 extraction disks silica Empore™ 47 mm	CDS Analytical LLC, Oxford, USA
Cell counter Countess™ II automated	Thermo Fisher Scientific, Inc., Waltham, USA
Cell counting chamber slides Countess™	Thermo Fisher Scientific, Inc., Waltham, USA
Cell culture black glass-bottom 10-well CELL view plate	Greiner Bio-One, Kremsmünster, Austria
Cell culture black glass-bottom 96-well plate	Greiner Bio-One, Kremsmünster, Austria
Cell culture dish (all sizes)	Sarstedt AG & CO, Nürmbrecht, Germany
Cell culture flask (all sizes)	Sarstedt AG & CO, Nürmbrecht, Germany
Cell culture multiwell plates	Sarstedt AG & CO, Nürmbrecht, Germany
Centrifuge Rotina 420R	Andreas Hettich GmbH & Co. KG, Tuttlingen, Germany
Cloning discs sterile Ø3.2 mm	Sigma-Aldrich, St. Louis, USA
CO_2 incubator Heracell™	Thermo Fisher Scientific, Inc., Waltham, USA
Confocal Scanner CSU-X1	Rota Yokogawa GmbH & Co. KG, Wehr, Germany
Confocal spinning disk microscope CSUW1 Sora	Nikon Corporation, Tokyo, Japan
CoolSNAP HQ2 monochrome camera	Teledyne Photometrics, Tucson, USA

Coverslips 0.17 mm, 1.5H, round, Ø12 mm	Carl Roth GmbH + Co. KG, Karlsruhe, Germany
EASY-nLC™ 1200 system	Thermo Fischer Scientific, Inc., Waltham, USA
Electrophoresis power supply PowerPac™ HC	Bio-Rad Laboratories, Inc., Hercules, USA
Epifluorescence microscope Zeiss Axio Observer Z1	Carl Zeiss AG, Oberkochen, Germany
Epifluorescence microscope Eclipse Ti2-E with Spectra III	Nikon Corporation, Tokyo, Japan
Flow Cytometer Attune™ NxT	Thermo Fisher Scientific, Inc., Waltham, USA
Gel imaging system Azure c500	Azure Biosystems, Inc., Dublin, USA
Heat Block	Störk Tronic, Stuttgart, Germany
Homogenizer Bandelin HD 2200	Bandelin electronic GmbH & Co. KG, Berlin, Germany
HPLC column	PicoTip Emitter™ New Objective, Inc., Littleton, USA
Inverse-Microscope AE 2000-Trino	Motic®, Vacnouver, Canada
Laser Stack (473 nm, 561 nm, 640 nm)	Intelligent Imaging Innovations, Denver, USA
Magnetic separation rack	Thermo Fisher Scientific, Inc., Waltham, USA
Mass spectrometer Q Exactive™ HF	Thermo Fischer Scientific, Inc., Waltham, USA
Mass spectrometry Nanospray Flex™ Ion	Thermo Fisher Scientific Inc., Waltham, Source USA
Microcentrifuge Eppendorf 5415R	Eppendorf SE, Hamburg, Germany refrigerated
Microscope slide SuperFrost Plus™ 25x75	Thermo Fisher Scientific, Inc., Waltham, mm USA
Multiwell plate Microtiter™ transparent 96	Thermo Fisher Scientific, Inc., Waltham, well USA
Nitrocellulose blotting membrane GE	HealthCare Technologies, Inc.
Objectives 20x air, 40x air, 60x oil	Carl Zeiss AG, Oberkochen, Germany
PH meter inoLab® pH7110	Xylem Analytics Germany Sales GmbH & Co. KG, Weilheim, Germany

Plate reader GloMax® Explorer	Promega Corporation, Madison, USA
Polyacrylamide electrophoresis system	Mini-Bio-Rad Laboratories, Inc., Hercules, USA
Polyacrylamide Mini-PROTEAN® short	Bio-Rad Laboratories, Inc., Hercules, USA plates
Polyacrylamide Mini-PROTEAN® spacer	Bio-Rad Laboratories, Inc., Hercules, USA
plates (1.0 mm) Precision Scale	PCB KERN & SOHN, Balingen, Germany
Real-Time PCR Detection System CFX96	Bio-Rad Laboratories, Inc., Hercules, USA
Rotator Revolver mixer for test and sample tubes	Carl Roth GmbH + Co. KG, Schoemperlenstraße 3-5 D-76185, Karlsruhe, Germany
Touch Rotator SB3	Stuart Cole-Parmer, Vernon Hills, USA
Safety bench hood	Hersafe™ Thermo Fisher Scientific, Inc., Waltham, USA
Sonication device Bioruptor®	Pico Diagenode LLC., Denville, USA
Spectrophotometer DS-11	DeNovix Inc., Wilmington, USA
Thermal Cycler C1000 Touch	Bio-Rad Laboratories, Inc., Hercules, USA
Tube roller LLG-uniRoller 10	Lab Logistics Group, Meckenheim, Germany
UHPLC silica media	ReproSil-Pur C18-AQ Dr. Maisch, Ammerbuch, Germany
Ultrasonic bath	SONOREX Bandelin electronic GmbH & Co. KG, Berlin, Germany
UV-Transilluminator 312 nm	Bachofer GmbH & Co. KG, Reutlingen, Germany
Vacuum pump	Integra Vacusafe Integra Bioscience GmbH, Biebertal, Germany
Vortex Genie 2	Scientific Industries, Inc., Bohemia, USA
Water bath Typ1008	GFL GmbH, Burgwedel, Germany

2.2 Chemicals

Table 2 | List of chemicals

Chemical	Manufacturer
2-Chloroacetamide	Sigma-Aldrich, St. Louis, USA
4-(2-hydroxyethyl)-1-piperazineethanesulfonic acid (HEPES)	VWR International, Darmstadt, Germany
Acetic acid	Sigma-Aldrich, St. Louis, USA
Agarose	Carl Roth GmbH + Co. KG, Karlsruhe, Germany
Albumin Bovine Serum (BSA)	BWR Life Sciences, Leuven, Belgium
Ammonium chloride (NH_4Cl)	Sigma-Aldrich, St. Louis, USA
Ammonium persulfate (APS)	Sigma-Aldrich, St. Louis, USA
Bromophenol blue	Sigma-Aldrich, St. Louis, USA
Dimethyl sulfoxide (DMSO)	Carl Roth GmbH + Co. KG, Karlsruhe, Germany
Dipotassium phosphate (KH_2PO_4)	Carl Roth GmbH + Co. KG, Karlsruhe, Germany
Disodium hydrogen phosphate (Na_2HPO_4)	Carl Roth GmbH + Co. KG, Karlsruhe, Germany
Dithiothreitol (DTT)	Carl Roth GmbH + Co. KG, Karlsruhe, Germany
Ethanol (EtOH)	Sigma-Aldrich, St. Louis, USA
Ethylenediaminetetraacetic acid (EDTA)	Sigma-Aldrich, St. Louis, USA
Glycerol	Sigma-Aldrich, St. Louis, USA
Glycine	AppliChem, Darmstadt, Germany
H_2O nuclease-free	Sigma-Aldrich, St. Louis, USA
Hydrochloric acid (HCl)	Thermo Fisher Scientific, Inc., Waltham, USA
Isopropanol	Thermo Fisher Scientific, Inc., Waltham, USA
LB Agar	Carl Roth GmbH + Co. KG, Karlsruhe, Germany
Magnesium chloride ($MgCl_2$)	Sigma-Aldrich, St. Louis, USA

Methanol analytical reagent grade	Thermo Fisher Scientific, Inc., Waltham, USA
Nonidet P40 (NP-40) 10%	Bio Vision, In., Milpitas, USA
Paraformaldehyde (PFA)	Sigma-Aldrich, St. Louis, USA
Polyethylene glycol (PEG)	Sigma-Aldrich, St. Louis, USA
Ponceau S	Sigma-Aldrich, St. Louis, USA
Potassium chloride (KCl)	Carl Roth GmbH + Co. KG, Karlsruhe, Germany
Skim milk powder	SERVA Electrophoresis, Heidelberg, Germany
Sodium azide (NaN_3)	Sigma-Aldrich, St. Louis, USA
Sodium chloride (NaCl)	Sigma-Aldrich, St. Louis, USA
Sodium citrate	Sigma-Aldrich, St. Louis, USA
Sodium deoxycholate	Carl Roth GmbH + Co. KG, Karlsruhe, Germany
Sodium dodecyl sulfate (SDS)	Carl Roth GmbH + Co. KG, Karlsruhe, Germany
Tetramethyl ethylenediamine (TEMED)	AppliChem, Darmstadt, Germany
Tris	Carl Roth GmbH + Co. KG, Karlsruhe, Germany
Triton X-100	Carl Roth GmbH + Co. KG, Karlsruhe, Germany
Trypan blue	Thermo Fisher Scientific, Inc., Waltham, USA
Tween® 20	Sigma-Aldrich, St. Louis, USA
Urea	AppliChem, Darmstadt, Germany
β-Mercaptoethanol	AppliChem, Darmstadt, Germany

2.3 Buffers and Solutions

Table 3 | List of prepared buffers and solutions

Name	Composition
General	
Phosphate-buffered saline (PBS) 10x	1.37 M NaCl, 27 mM KCl, 100 mM Na_2HPO_4, 18 mM KH_2PO_4 in H_2O
Phosphate-buffered saline with Tween-20 (PBST) 1x	0.1 % Tween-20 in 1x PBS
TAE 50x	2 M Tris, 0.05 M EDTA (pH 8.0), 1 M acetic acid
TE buffer 1x (pH 8.0)	10 mM Tris, 1 mM EDTA in H_2O
Tris-buffered saline (TBS) 10x (pH 7.5)	500 mM Tris, 1.5 M NaCl
Tris-buffered saline with Tween-20 (TBST 1x)	0.1 % Tween-20 in 1x TBS
Cell culture	
Freezing mix	10% DMSO in fetal bovine serum (FBS)
Chromosome spreads	
Hypotonic solution	75 mM KCl in H_2O
Fixative solution	25% acetic acid, 75 % methanol
Sorensen phosphate buffer (pH 6.8) 1x	50 % 0.1 M Na_2HPO_4, 50 % 0.1 M KH_2PO_4
Salt sodium citrate (SSC) buffer (pH 7.0) 20x	3 M NaCl, 300 mM sodium citrate
Colony formation assay	
Crystal violet fixative	20 % methanol, 0.5 % w/v crystal violet in H_2O
Cell lysis	
Radioimmunoprecipitation assay (RIPA)	10 % NP-40, 10 % sodium deoxycholate, 5 M (pH 7.5) NaCl, 0.5 M EDTA, 1 M Tris-HCl (pH 7.5), 1x protease inhibitor cOmplete Mini EDTA-free and 1x phosSTOP phosphatase inhibitor
SDS-polyacrylamide gel electrophoresis (SDS-Page) and Western blotting	
Blocking solution	5 % skim milk/3 % BSA in 1x TBST

Bradford solution	20 % Bradford reagent in H_2O
Laemmli buffer (pH 6.8) 1x	62.5 mM Tris-HCl (pH 6.8), 2 % SDS, 10 % glycerol, 0.01 % bromophenol blue, 1 % β-mercaptoethanol in H_2O
Ponceau solution	0.2 % Ponceau S, 1 % acetic acid in H_2O
Resolving gels (pH 8.8) 2x 7.5 %	3.75 ml 30 % acrylamide; 3.75 ml resolving gel SDS-buffer (pH 8.8); 7.5 ml H_2O, 300 µl 10% APS, 15 µl TEMED
Resolving gel SDS-buffer (pH 8.8)	1.5 M Tris-HCl (pH 8.8), 0.4% (w/v) SDS in H_2O
Running buffer (pH 8.3) 1x	25 mM Tris-HCl (pH 8.3); 190 mM glycine; 0.1 % SDS in H_2O
Stacking gels (pH 6.8) 2x 5 %	0.8 ml 30% acrylamide, 1.2 ml stacking gel SDS-buffer pH 6.8, 3 ml H_2O, 50 µl 10% APS, 5 µl TEMED
Stacking gel SDS-buffer (pH 6.8)	0.5 M Tris-HCl (pH 6.8), 0.4 % (w/v) SDS in H_2O
Wet-Transfer buffer 1x	25 mM Tris, 192 mM glycine, 20 % (v/v) methanol, in H_2O
Microscopy	
Aldehyde deactivation buffer	50 mM NH_4Cl in 1x PBS
Blocking solution for methanol-fixation	5 % FBS, 3 % Triton X-100, 1 % NaN_3 in 1x PBS
Blocking solution for PFA-fixation	3% BSA, 1% NaN_3 in 1x PBST
Fixation solution with methanol	100 % ice-cold methanol
Fixation solution with PFA	3% PFA, 0.1% Triton X-100 in 1x PBS
Permeabilization buffer for PFA-fixation	0.5% Triton X-100 in 1x PBS
Staining solution with DAPI	10 µg/ml RNase, DAPI 0.1 µg/ml in 1x PBS
Staining solution with Sytox™ green	10 µg/ml RNase, 167 nM Sytox™ green in 1x PBS
Pull downs	
Elution buffer I	2 M Urea, 50 mM Tris (pH 7.5), 2 mM DTT, 20 µg/ml trypsin in H_2O
Elution buffer II	2 M Urea, 50 mM Tris (pH 7.5), 10 mM chloroacetamide in H_2O

Fast-IP buffer	150 mM NaCl, 5 mM EDTA (pH 7.5), 5 mM Tris (pH 7.5), 1 % Triton X-100, 0.5 % NP-40, 1x protease inhibitor cOmplete Mini EDTA-free and 1x phosSTOP phosphatase inhibitor, in H_2O
High salt wash buffer	50 mM HEPES (pH 7.5), 500 mM NaCl, 1 % Triton X-100 in H_2O
Low salt wash buffer	50 mM HEPES (pH 7.5), 140 mM NaCl, 1 % Triton X-100 in H_2O
Shearing buffer	1 % SDS, 10 µM EDTA (pH 8.0), 50 mM Tris (pH 8.0) in H_2O
IP RIPA buffer	10 mM Tris-HCl (pH 7.5), 150 mM NaCl, 0.5 mM EDTA, 0.1 % SDS, 1 % Triton X-100, 1 % deoxycholate, 2.5 mM MgCl2, 1 mM PMSF, 1x protease inhibitor cOmplete Mini EDTA-free and 1x phosSTOP phosphatase inhibitor, in H2O, pH adjusted at 4°C
Wash buffer I	10 mM TRIS pH 7.5, 150 mM NaCl, 0.25% NP-40 in H_2O
Wash buffer II	10 mM TRIS pH 7.5, 150 mM NaCl in H_2O
Mass spectrometry	
Buffer A	0.1 formic acid
Buffer B	80 % acetonitrile, 0.1 % formic acid
Buffer A*	2 % acetonitrile, 0.1 % TFA pH 2

2.4 Molecular biology

Table 4 | List of molecular biological reagents and cloning buffers

Reagents and buffers	Manufacturer
DMSO	New England Biolabs, Ipswich, USA
dNTPs 10 mM	New England Biolabs, Ipswich, USA
Ethidium bromide	Thermo Fisher Scientific Inc., Waltham, USA
Fast Digest buffer 10x	Thermo Fisher Scientific, Inc., Waltham, USA
Gel loading dye, purple 6x	New England Biolabs, Ipswich, USA

Lipofectamine™ 2000	Thermo Fisher Scientific Inc., Waltham, USA
rNTP each 100 mM	New England Biolabs, Ipswich, USA
$MgCl_2$	New England Biolabs, Ipswich, USA
Quick ligation reaction buffer 2x	New England Biolabs, Ipswich, USA
Quick-Load 1 kilobase (kb) DNA ladder	New England Biolabs, Ipswich, USA
Quick-Load 100 base pairs (bp) DNA ladder	New England Biolabs, Ipswich, USA

Table 5 | List of general enzymes

Enzyme	Manufacturer
Proteinase K	Carl Roth GmbH + Co. KG, Karlsruhe, Germany
Quick ligase	New England Biolabs, Ipswich, USA
RNase A	Macherey-Nagel, Düren, Germany
T4 DNA ligase	New England Biolabs, Ipswich, USA
Taq DNA polymerase	New England Biolabs, Ipswich, USA
TrueCut™ Cas9 Protein v2	Thermo Fisher Scientific, Carlsbad, CA, USA

2.5 Plasmids and siRNA

Table 6 | List of plasmids

Name	Used for	Size (bp)	Bacterial resistance	Manufacturer
pLIX401 APE1 WT	Rescuing APEX1 WT gene in APEX1 KO Cell line	8653	Ampicillin	Kind gift of David Pellman
pLIX401 APE1 SO	Rescuing APEX1 catalytically inactive gene in APEX1 KO Cell line	8653	Ampicillin	Kind gift of David Pellman
pLIX401 APE1 CI	Rescuing APEX1 catalytically inactive gene in APEX1 KO Cell line	8653	Ampicillin	Kind gift of David Pellman
GV-W-pHDM-VSV-G	Lentivirus packaging plasmid	6237	Ampicillin	Kind gift of Behrends C.
GV-pHDM-tat1b	Lentivirus packaging plasmid	4827	Ampicillin	Kind gift of Behrends C.

GV-W-pRC-CMV-rev1b	Lentivirus packaging plasmid	5900	Ampicillin	Kind gift of Behrends C.
GV-W-pHDM-Hgpm2	Lentivirus packaging plasmid	8908	Ampicillin	Kind gift of Behrends C.

Table 7 | Target sequences and genomic positions of the APEX1 guide RNAs.

Guide	Target sequence (5′–3′)	PAM	GRCh38 target locus	Strand	Assay ID
APEX1 gRNA 1	TCAATACTGGTCAGCTCCTT	CGG	Chr. 14: 20,456,769–20,456,791	Forward	CRISPR943763_SGM
APEX1 gRNA 2	ATGCCGAAGCGTGGGAAAAA	GGG	Chr. 14: 20,455,646–20,455,668	Forward	Not documented

2.6 Immunoprecipitation reagents

Table 8 | List of Immunoprecipitation reagents specific reagents

Reagents	Manufacturer
GFP-Trap® agarose	ChromoTek GmbH, Planegg, Germany
RFP-Trap® agarose	ChromoTek GmbH, Planegg, Germany
ChIP Grade Protein G Agarose Beads	Cell Signalling Technology, Inc., Danvers, USA

2.7 Bacteria culture

Table 9 | List of bacteria culture specific reagents

Reagents	Manufacturer
Lysogeny broth (LB) medium	Carl Roth GmbH + Co. KG, Karlsruhe, Germany
Ampicillin sodium salt	Sigma-Aldrich, St. Louis, USA
Chloramphenicol	Sigma-Aldrich, St. Louis, USA

2.8 Cell culture

Table 10 | List of human cell lines

Name	Cell type	origin	Description	Provider

HCT116	Colorectal carcinoma	Colon	Mutation in codon 13 of the ras proto-oncogene	ATCC, Manassas, USA
HCT116 Tet-OsTIR1 WT	Colorectal carcinoma	Colon	Mutation of ras proto- oncogene, OsTIR1 expression AAVS1 locus	Kind gift of Holger Bastian laboratory, Göttingen, Germany
HCT116 Tet-OsTIR1 BLMAID/AID clone B1	Colorectal carcinoma	Colon	Mutation of ras protooncogene, OsTIR1 expression, homozygous BLMAID/GFP expression	Generated in HCT116 Tet-OsTIR1 WT cells (Angela Wieland)
HCT116 Tet-OsTIR1 BLM-AID-eGFP PICH-mCherry clone F9	Colorectal carcinoma	Colon	Mutation of ras protooncogene, OsTIR1 expression, homozygous BLMAID/GFP expression, homozygous PICH/mCherry expression	Generated in HCT116 B1 clone (Andrea Tirincsi)
HCT116 F9AK	Colorectal carcinoma	Colon	Mutation of ras protooncogene, OsTIR1 expression, homozygous BLMAID/GFP expression, homozygous PICH/mCherry expression, APEX1 KO	Generated in HCT116 F9 clone (Amr Abdrbo)
HCT116 F9R1	Colorectal carcinoma	Colon	Mutation of ras protooncogene, OsTIR1 expression, homozygous BLMAID/GFP expression, homozygous PICH/mCherry expression, APEX1 WT gene with Tet-On promoter in APEX1 KO cells	Generated in HCT116 F9AK clone (Farbod Mohseni)
HCT116 F9SO	Colorectal carcinoma	Colon	Mutation of ras protooncogene, OsTIR1 expression, homozygous BLMAID/GFP expression, homozygous PICH/mCherry expression, APEX1 mutant gene with Tet-On promoter in APEX1 KO cells	Generated in HCT116 F9AK clone (Katharina Gauch)

Table 11 | List of cell culture specific reagents

Reagents	**Manufacturer**
3-Indole-acetic acid (IAA)	Sigma-Aldrich, St. Louis, USA
Aphidicolin	Sigma-Aldrich, St. Louis, USA
Colchicine solution 10 µg/ml	SERVA Electrophoresis, Heidelberg, Germany
Doxorubicin (Doxo)	Sigma-Aldrich, St. Louis, USA
Doxycycline (Dox)	Sigma-Aldrich, St. Louis, USA

Dulbecco's Modified Eagle Medium (DMEM), high glucose, GlutaMAX™	Thermo Fisher Scientific, Inc., Waltham, USA
Dulbecco's Modified Eagle Medium (DMEM), high glucose, no glutamine, no phenol red	Thermo Fisher Scientific, Inc., Waltham, USA
Fetal bovine serum (FBS)	Thermo Fisher Scientific, Inc., Waltham, USA
G418 for Neomycin (Neo) selection	InvivoGen, San Diego, USA
Hydroxyurea (HU)	Sigma-Aldrich, St. Louis, USA
Hygromycin (Hygro) B Gold	InvivoGen, San Diego, USA
L-Glutamine 200 mM	Thermo Fisher Scientific, Inc., Waltham, USA
Minimal Essential Medium (MEM) alpha	Thermo Fisher Scientific, Inc., Waltham, USA
Opti-MEM™ I Reduced Serum Medium	Thermo Fisher Scientific, Inc., Waltham, USA
Penicillin/Streptomycin (Pen/Strep)	Thermo Fisher Scientific, Inc., Waltham, USA
Polyethyleneimine (PEI)	Polysciences, Inc., Warrington, USA
Puromycin (Puro)	Thermo Fisher Scientific, Inc., Waltham, USA
Palbociclib	Selleck Biotechnology, Mathias-Brueggen-Str. 160, Cologne
Thymidine	Sigma-Aldrich, St. Louis, USA
Trypsin-EDTA 0.25 %	Thermo Fisher Scientific, Inc., Waltham, USA

2.9 SDS-PAGE and Western blotting

Table 12 | List of immunoblotting reagents

Reagents	Manufacturer
Acrylamide/Bis Solution 37.5:1, 30% w/v	SERVA Electrophoresis, Heidelberg, Germany
Bradford dye reagent concentrates 5x	Bio-Rad Laboratories, Inc., Hercules, USA
Clarity™ Western enhanced chemiluminescence (ECL) Substrate	Bio Rad Laboratories, Hercules, USA
cOmplete™ Mini, EDTA-free protease inhibitors	Roche Diagnostics, Mannheim, Germany
Lumigen ECL Ultra (TMA-100) Solution	Lumigen, Southfield, USA

PhosSTOP™ EASYpack phosphatase inhibitors	Roche Diagnostics, Mannheim, Germany
Precision Plus Protein™ All Blue Standards	Bio Rad Laboratories, Hercules, USA
Color Prestained Protein Standard	New England Biolabs, Ipswich, USA

2.10 Microscopy

Table 13 | List of immunofluorescence specific reagents

Reagents	Manufacturer
5-bromo-2'-deoxyuridine (BrdU)	Thermo Fisher Scientific, Inc., Waltham, USA
Antifade Mounting Medium with DAPI, VECTASHIELD	Biozol Diagnostica Vertrieb GmvH, Eching, Germany
Antifade Mounting Medium, VECTASHIELD	Biozol Diagnostica Vertrieb GmvH, Eching, Germany
DAPI	Carl Roth GmbH + Co. KG, Karlsruhe, Germany
Giemsa	Sigma-Aldrich, St. Louis, USA
Hoechst 33258	Thermo Fisher Scientific, Inc., Waltham, USA
Sytox™ Green	Thermo Fisher Scientific, Inc., Waltham, USA
NucSpot® Live 650	Biotium, Inc., Fremont, USA

2.11 Flow cytometry

Table 14 | List of flow cytometry-specific reagents

Reagents	Manufacturer
Bafilomycin	Sigma-Aldrich, St. Louis, USA
DDAO galactoside	Thermo Fisher Scientific, Inc., Waltham, USA
FxCycle™ propidium iodide (PI)/RNase staining solution	Thermo Fisher Scientific, Inc., Waltham, USA

2.12 Mass spectrometry

Table 15 | List of mass spectrometry specific chemicals and reagents

Reagents	Manufacturer

Acetonitrile 80%, H_2O 20%, formic acid 0.1 %	Thermo Fisher Scientific, Inc., Waltham, USA
Acetonitrile anhydrous	Sigma-Aldrich, St. Louis, USA
Acetonitrile LC-MS grad	Honeywell, Charlotte, USA
Formaldehyde (Methanol-free) 16%	Thermo Fisher Scientific, Inc., Waltham, USA
Formic acid	Honeywell, Charlotte, USA
H_2O LC-MS grade	Thermo Fisher Scientific, Inc., Waltham, USA
H_2O with formic acid 0.1%	Thermo Fisher Scientific, Inc., Waltham, USA
Methanol LC-MS grade	Honeywell, Charlotte, USA
Tri-fluoracetic acid (TFA)	Carl Roth GmbH + Co. KG, Karlsruhe, Germany
Trypsin proteomics grade	Sigma-Aldrich, St. Louis, USA

2.13 List of antibodies

Table 16 | List of primary antibodies

Name	Dilution	Host	Molecular weight [kDa]	Manufacturer	Reference
53BP1	IF: 1:500	Mouse	214	Merck KGAA, Darmstadt, Germany	MAB3802
Alpha-Actinin	WB: 1:1000	mouse	100	Santa Cruz Biotechnology Inc., Dallas, USA	sc-17829
BLM	WB: 1:250	Mouse	180	Santa Cruz Biotechnology Inc., Dallas, USA	Sc-365753
CENP-B (C-10)	1:1000	Mouse	80	Santa Cruz Biotechnology Inc., Dallas, USA	sc-376392
Cyclin A2	IF: 1:500	Rabbit	49	Abcam, Cambridge, UK	Ab181591
Cyclin B1	WB. 1:1000	Mouse	55	Cell Signalling	4135
FANCD2	IP: 2 µg/IP	Rabbit	164.1	Novus Biologicals,	NB100-182

FANCD2	WB: 1:1000	Rabbit	164.1	Abcam, ac108928	ab108928
GAPDH	WB: 1:1000	Rabbit	36	Cell Signalling	14C10
GFP	WB: 1:250	Rat	27	ChromoTek	3H9
Histone 3	WB: 1:5000	Goat	15	Abcam	Ab12079
MPM-2 Antiphospho-Ser/Thr-Pro	Flow: 1:1000	Mouse	Varies	Merck	05-368
Normal IgG	mouse IP: 1:1000	Mouse	150	Santa Cruz Biotechnology	Sc-2025
Phospho RPA2 (S33)	IF/Flow: 1:500	Rabbit	32	Life Science	A300-246A
PICH	IF: 1:150	Rabbit	140	Abnova	H00054821
RMI1	WB: 1:500	Rabbit	75	Proteintech Group	14630-1
RPA32/RPA2	IF: 1:1000	Mouse	32	Abcam	ab2175

Table 17 | List of secondary antibodies

Name	Dilution	Host	Manufacturer	Reference
Anti-mouse HRP	WB: 1:5000	Goat	R&D Systems	HAF007
Anti-mouse, Alexa Fluor® 594	IF/Flow: 1:500	Donkey	Jackson ImmunoResear	715-585-150
Anti-mouse, Alexa Fluor® 488	IF/Flow: 1:500	Goat	Jackson ImmunoResear	115-545-003
Anti-rabbit HRP	WB: 1:5000	Goat	R&D Systems	HAF008
Anti-rabbit, Alexa Fluor® 594	IF/Flow: 1:500	goat	Jackson ImmunoResear	711-586-152
Anti-rabbit, Alexa Fluor® 647	IF/Flow: 1:500	Donkey	Jackson ImmunoResear	JIM-711-605152
Anti-rabbit, Alexa-Fluor® 488	IF/Flow: 1:500	Goat	Jackson ImmunoResear	111-545-003

Anti-rat HRP	WB: 1:5000	Chicken	R&D Systems	HAF005

2.14 Kits

Table 18 | List of kits

Kit	Manufacturer
CellTiter-Glo® Luminescent Cell Viability Assay	Promega, Fitchburg, USA
DNeasy® Blood & Tissue kit	Qiagen, Venlo, Netherlands
Duolink® PLA Probe kit	Merck KGaA, Darmstadt, Germany
Duolink® Fluorescent Detection kit	Merck KGaA, Darmstadt, Germany
FxCycle™ PI/RNase Staining Solution	Thermo Fisher Scientific, Inc., Waltham, USA
Lipofectamine™ CRISPRMAX™ Cas9 Transfection Reagent kit (includes Lipofectamine CRISPRMAX reagent and Cas9 Plus™ reagent)	Thermo Fisher Scientific, Inc., Waltham, USA
MycoStrip® Mycoplasma Detection kit	InvivoGen, San Diego, USA
Pierce™ BCA Protein Assay Kit	Thermo Fisher Scientific, Inc., Waltham, USA
PureLink™ HiPure plasmid midiprep kit	Thermo Fisher Scientific, Inc., Waltham, USA
QIAprep® Spin Miniprep kit	Qiagen, Venlo, Netherlands
QIAquick® PCR Purification kit	Qiagen, Venlo, Netherlands
Quick Ligation™ kit	New England Biolabs, Ipswich, USA

2.15 Software

Table 19 | List of software

Software	Manufacturer
Adobe Illustrator CC 2018	Adobe Inc., San José, USA
Agilent platform	Agilent Technologies, Inc., Santa Clara, USA
Benchling platform	Benchling, Inc., San Francisco, USA
BioRender	BioRender, Toronto, Canada

CellProfiler 4.2.1	Broad Institute
Chat GPT sol 5.6	OpenAI, San Francisco, CA, USA
Cytoscape v3.9.0	National Human Genome Research Institute, Rockville Pike, USA
FlowJo™ V10	Becton, Dickinson and Company, New Jersey, USA
ImageJ/FIJI 1.52i	ImageJ, National Institutes of Health, Bethesda, USA
GraphPad Prism 5 and 9 and 10	GraphPad Software Inc.
ImageJ	National Institutes of Health, Bethesda, USA
MaxQuant 2.0.1.0	Max Planck institute of biochemistry, Martinsried, Germany
Microsoft 365 Apps	Microsoft Corporation, Redmond, USA
Perseus 1.6.15.0	Max Planck institute of biochemistry, Martinsried, Germany
RStudio 1.1.463 and R language 3.5.3	Posit PBC, Boston, USA
SlideBook 6.0	Intelligent Imaging Innovations Inc., Denver, USA
SnapGene® Viewer 5.0.7	GSL Biotech LLC, San Diego, USA

3 Methods

3.1 Cell culture techniques

All cell culture experiments were performed under sterile conditions in a laminar flow hood to prevent microbial contamination. All equipment and surfaces were sterilized with 70% ethanol before use. Cell density and morphology were routinely monitored by light microscopy. In addition, cells were regularly screened for mycoplasma contamination using the MycoStrip® Mycoplasma Detection Kit according to the manufacturer's instructions. All experiments described in this thesis were performed using mycoplasma-free cells. HCT116 Tet-OsTIR1 cells were kindly provided by Masato Kanemaki. The HCT116 Tet-OsTIR1 BLM AID/AID cell line contains biallelic modifications of the endogenous BLM locus, resulting in C-terminally tagged BLM-AID-eGFP fusion proteins. This homozygous cell line also carries a puromycin resistance cassette.

Cells were cultured in Dulbecco's Modified Eagle Medium (DMEM) supplemented with 10% fetal bovine serum (FBS) and 1% penicillin/streptomycin (P/S). Cells were maintained at 37 °C in a humidified incubator with 5% CO_2. Cells were passaged when they reached approximately 70–80% confluency. For passaging, the old medium was removed, and cells were washed with pre-warmed phosphate-buffered saline (PBS). Cells were then incubated with pre-warmed 0.25% trypsin-EDTA for 5 min at 37 °C. After detachment, trypsin was inactivated by adding pre-warmed DMEM supplemented with FBS and penicillin/streptomycin. A portion of the cell suspension was reseeded into fresh culture flasks or plates, depending on the experimental setup.

3.1.1 Freezing of human cell lines

Cells were trypsinized and collected from culture flasks at approximately 70% confluency. The cell suspension was transferred to a 15 mL tube and centrifuged at 1,300 rpm for 3 min at room temperature. The supernatant was removed, and the cell pellet was resuspended in 1 mL freezing medium. The cell suspension was transferred to a cryotube, and the cap was closed and loosened by one full turn. Cells were slowly frozen overnight at −80 °C in a freezing container containing isopropanol. The next day, cryotubes were transferred to liquid nitrogen for long-term storage.

3.1.2 Thawing of human cell lines

Frozen cells were thawed rapidly by placing cryotubes from liquid nitrogen into a 37 °C water bath until the medium began to thaw. The cell suspension was then transferred stepwise into a new tube containing 10 mL pre-warmed growth medium and centrifuged at 1,300 rpm for 3 min at room temperature. After removal of the supernatant, the cell pellet was resuspended in 10 mL fresh growth medium to remove residual DMSO from the freezing medium. Cells were transferred to a culture flask

and evenly distributed by gently moving the flask crosswise before incubation at 37 °C. The following day, the medium was replaced to remove dead cells. Further passaging was performed as described above.

3.1.3 Cell counting

For each experiment, defined cell numbers were seeded according to the experimental setup. Cell numbers were determined using the Countess™ II Automated Cell Counter. For counting, 10 µL of cell suspension was mixed with trypan blue at a 1:1 dilution and applied to the counting chamber. The cell concentration per milliliter was then determined.

3.2 Generation of APEX1 knockout and rescue cell lines

3.2.1 CRISPR–Cas9-mediated APEX1 knockout

APEX1 knockout cells were generated from wild-type cells by CRISPR–Cas9-mediated genome editing. For CRISPR–Cas9-mediated knockout, 3×10^5 cells were seeded per well in 6-well plates containing DMEM without serum or antibiotics to reach approximately 30–70% confluency at the time of transfection.

The following day, the transfection mixture was prepared using Cas9 nuclease, gRNA, Cas9 Plus™ reagent, and CRISPRMAX™ transfection reagent. Two separate solutions were prepared. Tube 1 contained Cas9 nuclease, gRNA solution, and Cas9 Plus™ reagent, which were added sequentially and mixed thoroughly by pipetting and vortexing. Tube 2 contained CRISPRMAX™ transfection reagent diluted in Opti-MEM™ I transfection medium and was briefly vortexed. To form the transfection complex, the solution from Tube 1 was added to Tube 2, mixed well, and incubated for 5–10 min at room temperature.

The transfection complex was then added directly to the cells in culture medium. Cells were incubated for 2–3 days at 37 °C in a CO_2 incubator. After incubation, cells were trypsinized. A portion of the cells was maintained in culture, whereas the remaining cells were harvested for protein isolation and quantification as described below. Protein samples were analysed by Western blotting to assess target protein depletion and the efficiency of CRISPR–Cas9-mediated knockout. Non-transfected wild-type cells were used as controls.

3.2.2 Single-cell clone selection of APEX1 knockout cells

After confirmation of target protein depletion, cells were trypsinized and collected for single-cell clone selection. Depending on the observed depletion efficiency, 500 and 1,000 cells were seeded into

separate 15 cm Petri dishes to allow colony formation. The number of colonies selected for expansion was determined based on the overall depletion efficiency.

Single colonies were isolated using sterile cloning discs. Cloning discs were wetted with trypsin, placed on individual colonies for 5 min, and then transferred to 96-well plates to establish single-cell-derived clones. Clones were subsequently expanded by sequential transfer from 96-well plates to 48-well, 24-well, 12-well, and finally 6-well plates. During clone expansion, cells from each clone were collected while a small fraction was maintained in culture. Protein lysates were prepared from each clone and analysed by Western blotting to distinguish successful knockout clones from unsuccessful clones.

3.2.3 Molecular cloning and verification of APEX1 rescue constructs

3.2.3.1 Restriction digest and ligation

The pLIX401 APEX1-WT, APEX1-CI, and APEX1-SO constructs were verified by restriction digestion. In addition, classical restriction enzyme-based cloning was performed when required. Restriction digest and ligation reactions were carried out separately. For restriction digestion, 1 µg DNA was mixed with 2.5 µL rCutSmart buffer, 1 µL restriction enzyme mixture, and ddH_2O to a final volume of 25 µL. The restriction digest was incubated at 37 °C for 1 h. After digestion, DNA fragments were purified using a PCR purification kit, and DNA concentration was measured using a Nanodrop spectrophotometer. For ligation, 100 ng plasmid backbone and 200 ng insert were mixed with 2 µL 10× T4 DNA ligase buffer, 1 µL T4 DNA ligase, and nuclease-free water to a final volume of 20 µL. The ligation reaction was incubated at room temperature for 2 h, followed by heat inactivation of T4 DNA ligase at 65 °C for 10 min.

3.2.3.2 Bacterial transformation

To amplify plasmid DNA, chemically competent E. coli DH5 alpha cells were transformed with the plasmid of interest. For each transformation, 100 ng plasmid DNA was added to 50 µL chemically competent E. coli cells. The mixture was incubated on ice for 20 min, followed by heat shock at 42 °C for 60 s to promote plasmid uptake. Cells were immediately placed back on ice for 2 min. After recovery on ice, 500 µL LB medium was added, and cells were incubated at 37 °C with shaking at 650 rpm for 1 h to allow expression of the antibiotic resistance gene. Different volumes of the transformed cells, usually 100 µL and 400 µL, were plated onto LB agar plates containing the appropriate antibiotic corresponding to the plasmid resistance marker. Plates were incubated overnight at 37 °C. Individual colonies were selected for downstream analyses, including plasmid isolation and verification of successful transformation.

3.2.3.3 Plasmid isolation

Plasmid DNA was isolated from E. coli using the QIAprep Miniprep Kit (Qiagen) to obtain small quantities of DNA suitable for sequencing, downstream experiments, or transfection of a limited number of cells. For applications requiring larger amounts of plasmid DNA, purification was performed using either the PureYield™ Midi Prep System or the QIAGEN Plasmid Maxi Kit according to the manufacturer's instructions.

3.2.4 Transfection and lentiviral transduction

3.2.4.1 siRNA transfection

HCT116 cells were seeded one day before transfection in 6-well plates. A total of 5×10^5 cells were seeded per well in 2 mL antibiotic-free growth medium supplemented with FBS. Cells were incubated at 37 °C in a CO_2 incubator until they reached approximately 60–80% confluency, which usually required 18–24 h. siRNAs targeting APEX1 or ALYREF, as well as scrambled control siRNA, were resuspended in RNase-free water. For each transfection, the siRNA solution was prepared by diluting 0.5 µg siRNA, corresponding to 2 µL siRNA stock solution, in 98 µL Opti-MEM. In a separate tube, the transfection reagent solution was prepared by diluting Lipofectamine in Opti-MEM. The optimal amount of Lipofectamine was determined experimentally. In the final protocol, 2 µL of Lipofectamine was diluted in 98 µL of Opti-MEM. The diluted siRNA solution was then added directly to the diluted Lipofectamine solution, gently mixed by pipetting, and incubated for 15–45 min at room temperature to allow complex formation. For each transfection, 0.8 mL of Opti-MEM was added to the siRNA–Lipofectamine complexes. The solution was mixed gently, and the complete transfection mixture was added to the washed cells. Cells were incubated with the transfection mixture for 5–7 h at 37 °C in a CO_2 incubator. Afterwards, the transfection mixture was removed and replaced with fresh antibiotic-free growth medium. Cells were incubated for an additional 18–24 h, after which the medium was replaced with fresh growth medium. Cells were harvested or processed for further analysis 24–72 h after medium replacement, depending on the experimental setup.

3.2.4.2 PEI transfection

For PEI-mediated transfection, HCT116 cells were seeded into 6-well plates 24 h before transfection. HCT116 cells were seeded at a density of 5×10^5 cells per well. The following day, transfection mixtures were prepared for each well. In Tube 1, 2 µg DNA per plasmid was diluted in 350 µL serum-free medium or Opti-MEM. In Tube 2, 6 µL PEI was diluted in 350 µL serum-free medium or Opti-MEM. The PEI-containing solution was added to the DNA-containing solution, gently mixed, and incubated for 30 min at room temperature to allow complex formation. After incubation, 700 µL transfection mixture was added dropwise to each well. Cells were incubated at 37 °C for 6 h, after which the medium was

replaced with fresh culture medium to remove PEI. Forty-eight hours after transfection, cells were harvested or seeded for further analysis.

3.2.4.3 Lentiviral transduction

Lentiviral particles were produced in HEK293T cells. For this, 7.5×10^5 HEK293T cells were seeded per well in 6-well plates. The following day, cells were transfected using Lipofectamine™ 2000 according to the manufacturer's instructions. For each transfection, ALY siRNA (h): sc-45390 Santa Cruz Santa Cruz and the lentiviral expression vector were diluted in 200 µL Opti-MEM. In a separate tube, 10 µL Lipofectamine™ 2000 was diluted in 200 µL Opti-MEM and incubated for 5 min at room temperature. The diluted Lipofectamine™ 2000 solution was then combined with the plasmid mixture and incubated for an additional 20 min at room temperature to allow complex formation. The transfection mixture was added dropwise to each well, and the plate was gently rocked to distribute the mixture evenly. Cells were incubated at 37 °C for 6 h, after which the medium was replaced with 2 mL fresh growth medium. The following day, recipient HCT116 cells were seeded into a second 6-well plate at a density of 1×10^6 cells per well. One well was left uninfected as a selection control. Recipient cells were infected 48 h after the medium change of the transfected HEK293T cells. Viral supernatant was collected from each 6-well plate and filtered through a sterile 0.45 µm syringe filter into a 15 mL tube. Polybrene was added to a final concentration of 8 µg/ml. The medium was removed from the recipient cells, and the virus-containing medium was added to the corresponding wells. Regular growth medium was added to the uninfected control well. Cells were incubated with the viral supernatant overnight. After 16 h, the medium was replaced with 2 mL antibiotic-free growth medium. Forty-eight hours after infection, antibiotic selection was started.

3.3 Thymidine cell cycle synchronization

To determine mitotic time points after thymidine release, HCT116 cells were synchronized using a single thymidine block. Cells were grown at 37 °C in a humidified atmosphere with 5% CO_2. The next day, cells were treated with 2 mM thymidine for 24 h. Cells were released from thymidine by washing three times with 1× PBS and were then cultured in fresh medium. Where indicated, cells were treated with low concentrations of aphidicolin, doxycycline, or auxin after release. Cells were harvested at different time points according to the cell cycle phase analysed, including 0 h, 5 h, 10.5 h after release. For aphidicolin treatment, cells were synchronized with 2 mM thymidine for 24 h, released, and immediately treated with aphidicolin. Cells enriched in anaphase were fixed or harvested 10.5 h after release and used for downstream experiments, including ChIP-MS and immunofluorescence microscopy.

3.4 Cell cycle-specific depletion of BLM

To investigate cell cycle-specific functions of BLM we used HCT116 Tet-OsTIR1 BLM-AID/AID-GFP PICH-mCherry cell line, BLM was depleted in synchronized cells using the auxin-inducible degron (AID) system. Cells were synchronized as described above. For BLM depletion, cells were first treated with doxycycline (DOX, 1 µg/mL) for 24 h before the thymidine block to induce expression of the plant F-box protein TIR1, which is required for the AID system. During the 24 h thymidine block, 500 µM indole-3-acetic acid (IAA; auxin) was added together with DOX to induce degradation of AID-tagged BLM. In the presence of TIR1, IAA promotes recognition of the AID-tagged protein by the SCF E3 ubiquitin ligase complex, leading to ubiquitination and subsequent proteasome-mediated degradation. After release from the thymidine block into fresh medium, both DOX and IAA were supplemented again to maintain BLM depletion throughout the experiment.

3.5 Cell cycle-specific expression of APEX1

To induce APEX1 expression in the F9R1 rescue cell line, cells were treated with doxycycline (DOX, 2 µg/mL). F9R1 cells were derived from an APEX1 knockout background and contained a plasmid encoding wild-type APEX1 under the control of a Tet-On promoter. Therefore, DOX treatment was used to induce expression of wild-type APEX1. Cells were synchronized using a single thymidine block as described above and fixed 10.5 h after thymidine washout. To compare different durations of APEX1 expression, DOX was added either throughout the experiment, including the thymidine block and the release period, resulting in a total induction time of 34 h, or only after release from the thymidine block for the final 10.5 h before fixation. After release, cells were treated with aphidicolin to induce replication stress or with DMSO as a control. Cells were harvested and fixed 10.5 h after release.

3.6 Colony formation assay

For the colony formation assay, 500 HCT116 cells were seeded per well in 6-well plates and distributed evenly. After 24 h, the medium was replaced with fresh medium containing doxycycline (DOX, 1 µg/mL) to induce TIR1 expression. After an additional 24 h, cells were treated with the indicated combinations of 500 µM auxin (IAA) and 100 nM aphidicolin (APH). Medium containing the corresponding treatments was replaced every 24 h. After 10 days of treatment, colonies were washed twice with pre-warmed 1× PBS and fixed with crystal violet fixative for 20 min at room temperature. The crystal violet fixative was then removed and retained for reuse. Colonies were washed once with 1× PBS and subsequently washed one to two times with H_2O. Plates were dried with the lid open under a fume hood for two days. Colony formation was analysed using Fiji software.

3.7 Protein detection

3.7.1 Sample preparation for Western blotting

For Western blot analysis, cells were grown in 6-well plates or larger culture vessels, depending on the experimental setup. Cells were detached by incubation with trypsin for 5 min and collected by centrifugation. Cell pellets were washed once with 1× PBS, the supernatant was discarded, and pellets were stored at −20 °C until further use. For protein extraction, cell pellets were resuspended in 50–200 µL RIPA buffer supplemented with freshly added protease and phosphatase inhibitors. Samples were sonicated for 15 min and centrifuged at full speed for 10–15 min at 4 °C. The supernatant containing the protein lysate was transferred to a new tube and used for protein concentration determination.

3.7.2 Protein concentration determination

3.7.2.1 Bradford assay

Protein concentration was determined using the Bradford assay. Bradford reagent was diluted with water at a ratio of 1:5. For each sample, 800 µL of diluted Bradford reagent was prepared in a separate tube, and 1 µL of protein lysate was added. Each sample was pipetted in triplicate into a round-bottom 96-well plate, and absorbance was measured using a plate reader.

3.7.2.2 BCA assay

Protein concentration was alternatively determined using the BCA assay in round-bottom 96-well plates. A BSA standard curve was prepared in triplicate using a BSA stock solution of 2 µg/µL. Increasing BSA standard concentrations were prepared, resulting in reference concentrations ranging from 0.00 to 1.50 µg/µL. BCA solutions A and B were mixed at a ratio of 50:1, and 200 µL BCA working solution was added to each well. For each sample, 1 µL of protein lysate was pipetted in triplicate. Plates were incubated for 30 min at 37 °C, and absorbance was measured using a plate reader.

3.7.3 SDS–PAGE and immunoblotting

For SDS–PAGE, resolving gels with acrylamide/bis-acrylamide concentrations of 7.5%, 10%, or 12.5% and stacking gels with a concentration of 5% were prepared. Gels were placed in an electrophoresis chamber containing 1× running buffer. Protein marker (3 µL) and protein samples, typically 20 µg per lane, were loaded onto the gel. Electrophoresis was performed at 120 V for at least 1.5 h or until the running front reached the bottom of the gel. Before wet transfer, the stacking gel was removed. Proteins were transferred to a membrane by wet transfer at 100 V for 1 h at 4 °C or alternatively at 50 V for 16 h at 4 °C. After transfer, membranes were stained with Ponceau Red solution for 5 min to assess transfer efficiency. Membranes were carefully washed with water and imaged using the Azure

c300 imaging system. When required, membranes were cut into separate pieces to allow simultaneous detection of multiple proteins. Membranes or membrane pieces were blocked in 5% milk in TBST for 1 h at room temperature. For immunodetection, primary antibodies were diluted in blocking solution with TBST and added to the membranes using approximately 5 mL antibody solution per membrane or membrane piece. Membranes were incubated overnight at 4 °C on a roller. The following day, membranes were washed three times for 5 min with TBST. Secondary antibodies were diluted in TBST at 1:1,000 or 1:10,000, and 5 mL secondary antibody solution was added to each membrane or membrane piece. Membranes were incubated for 1 h at room temperature and then washed three times for 5 min with TBST. For detection, membranes were placed on a black plate, and freshly prepared ECL solution was added directly to each membrane. Chemiluminescent signals were detected using the Azure c300 imaging system. Band intensity was analysed using Fiji.

3.8 ChIP–WB

3.8.1 Protein isolation

For ChIP–WB analysis, HCT116 cells were seeded into 15 cm dishes, with two dishes used per sample. Approximately 4 × 10^6 cells were seeded per dish. After one day, cells were treated with 2 mM thymidine for 24 h. Cells were released from thymidine by washing three times with 1× PBS and were then cultured in DMEM supplemented with FBS and penicillin/streptomycin. Cells were treated with 100 nM aphidicolin diluted in cell culture medium and incubated for 10.5 h. Because many mitotic cells detached during the experiment, the medium and PBS wash were collected to increase recovery of mitotic cells. Samples were centrifuged at 1,300 rpm for 3 min at room temperature. Attached cells were then trypsinized and collected. For formaldehyde-treated samples, pellets were resuspended in 8 mL medium containing 1% methanol-free formaldehyde and incubated for 10 min at room temperature on a roller. Crosslinking was stopped by adding 0.96 mL of 1.25 M glycine, followed by incubation for 5 min at room temperature. Cell pellets were washed twice with ice-cold 1× PBS and centrifuged at 1,550 rpm for 5 min. For lysis, pellets were resuspended twice in 1 mL ice-cold RIPA buffer containing 150 mM NaCl, 0.5 mM EDTA pH 7.5, 10 mM Tris pH 7.5, 1% Triton X-100, 0.1% SDS, 1× PMSF, 1% deoxycholate, 2.5 mM $MgCl_2$, and 1× protease/phosphatase inhibitors. Samples were incubated on ice for 10 min after each resuspension step and centrifuged at 12,000 rpm for 1 min at 4 °C to remove the buffer. The pellet was resuspended in 1.8 mL ice-cold shearing buffer containing 1% SDS, 10 µM EDTA pH 7.5, and 50 mM Tris pH 7.5. Samples were distributed into six Diagenode 1.5 mL tubes for sonication. Chromatin was sonicated using a Bioruptor Pico at 4 °C for 15 cycles of 30s on and 30 s off to obtain chromatin fragments of approximately 200–500 bp. Lysates were centrifuged at 13,000 rpm for 20 min at 4 °C to remove cell debris, and the supernatant containing sheared chromatin was transferred to new tubes. Protein concentrations were determined using the BCA protein assay.

For each sample, 1 mg protein was used for immunoprecipitation. In addition, 50 µL of protein lysate was retained as input material. Input samples were mixed with 4× Laemmli buffer and denatured for 10 min at 95 °C before loading onto gels.

3.8.2 Immunoprecipitation

GFP and RFP nanobody beads were activated by resuspending 25 µL bead slurry per replicate in 500 µL ice-cold Wash I buffer. Beads were centrifuged at 2,500 rcf for 2 min at 4 °C. For each replicate, 1 mg of protein was adjusted to a final volume of 500 µL with RIPA buffer and incubated with 25 µL of nanobody beads for 1 h at 4 °C on a microtube rotator. After bead precipitation, 50 µL of supernatant was retained as a negative control and mixed with 4× Laemmli buffer before incubation at 95 °C for 10 min. The remaining supernatant was discarded. Beads were washed twice with 500 µL ice-cold IP Wash I buffer to reduce nonspecific binding, followed by four washes with 500 µL ice-cold IP Wash II buffer. Immune complexes were eluted from GFP-Trap® or RFP-Trap® agarose beads by resuspending the beads in 4× Laemmli buffer and boiling for 10 min at 95 °C. Beads were collected by centrifugation at 2,500 rcf for 2 min at 4 °C, and the supernatant was used for SDS–PAGE. SDS–PAGE and immunoblotting were performed as described above. All the IP fractions were loaded onto the gel.

3.9 ChIP-MS sample preparation and mass spectrometry analysis

3.9.1 Crosslinking and harvesting

For ChIP-MS experiments, HCT116 cells were synchronized and treated as described for UFB staining and aphidicolin treatment. Cells were seeded in 15 cm dishes at a density of 4.5×10^6 cells per dish for thymidine synchronization. Cells reached approximately 80–90% confluency at the time of harvest. Because many mitotic cells detached during the experiment, the medium and 1× PBS wash were collected to increase recovery of mitotic cells. Samples were centrifuged at 1,300 rpm for 3 min at room temperature. Attached cells were trypsinized, collected, and combined with the detached cell fraction. After centrifugation, the supernatant was discarded. The cell pellet was resuspended in 8 mL medium containing 1% methanol-free formaldehyde and incubated for 10 min at room temperature on a roller. Crosslinking was stopped by adding 0.96 mL of 1.25 M glycine, followed by incubation for 5 min at room temperature. Samples were then washed twice with ice-cold 1× PBS and centrifuged for 5 min at 1,550 rpm. Cell pellets were snap-frozen in liquid nitrogen and stored at −80 °C.

3.9.2 Chromatin preparation by sonication

Cell pellets were resuspended twice in 1 mL ice-cold RIPA buffer containing 150 mM NaCl, 0.5 mM EDTA pH 7.5, 10 mM Tris pH 7.5, 1% Triton X-100, 0.1% SDS, 1× PMSF, 1% deoxycholate, 2.5 mM $MgCl_2$, and 1× protease/phosphatase inhibitors. After each resuspension step, samples were incubated on ice

for 10 min and centrifuged at 12,000 rpm for 1 min at 4 °C to remove the buffer. The pellet was then resuspended in 1.8 mL ice-cold shearing buffer containing 1% SDS, 10 µM EDTA pH 7.5, and 50 mM Tris pH 7.5. Samples were distributed into six Diagenode 1.5 mL tubes for sonication. Chromatin was sonicated using a Bioruptor Pico at 4 °C for 15 cycles of 30s on and 30 s off to obtain a fragment size of approximately 200–500 bp. Samples were centrifuged at 12,000 rpm for 20 min at 4 °C, and the supernatant containing sheared chromatin was transferred to a new tube. The sheared chromatin lysate was kept at 4 °C until chromatin fragmentation was analysed.

3.9.3 Determination of chromatin fragmentation

To assess chromatin fragmentation, 50 µL sheared chromatin was incubated with 2 µL of 5 M NaCl at 99 °C for 15 min. Samples were then cooled on ice for 5 min. Afterwards, 2 µL of RNase A (10 mg/mL) was added, and samples were incubated at 37 °C for 20 min. Proteinase K solution was then added to each tube, and samples were incubated at 56 °C for 20 min. The sheared chromatin was purified using a QIAGEN PCR purification kit and eluted in 50 µL hot RNase-free water. The eluted chromatin was analysed on an agarose gel, and chromatin concentration was measured using a Nano Drop spectrophotometer.

3.9.4 ChIP-MS with GFP and RFP nanobody beads

GFP and RFP nanobody beads were activated by resuspending 25 µL bead slurry per replicate in 500 µL ice-cold Wash I buffer. Beads were centrifuged at 2,500 rcf for 2 min at 4 °C. The supernatant was discarded, and the beads were washed again. For each replicate, 25 µg of chromatin was adjusted to a final volume of 500 µL with RIPA buffer and incubated with 25 µL of nanobody beads for 1 h at 4 °C on a microtube rotator. GFP and RFP beads were washed twice with 500 µL ice-cold IP Wash I buffer containing 10 mM Tris pH 7.5, 150 mM NaCl, and 0.25% NP-40 to reduce nonspecific binding. Beads were then washed four times with 500 µL ice-cold IP Wash II buffer containing 10 mM Tris pH 7.5 and 150 mM NaCl. Precipitated proteins were eluted by incubating the beads for 30 min with elution buffer 1 containing 2 M urea, 50 mM Tris pH 7.5, 2 mM DTT, and 20 µg/mL trypsin. A second elution was performed using elution buffer 2 containing 2 M urea, 50 mM Tris pH 7.5, and 10 mM chloroacetamide for 5 min at 37 °C. Both eluates were combined and incubated overnight at 25 °C. Trypsin-digested peptides were acidified by adding 10% trifluoroacetic acid (TFA) to reach approximately pH 2. Samples were purified using three-layered C18 membrane stage tips. C18 membranes were activated by washing the tips with 100 µL methanol, followed by two washes with 100 µL buffer A containing 0.5% acetic acid and 3% acetonitrile. Acidified samples were loaded onto the C18 stage tips and washed with 100 µL buffer A. Peptides were eluted with 40 µL buffer B containing 0.5% acetic acid and 80%

acetonitrile into small PCR tubes. Samples were centrifuged in a SpeedVac for approximately 1 h to evaporate acetonitrile. Peptides were resuspended in 9 µL buffer A or A* before LC–MS/MS analysis.

3.9.5 LC–MS/MS analysis

Peptides were separated on reverse-phase columns packed in-house with ReproSil-Pur C18-AQ 1.8 µm resin. Peptides were directly injected into a linear ion trap mass spectrometer using nanoflow HPLC. Peptides were loaded in buffer A and eluted using a gradient of 5–95% buffer B containing 80% acetonitrile and 0.5% acetic acid at a constant flow rate of 250 nl/min. Raw mass spectrometry data were analysed using MaxQuant version 2.0.1.0 and Perseus software. Statistical significance was determined using a permutation-controlled Student's t-test with an FDR threshold of 0.05 by comparing replicate ChIP-MS samples between experimental conditions.

3.9.6 Analysis of proteome data for individual ChIP-MS experiments

Proteome data were analysed using Perseus software version 1.6.15.0. Identified protein groups were first filtered to remove potential contaminants, reverse hits, and proteins identified only by site. LFQ intensity values were then $\log_2$-transformed, and only proteins with at least one valid value per row were retained for further processing. Functional annotations for Gene Ontology Biological Process (GOBP), Molecular Function (GOMF), Cellular Component (GOCC), KEGG pathways, and CORUM protein complexes were added to the dataset. R-loop factors were annotated using the high-confidence R-loop-binding protein dataset[152]. Missing values were imputed separately for each sample column using a normal distribution with a width of 0.3 and a downshift of 1.8. After imputation, proteins were further filtered to retain only rows with at least three valid values across the complete dataset. For comparative analysis and volcano plot generation, statistical testing was performed in Perseus using a permutation-based Student's t-test. The false discovery rate (FDR) threshold was set to 0.05, and the significance parameter s0 was set to 0.1. This analysis was applied to triplicate or quadruplicate ChIP-MS samples for each condition to identify proteins with significantly different abundance between experimental groups.

3.9.7 Processing proteomics data for meta-analysis

Mass spectra were quantified separately for each project using MaxQuant. The quantified protein groups from all projects (P96, P144, P154, P160, P165, P168, P192, P212, and P217) were then combined, and intensity values were $\log_2$-transformed using R version 4.5.2 (R Core Team, 2025). Missing values were imputed within each control experiment (IgG, IgG(m), IgG(r), or RFP nanobody) when fewer than two observations were available for a given protein group. Perseus-style imputation

was implemented[153]. Within each experimental replicate, the mean μ_r and standard deviation σ_r were estimated across proteins. Missing protein intensities X were sampled from a normal distribution:

$$X \sim \mathrm{N}(\mu, \sigma)$$

The imputation distribution was defined as:

$$\mu = \mu_r - s \cdot \sigma_r, \quad \sigma = w \cdot \sigma_r$$

where the down-shift parameter was s = 2.58 and the width parameter was w = 0.3.

3.9.7.1 Meta-analysis and statistical testing

To perform a meta-analysis across all proteomics pull-down experiments, differential abundance was first tested separately for each protein in each pull-down experiment and its corresponding control. One-tailed, unpaired two-sample t-tests were used. The null hypothesis was that a protein was not more abundant in the bait pull-down than in the matched control under the same treatment. The mean $\log_2$ fold change (Log2FC) was calculated, and multiple-testing correction was performed using the Benjamini–Hochberg procedure to control the false discovery rate (FDR) (Benjamini and Hochberg, 1995).

Before meta-analysis, S-phase-arrested and doxycycline-treated experiments were excluded. After differential abundance testing and filtering, a harmonic-mean p-value (HMP) was calculated for each protein across all included experiments by applying the p.hmp function from the harmonic-mean-p R package to the unadjusted p-values, using equal weights for each protein across all tests that generated valid p-values (Wilson, 2019). This approach controls the strong-sense family-wise error rate (FWER) for each protein across experiments without requiring independence among experiments, unlike Fisher's combined probability test (Fisher, 1932).

The resulting HMPs were then adjusted across all proteins using the Benjamini–Hochberg procedure to control the FDR. A significance score was defined by combining the mean Log2FC (FC) for each protein across all differential abundance analyses with its adjusted HMP (HMPadj):

$$S = max\left(0, log_{10}(\alpha) - log_{10}\left(HMP_{adj}\right)\right) \cdot max(0, FC - FC_{thresh})$$

Here, α = 0.05 was used as the FDR threshold, and FC thresh = 1 was used as the Log2FC threshold. The HMP-based meta-analysis was repeated separately for aphidicolin- and DMSO-treated experiments. Experiments using APEX1 or ALYREF as baits were excluded from these treatment-specific meta-analyses. This part of analysis was performed by Eric Heller.

3.9.8 Pathway enrichment analysis

Pathway enrichment analysis was performed in R using the gprofiler2 package and custom pathway annotations. For the individual ChIP-MS datasets, significantly enriched proteins were identified using an adjusted p-value threshold of 0.05, and over-representation analysis was performed separately for each experimental condition using all detected and annotated proteins as the background. Enrichment was evaluated for Gene Ontology Biological Process terms and custom pathway collections, including UFB-associated and R-loop-associated protein sets. Statistical significance was assessed using Fisher's exact test, followed by Benjamini–Hochberg correction for multiple testing.

For the ChIP-MS meta-analysis, proteins identified as significant in at least two independent experiments were ranked according to their meta-analysis significance score. The top-ranked proteins from the APH and NoAPH datasets were analysed separately using ranked Gene Ontology Biological Process enrichment with "gprofiler2". The enrichment ratio was calculated as the proportion of pathway-associated proteins among the selected proteins divided by the proportion of pathway-associated proteins in the effective background. The enrichment score was defined as $-\log_{10}$ of the adjusted p-value. Enrichment results were compared between APH and NoAPH conditions and visualized using heatmaps and dot plots.

3.10 Flow cytometric cell cycle analysis

HCT116 cells were seeded in 10 cm plates at a density of 0.6×10^6 cells per dish. Cells were synchronized and harvested by collecting the medium and 1× PBS wash to recover detached cells. The collected fraction was centrifuged at 2,000 rpm for 5 min at room temperature. Attached cells were trypsinized, collected, and combined with the pellet from the detached cell fraction. For fixation, the cell pellet was resuspended by vortexing, and 500 µL ice-cold 70% ethanol was added dropwise. Fixed cells were incubated for at least 1 h and up to 2 days at 4 °C. Ethanol was removed by centrifugation at 2,000 rpm for 5 min. The cell pellet was resuspended in 500 µL 1× PBS containing 0.25% Triton X-100 and incubated on ice for 15 min. After centrifugation, the cell pellet was resuspended in 100 µL PBS containing 1% BSA and MPM-2 monoclonal antibody and incubated for 1 h at room temperature. After centrifugation and washing with 1× PBS containing 1% BSA, cells were resuspended in Alexa Fluor 488-conjugated goat anti-mouse IgG antibody diluted 1:300 in 100 µL PBS containing 1% BSA. Cells were incubated for 30 min at room temperature in the dark. After centrifugation at 2,000 rpm for 5 min, 500 µL FxCycle™ PI/RNase staining solution was added to the pellet, mixed well, and incubated for 15–30 min at room temperature in the dark. Stained cells were analysed by flow cytometry, and FlowJo software was used to calculate the percentage of cells in different cell cycle phases and to generate histograms.

3.10.1 Immunostaining for flow cytometry analysis

Cells were harvested by trypsinization and washed with 1× PBS by centrifugation at 2,000 rpm for 2 min. For fixation, cells were resuspended by vortexing, and 500 µL ice-cold 70% ethanol was added dropwise. Fixed cells were incubated at 4 °C overnight. The following day, cells were washed once with 1× PBS containing 0.25% Triton X-100 and centrifuged at 2,000 rpm for 5 min to remove residual ethanol. The cell pellet was resuspended in 100 µL PBS containing 1% BSA and the corresponding primary antibody and incubated for 1 h at room temperature. After washing, cells were resuspended in 100 µL PBS containing 1% BSA and secondary antibody diluted 1:300 and incubated for 30 min at room temperature in the dark. For DNA staining and RNA degradation, cells were incubated with 500 µL FxCycle™ PI/RNase staining solution for 30 min at room temperature in the dark. Samples were measured using the Attune™ NxT Flow Cytometer with the appropriate excitation wavelength and emission bandpass filter. Propidium iodide (PI) signal was detected using a 574/26 bandpass filter. Data were analysed using FlowJo software.

3.11 Fluorescence microscopy

3.11.1 DAPI staining for fluorescence microscopy

Synchronized HCT116 cells were seeded into 6-well plates at a density of 3.5×10^5 cells per well. Cells were washed with 1× PBS and fixed and permeabilized with Fix-Perm buffer containing 3% paraformaldehyde, 0.1% Triton X-100, and 1× PBS for 20 min at room temperature. Samples were washed three times with 1× PBS and incubated with NH_4Cl for 20 min at room temperature to quench residual aldehydes. After three additional washes with 1× PBS, cells were incubated with 0.5% Triton X-100 for 20 min at room temperature and washed three times with PBS for 5 min each. DNA was stained with a solution containing 0.02 mM SYTOX Green for 5–10 min while protected from light. Cells were washed once with 1× PBS and once with Milli-Q water. Sodium azide was added to a final concentration of 0.01% to prevent bacterial contamination, and plates were wrapped with parafilm and foil and stored at 4 °C protected from light.

3.11.2 Microscopic detection of mitotic aberrations

Mitotic aberrations in HCT116 cells were analysed by fluorescence microscopy. Approximately 0.25×10^6 cells were seeded per well in 6-well plates containing sterile 12 mm coverslips with a thickness of 0.17 mm. Cells were seeded to reach approximately 60–70% confluency after 24 h and then treated according to the synchronization protocol described above. At 10.5 h after release from the thymidine block, cells were gently washed once with 1× PBS and fixed with PFA-containing fixation buffer for 30 min at room temperature. The fixation buffer was carefully removed, leaving approximately 200 µL in

each well to prevent drying of the cells. Cells were washed three times with 1× PBS by gradually reducing the remaining fixation buffer during each washing step. After fixation, cells were permeabilized for 20 min and washed three times with 1× PBS. Cells were then incubated with PFA-specific blocking buffer for 1 h at room temperature. Primary antibodies diluted in blocking buffer were added, and coverslips were incubated overnight at 4 °C in a humidified chamber. The next day, coverslips were washed three times with 1× PBS and incubated with secondary antibodies diluted in blocking buffer for 1 h at room temperature in a humidified chamber. Secondary antibodies were removed by washing three times with 1× PBS. DNA was stained by adding staining solution for 3 min at room temperature in the dark. Coverslips were then washed once with 1× PBS and once with H_2O before mounting on dry glass slides that had been stored at −20 °C in 70% ethanol. Coverslips were sealed with nail polish and stored at 4 °C in the dark until microscopic analysis. For each replicate, 25 anaphase cells were imaged using a Nikon Ti2-E epifluorescence microscope equipped with a 63× oil immersion objective and a 10× eyepiece. Images were acquired with an exposure time of 500 ms. For DAPI, 20% laser power was used, whereas all other channels were acquired using 60% laser power. Z-stacks were acquired using 25 steps with a step size of 0.3 µm, covering a total range of 7.2 µm. Mitotic aberrations in anaphase, including chromatin bridges, lagging chromatin, and misaligned chromatin, were identified based on DAPI staining. Although these aberrations did not require antibody staining, they were analysed in the same anaphase cells used for ultrafine bridge marker staining; therefore, all images included antibody staining. Images were analysed using ImageJ/Fiji. Colocalization analysis was performed using the JACOP plugin in ImageJ to determine Pearson's correlation coefficient (r). BLM signal intensity was measured in ImageJ, and background intensity was subtracted from each measurement.

3.11.3 Staining and visualization of UFBs with interacting proteins

HCT116 cells were seeded at a density of 0.35×10^6 cells per well in black glass-bottom 6-well plates and grown for one day before synchronization. Cells were then treated with 2 mM thymidine for 24 h. After thymidine release, cells were washed twice with 1× PBS and cultured in supplemented medium. Cells were treated with 100 nM aphidicolin or DMSO and incubated for 10.5 h at 37 °C in a humidified atmosphere with 5% CO_2. Cells were gently washed twice with 1× PBS before fixation and permeabilization with fixation buffer for 20–30 min. Samples were washed three times with 1× PBS and incubated with NH_4Cl for 20 min at room temperature to quench residual aldehydes. After three washes with 1× PBS, cells were incubated with 0.5% Triton X-100 for 20 min at room temperature and washed three times with 1× PBS. Cells were blocked with 3% BSA in 1× PBST for 1 h at room temperature in a humidified chamber. Primary antibodies were diluted in blocking solution and added to the samples. Antibody dilutions were 1:250 for PICH, 1:150 for BLM, and 1:200 for FANCD2. Samples

were incubated overnight at 4 °C in a humidified chamber. The next day, cells were washed three times with 1× PBS and incubated with secondary antibody diluted in blocking solution for 1 h at room temperature in the dark. Cells were then washed three times with 1× PBS for 5 min each in the dark. DNA was stained with DAPI-containing staining solution for 5–10 min in the dark. Samples were rinsed once with 1× PBS and once with Milli-Q water. Coverslips were mounted on glass slides using mounting medium and sealed.

3.11.4 Metaphase spread analysis by microscopy

HCT116 cells were seeded at approximately 1–4 × 10^6 cells per 10 cm plate to reach 60–70% confluency after 24 h. Cells were treated with 400 ng/mL colchicine for 6 h to arrest cells in metaphase. Cells were gently washed once with 1× PBS. The medium and PBS containing detached mitotic cells were collected in tubes and combined with the trypsinized cell suspension from the same plate. Cells were centrifuged at 1,200 rpm for 3 min at room temperature. The cell pellet was washed once with 1× PBS and centrifuged again. After aspiration of most of the supernatant, approximately 500 µL was left in the tube, and the pellet was carefully resuspended in the remaining liquid. For hypotonic treatment, 7 mL pre-warmed hypotonic solution was added to each sample while gently tapping the tube. Samples were incubated at 37 °C for approximately 20 min to allow cell swelling. Swelling was monitored by placing 10 µL cell suspension under a microscope. Cells were then centrifuged at 1,000 rpm for 5 min at room temperature. After removal of the supernatant, cells were resuspended in the remaining 500 µL.

Cells were fixed by slowly adding 7 mL fixative solution to each sample. Samples were centrifuged at 1,200 rpm for 3 min at room temperature, the supernatant was aspirated, and cells were resuspended in the remaining 500 µL. The fixation and centrifugation steps were repeated two additional times. After the final centrifugation, the supernatant was completely removed, and the cell pellet was resuspended in 500 µL fresh fixative solution. Samples were stored at −20 °C until metaphase spreading. For metaphase spreading, the fixed cell suspension was dropped onto dry glass slides, which had been stored at −20 °C in 70% ethanol, from a height of approximately 100 cm. Slides were allowed to air-dry before mounting. Coverslips with a thickness of 0.17 mm were mounted using mounting medium containing DAPI and sealed with nail polish. For each replicate, 25 metaphase spreads were imaged using a Nikon Ti2-E epifluorescence microscope equipped with a 63× oil immersion objective and a 10× eyepiece. Images were acquired without z-stacks using an exposure time of 500 ms and 20% laser power for DAPI. Images were analysed using ImageJ/Fiji. Chromosomal gaps and breaks were quantified together, as they could not be reliably distinguished due to difficulties in defining clear boundaries between these aberrations. To assess chromosomal instability, two

complementary parameters were quantified from metaphase spreads: the percentage of metaphase cells with chromosomal breaks and the average number of breaks per cell. The percentage of metaphase cells with breaks reflected the frequency of cells entering mitosis with chromosomal damage, whereas the average number of breaks per cell reflected the severity of damage within individual cells.

3.11.5 Microscopy setup and image analysis

The Nikon/Andor spinning disk confocal microscope was equipped with an Andor EMCCD camera and a Nikon PerfectFocus autofocus system. Either a 60× oil immersion objective (Plan Apo, NA 1.40, WD 0.13 mm) or a 40× air objective (Plan Apo, NA 0.95, WD 0.25 mm) was used. Excitation was performed at 405 nm, 488 nm, 561 nm, and 633 nm for DAPI/eBFP2, Alexa Fluor 488/eGFP, Alexa Fluor 568/mRFP, and Alexa Fluor 647/iRFP, respectively. The setup was controlled using NIS-Elements software. Image processing and analysis were performed using NIS-Elements and ImageJ/Fiji where indicated.

3.11.6 Live-cell microscopy using the Lattice Lightsheet 7

Multiple 3.5 cm glass-bottom dishes were seeded at various densities. Cells that reached approximately 70% confluency were selected for imaging. Twelve hours before imaging, cells were stained with 1 nM of the nuclear stain SPY555-DNA (λabs 555 nm) at 37 °C. In addition, 1 µM verapamil was added to prevent dye efflux. The cells were placed in a humidified chamber with 5% CO_2 at 37 °C. Images were acquired every 2 min for at least 12 h. The images were analysed manually using Fiji software.

3.11.7 Proximity ligation assay (PLA)

Protein proximity was analysed using the Duolink® in situ proximity ligation assay (PLA) according to the manufacturer's fluorescence protocol. Cells grown on glass coverslips were fixed and permeabilized before the assay. Samples were blocked with Duolink® Blocking Solution for 1 h at 37 °C and then incubated with the appropriate primary antibody pairs under optimized conditions. After washing, species-specific PLUS and MINUS PLA probes were diluted 1:5 in antibody diluent and applied to the samples for 1 h at 37 °C. The samples were subsequently washed and incubated with ligation solution containing ligase for 30 min at 37 °C.

Following ligation, the samples were incubated with amplification solution containing polymerase for 100 min at 37 °C while protected from light. The coverslips were washed with Duolink® Wash Buffer B and mounted using Duolink® in Situ Mounting Medium containing DAPI. PLA signals were detected by fluorescence microscopy using identical acquisition settings for all experimental and control samples. Negative controls were processed in parallel by omitting one or both primary antibodies. Individual

fluorescent PLA puncta were interpreted as regions in which the two target epitopes were located within approximately 40 nm of each other.

3.12 Statistical analysis

Statistical analyses were performed using GraphPad Prism. Measured data were exported from Excel and entered grouped tables in GraphPad Prism. For immunofluorescence microscopy experiments, graphs were generated and analysed using unpaired parametric t-tests with 95% confidence intervals. Statistical significance was reported with four significant digits where applicable.

3.13 Data visualization

All data visualizations were generated using R version 4.3.0. Data were prepared and organized using the dplyr, tidyr, and stringr packages. Scatter plots, protein-ranking plots, dot plots, and enrichment plots were generated using ggplot2. Protein labels were added using ggrepel, and multi-panel figures were assembled using patchwork. Enrichment heatmaps were generated using ggplot2 or pheatmap. Figures were exported as high-resolution PNG files and vector-based PDF files using the Cairo package and the cairo_pdf graphics device. Final figures were assembled and edited using Adobe Illustrator.

4 Results

4.1 Proteomic screening for candidate UFB-resolution proteins

One of the major objectives of this study was to investigate the resolution of ultrafine bridges (UFBs) and identify potential interacting partners involved in this process. To address this question, we first characterized the mitotic interaction partners of UFB binding proteins and determined how these factors contribute to proper chromosome segregation and mitotic DNA repair. For this purpose, we used chromatin immunoprecipitation coupled with mass spectrometry (ChIP-MS). ChIP-MS is a robust approach that provides insight into the composition of chromatin-bound protein complexes within their native *in vivo* environment[146]. The use of antibodies raised against known UFB-associated proteins such as BLM, FANCD2, FANCI, TOP3A and PICH, followed by a meta-analysis of all datasets allowed us to identify promising candidate factors.

4.1.1 BLM ChIP-MS identifies replication stress-associated interactors

We selected Bloom helicase (BLM) as the initial bait protein because previous studies reported its association with all known classes of UFBs[59,64,94,110,112,113]. We synchronized HCT116-Tet-OsTIR1 BLM-AID-eGFP cells at the G1/S boundary using thymidine and subsequently released them into fresh medium in the presence or absence of a very low dose of the replication inhibitor aphidicolin to induce mild replication stress without arresting cells at the G2/M DNA damage checkpoint (Figure 4.1A). Cells were harvested during S phase and mitosis. Mitotic cells were harvested 10.5 h after release from the single thymidine block, when most cells had entered mitosis and the highest fraction of UFB-containing cells was observed, approximately 15%[140]. As control, cells were also harvested 5 h after release, when most cells were still in S phase[140]. To stabilize protein-DNA complexes, we crosslinked cells with formaldehyde. After cell lysis, we extracted the insoluble chromatin fraction, fragmented the chromatin by sonication, and used the resulting material for immunoprecipitation with GFP-Trap® agarose beads. Recovered proteins were digested with trypsin and analysed by mass spectrometry (Figure 4.1A).

In these experiments, BLM-eGFP/AID was typically enriched more than 250-fold compared with control immunoprecipitations performed with nonspecific IgG or RFP-Trap agarose beads (Figure 4.1B). To identify significantly enriched proteins, we performed Student's t-tests and corrected for multiple testing using a permutation-based FDR estimation procedure[153]. It should be noted that the experiments compared in this analysis were not all performed side by side. This analysis identified several significantly enriched proteins in APH-treated mitotic samples. Notably, numerous R-loop-associated proteins were enriched under these conditions (Figure 4.1B, shown in pink). In addition, in

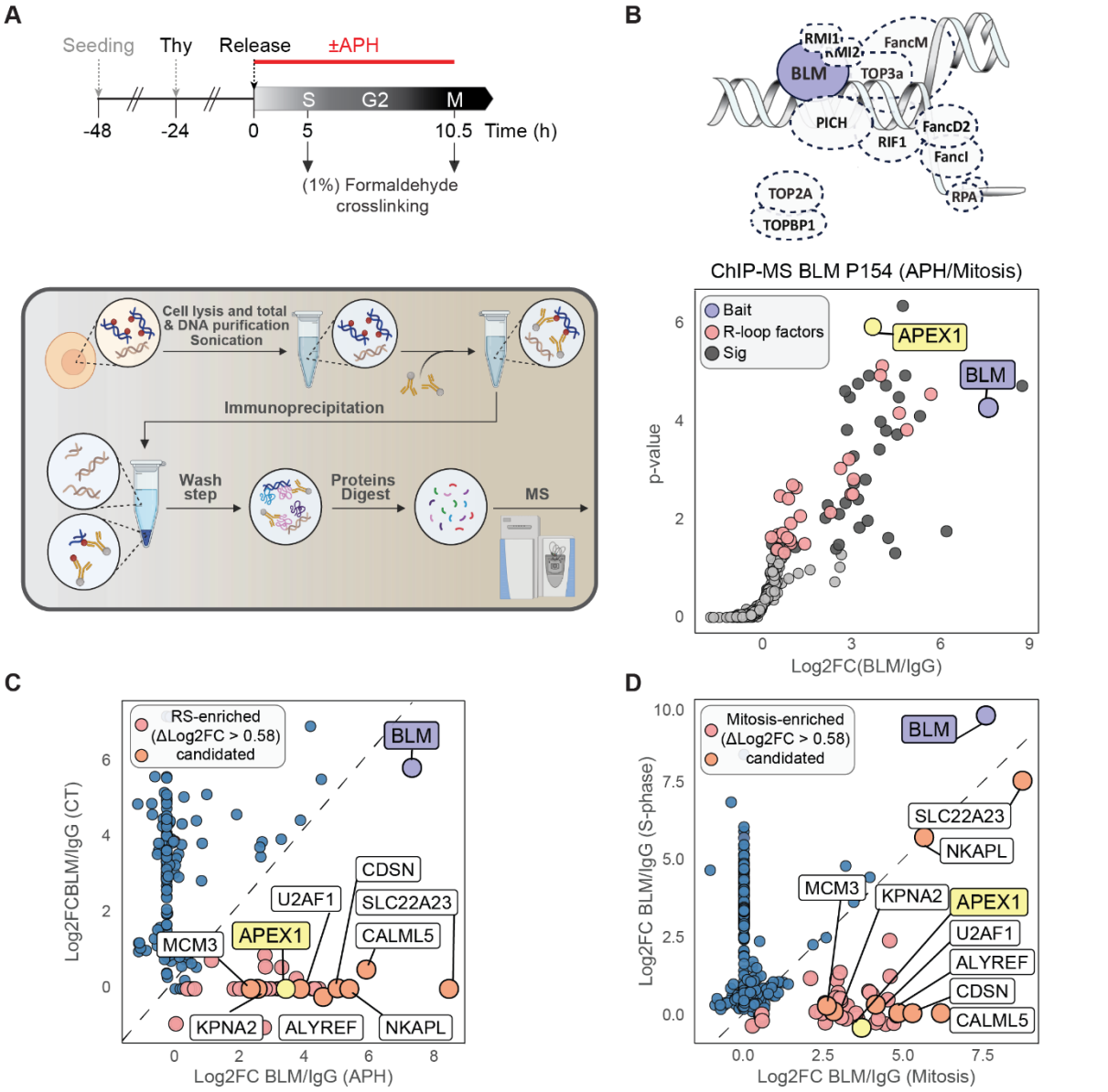


Figure 4.1 | ChIP-MS analysis of BLM interactors.
(A) Schematic overview of the ChIP-MS experimental workflow. (B) Volcano plot of the BLM helicase ChIP-MS (P154) generated using a GFP nanobody as bait. Cells were synchronized with thymidine for 24 h, released into fresh medium containing aphidicolin (APH), and crosslinked with formaldehyde 10.5 h after release, when cells had entered mitosis. (C) Scatter plot comparing fold changes (FC) of BLM ChIP-MS interactors in mitotic versus S-phase cells. All proteins shown were significantly enriched in at least one condition. Proteins enriched by at least onefold mitosis are highlighted. (D) Scatter plot comparing fold changes (FC) of BLM ChIP-MS interactors in mitotic cells treated with either APH or DMSO. All proteins shown were significantly enriched in at least one condition. Proteins enriched by at least onefold in APH-treated cells are highlighted. Statistical analysis for all ChIP-MS experiments using a one-sided Student's T-test comparing IP samples with control pull-downs. Four biological replicates were analyzed per condition with S0 = 0.1 and FDR < 0.05. R-loop factors were annotated using the high-confidence R-loop-binding protein dataset reported by Lin *et al.* (2021).

this initial experiment one of the most significantly enriched protein was the APEX1 DNA endonuclease, a key enzyme of the base excision DNA repair pathway (Figure 4.1B). As described above, we also analysed mitotic DMSO-treated cells and APH-treated S-phase cells as control conditions (Supplementary Figure 1A, B).

Comparative analysis of the BLM ChIP-MS datasets revealed that several proteins, including APEX1, MCM3, ALYREF, KPNA2, and U2AF1, were preferentially enriched in APH-treated mitotic samples, but not in APH-treated S-phase cells (Figure 4.1C, D). This suggested that their association with BLM was linked to mitotic cells with replication stress rather than to aphidicolin treatment alone.

One limitation of this initial ChIP-MS experiment was the absence of other members of the UFB complex (compare schematic in Figure 4.1B) such as the subunits of the TRR complex (TOP3A, RMI1, RMI2), which was also reflected by a rather low sequence coverage observed for the potential BLM interacting proteins. These observations suggested that technical factors during sample preparation may be further optimized to reduce the loss of weakly associated proteins. To improve protein recovery, we repeated the mitotic APH-treated condition using the same experimental design (P168; Figure 4.2A). In this repeat experiment, the number of significantly enriched proteins substantially increased compared to the initial experiment (compared Figure 4.2B with Figure 4.1B). We now detect multiple established UFB-associated factors, including TOP3A, TOP2A, RPA1, and UBTF. APEX1 was again detected, although its enrichment was lower compared to the initial experiment (Figure 4.2B). Notably, we also identified a considerable number of RNA-associated and R-loop-related factors within the BLM interactome (Figure 4.2B, shown in pink).

To unambiguously identify functional groups among the enriched proteins, we performed quantitative pathway enrichment analyses for cells (Figure 4.2C, Supplementary Figure 1E Materials and Methods for details). For enrichment analysis we used R-loop factor annotation based on the high-confidence R-loop-binding protein dataset reported[152]. In this study they classify the R-loop factors in 5 tiers from the most significant protein involve with R-loop as tier 1 to the lowest significant as Tier 5.

Strikingly, rRNA-processing factors were specifically overrepresented in BLM pull-downs from APH-treated mitotic cells compared with S-phase cells and DMSO-treated mitotic cells. Further analysis showed that proteins assigned to this pathway had significantly higher mean fold changes in mitotic cells than in S-phase cells. And replication stress influenced the association of BLM with rRNA-processing factors (Figure 4.2D). Other pathways like: RNA splicing, mRNA processing, chromosome organization, and Tier 1 R-loop-associated factors, were also similarly or even stronger enriched in S-phase cells. This likely reflects the various functions of the BLM that it carries out across multiple cell-cycle phases, such as the stabilization of stalled replication forks. Additional comparisons using the repeated APH-treated mitotic BLM ChIP-MS dataset (P168) further supported increased enrichment of factors such as U2AF1 when compared with mitotic DMSO-treated samples or APH-treated S-phase samples. In contrast, APEX1 showed less consistent enrichment in the repeated dataset (Supplementary Figure 1C, D). These analyses indicated that the BLM interactome under mild

replication stress included RNA-processing, R-loop-associated, and rRNA-processing factors, with rRNA-processing proteins showing the strongest mitosis-specific enrichment.

Together, the first two BLM ChIP-MS experiments revealed two main findings. First, APEX1 was transiently enriched with BLM, suggesting that its association with BLM was linked to mitotic cells under replication stress. Second, the repeated BLM ChIP-MS experiment supported the idea that the BLM interactome under mild replication stress was connected not only to DNA repair and UFB-associated proteins, but also to rRNA-processing pathways.

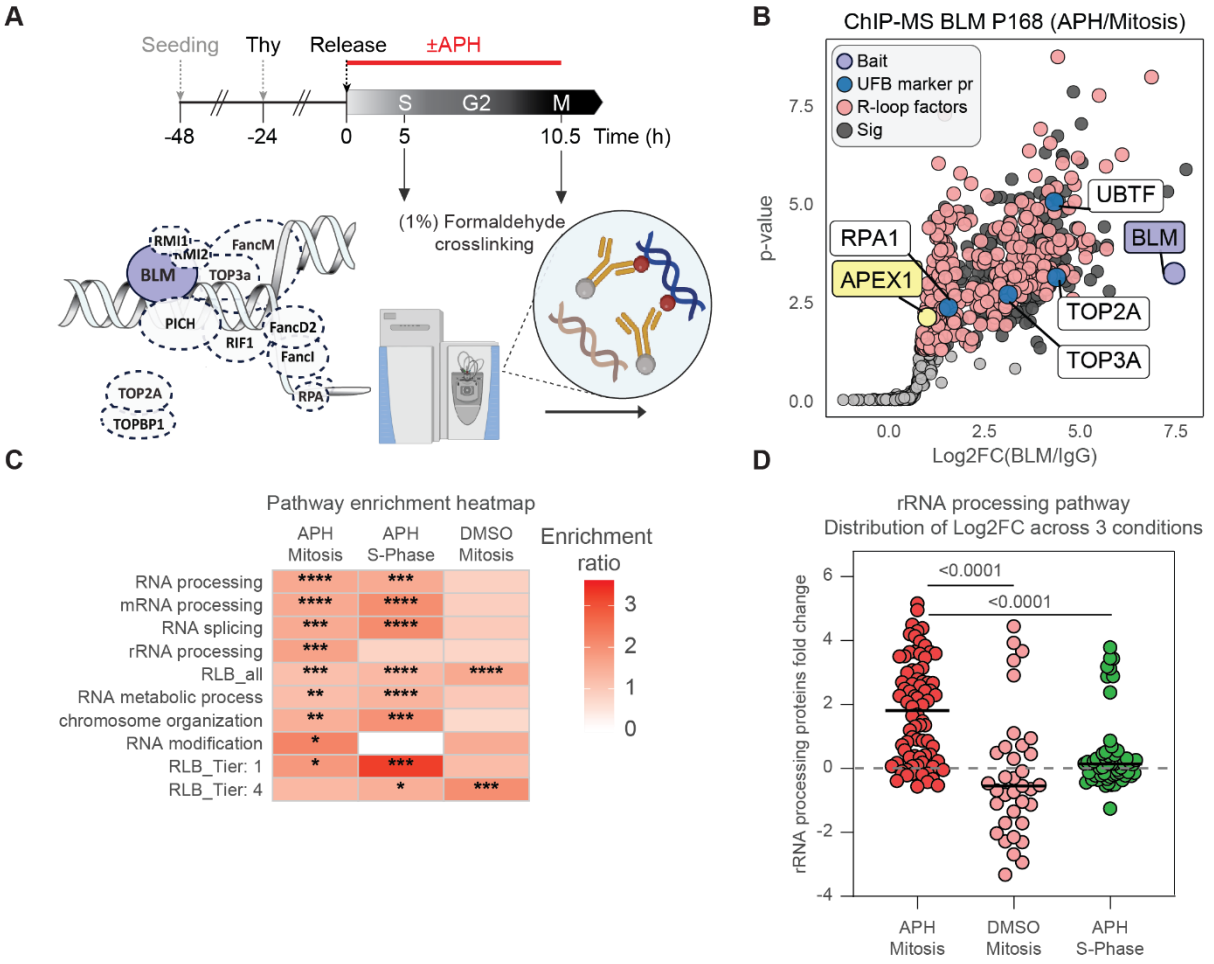


Figure 4.2 | ChIP-MS analysis of BLM interactors.
(A) Schematic overview of the ChIP-MS experimental workflow. (B) Volcano plot of the ChIP-MS dataset obtained using a GFP nanobody to immunoprecipitated BLM helicase–eGFP from aphidicolin-treated cells synchronized in mitosis (P168). (C) Enrichment analysis of top 20 pathways (Gene Ontology Biological Process (GOBP) terms and R-loop–associated factors) across the three principal conditions: APH/S phase, APH/mitosis, and DMSO/mitosis. (D) Fold-change of rRNA-processing pathways, showing increased enrichment under replication stress in mitotic cells.

4.1.2 TOP3A ChIP-MS detects R-loop factors under mild replication stress

Another UFB binding factor analyzed in this study was TOP3A. TOP3A is a type IA topoisomerase that functions together with BLM helicase in the BTRR complex to resolve DNA recombination and replication intermediates. In addition, TOP3A plays an essential role in the resolution of homologous

recombination and fragile site UFBs[64,151]. These functions made TOP3A an attractive candidate for further ChIP-MS analysis. We performed cell culture, synchronization, and sample preparation using the same experimental workflow described for the previous ChIP-MS experiments, in which cell populations were enriched in mitosis (Supplementary Figure 2A). In this experiment, we used a TOP3A antibody for immunoprecipitation, whereas IgG served as the control pull-down. Cells were treated with either APH, to induce mild replication stress, or DMSO, as a control, to assess the effect of replication stress on the TOP3A interactome (Figure 4.3A).

Statistical analysis using a t-test comparing TOP3A immunoprecipitations with control pull-downs identified significant enrichment of TOP3A in both APH- and DMSO-treated samples. Several established TOP3A interaction partners were also enriched, including members of the BTRR complex, BLM, RMI1, and RMI2, as well as RPA1 and RPA2 (Figure 4.3B and Supplementary Figure 2B). This confirmed successful recovery of TOP3A-associated chromatin complexes. It is important to note that interactions among UFB marker proteins may be transient and therefore difficult to capture comprehensively by ChIP-MS. For example, although TOP3A efficiently enriched members of the BTRR complex in this experiment, these interactions were not consistently detected in the BLM pull-down datasets. This difference may reflect variation in bait accessibility, pull-down efficiency. The TOP3A ChIP-MS analysis also identified multiple significantly enriched R-loop-associated proteins (Figure 4.3B, points in pink colour). In contrast to the BLM and FANCD2 ChIP-MS datasets, however, APEX1 was not significantly enriched in either the APH- or DMSO-treated TOP3A samples (Figure 4.3B). These results suggested that the TOP3A interactome contained established BTRR-complex components and R-loop-associated factors but did not show a strong association with APEX1 under these conditions.

To specifically evaluate the effect of replication stress, we compared the Log2FC values of proteins enriched in APH-treated and DMSO-treated samples. This comparison revealed stronger enrichment of several DNA replication proteins in APH-treated mitotic cells, including MCM7 and MCM3, both of which are components of the MCM helicase complex involved in replication fork progression and stability. In addition, proteins associated with RNA processing and RNA splicing pathways, including KRR1, RBM25, CCT6A, DDX24, and DDX6, showed stronger enrichment under APH treatment (Figure 4.3C). Pathway enrichment analysis further demonstrated enrichment of DNA recombination and DNA metabolic process pathways in APH-treated samples relative to DMSO-treated controls (Figure 4.3D). Enrichment of the DNA metabolic process indicated that APH treatment promoted the recruitment of genome maintenance factors to the TOP3A interactome, consistent with a role for TOP3A in resolving stress-induced DNA structures during mitosis. Mapping of significantly enriched proteins within the DNA recombination pathway further showed that replication stress increased both the number and enrichment levels of DNA repair factors in the TOP3A interactome (Figure 4.3D, E). Together, the results

revealed two main findings. First, TOP3A ChIP-MS confirmed successful recovery of TOP3A-associated chromatin complexes (BTRR). Second, mild replication stress increased the association of DNA repair, replication, and R-loop-associated factors with TOP3A, suggesting that the TOP3A interactome became more strongly linked to genome maintenance pathways under APH-treated mitotic conditions.

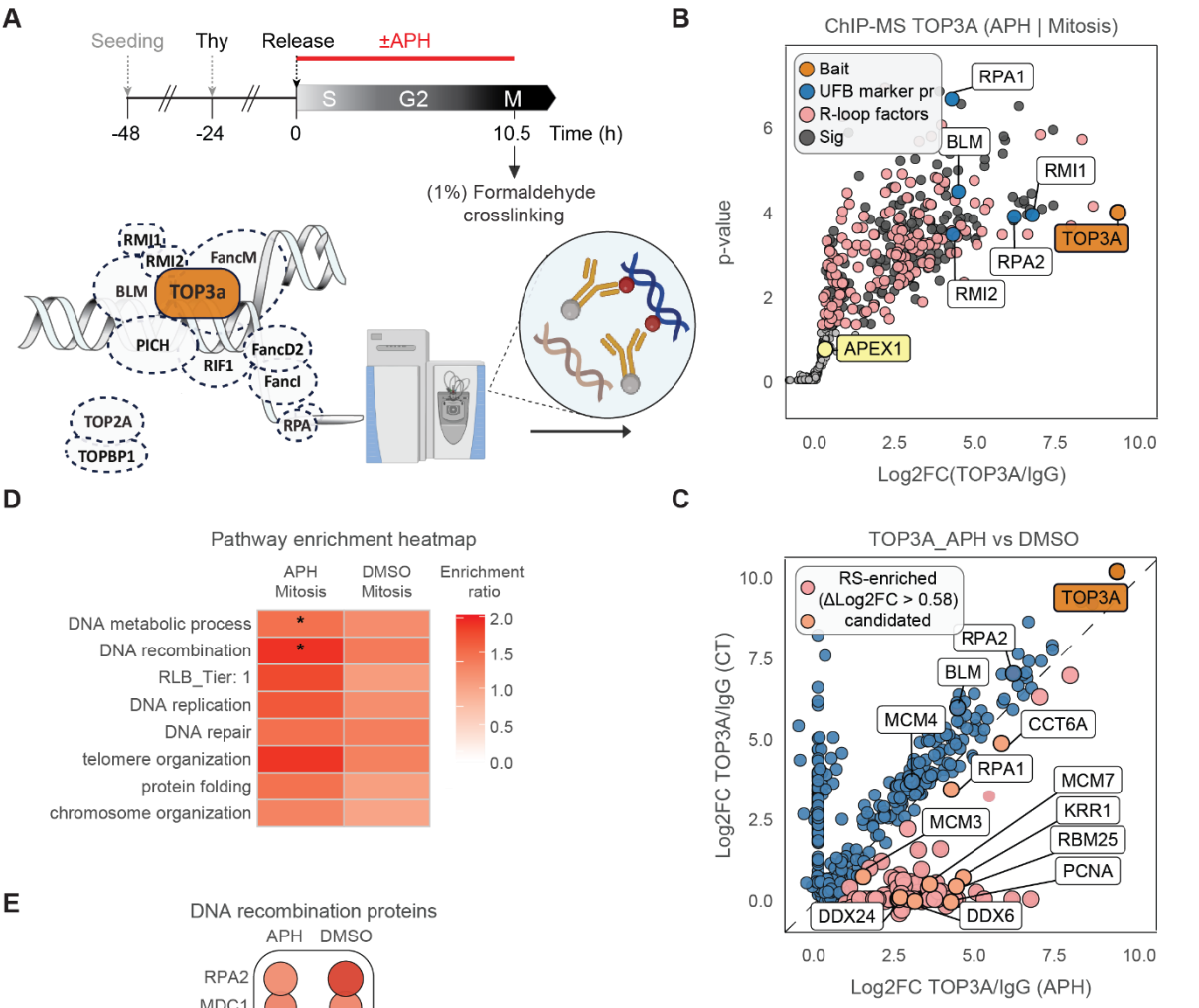


Figure 4.3 | ChIP–MS analysis of TOP3A interactors.
(A) Schematic overview of the ChIP–MS experimental workflow. (B) Volcano plot of the TOP3A ChIP–MS dataset generated using a TOP3A antibody as bait. Cells were synchronized with thymidine for 24 h, released into fresh medium containing aphidicolin (APH), and crosslinked with formaldehyde 10.5 h after release, when cells had entered mitosis. (C) Scatter plot comparing fold changes (FC) of TOP3A ChIP–MS interactors in mitotic cells treated with APH or DMSO. All proteins shown were significantly enriched in at least one condition. Proteins enriched by at least onefold in APH-treated cells are highlighted. (D) Enrichment analysis of pathways, including Gene Ontology Biological Process (GOBP) terms, comparing APH/mitosis and DMSO/mitosis conditions. (E) Fold-change analysis of DNA recombination pathway proteins in APH versus DMSO TOP3A ChIP–MS conditions, showing increased enrichment under replication stress.

4.1.3 FANCD2 ChIP-MS supports the replication stress-dependent recruitment of APEX1

Another UFB-associated factor examined in this study was FANCD2. FANCD2 is a central component of the Fanconi anemia (FA) DNA repair pathway and plays an essential role in the repair of DNA interstrand crosslinks and the maintenance of replication fork stability[154]. Importantly, FANCD2 serves as a marker of fragile site-associated UFBs (FS-UFBs), where it localizes to the ends of BLM-coated bridges presumably at sites of stalled replication forks. Previous studies demonstrated that aphidicolin treatment increases the frequency of FS-UFBs, which prompted us to use FANCD2 as bait for the next ChIP-MS experiment[110]. Cell synchronization and sample preparation were performed as described for the BLM ChIP-MS experiments, except that a FANCD2-specific antibody was used for immunoprecipitation instead of GFP-Trap agarose beads (Figure 4.4A). Statistical analysis of APH-treated mitotic samples identified both FANCD2 and its binding partner FANCI as the most significantly enriched proteins, with enrichment exceeding 100-fold over the control pull-down (Figure 4.4B). Similar to the BLM ChIP-MS dataset, APEX1 was significantly enriched together with several R-loop-associated proteins. And APEX1 was not enriched in FANCD2 immunoprecipitated from DMSO-treated cells, further supporting its replication stress-dependent association with the FANCD2 protein.

To determine the effect of replication stress, we first compared the log2 fold changes (log2FC) of proteins significantly enriched in APH-treated and DMSO-treated mitotic cells (Supplementary Figure 3). This comparison further supported the replication stress-dependent recruitment of APEX1 to the FANCD2 complex. In addition, MCM5 showed stronger enrichment in APH-treated samples than in DMSO controls, consistent with activation of replication stress-associated pathways. We also observed enrichment of the DEAD-box RNA helicases DDX46 and DDX47, as well as ALYREF, an RNA-binding protein involved in R-loop regulation and genome stability (Figure 4.4C). To further characterize the proteins enriched under replication stress, we performed an unbiased pathway enrichment analysis (Figure 4.4D). Although only a limited number of pathways reached statistical significance, the DNA repair pathway was significantly enriched in APH-treated samples. Mapping individual DNA repair proteins according to their fold change and statistical significance further showed that APH treatment increased both the number and fold change of DNA repair factors associated with FANCD2 compared with DMSO-treated cells (Figure 4.4E). Overall, the FANCD2 ChIP-MS analysis confirmed several observations from the BLM pull-down, including the replication stress-dependent enrichment of APEX1 and multiple R-loop-associated proteins. At the same time, the FANCD2 interactome showed a stronger enrichment of DNA repair factors, consistent with the distinct localization of FANCD2 at the termini of FS-UFBs, whereas BLM coats the bridge itself. Together, these findings suggest that although BLM and FANCD2 occupy different regions of FS-UFBs, both proteomic datasets identify overlapping

replication stress-associated protein networks and support the recruitment of APEX1 to replication stress-associated DNA intermediates.

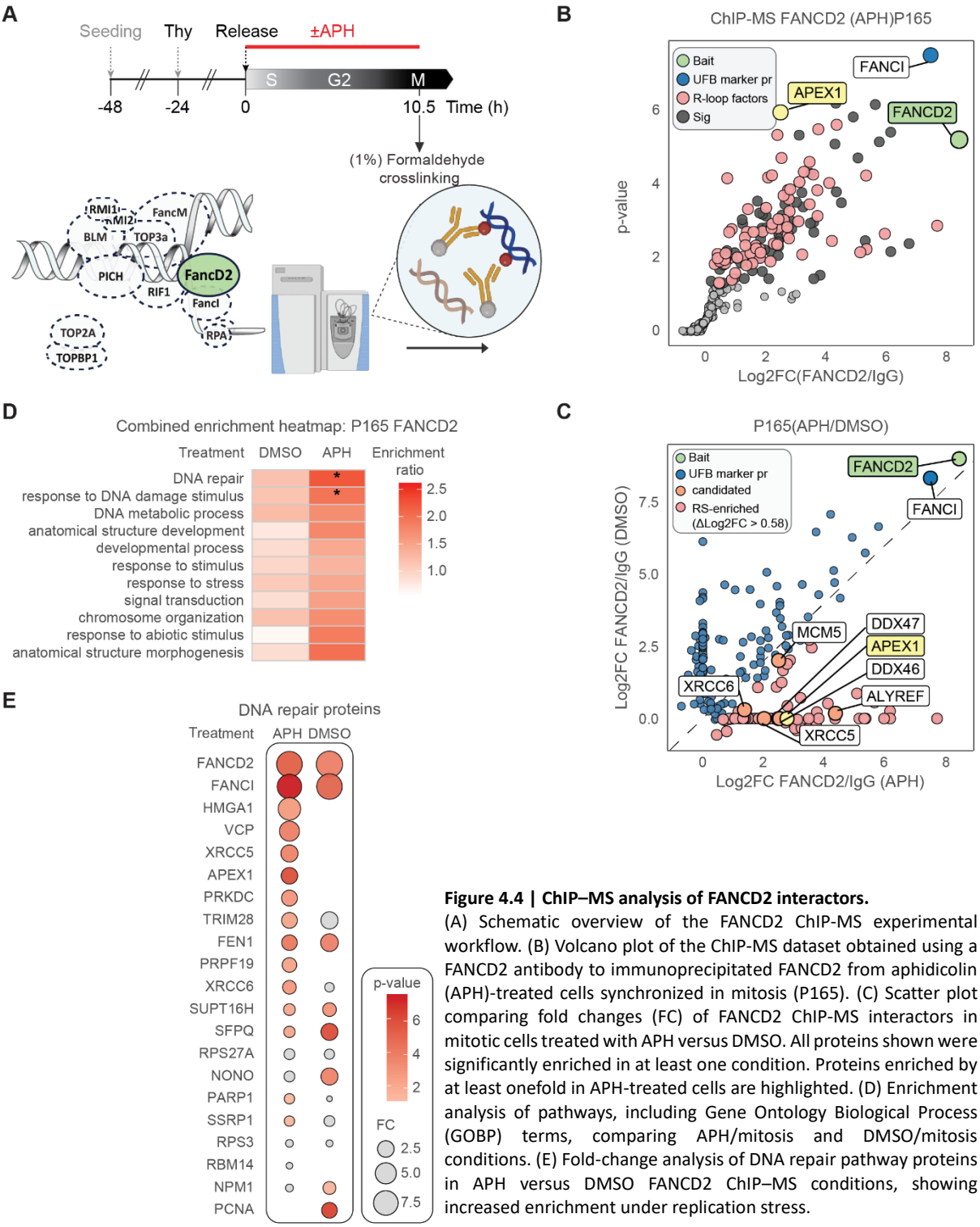


Figure 4.4 | ChIP–MS analysis of FANCD2 interactors.
(A) Schematic overview of the FANCD2 ChIP-MS experimental workflow. (B) Volcano plot of the ChIP-MS dataset obtained using a FANCD2 antibody to immunoprecipitated FANCD2 from aphidicolin (APH)-treated cells synchronized in mitosis (P165). (C) Scatter plot comparing fold changes (FC) of FANCD2 ChIP-MS interactors in mitotic cells treated with APH versus DMSO. All proteins shown were significantly enriched in at least one condition. Proteins enriched by at least onefold in APH-treated cells are highlighted. (D) Enrichment analysis of pathways, including Gene Ontology Biological Process (GOBP) terms, comparing APH/mitosis and DMSO/mitosis conditions. (E) Fold-change analysis of DNA repair pathway proteins in APH versus DMSO FANCD2 ChIP–MS conditions, showing increased enrichment under replication stress.

4.1.4 FANCI ChIP-MS reveals RNA-processing factors under mild replication stress

Encouraged by the efficient recovery of the FANCI–FANCD2 complex in the FANCD2 ChIP-MS experiments, we next performed a reciprocal ChIP-MS experiment using a FANCI antibody. FANCI is a central component of the Fanconi anemia DNA repair pathway and functions together with FANCD2 as part of the FANCI–FANCD2, or ID, complex. Since both proteins have been reported to mark the termini of replication stress-induced UFBs[110,155,156]. We asked whether exposure to a low concentration of aphidicolin affected the recovery of co-precipitating proteins in FANCI ChIP-MS experiments.

We used the same experimental workflow as in the previous ChIP-MS experiments, with enrichment of mitotic cell populations and comparison of APH-treated samples with DMSO-treated controls (Figure 4.5A). As expected, FANCI was enriched as the bait protein, with an approximately 1000-fold enrichment compared with the IgG control. Its known partner FANCD2 was also enriched, with an approximately 5.6- to 32-fold enrichment compared with the control pull-down (Figure 4.5B, C). Similar to the FANCD2 ChIP-MS experiments, mild replication stress did not markedly affect recovery of the bait protein, but slightly increased recovery of its known partner protein (Figure 4.5D). Comparison of Log2FC values between APH- and DMSO-treated samples showed increased enrichment of several RNA-processing proteins, including ALYREF, CHTOP, RBM3, RALY, and U2AF1, specifically under replication stress conditions (Figure 4.5D). However, the FANCI ChIP-MS dataset showed limited proteomic depth and identified fewer interaction partners than several other ChIP-MS datasets.

We next performed pathway enrichment analysis separately for APH- and DMSO-treated samples and ranked the pathways according to the enrichment score of the APH-treated condition (Figure 4.5E). This analysis revealed significant enrichment of pathways related to transcription, RNA catabolic processes, and translation. Most significantly enriched pathways also showed higher enrichment ratios in APH-treated samples compared with DMSO-treated controls. Consistent with this pattern, analysis of proteins enriched in APH-treated samples revealed a significant increase in the mean fold change of transcription factors under replication stress conditions (Figure 4.5F). Although FANCI is not primarily known as a transcription-regulatory factor, these findings suggested that its interactome changed under mild replication stress and became enriched for proteins involved in RNA metabolism and transcription processes. This may reflect recruitment of the FANCI–FANCD2 complex at sites of replication–transcription conflict, where it could contribute to the processing of replication stress DNA structures, including those linked to R-loop accumulation[157].

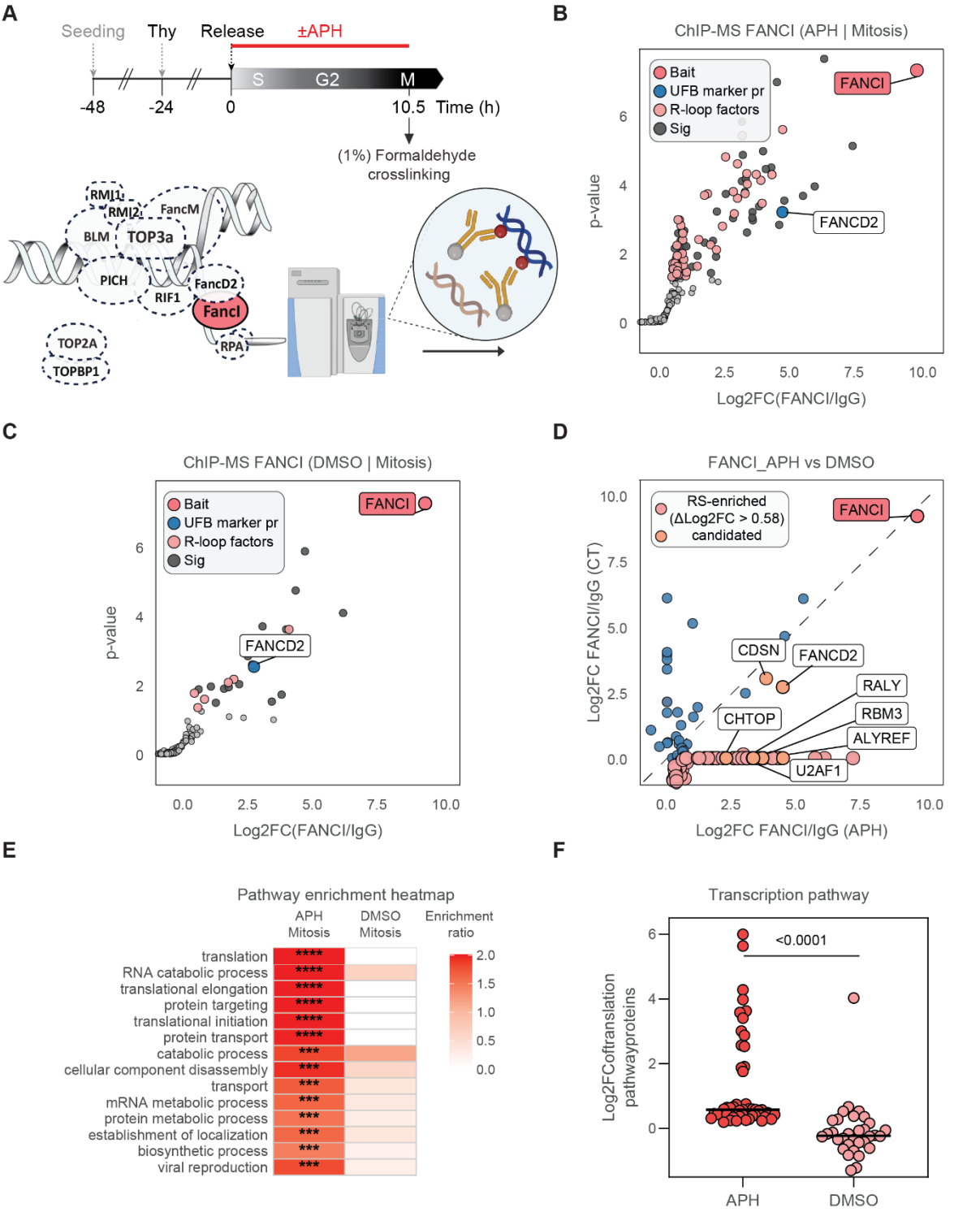


Figure 4.5 | ChIP-MS analysis of FANCI interactors.
(A) Schematic overview of the ChIP-MS experimental workflow. (B–C) Volcano plots of FANCI ChIP-MS datasets generated using a FANCI antibody as bait. Cells were synchronized with thymidine for 24 h, released into fresh medium, and crosslinked with formaldehyde 10.5 h after release in mitosis. (B) aphidicolin (APH)-treated cells. (C) DMSO-treated cells. (D) Scatter plot comparing fold changes (FC) of FANCI ChIP-MS interactors in mitotic cells treated with APH or DMSO. All proteins shown were significantly enriched in at least one condition. Proteins enriched by at least onefold in APH-treated cells are highlighted. (E) Enrichment analysis of pathways, including Gene Ontology Biological Process (GOBP) terms, comparing APH/mitosis and DMSO/mitosis conditions. (F) Fold-change analysis of transcription-related pathway proteins in APH versus DMSO FANCI ChIP-MS conditions, showing increased enrichment under replication stress.

4.1.5 Meta-analysis of UFB marker proteins highlights APEX1

To consolidate the results from the individual ChIP-MS experiments, we performed an integrated meta-analysis. The aim was to identify proteins that were repeatedly enriched across different UFB-marker pull-downs and that responded consistently to mild replication stress. For this purpose, we developed a scoring system that considered stress-dependent enrichment, repeated detection across multiple ChIP-MS datasets, and statistical significance. We referred to this value as the Meta-analysis Significance Score.

For this meta-analysis, we combined ChIP-MS data generated from four UFB-marker bait proteins: BLM, FANCD2, FANCI, and TOP3A (Figure 4.6A). For some bait proteins, including BLM and FANCD2, repeated experiments were also available and were included in the analysis. In addition, we incorporated a previously generated PICH ChIP-MS dataset, performed by Dr. Angela Wieland under comparable experimental conditions, to expand the dataset and improve the identification of shared UFB-associated candidates (Supplementary Figure 4).

In this meta-analysis, we calculated a significance score by combining the fold changes and associated p-values obtained from the individual one-sided Student's t-tests. Each dataset was corrected for multiple testing using the Benjamini–Hochberg procedure, and the corrected p-values were integrated using the harmonic mean p-value method (see Materials and Methods for details). Eric Heller, a bioinformatician in the laboratory, performed the meta-analysis calculations. One representative example of the underlying t-test results was the FANCD2 ChIP-MS dataset generated from APH-treated cells (Figure 4.6B). As expected, the UFB-marker proteins used as bait in the individual ChIP-MS experiments received high Meta-analysis Significance Scores. These proteins were strongly enriched when used as bait and were also repeatedly detected in reciprocal pull-downs.

Mapping of significantly enriched UFB binding proteins together with selected high-priority candidates revealed that several proteins responded specifically to mild replication stress and were detected mainly or exclusively in APH-treated samples. Among these candidates, APEX1 and ALYREF showed particularly interesting enrichment patterns (Figure 4.6C). ALYREF was detected at least once with every bait protein under APH treatment, whereas APEX1 showed stronger and more reproducible enrichment in the BLM and FANCD2 ChIP-MS datasets.

We also mapped known interaction partners of APEX1 and ALYREF to determine whether they followed similar replication stress-dependent enrichment patterns. For APEX1, these proteins included FEN1, PCNA, and PARP1, whereas for ALYREF they included DDX39A, DDX39B, EJC complex (EIF4A3, RBM8A, and MAGOH). However, these proteins did not show the same consistent enrichment profile as APEX1 and ALYREF across the ChIP-MS datasets (Figure 4.6C). These results suggest that the replication stress-

induced enrichment of APEX1 and ALYREF was not simply explained by the co-enrichment of their known interaction partners.

Next, we ranked all proteins according to their meta-analysis significance score and retained proteins that were significantly detected in at least two independent datasets. From this filtered list, the top 200 proteins were selected for further analysis (Figure 4.6D). This group included PCNA, DDX46, and DDX47. The complete list of the top 200 proteins is provided in Supplementary Data 1.

For the Gene Ontology Biological Process enrichment analysis, we used a broader set of proteins with a Meta-analysis Significance Score >1. This analysis revealed strong enrichment of RNA- and rRNA-processing pathways in APH-treated samples (Figure 4.6E), consistent with the results obtained from several individual ChIP-MS enrichment analyses. Comparison of enrichment ratios between APH-treated and untreated conditions further showed that pathways related to ribosome biogenesis, protein localization to the nucleus, transcription, and translation displayed higher enrichment under APH treatment (Supplementary Figure 5A). In addition, several pathways, including regulation of DNA biosynthetic process, were significantly enriched in APH-treated samples and showed markedly higher enrichment ratios compared with untreated conditions (Supplementary Figure 5B).

To further characterize the functional relationships among the top-ranked proteins, we analysed the top 200 candidates using STRING and visualized the resulting network in Cytoscape. This analysis revealed three major functional groups, including a DNA repair-associated cluster that contained APEX1, an endonuclease involved in the base excision repair pathway (Figure 4.6F). Additional network analysis further highlighted clusters associated with specific biological functions, including RNA splicing and ribosome biogenesis, consistent with the enrichment analysis (Supplementary Figure 5C).

Together, the meta-analysis identified APEX1 and ALYREF as high-priority candidates for further experimental validation and suggested that the mitotic response to unresolved replication intermediates involved coordinated contributions from DNA repair and RNA-associated genome maintenance pathways.

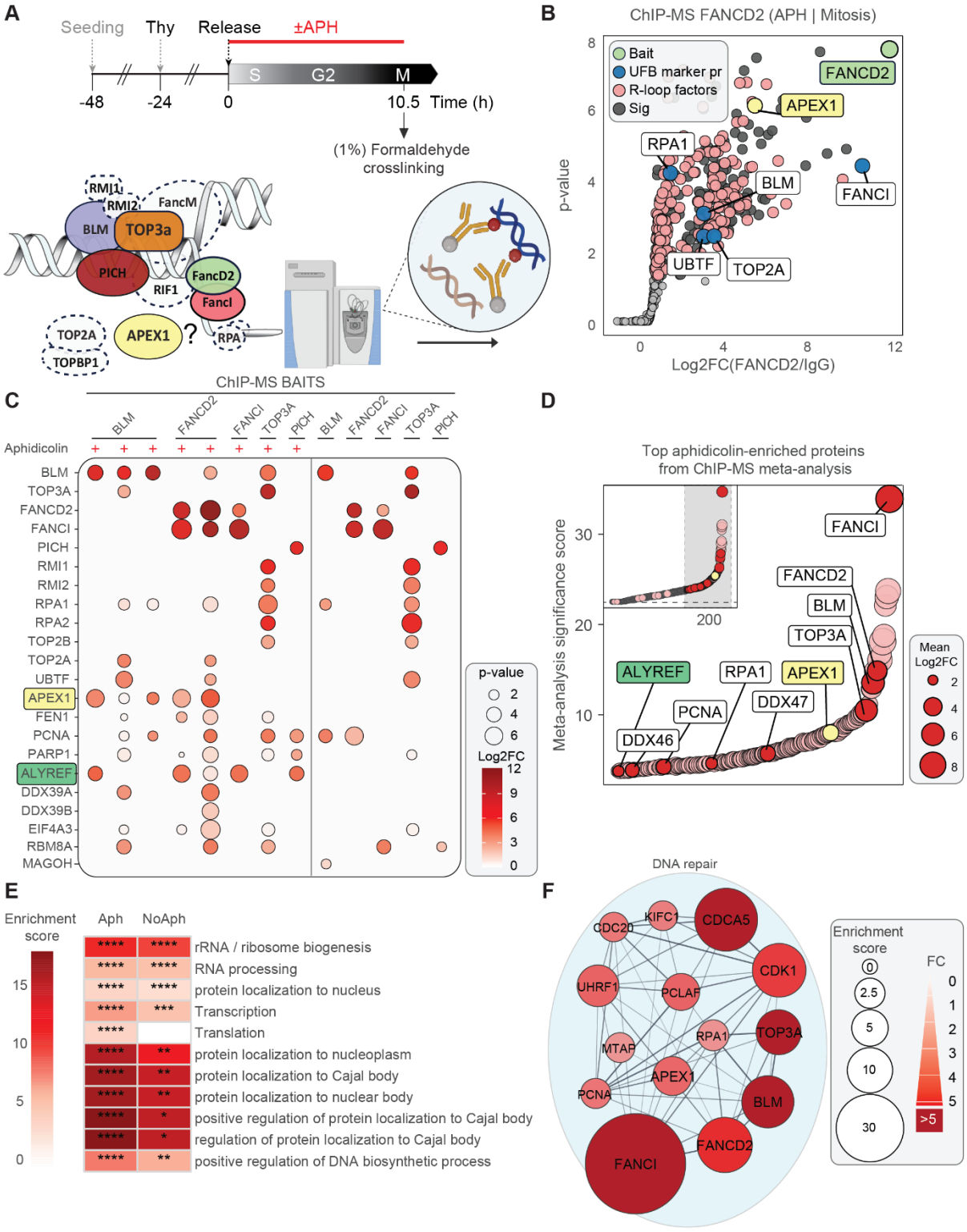


Figure 4.6 | ChIP-MS meta-analysis of UFB-associated protein interactomes.
(A) Schematic overview of the integrated ChIP-MS meta-analysis workflow. ChIP-MS datasets generated with different UFB-associated bait proteins. (B) Representative volcano plot of the FANCD2 ChIP-MS dataset generated using a FANCD2 antibody as bait. (C) Heat map showing the bait proteins and experimental conditions included in the ChIP-MS meta-analysis of mitotic cells. Candidate proteins and selected known interaction partners are shown across APH- and DMSO-treated conditions. (D) Meta-analysis ranking of the top 200 significantly enriched proteins identified under mild replication stress conditions. (E) Gene Ontology Biological Process enrichment analysis of the top-ranked candidates (enrichment score >0), highlighting pathways enriched under APH treatment. (F) STRING interaction network of top-ranked proteins associated with DNA repair and related genome maintenance pathways. Point size represents the Meta Analysis Significance Score and point color represents the mean fold change.

4.1.6 RNAseH1 overexpression impairs APEX1 recruitment

After completing the meta-analysis, one of the major remaining questions was why APEX1 and numerous R-loop-associated proteins were consistently enriched under mild replication stress across the ChIP-MS datasets. Based on previous studies showing that aphidicolin-induced replication stress promotes transcription-replication conflicts (TRCs) and R-loop accumulation[158,159], particularly at common fragile sites (CFSs)[160] and ribosomal DNA (rDNA) loci[161], we hypothesized that R-loops formed at these conflict sites contribute to the recruitment of APEX1 and other R-loop-associated proteins to replication stress-associated chromatin. To test this hypothesis, we used an HCT116 cell line (kind gift from the laboratory of Holger Bastians) that allowed doxycycline (Dox)-inducible overexpression of RNase H1, an endonuclease that specifically degrades the RNA strand of RNA–DNA hybrids. We reasoned that removal of R-loops by RNase H1 overexpression would reduce transcription-replication conflicts and consequently decrease the recruitment of R-loop-associated factors and APEX1 detected in the BLM and FANCD2 interactomes.

We performed cell culture and synchronization as described for the previous ChIP-MS experiments, with the addition of Dox treatment for 34 hours to induce RNase H1 overexpression. In this experiment, we used antibodies against BLM and FANCD2 for immunoprecipitation, whereas IgG served as the control pull-down. All samples received APH treatment to induce mild replication stress (Figure 4.7A). In parallel, western blot analysis confirmed successful RNase H1 overexpression under both DMSO and APH conditions, with RNase H1 levels increasing approximately two- to threefold relative to untreated controls (Supplementary Figure 6A).

We initially analyzed each condition separately by performing t-tests comparing IP samples with IgG controls to identify significantly enriched proteins (Figure 4.7B and Supplementary Figure 6B–D). In the BLM ChIP–MS dataset under mild replication stress, APEX1 and RPA1 were significantly enriched (Figure 4.7B). Following RNase H1 overexpression, APEX1, PCNA, and XRCC5 were no longer significantly enriched (Figure 4.7C). Notably, RPA1 was significantly enriched only under endogenous RNase H1 conditions and not following RNase H1 overexpression.

A similar pattern was observed in the FANCD2 ChIP–MS dataset. Under mild replication stress, APEX1 was enriched together with several established UFB-associated proteins, including FANCI, BLM, RPA1, UBTF, and TOP2A (Supplementary Figure 6B). Numerous R-loop-associated proteins were also significantly enriched. Direct comparison of fold changes between FANCD2 ChIP–MS samples with and without RNase H1 overexpression showed reduced enrichment of APEX1 and ADAR, proteins connected to BER-related DNA processing (Figure 4.7D). In addition, DDX46, BLM, and PCNA were no longer detected in the FANCD2 ChIP–MS dataset following RNase H1 overexpression.

Analysis of APEX1 fold changes across all four experimental conditions further demonstrated reduced enrichment following RNase H1 overexpression. To determine whether this reduction was statistically significant, we examined normalized raw intensity values for APEX1 in both BLM and FANCD2 ChIP-MS datasets. This analysis revealed a significant decrease in APEX1 signal intensity in samples overexpressing RNase H1 (Supplementary Figure 6E, F). Overall, the FANCD2 ChIP-MS datasets identified more enriched proteins than the BLM ChIP-MS datasets. This may reflect better pull-down efficiency or antibody performance in the FANCD2 experiments (Figure 4.7B and Supplementary Figure 6B–D).

Next, we performed pathway enrichment analysis on both FANCD2 and BLM ChIP-MS datasets in the presence and absence of RNase H1 overexpression (Figure 4.7E). Pathways were ranked according to enrichment score (−log10 FDR), and we focused on pathways showing reduced enrichment ratios following RNase H1 overexpression. Among the significantly enriched pathways, DNA repair and DNA recombination were particularly notable. Detailed examination of DNA recombination-associated proteins revealed that APH-treated samples without RNase H1 overexpression contained a larger number of significantly enriched proteins than samples overexpressing RNase H1 under replication stress conditions (Figure 4.7F). Although the BLM ChIP-MS datasets contained fewer significantly enriched proteins and therefore did not achieve the same level of statistical significance observed in the FANCD2 datasets, both experiments showed a similar reduction trend following RNase H1 overexpression.

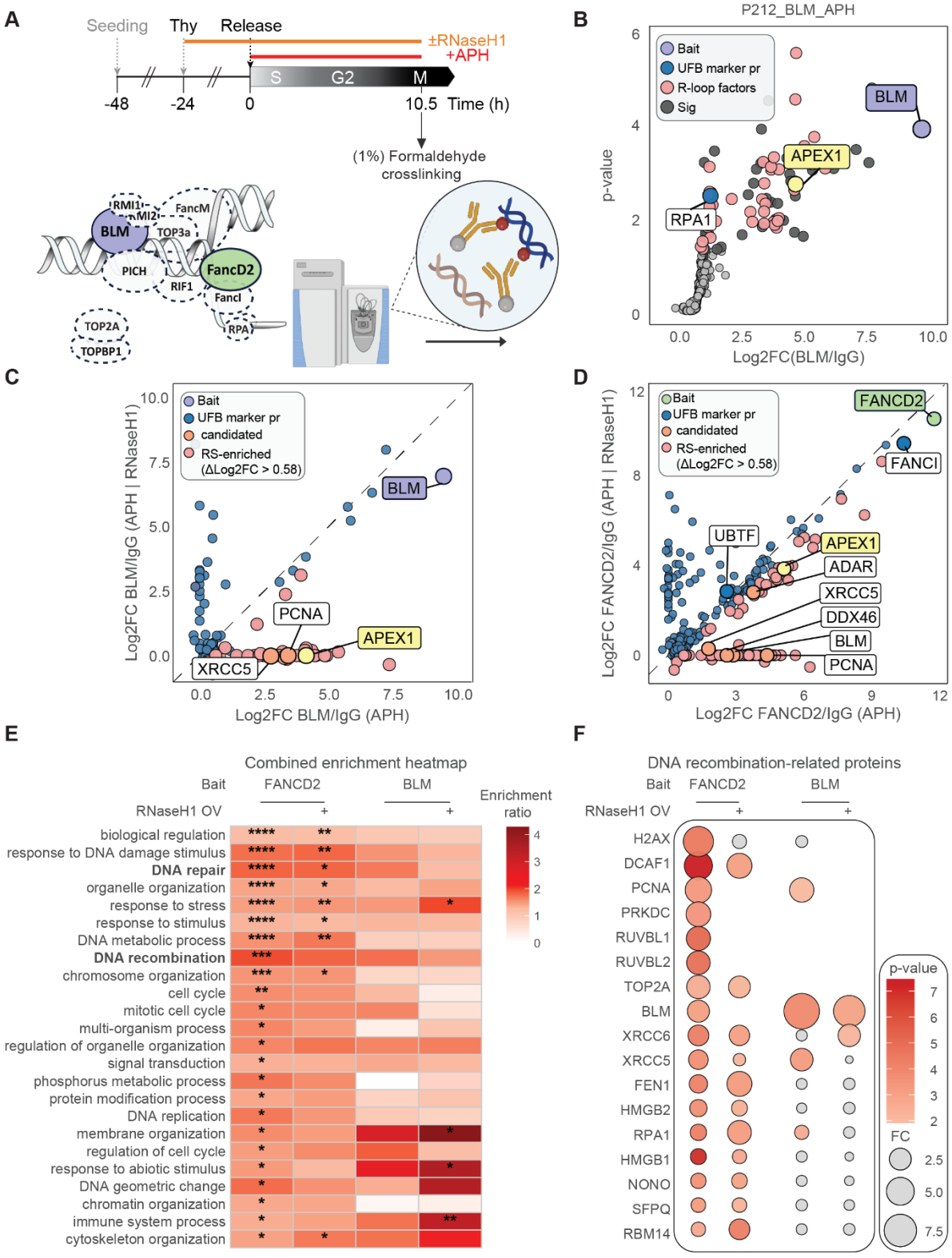


Figure 4.7 | ChIP-MS analysis of FANCD2 and BLM helicase under RNase H1 overexpression.
(A) Schematic overview of the ChIP-MS workflow. (B) Volcano plot of BLM ChIP-MS from aphidicolin (APH)-treated mitotic cells (P212). (C–D) Scatter plots comparing fold changes (FC) of BLM and FANCD2 interactors in mitotic cells treated with APH versus APH plus doxycycline (DOX)–induced overexpression of RNase H1. Proteins significantly enriched in APH condition are shown; those with ≥1-fold enrichment in APH are highlighted. (E) Pathway enrichment analysis (Gene Ontology Biological Process terms) across FANCD2 and BLM ChIP-MS datasets under APH and APH/DOX conditions. (F) Fold-change analysis of DNA recombination proteins, showing reduced enrichment upon RNase H1 overexpression in both FANCD2 and BLM datasets.

4.2 Validation of APEX1 and ALYREF association with UFB marker proteins

After validation and evaluation of the meta-analysis data, we selected two candidate proteins for further investigation: APEX1 and ALYREF. Because both candidates showed replication stress enrichment across the ChIP-MS datasets, it was important to confirm whether they could reciprocally co-immunoprecipitated known UFB-associated proteins under the same experimental conditions. we next examined whether known UFB marker proteins were reciprocally enriched in APEX1- and ALYREF-chromatin complexes.

4.2.1 Reciprocal APEX1 ChIP-MS supports an association with UFB marker proteins

For the reciprocal APEX1 ChIP-MS experiment, we processed cells under the same conditions used for the previous bait proteins. Briefly, we enriched mitotic cell populations and isolated APEX1-associated chromatin complexes from either DMSO-treated cells or APH-treated cells (Figure 4.8A). To assess protein enrichment, we compared normalized raw intensities from APEX1 immunoprecipitations with control pull-downs using a student's t-test. This analysis confirmed efficient recovery of APEX1 as the bait protein in both DMSO- and APH-treated samples (Figure 4.8B and Supplementary Figure 7A) We used normalized raw intensity values instead of LFQ intensities because several proteins were detected with insufficient peptide counts to generate reliable LFQ values.

APEX1 is a key enzyme in the base excision repair (BER) pathway. It recognizes abasic sites and introduces a nick in the DNA backbone, thereby allowing downstream repair factors to process and restore the damaged DNA strand[162]. Consistent with this function, we specifically examined the BER pathway using KEGG annotation. More than half of the proteins assigned to this pathway were detected in the mitotic APEX1 ChIP-MS dataset, and several BER-associated proteins showed strong enrichment including PCNA, PARP1, XRCC1, and ADAR (Figure 4.8C, D). These findings demonstrated the specificity of the APEX1 pull-down and indicated that BER complexes were efficiently recovered under these experimental conditions.

Importantly, we detected several UFB-associated proteins in the APEX1 interactome, including BLM, RPA1, RPA2, and UBTF (Figure 4.8B, E). However, BLM was identified by only two peptides, indicating that its association with APEX1 was weak or that only a small fraction of chromatin-bound APEX1 was present in BLM-containing protein complexes. Although the APEX1 ChIP-MS experiment detected only a limited number of UFB marker proteins, APH treatment increased their enrichment (Figure 4.8E).

To assess the effect of replication stress, we compared the log2 fold changes (log2FC) of proteins significantly enriched in APH-treated and DMSO-treated mitotic cells (Supplementary Figure 7B). MCM3 and MCM7 also showed stronger enrichment after APH treatment, suggesting that APEX1-

associated chromatin may contain stalled or incompletely processed replication intermediates that persist into mitosis. In addition, RFC1–RFC5 was enriched. Because the RFC complex contributes to PCNA loading during DNA replication and repair, its enrichment may indicate that APEX1-associated chromatin retains components involved in repair synthesis or post-replicative processing. Together, these findings suggest that replication stress shifts the APEX1-associated protein network toward factors involved in ssDNA processing, replisome-associated structures, and DNA repair.

We next performed pathway enrichment analysis separately for DMSO- and APH-treated samples. R-loop-associated factors and rRNA-processing pathways were significantly enriched under both conditions, suggesting a possible association between APEX1 and R-loop- or ribosomal DNA processes (Figure 4.8F). Consistent with the meta-analysis results (Figure 4.6E), translation-related pathways showed a higher enrichment ratio in APH-treated samples than in DMSO-treated controls. This finding supported a replication stress-dependent shift in the APEX1-associated protein network toward translation- and ribosome-related processes. Analysis of the individual proteins assigned to these pathways further showed a significant increase in the mean fold change of R-loop- and rRNA-processing factors under mild replication stress (Figure 4.8G). Together, these results suggested that mild replication stress increased the association of APEX1 with proteins involved in DNA repair, R-loop-related processes, rRNA processing, and translation in mitotic cells.

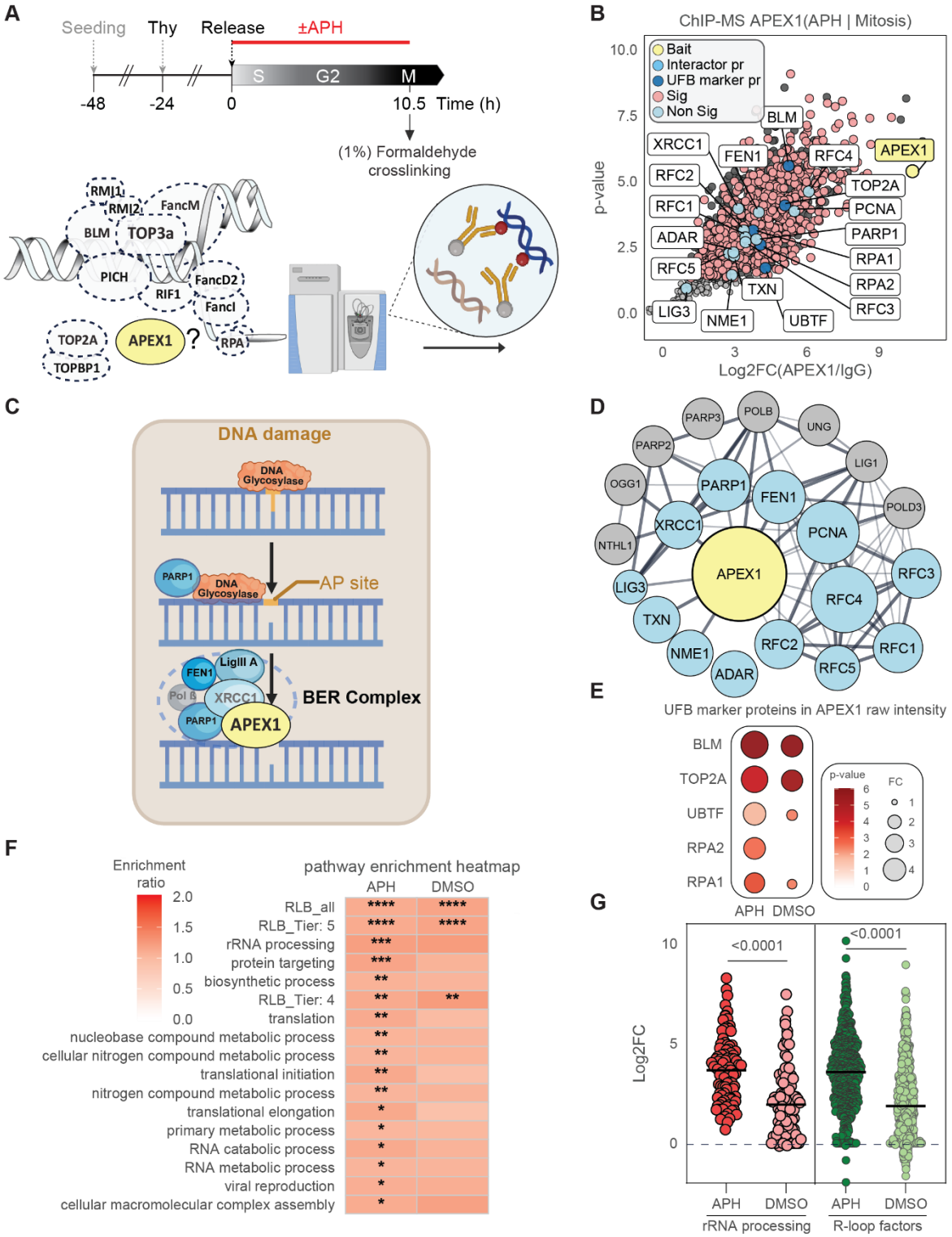


Figure 4.8 | ChIP-MS analysis of APEX1 interactors.
(A) Schematic overview of the ChIP-MS experimental workflow. (B) Volcano plot of the APEX1 ChIP-MS dataset generated using an APEX1 antibody from APH-treated mitotic cells. (C) Schematic overview of the role of APEX1 in base excision repair. (D) APEX1 protein interaction network generated using the STRING database. Proteins identified in the ChIP-MS dataset is highlighted in light blue, and node size represents the fold change (FC) of each protein. Edges represent known or predicted physical protein–protein interactions (E) Dot plot showing ultrafine anaphase bridge (UFB) marker proteins detected in the APEX1 ChIP-MS dataset under APH and DMSO conditions. (F) Enrichment analysis of pathways, including Gene Ontology Biological Process (GOBP) terms and R-loop-associated factors, comparing APH- and DMSO-treated conditions. (G) Dot plots showing the fold changes of rRNA-processing and R-loop-associated proteins in APEX1 ChIP-MS datasets from APH- and DMSO-treated cells. These proteins showed greater enrichment under replication stress.

4.2.2 ALYREF ChIP-MS reveals enrichment of R-loop factors

ALYREF was selected as a candidate because of its reported role in R-loop regulation, although its primary functions are mRNA processing and nuclear export. In human cells, ALYREF cooperates with the RNA helicase DDX39B to remove RNA from RNA–DNA hybrids, thereby limiting R-loop accumulation and its interference with DNA replication[137]. However, overexpression of its yeast orthologue Yra1 increased R-loop accumulation, suggesting that its contribution to R-loop homeostasis depends on tightly regulated protein levels[163]. Thus, ALYREF represented a plausible link between RNA processing, replication stress, and genome stability, but its association with replication-stress-induced chromatin structures and UFB-related proteins had not been established. We therefore examined whether replication stress altered the composition of ALYREF-associated chromatin complexes.

To address this question, we enriched mitotic cell populations and isolated ALYREF-associated chromatin complexes from DMSO-treated control cells and cells exposed to mild replication stress induced by APH (Figure 4.9A). To assess protein enrichment, we compared normalized raw intensities from ALYREF immunoprecipitations with IgG pull-downs using a t-test. This analysis confirmed efficient recovery of ALYREF as the bait protein in both DMSO- and APH-treated samples (Figure 4.9B and Supplementary Figure 8A). As in the APEX1 ChIP-MS experiment, we used normalized raw intensity values instead of LFQ intensities because several proteins were detected with insufficient peptide counts to generate reliable LFQ values.

ALYREF functions as part of the TREX complex, where it contributes to mRNA processing and nuclear RNA export. Consistent with this role, we detected several RNA export and RNA-processing factors in the ALYREF interactome, including NXF1 and NXT1. ALYREF is also functionally linked to DDX39B and exon junction complex-associated proteins (EJC), such as MAGOH and EIF4A3, which participate in mRNA processing and splicing. However, despite the recovery of several known ALYREF-associated RNA-processing factors, we did not detect significant enrichment of THO complex proteins in the ALYREF ChIP-MS dataset (Figure 4.9C, D). This indicated that the ALYREF pull-down recovered selected components of RNA export and splicing-associated complexes but did not capture all subunits of the TREX complex under these experimental conditions.

To evaluate the effect of replication stress on the ALYREF interactome, we compared the fold changes of significantly enriched proteins detected in APH-treated samples with those detected in DMSO-treated. This comparison showed stronger enrichment of several MCM complex proteins under mild replication stress, suggesting increased association of ALYREF with replication-associated protein networks in APH-treated mitotic cells. In addition, APEX1, DDX46, and DDX47 showed higher

enrichment under mild replication stress (Supplementary Figure 8B), further supporting a connection between ALYREF and proteins involved in DNA repair, and R-loop regulation.

Interestingly, ALYREF ChIP-MS in mitotic cells also detected several UFB-associated proteins including BLM, TOP2A, RPA1, and UBTF (Figure 4.9E). Under APH treatment, these proteins showed higher fold changes and stronger statistical enrichment. These results further support the notion that mild replication stress triggers the formation of a DNA intermediate that might require specialized set factors for their resolution.

We next performed pathway enrichment analysis separately for the DMSO- and APH-treated ALYREF ChIP-MS samples. We first identified all significantly enriched pathways and then ranked them according to their enrichment score (-log10 BH-adjusted p-value) under APH treatment (Figure 4.9F and Supplementary Figure 8C). This approach allowed us to compare the enrichment patterns between the two conditions and to identify pathways that were more strongly enriched under mild replication stress.

Similar to the APEX1 ChIP-MS dataset, the ALYREF ChIP-MS dataset showed significant enrichment of R-loop factors and rRNA-processing pathways. Analysis of the individual proteins assigned to these categories further revealed a significant increase in their mean fold change under APH (Figure 4.9G). Together, these results suggested that ALYREF associated with protein networks involved in RNA processing, R-loop regulation, rRNA processing, DNA replication, and UFB biology in mitotic chromatin, with several of these associations becoming stronger under replication stress.

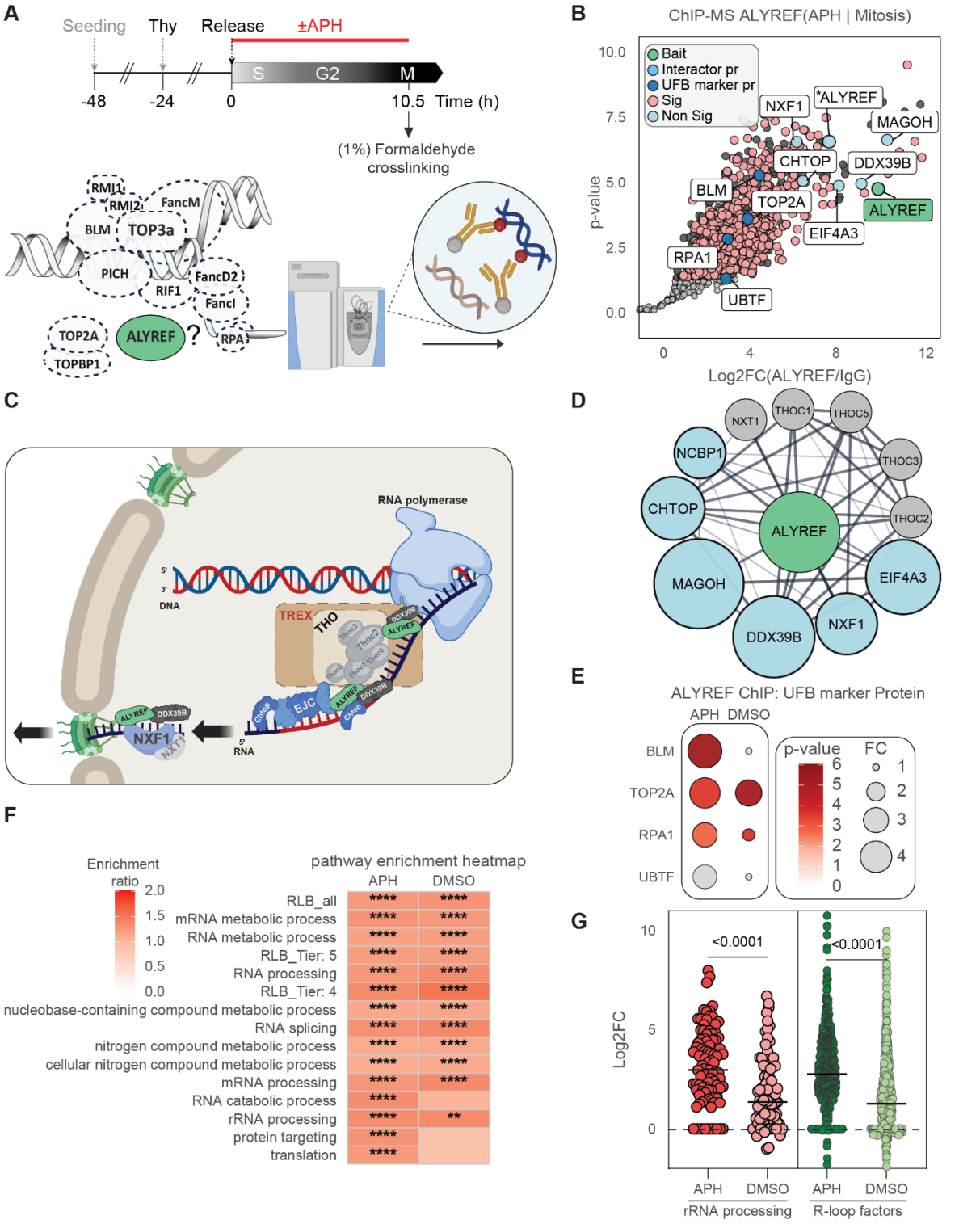


Figure 4.9 | ChIP-MS analysis of ALYREF interactors.
(A) Schematic overview of the ChIP-MS experimental workflow. (B) Volcano plot of the ALYREF ChIP-MS dataset generated using an ALYREF antibody from APH-treated mitotic cells. (C) Schematic overview of transcription and the role of ALYREF in mRNA processing and nuclear export. (D) ALYREF protein interaction network generated using the STRING database. Proteins identified in the ChIP-MS dataset is highlighted in light blue, and node size represents the fold change (FC) of each protein. Edges represent known or predicted physical protein–protein interactions. (E) Dot plot showing ultrafine bridge (UFB) marker proteins detected in the ALYREF ChIP-MS dataset under APH and DMSO conditions. (F) Enrichment analysis of pathways, including Gene Ontology Biological Process (GOBP) terms and R-loop factors, comparing APH and DMSO treated conditions. (G) Dot plots showing the fold changes of rRNA-processing and R-loop-associated proteins in ALYREF ChIP-MS datasets from APH- and DMSO-treated cells. These proteins showed greater enrichment under replication stress.

4.2.3 Stress-dependent association of BLM with APEX1 and ALYREF

Following the analysis of ChIP-MS data as control we preformed ChIP-western blotting by using antibodies against APEX1 and ALYREF. Given the low peptide coverage observed for the BLM protein in ChIP-MS experiments, we performed these experiments to confirm their interactions with BLM. And, to assess the effect of mild replication stress, we treated cells with APH.

The experimental setup was identical to that used for ChIP-MS, except that the bead-bound proteins were eluted by boiling in 10% SDS sample buffer after the washing steps. Then the protein digestion and peptide recovery were not needed for this experiment. We collected input lysates and post-immunoprecipitation supernatants to monitor pull-down efficiency. APEX1 and ALYREF were successfully recovered in their respective immunoprecipitations but were not detected in the IgG controls. APH treatment increased the recovery of both bait proteins from the chromatin fraction. BLM enrichment also increased in both the APEX1 and ALYREF pull-downs under mild replication stress (Figure 4.10A, B). Together, these results supported the ChIP-MS observations and confirmed the recovery of BLM in both the APEX1 and ALYREF pull-downs. The increased BLM enrichment under APH suggested that mild replication stress strengthened these associations as we saw in the ChIP-MS experiment. However, because biological triplicates were not performed, these findings were considered preliminary and required further validation.

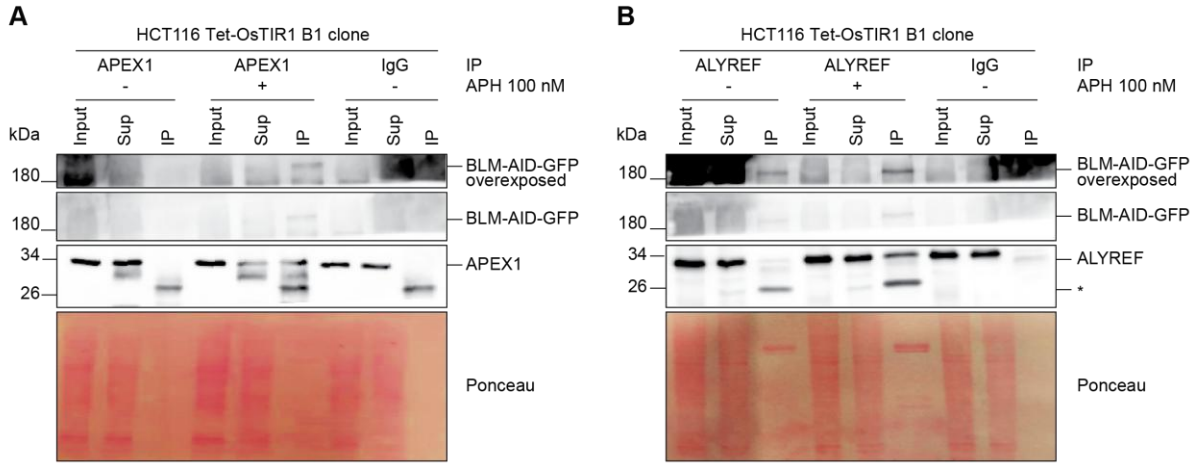


Figure 4.10 | Reciprocal ChIP–western blot analysis of APEX1 and ALYREF.
(A) Chromatin immunoprecipitation (ChIP) followed by Western blot analysis of APEX1-associated proteins in HCT116 B1 cells. Cells were synchronized with thymidine for 24 h, released into fresh medium containing either aphidicolin (APH, 100 nM) or DMSO, and harvested 10.5 h after release in mitosis. Following formaldehyde crosslinking, chromatin was isolated and immunoprecipitated using an APEX1-specific antibody. Immunoprecipitated were analyzed by Western blot using the indicated antibodies. Mouse IgG served as a negative control. Input represents chromatin collected before immunoprecipitation, and supernatant (SUP) represents the unbound fraction after immunoprecipitation. (B) Reciprocal ChIP–Western blot analysis using an ALYREF-specific antibody under the same experimental conditions as described in (A). This experiment was conducted by master student Nikita Kvasov and Diana.

4.2.4 APEX1–BLM–FANCD2 interactions occur independently of RNA or DNA

Because APEX1, BLM and FANCD2 all bind DNA with high affinity[164–166], it was important to rule out that the co-immunoprecipitation of the proteins was not due to DNA or RNA linking of individual protein assemblies. To address this question, I performed chromatin immunoprecipitation followed by western blotting (ChIP–WB) using an APEX1 antibody on nuclease-pretreated lysates, thereby ensuring the removal of DNA and RNA prior to immunoprecipitation. I carried out cell culture and synchronization under the same conditions used for the ChIP-MS experiments. Because I originally observed APEX1–BLM–FANCD2 interactions under replication stress conditions, I treated all samples with aphidicolin to induce mild replication stress and synchronized the cells with thymidine before releasing them into fresh medium for 10.5 hours to enrich for mitotic populations (Figure 4.11A).

Each prepared sample was then divided into three aliquots for nuclease treatment: Benzonase (to degrade all DNA and RNA), RNase A (to selectively remove RNA), or no treatment as a control. Subsequently, I performed immunoprecipitation using an APEX1 antibody following the same procedure as in the APEX1 ChIP-MS workflow, and I prepared the eluates for western blot analysis (Figure 4.11 B). As a control for nuclease efficiency, I treated the chromatin samples with proteinase K and analysed the DNA by gel electrophoresis (Figure 4.11C). Untreated samples displayed the expected smear of 200–500 bp fragments, whereas Benzonase-treated samples showed a near-complete loss of the DNA signal, confirming successful nuclease digestion. Western blot analysis showed efficient APEX1 pulldown with the APEX1 antibody and no detectable signal in the IgG controls. Notably, APEX1 co-immunoprecipitated BLM and FANCD2 under all IP conditions, including after Benzonase or RNase treatment, indicating that these associations did not depend on DNA or RNA (Figure 4.11D, Supplementary Figure 9A second replicate). As an additional control, I examined input lysates and post-IP supernatants to verify protein abundance and assess IP efficiency (Figure 4.11E, Supplementary Figure 9B second replicate).

We should keep in mind that Benzonase treatment was unlikely to remove all DNA, as protein-bound regions may have been protected from nuclease cleavage. Such residual DNA could therefore have contributed to the stability of the recovered complexes. Nevertheless, the nuclease-treatment experiments argued against the possibility that BLM and FANCD2 were co-precipitated solely because they bound independently to separate regions of the same DNA molecule. Together, these results supported DNA- and RNA-independent associations of APEX1 with BLM and FANCD2. However, these experiments did not establish direct protein–protein binding. Instead, they showed that the associations of APEX1 with BLM and FANCD2 persisted after DNA and RNA digestion.

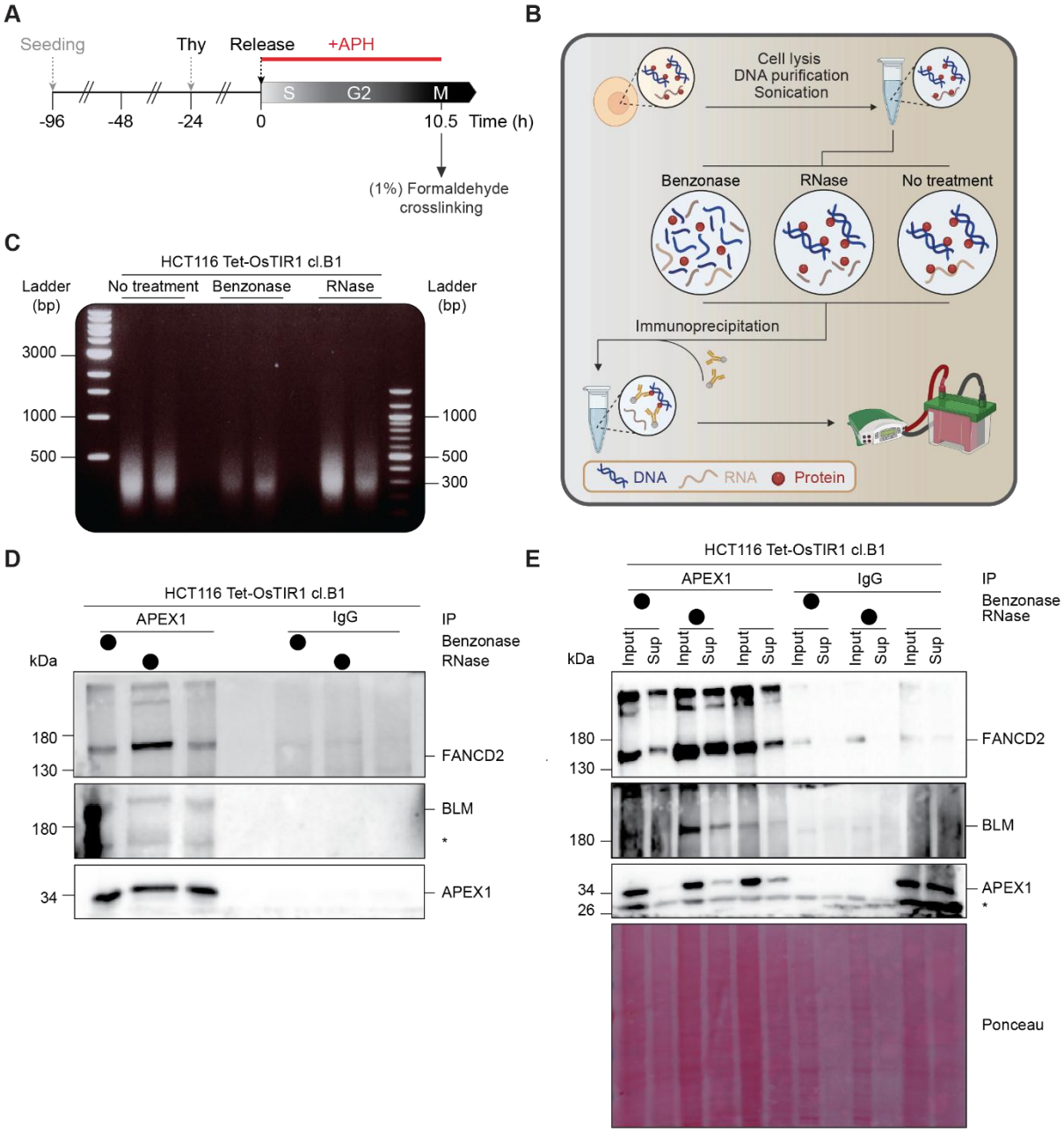


Figure 4.11 | APEX1 association with BLM and FANCD2 is maintained after RNA and DNA digestion.
(A) Schematic overview of the cell culture workflow. HCT116 F9 cells were synchronized using a single thymidine block, released into fresh medium containing aphidicolin (APH), and harvested 10.5 h after release. Cells were then crosslinked with 1% formaldehyde. (B) Overview of ChIP–Western blot sample preparation. Following chromatin isolation, samples were divided into three conditions: untreated, Benzonase-treated to degrade DNA and RNA, and RNase A-treated to remove RNA. (C) Agarose gel analysis confirming nucleic acid digestion in the indicated conditions. Purified nucleic acids were separated on a 1% agarose gel. (D) ChIP–Western blot analysis following immunoprecipitation with an APEX1-specific antibody. Mouse IgG was used as a negative control, and precipitated proteins were detected using the indicated antibodies. (E) Western blot analysis of input and post-immunoprecipitation supernatant fractions showing protein abundance and depletion from the unbound fraction under each treatment condition.

4.2.5 ALYREF–BLM interactions occur independently of RNA or DNA

ALYREF was identified as another candidate associated with UFB-related proteins in the ChIP-MS analysis. Under mild replication stress, ALYREF was enriched with BLM, FANCD2, FANCI, and PICH. To

determine whether the co-purification of ALYREF with UFB-marker proteins was mediated by DNA or RNA, I performed ChIP–WB using the same cell culture and nuclease-treatment workflow applied in the APEX1 experiments. BLM remained detectable in ALYREF immunoprecipitated following both Benzonase and RNase A treatment, indicating that the ALYREF–BLM association was maintained after nucleic acid digestion (Figure 4.12A). However, the BLM signal in the first replicate was weak for all three conditions. Therefore, the experiment was repeated, and the BLM co-immunoprecipitation signal was slightly stronger in the second replicate (Supplementary Figure 9C, D).

The FANCD2 result was less clear. In the first replicate, FANCD2 was also detected in the IgG control after nuclease treatment, indicating nonspecific binding to the beads. This background signal was not observed in the second replicate, but the FANCD2 signal in the ALYREF immunoprecipitate was weaker (Supplementary Figure 9C). Therefore, the association between ALYREF and FANCD2 could not be concluded from these experiments. Western blot analysis of the input and post-immunoprecipitation supernatant fractions confirmed the presence of the analyzed proteins across all conditions (Figure 4.12B). Ponceau staining showed lower total protein levels in the supernatant fractions than in the corresponding input samples. This difference likely resulted from dilution of the supernatant during incubation with the antibody-coupled beads, although the samples were subsequently treated as having the same protein concentration as the input. Overall, these results supported a nucleic acid-independent association between ALYREF and BLM, whereas the corresponding result for FANCD2 remained inconclusive.

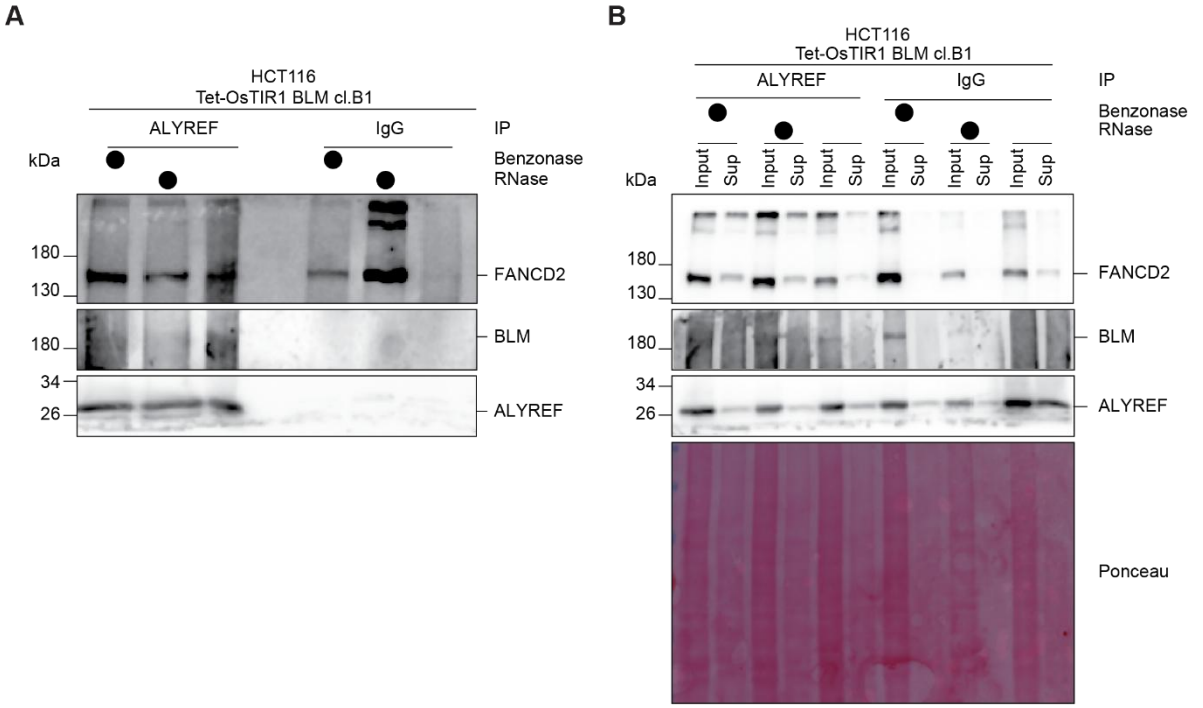


Figure 4.12 | ALYREF–BLM interactions occur independently of RNA or DNA.
(A) ChIP–WB analysis using ALYREF antibody. ALYREF immunoprecipitation and IgG control. (B) Western blot analysis of the inputs and post-IP supernatants confirms protein abundance and efficient immunoprecipitation across all conditions.

4.2.6 APEX1 co-localizes with BLM on ultra-fine anaphase bridges more frequently under mild replication stress

Collectively, our ChIP-MS data suggest that APEX1 is recruited to FANCD2 and BLM containing chromatin complexes that form specifically in mitosis and whose assembly is markedly enhanced by mild replication stress. To study the co-localization of APEX1 with BLM or FANCD2 along UFBs by immunofluorescence microscopy, HCT116 B1 cells (Figure 1.12) expressing an endogenously GFP tagged BLM fusion protein were synchronized by a single thymidine block and released into media containing APH to induce mild replication stress (Figure 4.13A). Anaphase cells were then examined to quantify UFBs and evaluate the extent of APEX1 localization on these structures (Figure 4.13B).

Consistent with previous observations[140], the average number of UFBs per anaphase cell increased significantly under mild replication stress, rising from 18% in DMSO-treated cells to 28% following APH treatment (Figure 4.13C). We next examined the fraction of UFBs exhibiting APEX1 colocalization. Although APEX1 displayed a high and diffuse background signal throughout anaphase cells, which complicated quantitative analysis, it was frequently observed at one or both ends of BLM-positive UFBs and, in some cases, along the entire length of the bridge. Notably, the frequency of APEX1-positive UFBs increased under mild replication stress, whereas the number of UFBs lacking APEX1 signal remained unchanged (Figure 4.13D). Quantitative analysis confirmed a significant increase in the fraction of UFBs showing APEX1 colocalization following APH treatment. Approximately 60% of the UFBs observed under APH treatment showed colocalization of APEX1 with BLM (Figure 4.13E). However, the substantial background signal associated with APEX1 limited the ability to confidently distinguish true UFB-associated localization from nonspecific staining. Therefore, to more accurately assess APEX1 association with UFBs, we sought to evaluate APEX1–BLM colocalization using a more robust and reliable approach in subsequent experiments.

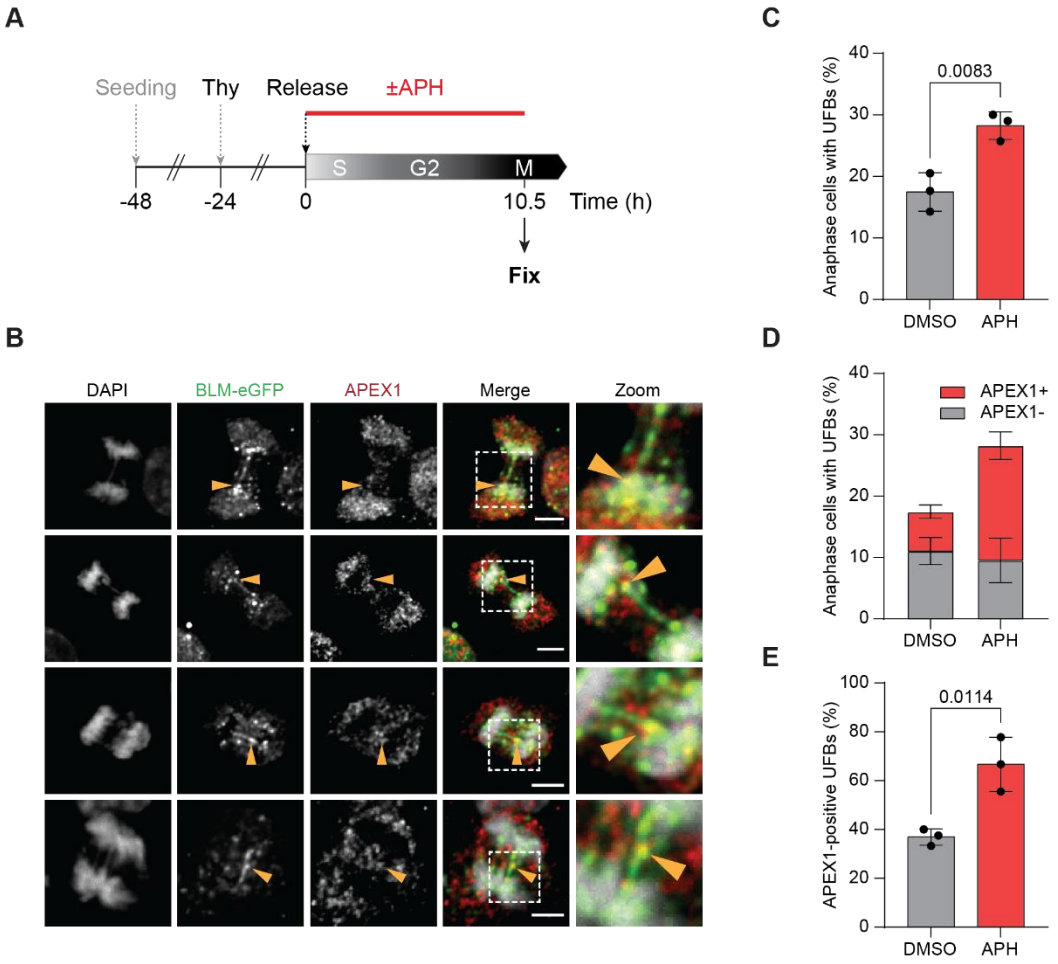


Figure 4.13 | APEX1 co-localizes with BLM on ultra-fine anaphase bridges frequently under mild replication stress. Schematic of the experiments using HCT116 B1 cell line expressing BLM–eGFP. (B) Representative immunofluorescence images showing APEX1 localization on BLM-positive UFBs. UFBs were visualized by BLM–eGFP, APEX1 was detected by immunostaining (red, 594 nm), and DNA was counterstained with DAPI. Scale bar: 5 µm. (C) Quantification of anaphase cells containing UFBs in DMSO- and APH-treated samples. (D) Quantification of APEX1-positive versus APEX1-negative UFBs in anaphase cells. (E) Fraction of APEX1-positive UFBs per anaphase cell. Data is presented as mean ± SD from three biological replicates (Student's t-test), with 25 anaphase cells analyzed per replicate. This experiment was conducted by master student Amr Abdro.

4.2.7 ALYREF association with UFBs shows no significant change under APH treatment

To validate whether ALYREF as our candidate is located to UFBs during mitosis, we used immunofluorescence microscopy association with UFBs. The experimental setup mirrored that used for APEX1 visualization (Figure 4.14A). Representative images of anaphase cells showed UFBs in which ALYREF is collocated with BLM (Figure 4.14B). We initially quantified the number of UFBs in DMSO-treated control cells and APH-treated cells. While the number of UFBs increased under APH treatment, the change was not statistically significant (Figure 4.14C). Analysis of ALYREF-positive UFBs revealed that a large proportion of UFBs exhibited ALYREF colocalization; however, the frequency of colocalization was comparable between DMSO and APH conditions (Figure 4.14D). It is important to note that ALYREF is a highly abundant protein, and antibody-based detection resulted in substantial background signal throughout anaphase cells, thereby complicating the distinction between true

colocalization and nonspecific staining. Examination of UFBs displaying ALYREF signal at one or both ends indicated that approximately 60% of bridges showed colocalization, and this fraction was unaffected by replication stress (Figure 4.14E). These results suggested that ALYREF localization to UFBs did not respond specifically to APH-induced replication stress and therefore did not corroborate the earlier findings from the ChIP-MS experiments.

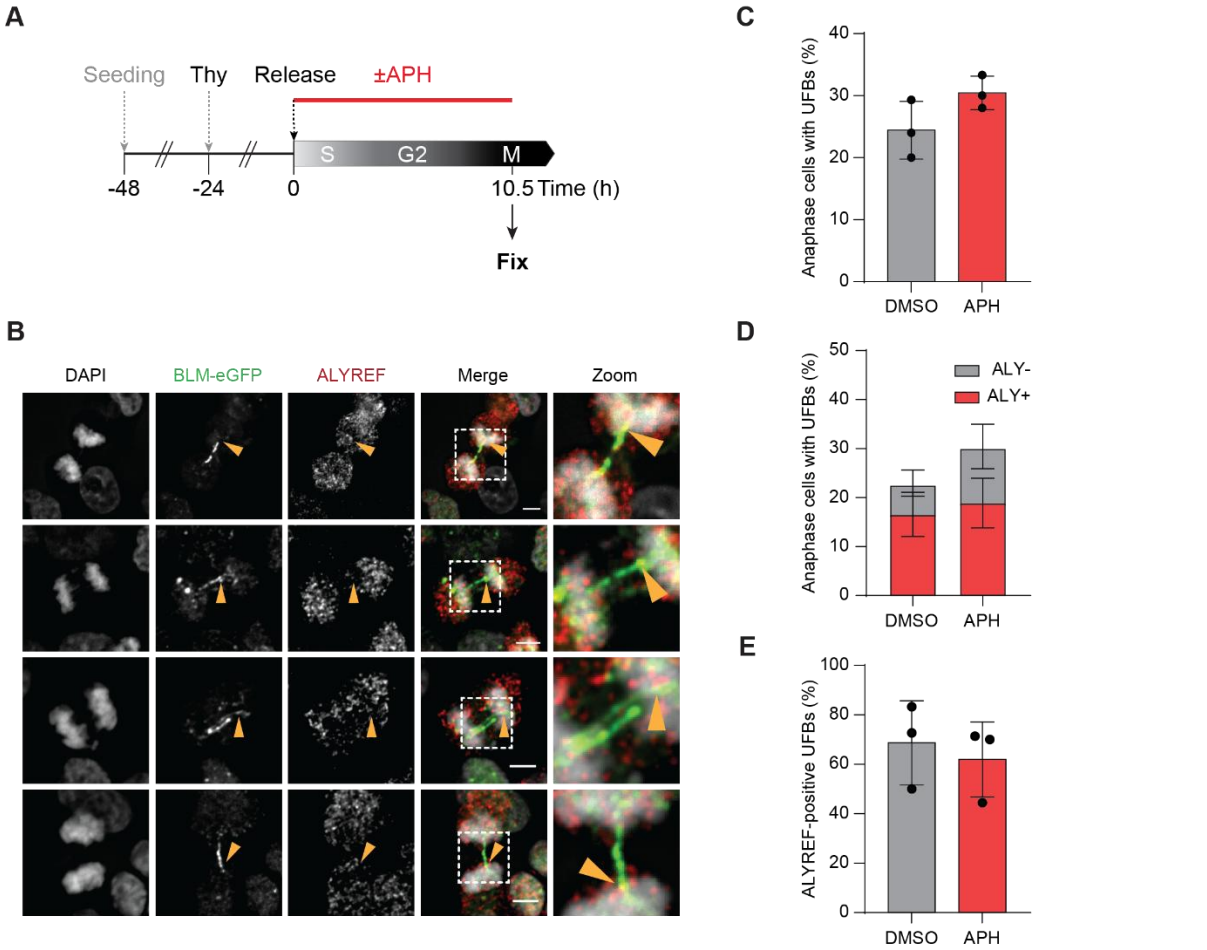


Figure 4.14 | ALYREF shows limited co-localization with BLM at ultra-fine anaphase bridges.
(A) Experimental scheme for the HCT116 B1 cell line expressing BLM–eGFP. Cells were synchronized at the G1/S boundary with thymidine, released into fresh medium containing aphidicolin (APH) or DMSO, and fixed 10.5 h after release. (B) Representative immunofluorescence images illustrating ALYREF localization relative to BLM-positive UFBs. UFBs were visualized by BLM–eGFP, ALYREF was detected by immunostaining (red, 594 nm), and DNA was counterstained with DAPI. Scale bar: 5 µm. (C) Quantification of anaphase cells containing UFBs under DMSO- and APH-treated conditions. (D) Quantification of ALYREF-positive and ALYREF-negative UFBs in anaphase cells. (E) Fraction of ALYREF-positive UFBs per anaphase cell. Data is presented as mean ± SD from three biological replicates (Student's t-test), with 25 anaphase cells analyzed per replicate. This experiment was conducted by master student Nikita Kvasov.

4.2.8 ALYREF knockdown does not affect UFBs formation

Next, we examined the effect of ALYREF depletion on UFB formation using siRNA-mediated knockdown. Four experimental conditions were analyzed: control siRNA and ALYREF siRNA, each in the presence or absence of APH to induce mild replication stress. Western blot analysis confirmed successful depletion through quantification of ALYREF protein levels normalized to a housekeeping

protein. Approximately 50% reduction in ALYREF expression was achieved following siRNA transfection under both DMSO and APH conditions (Figure 4.15A, B).

Next, we assessed the average number of UFBs per anaphase cell. No significant change in UFB frequency was observed following ALYREF depletion under either DMSO or APH treatment compared with control cells (Figure 4.15C). Similarly, analysis of chromatin bridges revealed the same trend: although replication stress increased the number of chromatin bridges, ALYREF depletion did not affect the frequency of these mitotic aberrations (Figure 4.15D).

Based on these observations, we concluded that ALYREF was unlikely to play a significant role in UFB formation or resolution under these conditions. Consequently, subsequent experiments focused on APEX1 as a more promising UFB-associated candidate protein.

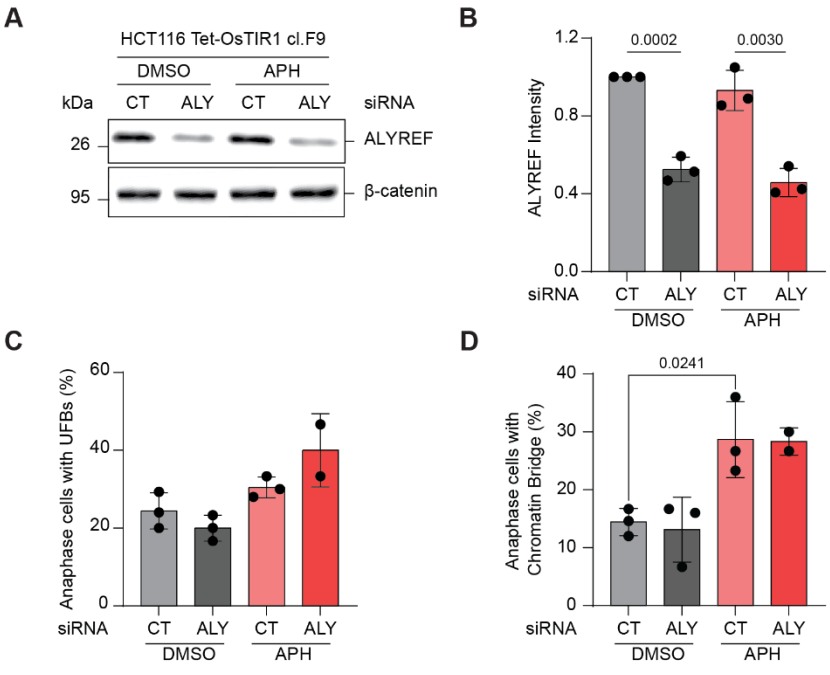


Figure 4.15 | ALYREF knockdown does not affect ultra-fine anaphase bridge formation.
(A) Western blot analysis of HCT116 F9 cells following two rounds of ALYREF siRNA transfection. Cells were synchronized with thymidine, released into fresh medium containing aphidicolin (APH) or DMSO, and fixed 10.5 h after release. (B) Quantification of ALYREF protein levels based on western blot signal intensity. (C) Quantification of anaphase cells containing ultra-fine anaphase bridges (UFBs). (D) Quantification of chromatin bridges in anaphase cells. Data is shown as mean ± SD from three biological replicates and two replicates for ALYREF/+APH (Student's t-test), with 25 anaphase cells scored per replicate. This experiment was conducted by master student Nikita Kvasov.

4.2.9 Proximity ligation assay reveals APEX1 co-localization with ultra-fine bridges

Reciprocal ChIP-MS analyses and immunofluorescence microscopy using an APEX1 antibody in BLM–eGFP-expressing cells suggested a potential colocalization of APEX1 with BLM at ultrafine anaphase bridges (UFBs) during mitosis. However, interpretation of the immunofluorescence data was complicated by substantial background signal, likely reflecting the high cellular abundance of APEX1[167], which made it difficult to distinguish specific UFB-associated localization from nonspecific staining. To overcome this limitation and assess whether APEX1 was positioned in close proximity to UFB marker proteins in a controlled manner, I decided to use a proximity ligation assay (PLA). The PLA technique

relies on secondary antibodies conjugated to complementary DNA oligonucleotides. When two target proteins are positioned within approximately 40 nm of each other, the oligonucleotides are ligated and subjected to rolling-circle amplification. The resulting concatemeric DNA product is then detected by fluorescently labelled probes, thereby enabling visualization of protein proximity while minimizing background signal and selectively reporting sites of colocalization (Figure 4.16A).

PLA was performed using the HCT116 B1 clone, which expresses BLM–eGFP and allows direct visualization of UFBs (Figure 4.16B). Two experimental PLA conditions were analyzed: APEX1 in combination with BLM antibodies and APEX1 in combination with FANCD2 antibodies. Control samples were processed simultaneously without the APEX1 antibody. In the absence of one of the antibodies, probe ligation could not occur, and therefore no PLA signal was expected to be detected. In both the APEX1–BLM and APEX1–FANCD2 conditions, PLA signals were observed along UFBs, including at the ends and along the length of the bridges, appearing as distinct dots. This pattern was consistent with the localization previously suggested by immunofluorescence microscopy, but here it was observed without substantial background signal. Using this method, we observed the colocalization of APEX1 with UFBs more clearly than in the immunofluorescence assay (Figure 4.16C).

PLA signals were also observed on lagging chromatin and bulk chromatin in anaphase cells, necessitating analysis at the level of individual anaphase cells. Quantification of PLA-positive anaphase cells revealed a low background signal in control samples (~10%), whereas PLA signals were detected in approximately 60% of anaphase cells in the APEX1–BLM condition and approximately 96% of anaphase cells in the APEX1–FANCD2 condition (Figure 4.16D and Supplementary Figure 10). Subsequent quantification showed that approximately 60% of UFBs exhibited PLA signals in both the APEX1–BLM and APEX1–FANCD2 conditions, whereas no PLA-positive UFBs were detected in the control samples (Figure 4.16E). Although these analyses were based on a single biological replicate with 22–25 anaphase cells per condition and therefore did not allow statistical testing, the results supported close spatial proximity between APEX1 and both BLM and FANCD2 at UFBs during mitosis. Consistent with our previous immunofluorescence analyses, approximately 60% of UFBs exhibited APEX1 colocalization under APH-treated conditions.

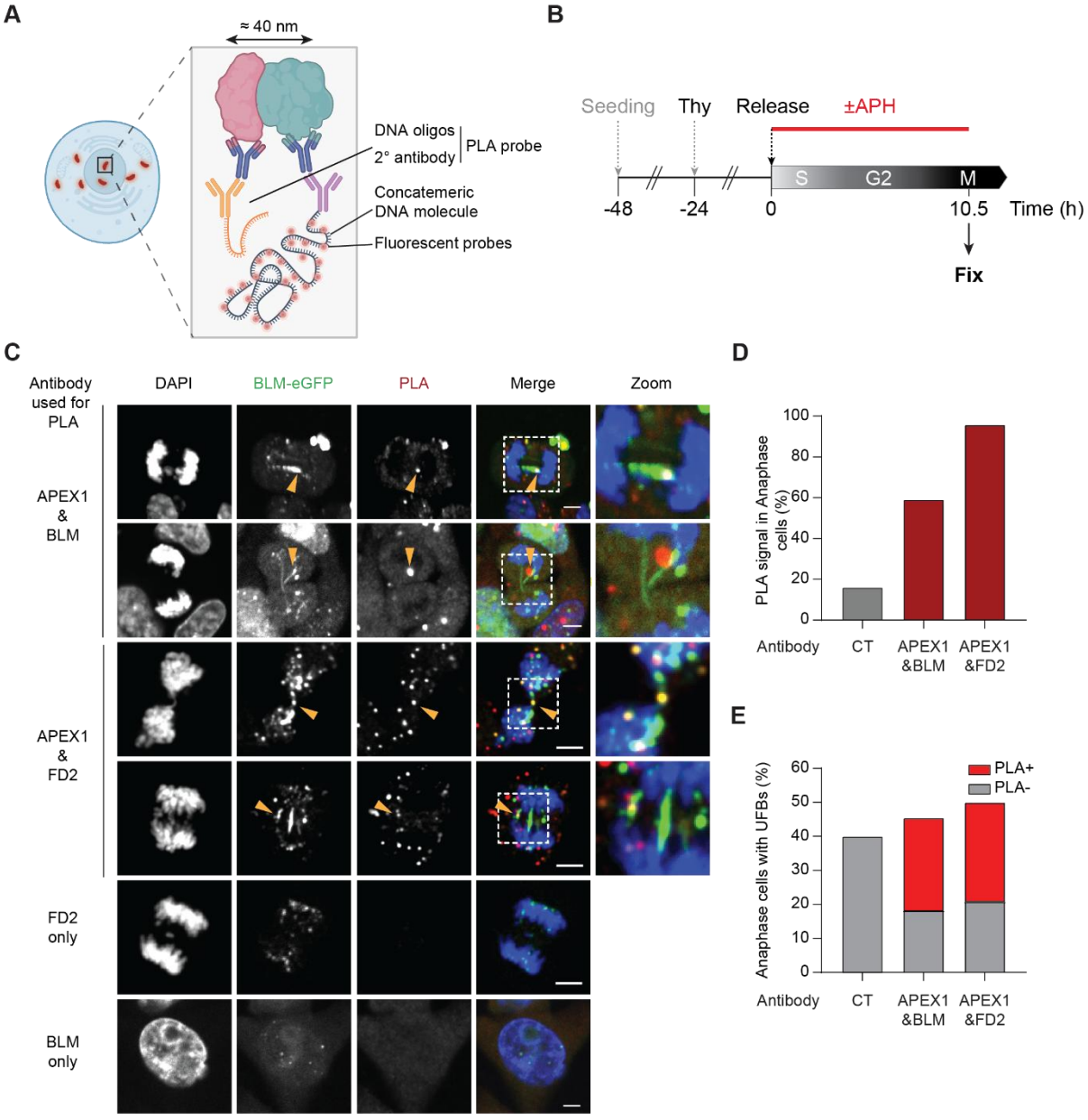


Figure 4.16 | Proximity ligation assay reveals APEX1 co-localization with BLM and FANCD2 at ultra-fine anaphase bridges. (A) Overview of the proximity ligation assay (PLA) workflow and experimental principle. (B) Schematic representation of the HCT116 B1 cell line expressing BLM helicase–eGFP. Cells were synchronized with thymidine, released into fresh medium containing aphidicolin (APH) to induce mild replication stress, and fixed 10.5 h after release. (C) Representative immunofluorescence images from the PLA assay showing co-localization of APEX1 with BLM helicase and FANCD2 at ultrafine bridges (UFBs). UFBs were visualized by BLM–eGFP, PLA signals are shown in red (594 nm), and DNA was counterstained with DAPI. Scale bar, 5 µm. (D) Quantification of PLA-positive anaphase cells in control samples and in samples probed with APEX1–BLM or APEX1–FANCD2 antibody pairs. (E) Quantification of BLM-positive UFBs in anaphase cells displaying PLA signals along the bridges. One biological replicate was analyzed, with approximately 22–25 anaphase cells scored per condition.

4.3 Consequences of APEX1 loss and BLM depletion on genome stability

4.3.1 CRISPR/Cas9-mediated knockout of APEX1 in F9 HCT116 cells

After confirming replication-stress induced interaction of the APEX1 endonuclease with BLM or FANCD2 at UFBs, we next determined, whether loss of APEX1 affects the formation or resolution of the UFBs. To address this question, we knocked-out APEX1 in HCT116 F9 cells, which expresses BLM-AID-eGFP and PICH-mCherry fusion proteins enabling tracking of UFBs both in live and fixed-cells. The APEX1 knockout cells were generated and expanded by Amr Abdrbo (MSc student in the Storchová lab) under my supervision. In brief, F9 cells were transfected a with TrueCut Cas9 v2 protein and TrueGuide modified synthetic single-guide RNAs (sgRNAs) targeting the APEX1 locus (Figure 4.17A). Forty-eight hours after transfection, western blot analysis of bulk cell populations showed an approximately 60% reduction in APEX1 protein levels compared with the F9 wild-type control (Figure 4.17B). To obtain clones with complete APEX1 knockout, single cells from the bulk-transfected population were seeded and expanded. Western blot validation of individual clones identified seven out of 32 independent clones with a complete loss of APEX1 expression (Figure 4.17C). Clone 2.3 was selected from these for use in all subsequent experiments and is referred to hereafter as F9AK.

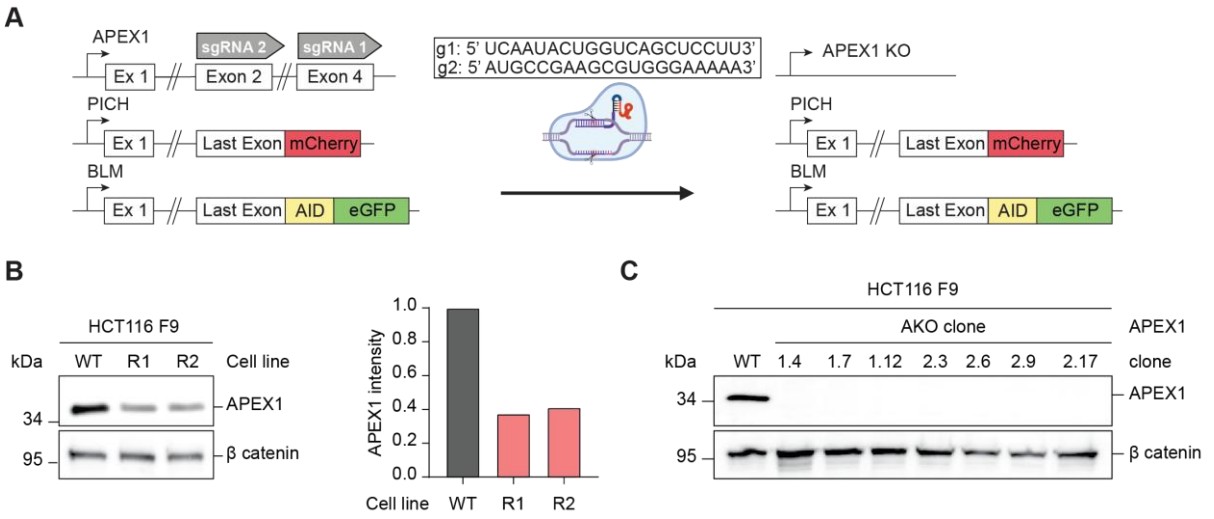


Figure 4.17 | CRISPR/Cas9-mediated knockout of APEX1 in HCT116 F9 cells.
(A) Schematic overview of the HCT116 F9 cell line and the experimental strategy for endogenous APEX1 knockout using two sgRNAs. (B) Western blot analysis of APEX1 protein levels in bulk cell populations following transfection of HCT116 F9 cells with CRISPR/Cas9 constructs targeting APEX1. Two biological replicates (R1 and R2) were performed to increase the success rate of knockout generation. (C) Western blot validation of single-cell clones derived from the bulk-transfected populations, confirming complete APEX1 knockout in seven independent clones.

4.3.2 Ultra-fine bridges arise more frequently in APEX1-deficient cells with replication stress

To test whether APEX1 contributed to UFB resolution, we quantified PICH-positive UFBs in F9AK and wild-type F9 cells. We synchronized cells using a single thymidine block and released them into medium containing DMSO as control or APH to induce mild replication stress. After 10.5 h, more than 70% of cells had entered mitosis, and the proportion of anaphase cells reached approximately 15%[140]. We then fixed the cells for analysis (Figure 4.18A). For BLM depletion, we added auxin at the start of synchronization and maintained it until cell harvest (Figure 4.18A). This treatment reduced BLM protein levels to below 25% (Figure 4.18B and Supplementary Figure 11). We analysed the cells by fluorescence microscopy using mCherry-tagged PICH and eGFP/AID-tagged BLM (Figure 4.18C).

Under DMSO treatment, approximately 20% of anaphase cells contained UFBs in wild-type F9 cells. APEX1 knockout alone did not increase UFB frequency under these conditions. In contrast, BLM depletion caused a mild but significant increase in UFB-positive anaphases to approximately 30%, consistent with the established role of BLM in UFB processing during mitosis[140]. Combined loss of APEX1 and BLM did not further increase UFB frequency compared with BLM depletion alone, indicating that BLM depletion accounted for the increase observed under DMSO conditions (Figure 4.18D). Under mild replication stress, APEX1 knockout significantly increased the proportion of UFB-positive anaphases from 31% in wild-type cells to 48% in F9AK cells. BLM depletion alone or combined loss of BLM and APEX1 did not cause an additional increase in UFB frequency (Figure 4.18D). These results supported two main conclusions. First, APEX1 contributed to UFB resolution specifically under mild replication stress. Second, the non-additive effect of combined APEX1 and BLM loss was consistent with both proteins acting in the same UFB-processing pathway or in closely connected steps. The replication stress-dependent phenotype further suggested that APEX1 may be particularly important for processing replication stress-induced UFBs, including fragile site-associated UFBs.

We next analysed telophase cells to determine whether UFBs persisted beyond anaphase (Figure 4.18E). Not all UFBs observed during anaphase remained detectable in telophase. In the DMSO-treated wild-type control, only approximately 10% of telophase cells contained persistent UFBs, indicating that almost half of anaphase UFBs had been resolved before telophase (Figure 4.18F). Under DMSO conditions, the frequency of telophase UFBs showed an increase for BLM depleted samples and double BLM depleted and APEX1 KO samples like the anaphase UFBs.

APH compair to DMSO treatment caused a slight but significant increase in persistent UFBs in wild-type cells. In APH-treated samples, the pattern of telophase UFBs differed from that observed in anaphase and provided additional insight into the relationship between APEX1 and BLM. Overall,

persistent UFBs increased significantly in the deficient conditions compared with APH-treated wild-type cells. However, combined APEX1 knockout and BLM depletion sample showed significantly higher level of persistent UFBs than APEX1 knockout alone, whereas no significant difference was observed between the double-deficient condition and BLM depletion alone. These results suggested that Although APEX1 may functionally cooperate with BLM in UFB resolution, BLM appeared to have a broader role in preventing persistent UFBs under replication stress conditions (Figure 4.18F).

As fragile site-associated UFB resolution is thought to require helicase-mediated unwinding of under-replicated DNA[89], we examined RPA-coated UFBs as a readout of single-stranded DNA formation. We immune-stained cells with an antibody against RPA and quantified RPA-positive UFBs (Figure 4.18G).

APH treatment caused an approximately twofold increase in RPA-coated UFBs in wild-type cells. Under DMSO conditions, APEX1 knockout did not significantly alter their frequency compared with wild-type cells. In contrast, BLM depletion significantly reduced the number of RPA-coated UFBs, consistent with a role for BLM in generating single-stranded DNA regions that can be coated by RPA.

Under APH treatment, APEX1 knockout increased RPA-coated UFBs by approximately 30%. In contrast, BLM-depleted cells and cells with combined BLM depletion and APEX1 knockout showed significantly fewer RPA-coated UFBs than wild-type cells (Figure 4.18H). Together, these results suggested that BLM acts upstream to generate RPA-coated single-stranded DNA on UFBs, whereas APEX1 may contribute to the subsequent processing or resolution of these structures under replication stress.

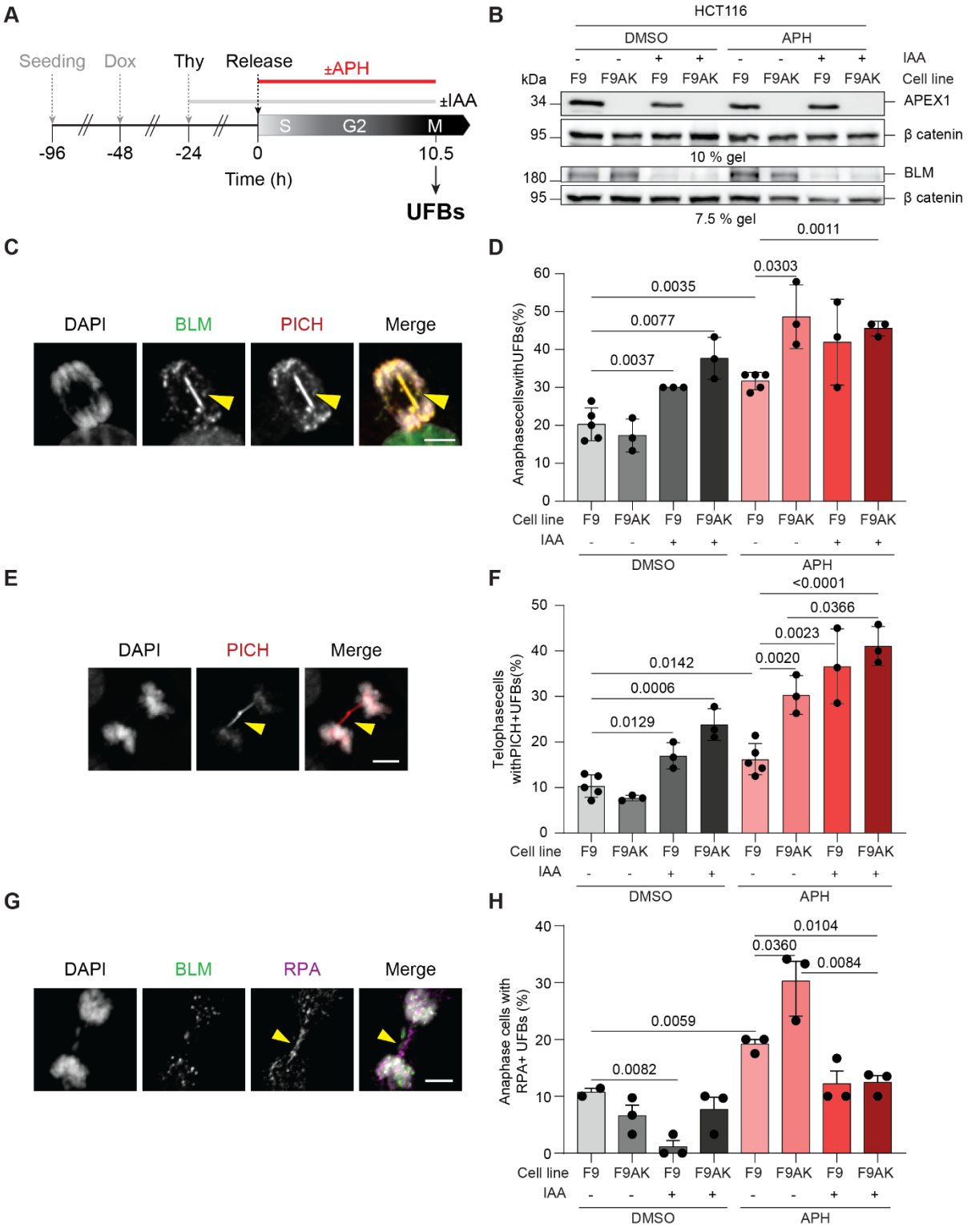


Figure 4.18 | Effects of APEX1 loss and BLM depletion on anaphase defects.
(A) Schematic overview of the experimental workflow. **(B)** Western blot confirming APEX1 knockout and auxin-induced BLM depletion. **(C)** Representative fluorescence microscopy image of an anaphase cell showing BLM–GFP, PICH–mCherry, and DAPI-stained DNA. **(D)** Quantification of anaphase cells containing PICH-positive UFBs following aphidicolin (APH) treatment. Indole-3-acetic acid (IAA) was added together with thymidine to induce BLM depletion. **(E)** Representative fluorescence microscopy image of a telophase cell containing persistent PICH-positive UFBs. **(F)** Quantification of telophase cells containing PICH-positive UFBs. **(G)** Representative fluorescence microscopy image of a mitotic cell containing RPA-positive UFBs. **(H)** Quantification of mitotic cells containing RPA-positive UFBs. Data in (D), (F), and (H) represent mean ± SD from two to five independent biological replicates and were analyzed using an unpaired Student's *t*-test. At least 15–25 mitotic cells were scored per replicate, as indicated in the Materials and Methods

4.3.3 Mitotic aberration arises more frequently in APEX1-deficient cells

Although our focus was on UFB formation and resolution, analyzing the impact of APEX1 depletion on chromatin bridges provided additional insight into its role in preserving genomic stability during mitosis. Chromatin bridges were quantified using the DAPI signal. First, aphidicolin treatment significantly increased the number of chromatin bridges by approximately threefold in wild-type cells.

In DMSO-treated cells, APEX1 knockout caused an increase in chromatin bridges compared with wild-type cells (from 8% to 18%), indicating a role for APEX1 in maintaining genome stability. BLM depletion alone showed a similar trend, whereas simultaneous depletion of APEX1 and BLM led to a slight additional increase relative to APEX1 knockout alone; however, this difference was not statistically significant (Figure 4.19A). Under replication stress, aphidicolin treatment increased the frequency of chromatin bridges in wild-type cells to 24%, whereas APEX1 knockout further increased this frequency to 52%. This finding supported a role for APEX1 in limiting replication stress-induced chromatin bridge formation. BLM depletion under aphidicolin treatment also increased chromatin bridge frequency to approximately 40%. However, combined loss of APEX1 and BLM did not produce an additive effect, suggesting that, as observed for UFBs, APEX1 and BLM may act in the same pathway or in closely connected steps to suppress chromatin bridge formation during replication stress (Figure 4.19A).

In the final step, we analyzed lagging chromatids or chromatid fragments in anaphase cells, which can arise from multiple sources, including chromosome mis-segregation or unrepaired DNA double-strand breaks. Because these structures could not be distinguished based on our experimental setup, all lagging chromatin events were analyzed as a single category[168,169]. DAPI-stained immunofluorescence analysis revealed a clear increase in lagging chromatids following aphidicolin treatment compared with wild-type DMSO-treated controls (Figure 4.19B), consistent with previous studies showing that mild replication stress increases chromosome mis-segregation[168]. In the absence of replication stress, both APEX1-knockout and BLM-depleted cells exhibited an approximately twofold increase in lagging chromatin per anaphase cell compared with wild-type controls, rising from 9% to 20%. Notably, simultaneous APEX1 knockout and BLM depletion did not produce an additive effect, as lagging chromatin levels remained comparable to those observed in the single-depletion conditions.

Under mild replication stress, APEX1-knockout cells showed a significant increase in lagging chromatin, reaching 61% compared with aphidicolin-treated wild-type cells (46%). In contrast, BLM-depleted and double-depletion cells did not display a significant additional increase, potentially reflecting the effect of aphidicolin on lagging chromatid formation. Overall, these results indicated that APEX1 depletion significantly increased mitotic aberrations under mild replication stress, whereas additional BLM

depletion did not further exacerbate these defects. This finding suggested that APEX1 and BLM may function within the same pathway to maintain mitotic fidelity.

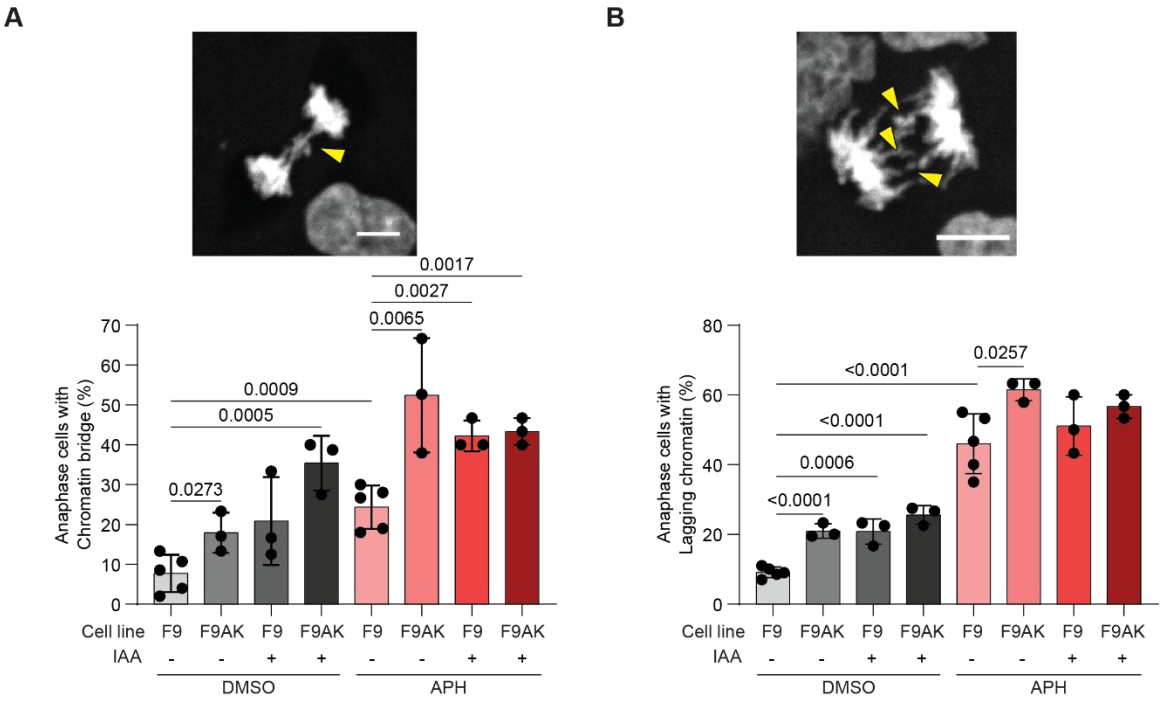


Figure 4.19 | Depletion of BLM and APEX1 increases the frequency of mitotic aberrations.
(A-B) Quantification of cells with chromatin bridges and lagging chromatins in control, APEX1 KO, and BLM depleted cells. Cells were synchronized with a single control, blocked and released into media with or without 100 nM aphidicolin, as shown in Figure 4.18. Data are shown as mean ± SD from three to five biological replicates, with 25 anaphase cells scored per replicate.

4.3.4 Loss of APEX1 increases post-mitotic genome instability

In the next step, we measured the consequences of unresolved anaphase bridges across the different experimental conditions. Persistent anaphase bridges can severely compromise genome stability if they extend beyond mitosis. These stretched bridges are prone to rupture during cytokinesis, thereby generating DNA double-strand breaks (DSBs) that are highly mutagenic and may lead to loss of genetic material, although such events are relatively infrequent[170]. In some cases, bridges interfere with cytokinesis itself, producing binucleated cells that contribute to polyploidy and chromosomal instability[73]. Alternatively, broken DNA fragments from bridges may be excluded from the daughter nuclei and encapsulated as micronuclei, which undergo defective replication and are particularly vulnerable to chromothripsis, leading to extensive chromosomal rearrangements[171]. It has been hypothesized that unresolved DNA bridges interfere with cytokinesis, thereby giving rise to binucleated cells. Indeed, previous studies observed a significant increase in binucleated cells following BLM depletion in fixed cells, and this phenotype was further exacerbated by mild replication stress. These findings suggested that loss of BLM function increased the occurrence of “wavy” ultrafine

bridge structures, which require longer times for resolution and can therefore still be detected in telophase[140].

To investigate the consequences of unresolved anaphase structures, we examined the frequency of binucleated interphase cells as a readout for cytokinesis failure. Cells were treated with thymidine, aphidicolin, and IAA under the same conditions used for UFB analysis, and cells were arrested in the subsequent G_1 phase (Figure 4.20A, Supplementary Figure 12). Cells were stained with α-tubulin to visualize the cytoskeleton and outline cell boundaries, whereas DAPI staining was used to label nuclei and detect micronuclei (Figure 4.20B).

Quantification of binucleated cells revealed a moderate increase in APEX1-deficient cells (6%) compared with control cells (2–3%), and this effect was observed both in the presence and absence of aphidicolin (Figure 4.20C). Similarly, BLM depletion increased binucleation to approximately 12%, consistent with previous studies. As expected, co-depletion of APEX1 and BLM did not further increase binucleation, and replication stress did not significantly alter binucleation levels (Figure 4.20C). Together, these results suggested that unresolved anaphase bridges and UFBs contributed to cytokinesis failure under these conditions, with BLM playing a dominant role, whereas APEX1 loss exerted a more modest effect.

To assess the impact of APEX1 depletion on genome stability, we quantified micronuclei as a marker of genomic instability. Under conditions without replication stress, the average number of micronuclei did not increase significantly in either APEX1- or BLM-deficient cells. Although the combined loss of APEX1 and BLM led to a significant increase compared with wild-type controls, the increase remained relatively modest (~1.5-fold). Mild replication stress induced by aphidicolin caused an approximately fourfold increase in micronuclei relative to DMSO-treated cells (Figure 4.20D). Notably, APEX1-deficient cells under aphidicolin treatment exhibited an even greater increase in micronuclei, indicating that APEX1 became particularly important under replication stress conditions. This observation was consistent with our previous findings on UFBs and lagging chromatids and supported a role for APEX1 in preventing replication stress-induced DNA damage and subsequent DSB formation. Co-depletion of BLM in APEX1-knockout cells resulted in a mild but not statistically significant additional increase in micronuclei frequency.

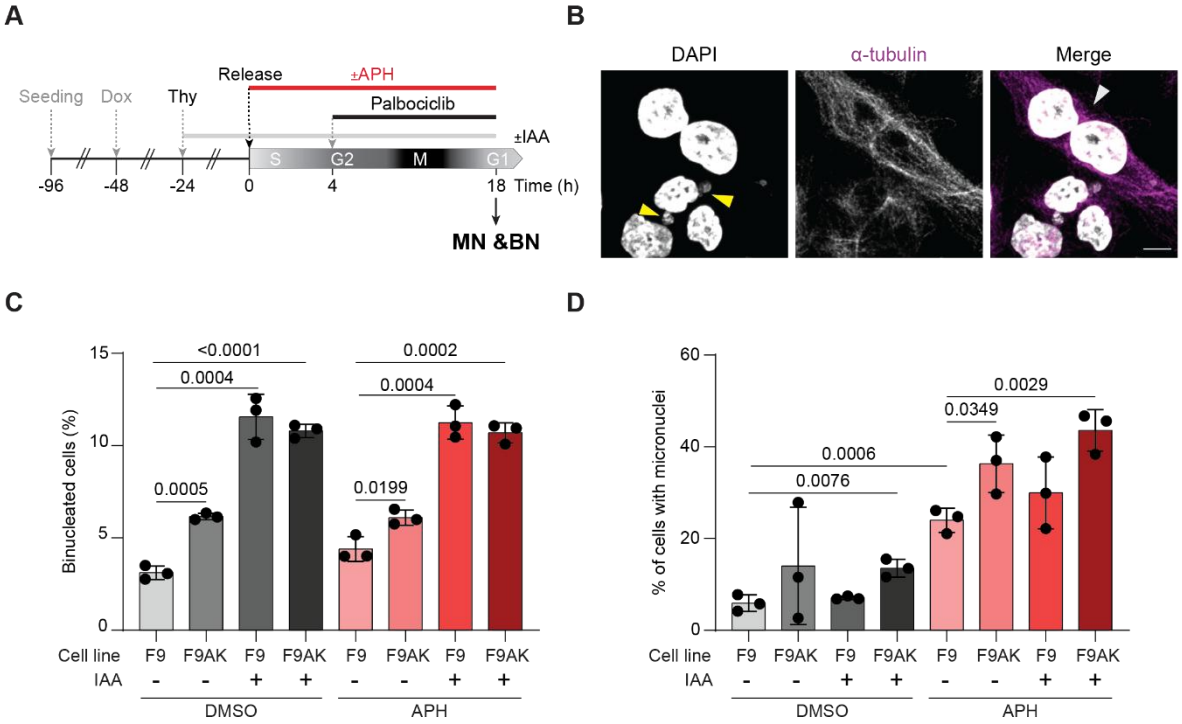


Figure 4.20 | post-mitotic consequences of APEX1 and BLM depletion.
(A) Schematic overview of experimental design. (B) Representative immunofluorescence image of a fixed cell. The cytoskeleton was visualized using α-tubulin staining, and DNA was stained with DAPI. Micronuclei are indicated by yellow arrows, and a binucleated cell is marked with a gray arrow. Scale bars, 10 µm. (C–D) Quantification of (C) binucleated cells and (D) micronuclei in G1-phase–arrested populations. The same image sets were used for both analyses. Cells were treated identically across conditions, as described in the experimental schematic. Statistical significance was determined using Student's t-test. Data are shown as mean ± SD for three biological replicates in F9 and F9 APEX1 knockout (F9AK) cells, with 200 cells analyzed per replicate.

4.3.5 Double strand DNA breaks arise frequently in APEX1-deficient cells

Although we observed a consistent increase in lagging chromatids during anaphase and micronuclei in subsequent G1-phase cells, it remained unclear whether the elevated micronucleation resulted primarily from chromosome mis-segregation or from the accumulation of DNA double-strand breaks (DSBs). To distinguish between these possibilities and identify the source of micronuclei formation in APEX1-deficient cells, we next examined DSB levels in metaphase-arrested cells.

To address this question, metaphase spreads were prepared to quantify chromosomal breaks and determine whether DSBs were already present before cells entered anaphase. Cells were treated with APH and auxin (IAA) for 24 hours to induce replication stress and achieve maximal BLM depletion, respectively. We arrested the cells with colchicine in metaphase, thereby enabling direct quantification of DSBs in metaphase spreads (Figure 4.21A). After fixation, metaphase spreads were analysed by microscopy. Chromosome breaks were quantified based on DAPI-stained metaphase chromosomes, allowing visualization and verification of DNA double-strand breaks in individual metaphase cells (Figure 4.21B). To confirm the efficiency of BLM depletion and APEX1 knockout, western blot analysis

was performed on samples processed under identical treatment conditions, serving as an experimental control (Figure 4.21C).

Quantification of chromosome breaks per metaphase cell revealed a significant increase in DSBs in APEX1-knockout cells compared with wild-type controls under DMSO treatment (64% versus 44% of cells showing breaks). In contrast, BLM depletion alone increased the number of breaks (53%), although this increase did not reach statistical significance, indicating that loss of BLM alone exerted a milder effect on basal DSB formation. Interestingly, combined depletion of BLM in the APEX1-knockout cell line resulted in an additive increase, with approximately 73% of metaphase cells exhibiting chromosome breaks, representing an increase of approximately 20% relative to the BLM-depleted single-knockout condition. These findings suggested that even in the absence of replication stress, APEX1 loss compromised DNA repair capacity and resulted in elevated DSB formation, whereas APEX1 and BLM appeared to function through partially independent pathways to maintain genome stability (Figure 4.21D).

When replication stress was induced with aphidicolin, the overall number of chromosome breaks increased markedly in all samples, reaching approximately 72% in wild-type cells. Under these conditions, loss of either APEX1 or BLM alone did not further elevate the number of breaks beyond the replication stress baseline, suggesting that the strong genotoxic effect of aphidicolin masked the individual contribution of each factor. However, combined BLM depletion and APEX1 knockout resulted in the highest incidence of metaphase cells with chromosome breaks, reaching approximately 90%, indicating a synergistic defect under replication stress conditions. Together, these findings demonstrated that APEX1 deficiency increased DSB formation even in the absence of replication stress and, when combined with BLM loss, resulted in severe genomic instability (Figure 4.21D).

To further evaluate the extent of chromosomal instability, we quantified the average number of chromosomal breaks per metaphase cell from metaphase spreads. This metric reflects the severity of chromosomal damage within individual cells, capturing the extent of replication-associated collapse or defective DNA repair[172]. Unlike the percentage of cells showing chromosomal breaks, which measures the fraction of affected cells, this analysis highlights the intensity of damage within each metaphase.

In DMSO-treated samples, wild-type cells exhibited an average of 0.6 breaks per metaphase cell, whereas BLM-depleted cells showed approximately 0.9 breaks per metaphase cell, representing a modest but significant increase. In contrast, APEX1-knockout cells displayed approximately 1.3 breaks per metaphase cell, indicating a stronger, although not statistically significant, impact of APEX1 loss on genome integrity. Combined depletion of APEX1 and BLM resulted in an average of 1.3 breaks per

metaphase cell, revealing no additive effect between the two deficiencies. These data suggested that even in the absence of replication stress, loss of APEX1 increased chromosomal instability, whereas simultaneous depletion of APEX1 and BLM did not further exacerbate the severity of DNA damage (Figure 4.21E).

Under mild replication stress, wild-type cells exhibited an average of 1.6 breaks per metaphase cell, consistent with the expected increase in replication-associated chromosome fragility[168]. APEX1-knockout cells exhibited an average of two breaks per metaphase cell, representing an upward trend compared with control cells, although this difference did not reach statistical significance. BLM depletion alone resulted in a comparable level of chromosomal damage (~1.4 breaks per metaphase cell) relative to wild-type APH-treated samples. However, APEX1/BLM double-deficient cells displayed the highest severity of chromosomal damage, averaging 2.4 breaks per metaphase cell, suggesting that the combined loss of these repair factors intensified chromosomal fragility (Figure 4.21E).

Together, these findings indicated that APEX1 loss increased both the frequency and severity of chromosomal breaks, particularly under conditions of replication stress. Moreover, the additive effect observed in double-depleted cells suggested that besides their role in UFB resolution, additional function of APE1 or BLM are required to preserve chromosome integrity prior to mitotic entry and cell viability.

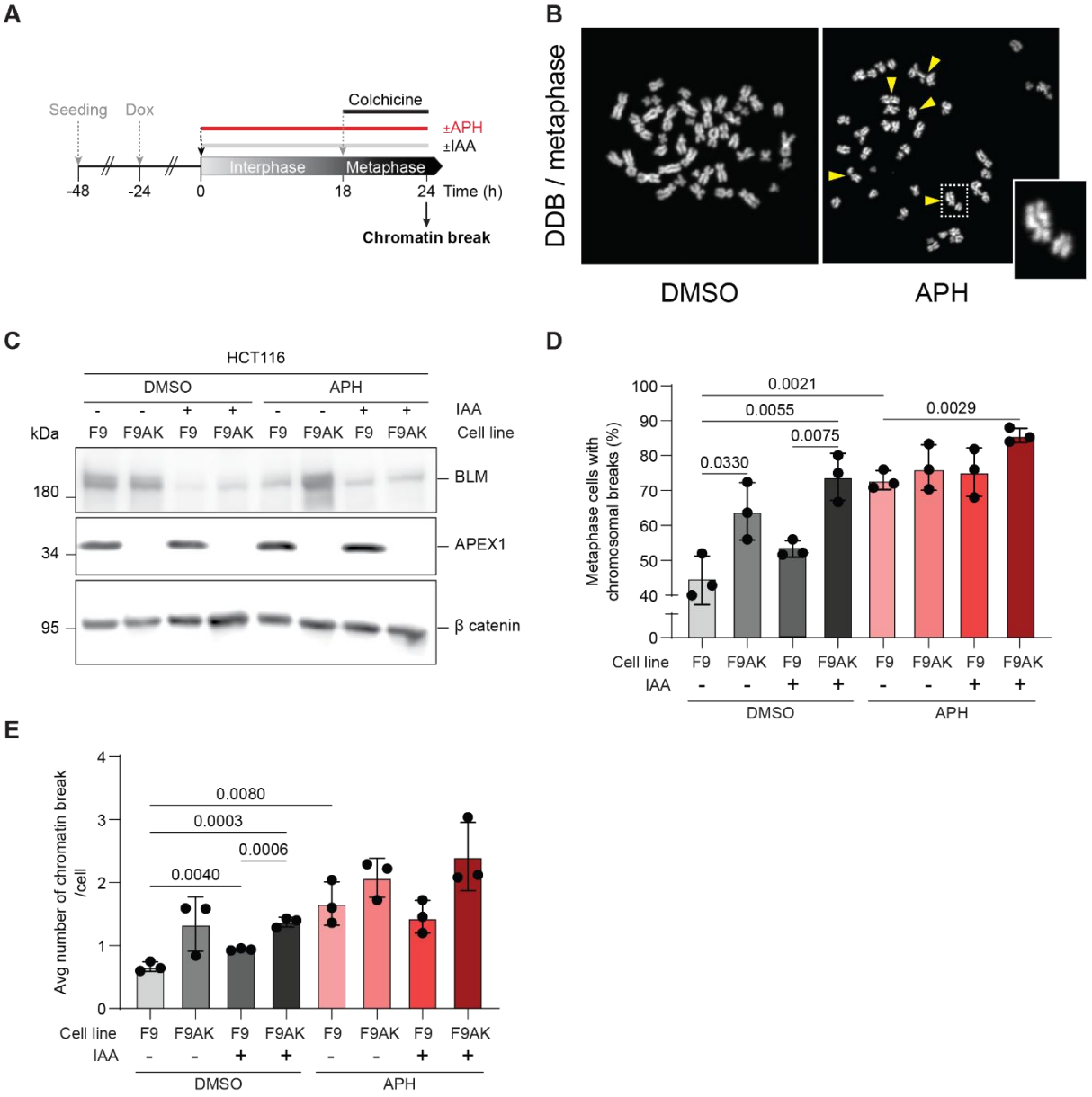


Figure 4.21 | Effects of APEX1 and BLM co-depletion on double-strand DNA breaks in metaphase.
(A) Schematic overview of experimental design. (B) Representative immunofluorescence image of a fixed metaphase cell. DNA was stained with DAPI; double-strand DNA breaks (DSBs) are indicated by yellow arrows. (C) Western blot confirming APEX1 knockout and BLM depletion. (D) Quantification of metaphase cells showing chromatin breaks after 6 h of colchicine treatment. (E) Average number of chromatins breaks per cell under the same treatment conditions. Student's t-test, mean ± SD is shown, based on three biological replicates in F9 and F9 APEX1 knockout (F9AK) metaphase cells with or without IAA and replication stress. A total of 25 metaphase cells were scored per replicate.

4.3.6 Effects of APEX1 and BLM co-depletion on long-term cell survival

To evaluate the long-term consequences of APEX1 and BLM loss on cell viability and proliferative capacity, we performed a colony formation assay. While our previous analyses focused on mitotic phenotypes such as UFBs, chromatin bridges, and lagging chromatids (each reflecting replication or segregation defects) the clonogenic survival assay provides a broader measure of genotoxic across multiple cell divisions. This approach allowed us to determine whether the accumulation of DNA damage and mitotic errors observed in APEX1- or BLM-deficient cells translates into reduced proliferative potential. To this end, F9 wild-type and APEX1 knockout (F9AK) cells were cultured for ten days with or without APH and IAA treatment, and on the tenth day, cells were fixed and stained with crystal violet (Figure 4.22A). To validate the efficiency of the depletion, Western blot was performed under identical treatment conditions. The results confirmed complete loss of APEX1 protein in knockout cells, and an efficient depletion of BLM following IAA treatment (Figure 4.22B).

Cell survival was quantified by counting the number of colonies formed in the presence or absence of mild replication stress, as illustrated in the representative images (Figure 4.22C), and normalized to the F9 wild-type (WT) DMSO-treated control. Under non–replication stress conditions, APEX1 knockout (F9AK) cells showed a reduction in survival by approximately 45 % compared to WT, indicating that APEX1 contributes to basal proliferative capacity (Figure 4.22D). Under no replication stress, BLM depletion alone had only little effect on survival, and its combination with APEX1 knockout did not cause any further reduction, suggesting no additive impact under normal conditions. Under mild replication stress induced by aphidicolin, overall survival decreased across all samples. Wild-type cells exhibited a 19 % decline compared to DMSO controls, while APEX1 knockout cells showed a pronounced drop of 68 %, demonstrating increased sensitivity to replication stress. BLM depletion led to a 50 % reduction in survival, and co-depletion of APEX1 and BLM did not further exacerbate this effect (Figure 4.22D). These findings indicate that APEX1 plays a key role in sustaining long-term cell viability, while BLM loss contributes to a lesser extent.

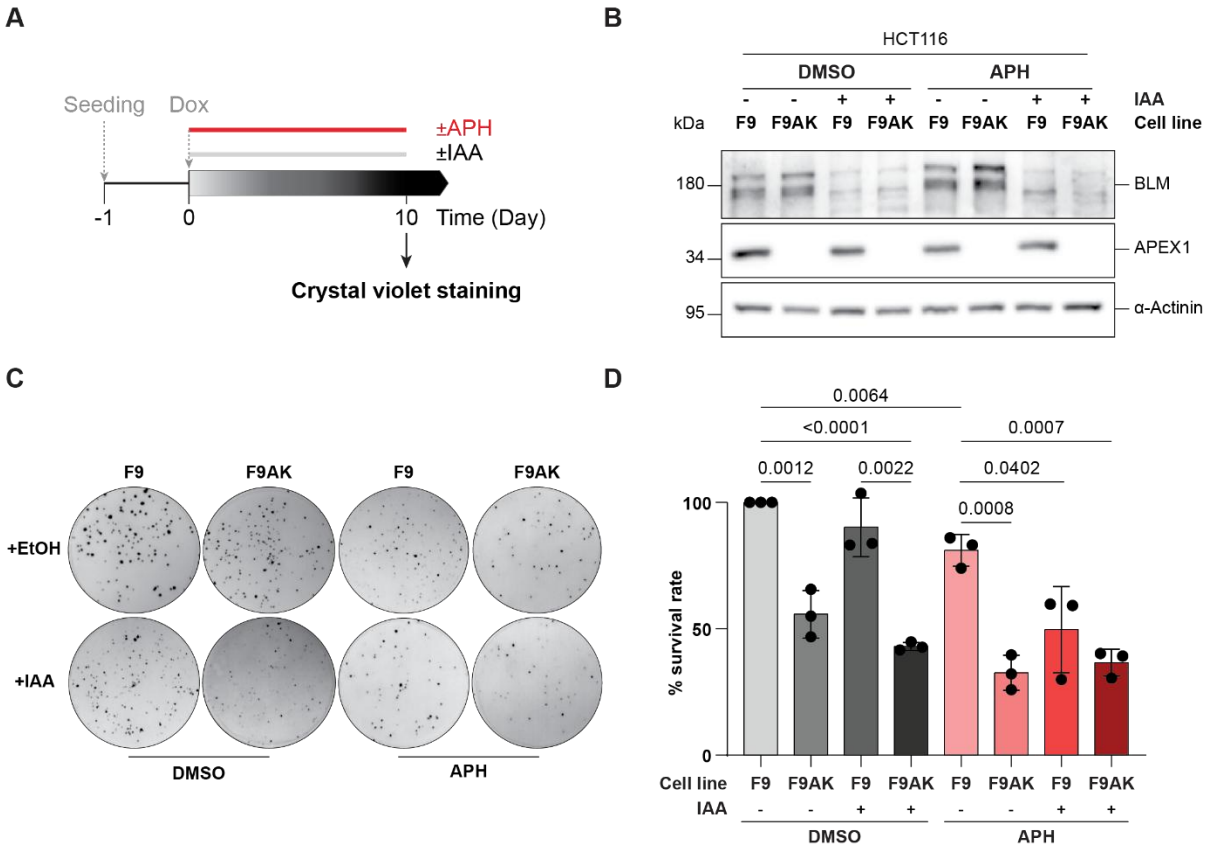


Figure 4.22 | Effects of APEX1 and BLM co-depletion on long-term cell survival.
(A) Experimental schematic. (B) Western blot confirming APEX1 knockout and BLM depletion. (C) Representative images from clonogenic survival assays showing colony formation after 10 days of treatment. (D) Quantification of the survival rate of cells normalized to wild-type (WT) DMSO-treated controls. Cells were treated with ± aphidicolin (APH) and ± auxin (IAA) for 10 days. Student's t-test; mean ± SD is shown. Each dot represents one biological replicate, calculated as the mean of at least two technical replicates (error bars represent SEM). Data represents three biological replicates performed in F9 and F9 APEX1 knockout (F9AK) cell lines with or without IAA and replication stress. Results from experiments were performed together with Amr Abdrbo.

4.3.7 APEX1 loss and BLM depletion show non-additive effects on genome instability

After collecting data from different mitotic and post-mitotic phenotypes, we compared the phenotypes by converting the values into Log2FC. For this analysis, each condition was normalized to the wild-type DMSO condition of the corresponding phenotype, which allowed direct comparison across different phenotypic readouts. The data were obtained from experiments performed by myself and by master's students under my supervision. The main aim of this analysis was to determine the consequences of APEX1 loss and to assess whether APEX1 functionally cooperated with BLM in maintaining mitotic genome stability.

Our dataset included two main treatment conditions: DMSO-treated control samples and APH-treated samples, which were used to induce mild replication stress. As shown in the Log2FC heatmaps (Figure 4.23 and Supplementary Figure 13), APEX1 loss in HCT116 cells, like BLM depletion, caused several

phenotypes associated with genome instability and reduced cell viability. These observations supported an important role for APEX1 in maintaining genome stability.

However, the combined APEX1 knockout and BLM depletion condition did not produce a statistically significant additive effect in any of the analysed phenotypes. To test for additive effects, we compared the double-deficient condition with APEX1 knockout alone and with BLM depletion alone. Across the different mitotic and post-mitotic phenotypes, the double-deficient condition did not show a significant increase compared with both single-deficient conditions.

Under DMSO conditions, the double-deficient cells showed significantly more binucleation and UFB formation than APEX1-knockout cells, but their phenotype was comparable to that of BLM-depleted cells. This indicating that BLM may play a more prominent role than APEX1 under unperturbed conditions (Supplementary Figure 13).

Under mild replication stress, APEX1 knockout significantly increased the number of UFBs, and chromatin bridges compared with APH-treated wild-type cells. In the subsequent G1 phase, APEX1 loss also caused a significant increase in binucleated cells, indicating that unresolved mitotic defects contributed to cytokinesis failure. In addition, one cell cycle later, the population of polyploid cells increased in the APEX1-knockout population (Figure 4.23). Together, these results suggested that APEX1 loss caused mitotic defects whose consequences persisted into the following cell cycle and contributed to increased polyploidy.

BLM depletion showed a similar trend for several phenotypes, although the increase was not always statistically significant. This may be explained by incomplete depletion of BLM (roughly 10 % remain[140]) in the experimental system. The combined APEX1 knockout and BLM depletion condition followed the same overall pattern, with increased UFBs, chromatin bridges, binucleation, and polyploidy. It worth mentioning, combined loss of APEX1 and BLM did not further worsen long-term cell viability compared with the single-deficient conditions.

We also wanted to understand the origin of the increased micronucleation observed after APEX1 loss. Therefore, we analysed lagging chromatin during anaphase and chromosome breaks in metaphase spreads. The heatmap showed that, under mild replication stress, micronuclei and chromosome breaks did not increase strongly enough in the double-deficient condition to produce a significant additive effect. This may be explained by the strong effect of APH itself on DNA double-strand break formation, which could mask additional effects caused by APEX1 loss or BLM depletion. Nevertheless, loss of either APEX1 or BLM increased micronucleation, indicating that both factors contributed to the prevention of genome instability.

Overall, these results suggested that APEX1 and BLM functionally cooperated in the same pathway for several mitotic phenotypes. At the same time, the analysis of chromosome breaks indicated that APEX1 and BLM may also contribute to genome stability through partially distinct mechanisms before mitotic entry. Long-term analysis using a colony formation assay further showed that APEX1 loss strongly reduced cell survival after 10 days under mild replication stress.

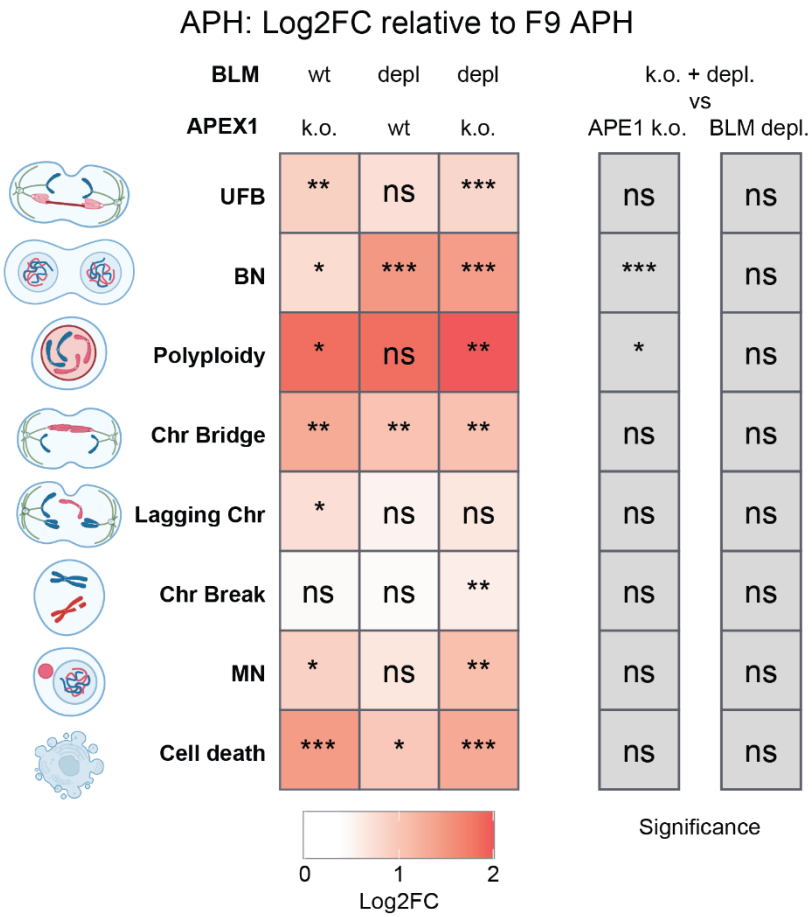


Figure 4.23 | APEX1 loss and BLM depletion show non-additive effects on genome instability.
Heatmap showing the log2 fold change (log2FC) of the different phenotypes in aphidicolin (APH)-treated cells following APEX1 knockout, BLM depletion using the auxin-inducible degron (AID) system, combined APEX1 knockout and BLM depletion. Color intensity represents log2FC relative to wild-type (WT) APH-treated cells, and asterisks indicate statistically significant differences determined by unpaired t-tests. For the main heatmap, log2FC values and statistical comparisons were calculated relative to the WT APH condition. The two columns on the right show additional significance comparisons between the combined APEX1 knockout/BLM-depletion condition and either APEX1 knockout or BLM depletion alone. Data represents three independent biological replicates. Experiments were performed in collaboration with the aim of Amr Abdrbo and Katarina Gauch.

4.3.8 APEX1 and BLM loss reveal two correlated routes to genome instability

After generating the Log2FC heatmap for the eight mitotic and post-mitotic phenotypes analysed in this study, we noticed that some phenotypes showed similar patterns across conditions. To examine these relationships more systematically, we performed Pearson correlation analysis using the Log2FC values across the different samples and treatment conditions. This analysis allowed us to determine which phenotypes showed the strongest associations with each other.

The correlation heatmap revealed a strong and significant positive correlation between UFB frequency and chromatin bridge frequency (r=0.92) (Figure 4.24). In addition, polyploidy correlated strongly with binucleation and reduced long-term cell viability, although these correlations did not reach statistical significance. Overall, UFBs, chromatin bridges, binucleation, and polyploidy showed strong correlations. This pattern supported the idea that under these conditions unresolved anaphase bridges can interfere with cytokinesis, leading to binucleated cells and, over time, an increase in polyploidy.

A second group of phenotypes, including lagging chromatin, chromosome breaks, and micronuclei, also showed strong correlations with each other, and these correlations were statistically significant (Lagging chr vs MN r=0.94 and Chr breck vs MN r=0.91). This supported the hypothesis that APEX1 loss and BLM depletion increased micronucleation mainly through DNA damage, appeared as chromosome breaks in metaphase spreads, and subsequently contributed to micronucleus formation in the following cell cycle.

Finally, we examined which phenotypes correlated most strongly with reduced long-term cell viability. Among all analysed phenotypes, chromatin bridges showed the strongest and only statistically significant correlation with reduced viability (r=0.81). Chromosome breaks showed the second strongest correlation (r≈0.75), followed by polyploidy (r=0.74), which was also strongly associated with chromatin bridge formation. These results suggested that, following APEX1 loss or BLM depletion, chromatin bridges and chromosome breaks were the phenotypes most closely associated with reduced long-term cell viability.

Together, the correlation analysis indicated two related but distinct phenotypic patterns. The first linked UFBs and chromatin bridges to cytokinesis failure, binucleation, polyploidy, and reduced long-term cell viability. The second linked chromosome breaks and lagging chromatin to micronucleus formation and reduced long-term cell viability.

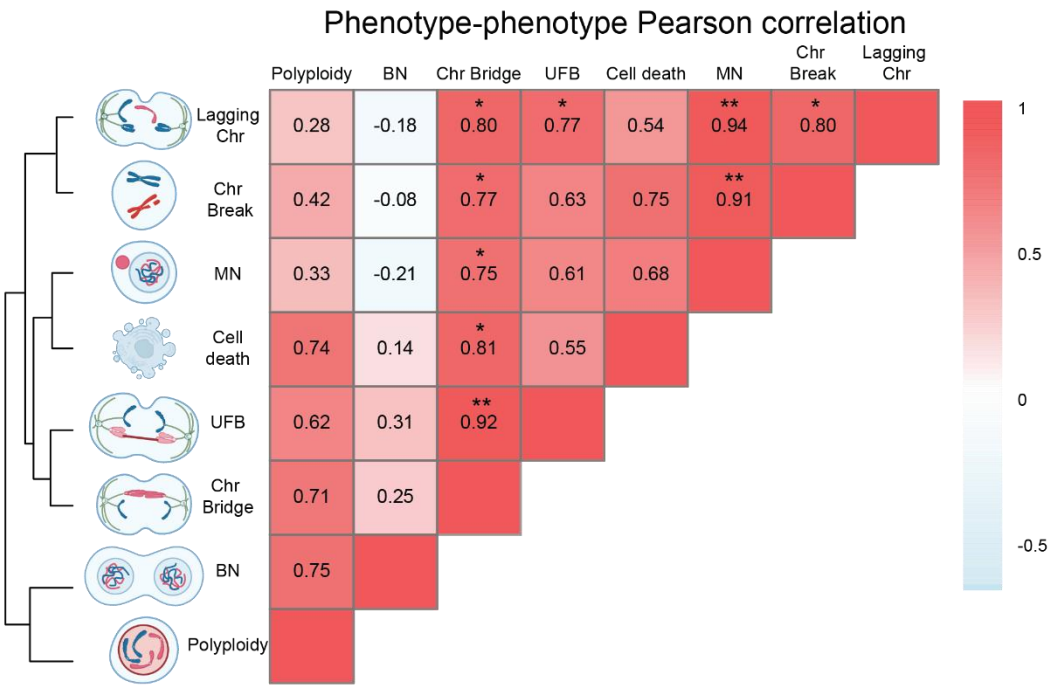


Figure 4.24 | APEX1 and BLM loss reveal two correlated routes to genome instability.
Pearson correlation heatmap showing the relationships among the eight genome instability phenotypes analyzed in wild-type, APEX1 knockout, BLM-depleted, and combined APEX1 knockout/BLM-depleted cells under DMSO and aphidicolin (APH) treatment conditions. Correlations were calculated using phenotype log2 fold-change (log2FC) values relative to the corresponding wild-type control. Color intensity represents the Pearson correlation coefficient (*r*), with red indicating positive correlations and blue indicating negative correlations. Correlation coefficients are displayed within each tile, and asterisks denote statistically significant correlations based on Pearson correlation tests. Hierarchical clustering was performed to group phenotypes with similar response patterns across the different genetic and treatment conditions. Correlation analysis was performed using data generated throughout this study, including experiments conducted in collaboration with Amr Abdrbo and Katharina Gauch.

4.3.9 APEX1 loss increases the persistence of wavy UFBs during mitosis

After characterizing the effects of APEX1 loss and BLM depletion on mitotic and post-mitotic phenotypes and their relationships with genome instability, we next examined how APEX1 loss affected UFB dynamics during mitosis. To follow UFB formation and resolution from early anaphase to late telophase, we performed live-cell imaging of HCT116 F9 wild-type cells and F9AK APEX1-knockout cells, both of which expressed BLM-eGFP and PICH-mCherry (Figure 4.25A).

As described in previous study[140], two distinct classes of PICH-positive UFBs were observed (Figure 4.25A). Straight UFBs appeared as linear PICH-positive structures and resolved within 10 min (Figure 4.25A, upper panel; Movie **1S**). In contrast, wavy UFBs transitioned from a straight to an undulating morphology and disintegrated into PICH-positive foci during late mitosis (Figure 4.25A, lower panel; Movie **2S**). We monitored UFB behaviour from G2 phase until the subsequent G1 phase over a period of 24 hours under DMSO and mild replication stress conditions (Figure 4.25B).

Consistent with the fixed-cell analysis (Figure 4.18D), APEX1-knockout cells did not show a significant increase in the proportion of anaphase cells with UFBs under DMSO conditions. Under mild replication stress, however, the proportion of UFB-positive anaphases increased from 26% in F9 cells to 36% in F9AK cells (Figure 4.25C). This increase resulted almost entirely from the wavy UFB fraction, which was more than threefold higher in APEX1-knockout cells than in wild-type cells (Figure 4.25D). In contrast, APEX1 loss did not significantly affect the frequency of straight UFBs (Figure 4.25E). it is worth mentioning that aphidicolin treatment itself caused a mild but significant 5% increase in straight UFBs.

Notably, wavy UFBs persisted into late anaphase and telophase, after straight UFBs had already resolved. However, the PICH signal gradually weakened during late mitosis and was no longer detectable after chromatin is fully decondense, when PICH dissociated from chromatin. Therefore, PICH-based live-cell imaging did not allow us to determine whether these structures were fully resolved after mitotic exit. Because previous studies suggested that persistent UFBs can interfere with cytokinesis[140], we tracked daughter cells into the subsequent G1 phase and classified cells as binucleated when the two daughter nuclei remained physically connected within a single cell. Interestingly, APEX1 loss significantly increased binucleation, and this phenotype was further enhanced by mild replication stress, reaching approximately 10% (Figure 4.26A). These findings supported that, in APEX1-deficient cells, delayed UFB resolution was associated with cytokinesis failure and a subsequent increase in binucleated cells in the next G1 phase.

We also examined additional mitotic abnormalities in cells progressing through mitosis. Under mild replication stress, APEX1 knockout increased the frequency of chromatin bridges, although this difference did not reach statistical significance compared with APH-treated wild-type cells (Figure 4.26B).

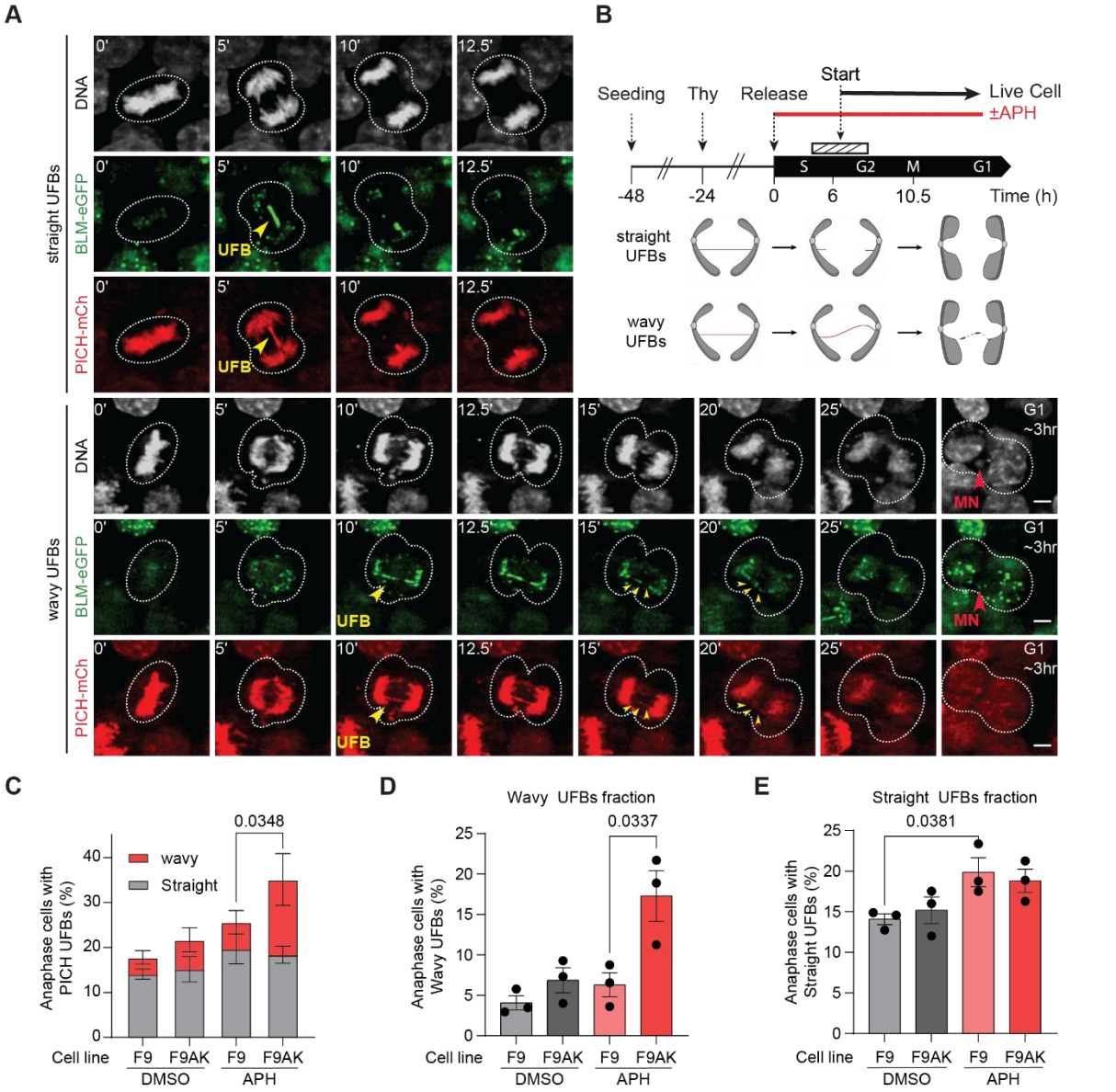


Figure 4.25 | Visualization of replication stress-induced UFBs in APEX1 knockout cells reveals persistent sister chromatid linkages.

(A) Representative still images of F9 control and APEX1 knockout (F9AK) cells. UFBs were visualized using PICH-mCherry and BLM-eGFP, and DNA was stained with SPY555. The schematic illustrates two possible mitotic outcomes: successful UFB resolution or persistent UFBs leading to segregation defects. Scale bar: 5 µm. (B) Schematic overview of the experimental workflow. F9 and F9AK cells were synchronized at the G1/S boundary with thymidine, released into fresh medium, and treated with either APH to induce mild replication stress or DMSO as a control. Live-cell imaging was initiated approximately 6 hours after release (hashed bar), when cells were entering mitosis. (C) Quantification of anaphase cells with PICH-positive UFBs detected by live-cell imaging. (D) Quantification of anaphase cells exhibiting wavy UFB morphology. (E) Quantification of binucleated cells. After anaphase, cells were followed over time using the DNA signal (SPY555). Cells that retained two separate DNA masses that stayed together were classified as binucleated. Data for panels (C–E) are shown as mean ± SD from three biological replicates (Student's t-test, n = 3), with 80–140 cells tracked per replicate. This experiment was performed by Kruno Kuscovi.

In contrast, lagging chromatin increased significantly in APEX1-deficient cells compared with APH-treated controls (Figure 4.26C). Both phenotypes showed the same general increase observed in the fixed-cell analysis (Figure 4.19).

We next quantified UFB resolution time. APEX1 loss prolonged UFB persistence by approximately 3 min on average, whereas aphidicolin treatment alone did not significantly alter UFB resolution time (Figure 4.26D). This indicated that mild replication stress increased the number of UFBs without substantially delaying their resolution in wild-type cells. In contrast, APEX1-deficient cells required longer to resolve these structures.

Together, the live-cell analysis showed that mild replication stress mainly increased the overall frequency of UFBs, while most structures were still resolved before mitotic exit in wild-type cells. APEX1 loss selectively increased the accumulation and persistence of wavy UFBs and prolonged their resolution time. These persistent structures were associated with increased binucleation, suggesting that delayed UFB resolution in APEX1-deficient cells contributed to cytokinesis failure and may promote subsequent polyploidy and genome instability.

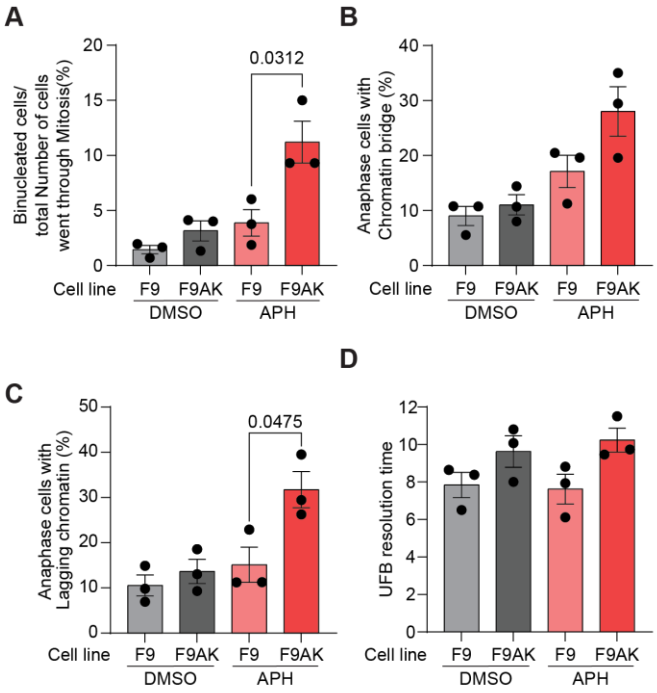


Figure 4.26 | Replication stress–induced mitotic aberrations in APEX1 knockout cells.
(A) Quantification of binucleated cells. After anaphase, cells were followed over time using the DNA signal (SPY555). Cells that retained two separate DNA masses that stayed together were classified as binucleated. (B) Quantification of chromatin bridges detected by SPY555 DNA staining. (C) Quantification of lagging chromatin detected by SPY555 DNA staining. (D) Quantification of UFB resolution time during mitosis. All data in panels (A–D) were obtained from the same experimental setup: F9 (control) and F9AK (APEX1 KO) cells synchronized with thymidine, released into fresh medium, and treated with APH (mild replication stress) or DMSO (control), as described in Figure 3.25. Data represent mean ± SD from three biological replicates (Student's t-test, n = 3), with 80–140 cells tracked per replicate.

4.4 Characterization of APEX1 function in UFB resolution

4.4.1 APEX1 rescue in the HCT116 F9AK cell line

To confirm that the increased UFB phenotype resulted specifically from APEX1 loss rather than off-target effects or clonal variation, and to determine whether APEX1 catalytic activity was required, we generated stable Tet-On rescue cell lines expressing randomly integrated wild-type or catalytically impaired APEX1 cDNA (Figure 4.27A). We transduced F9AK cells with lentiviral particles carrying the APEX1 constructs obtained from the David Pellman laboratory. After transduction, we treated the cells with or without doxycycline for 48 h to assess inducible expression. Western blot analysis confirmed APEX1 expression exclusively in doxycycline-treated cells, demonstrating tightly regulated induction of the wild-type construct (Figure 4.27B). However, neither mutant construct, including the catalytically inactive mutant (CI) and the catalytically inactive mutant with delayed DNA release (SO), was re-expressed in this initial experiment. Katharina Gauch, our master's student, subsequently repeated the procedure and successfully generated a stable F9AK cell line expressing the SO mutant, referred to as F9SO. For the wild-type construct, 6 of the 12 screened single-cell clones showed robust APEX1 expression. I selected clone 1 for all subsequent experiments and referred to it as F9R1 (Figure 4.27C).

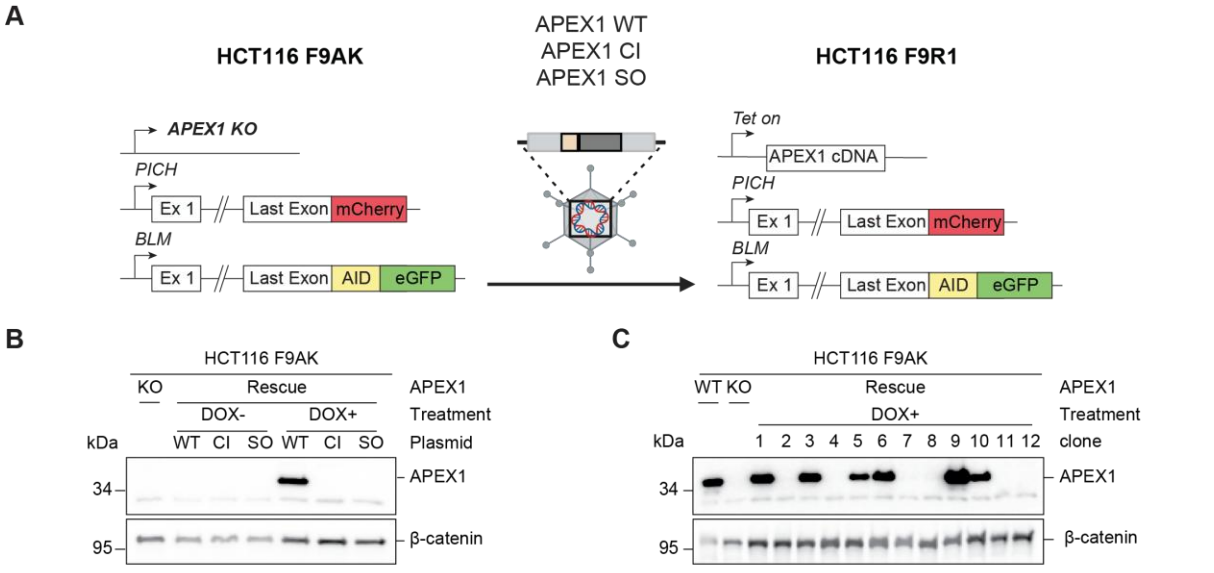


Figure 4.27 | APEX1 rescue in the HCT116 F9AK cell line.
(A) Schematic overview of the modified HCT116 F9AK cell line and the experimental strategy for reintroducing APEX1 (WT, CI, or SO variants) into the APEX1 knockout background via viral transduction using APEX1 cDNA. (B) Western blot analysis confirming re-expression of wild-type APEX1 in bulk cell populations following viral infection of HCT116 F9AK cells. APEX1 expression is controlled by a tetracycline-inducible (Tet-On) promoter and can be activated by doxycycline treatment. (C) Western blot validation of single-cell clones isolated from the bulk-infected population, confirming inducible APEX1 expression upon doxycycline addition in seven independent clones.

4.4.2 APEX1 re-expression suppresses UFB formation

To assess the effect of APEX1 rescue in APEX1-knockout cells, we used the F9R1 cell line expressing BLM-eGFP and PICH-mCherry and analyzed UFB formation under conditions with or without APEX1 re-expression. Doxycycline (Dox) treatment reactivated APEX1 expression, thereby allowing comparison between the APEX1-knockout (−Dox) and rescue (+Dox) states (Figure 4.28A). F9 wild-type cells were used as controls. Cells were synchronized in mitosis, and replication stress was induced using APH (Figure 4.28B). Western blot analysis showed that APEX1 expression in rescue cells (+Dox) remained substantially lower than the endogenous APEX1 levels observed in wild-type cells. However, no significant difference in APEX1 expression was detected in the F9 cell line in the presence or absence of replication stress (Figure 4.28C and D).

Anaphase cells were imaged by fluorescence microscopy, and mitotic aberrations were quantified based on the acquired images (Figure 4.28E). Quantitative analysis of anaphase cells containing PICH-positive UFBs revealed no significant difference between F9 wild-type and F9R1 cells under DMSO treatment, regardless of doxycycline (Dox) induction (28% versus 25%, respectively). This finding was consistent with earlier observations showing that APEX1 depletion did not significantly affect UFB frequency in the absence of replication stress. However, under replication stress, the proportion of anaphase cells containing UFBs increased markedly in APEX1-knockout (−Dox) cells, reaching 40%, compared with 28% in wild-type controls. Importantly, re-expression of APEX1 following Dox treatment for 34 hours reduced the UFB frequency to 26%, comparable to wild-type levels (Figure 4.28F). These results demonstrated that the elevated number of UFBs observed under mild replication stress was a direct consequence of APEX1 loss and that restoration of APEX1 expression effectively rescued this phenotype. Analysis of additional mitotic abnormalities in anaphase cells revealed that the frequency of lagging chromatin was significantly increased in APEX1-deficient F9R1 (−Dox) cells compared with wild-type controls (26% versus 9%), with no detectable rescue following APEX1 re-expression (+Dox; 25%). This lack of rescue suggested that lagging chromatin may have originated from irreversible DNA damage accumulated before APEX1 reintroduction. Under aphidicolin (APH) treatment, no significant difference in lagging chromatin frequency was observed between wild-type and F9R1 cells, indicating that replication stress did not further exacerbate this phenotype (Figure 4.28G). In contrast, quantification of chromatin bridges revealed no significant differences between wild-type and F9R1 cells under either DMSO or APH conditions. These findings suggested that APEX1 loss did not markedly affect chromatin bridge formation in the F9R1 cell line (Figure 4.28H).

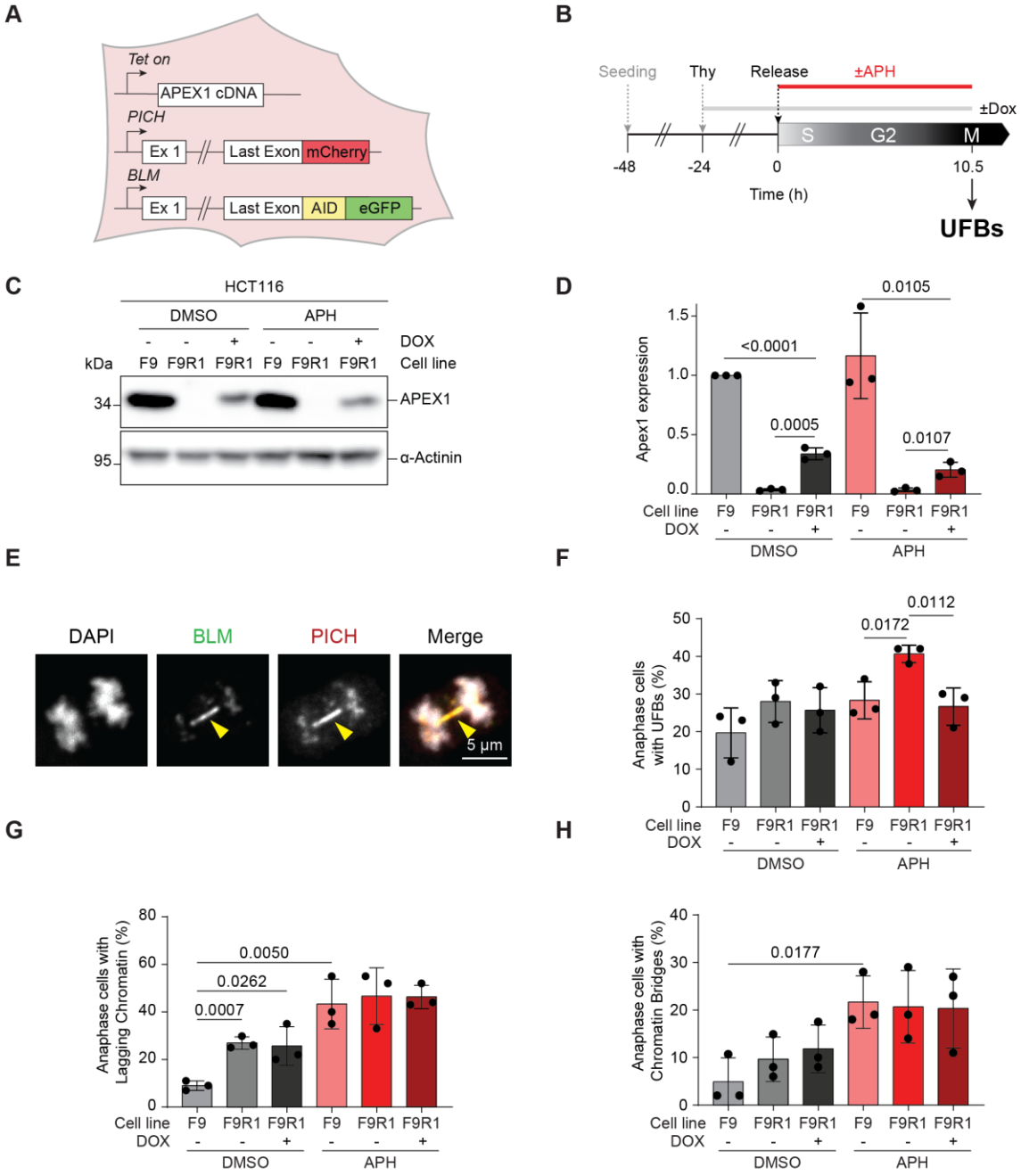


Figure 4.28 | APEX1 re-expression suppresses UFB formation.
(A) Schematic representation of the HCT116 F9R1 cell line expressing BLM–eGFP and PICH–mCherry with doxycycline (Dox)-inducible APEX1 expression under the Tet-On promoter. (B) Experimental workflow for Western blot and immunofluorescence analyses. (C) Western blot confirming APEX1 re-expression following Dox treatment. (D) Quantification of endogenous and exogenous APEX1 protein levels in the presence or absence of Dox under DMSO and aphidicolin (APH) treatment. (E) Representative fluorescence microscopy image of an anaphase cell showing BLM–eGFP, PICH–mCherry, and DAPI-stained DNA. (F) Quantification of PICH-positive UFBs in anaphase cells following 10.5 h of APH treatment. Dox was added together with thymidine to induce APEX1 expression. (G, H) Quantification of cells containing (G) lagging chromatin and (H) chromatin bridges in HCT116 F9, F9R1 cells. Data in (D) and (F–H) represent mean ± SD from three independent biological replicates and were analyzed using an unpaired Student's t-test. At least 25 anaphase cells were scored per replicate.

4.4.3 Time-dependent induction of APEX1 following doxycycline treatment

Our data showed that APEX1 depletion increased UFB formation under mild replication stress, whereas re-expression of wild-type APEX1 restored UFB levels to those observed in wild-type cells. Although complete APEX1 loss is embryonic lethal, previous studies reported only a modest 1.5- to 2-fold increase in abasic sites and relatively mild phenotypes in untreated cells lacking APEX1 endonuclease activity[173]. Because abasic sites can block replicative DNA polymerases[174], we sought to exclude the possibility that the increased UFB frequency in APEX1-knockout cells arose indirectly from under-replicated DNA generated by elevated abasic site levels during S phase. We therefore established a doxycycline treatment window that allowed APEX1 re-expression after DNA replication had largely been completed.

Using the F9R1 cell line, we synchronized cells at the G1/S boundary with thymidine for 24 h, released them into fresh medium, and added doxycycline at different time points after release (0, 2, 4, 6, 8, 9, and 10 h; Figure 4.29A). We fixed all samples 10.5 h after release and quantified APEX1 protein levels. Western blot analysis showed that doxycycline treatment initiated at the time of thymidine release restored APEX1 expression to approximately 50% of the level observed in samples treated with doxycycline 24 h before thymidine release (Figure 4.29C). When doxycycline was added 6 h after release, only a barely detectable amount of APEX1 was observed. Accordingly, no detectable APEX1 signal was present during the first 4.5 h after doxycycline addition, indicating a delay in protein induction (Figure 4.29B, C).

Flow cytometry analysis of synchronized HCT116 cells indicated that most cells progressed through S phase within approximately 4–5 h after thymidine release (Figure 4.29D). We therefore inferred that, even when doxycycline was added immediately after release, detectable APEX1 expression began only after most cells had completed S phase and entered G2/M. This timing allowed us to distinguish the effect of APEX1 during DNA replication from its later function in G2/M. Based on these findings, we designed subsequent experiments to compare early and late APEX1 re-expression and determine how the timing of APEX1 restoration affected UFB frequency during mitosis (Figure 4.29E).

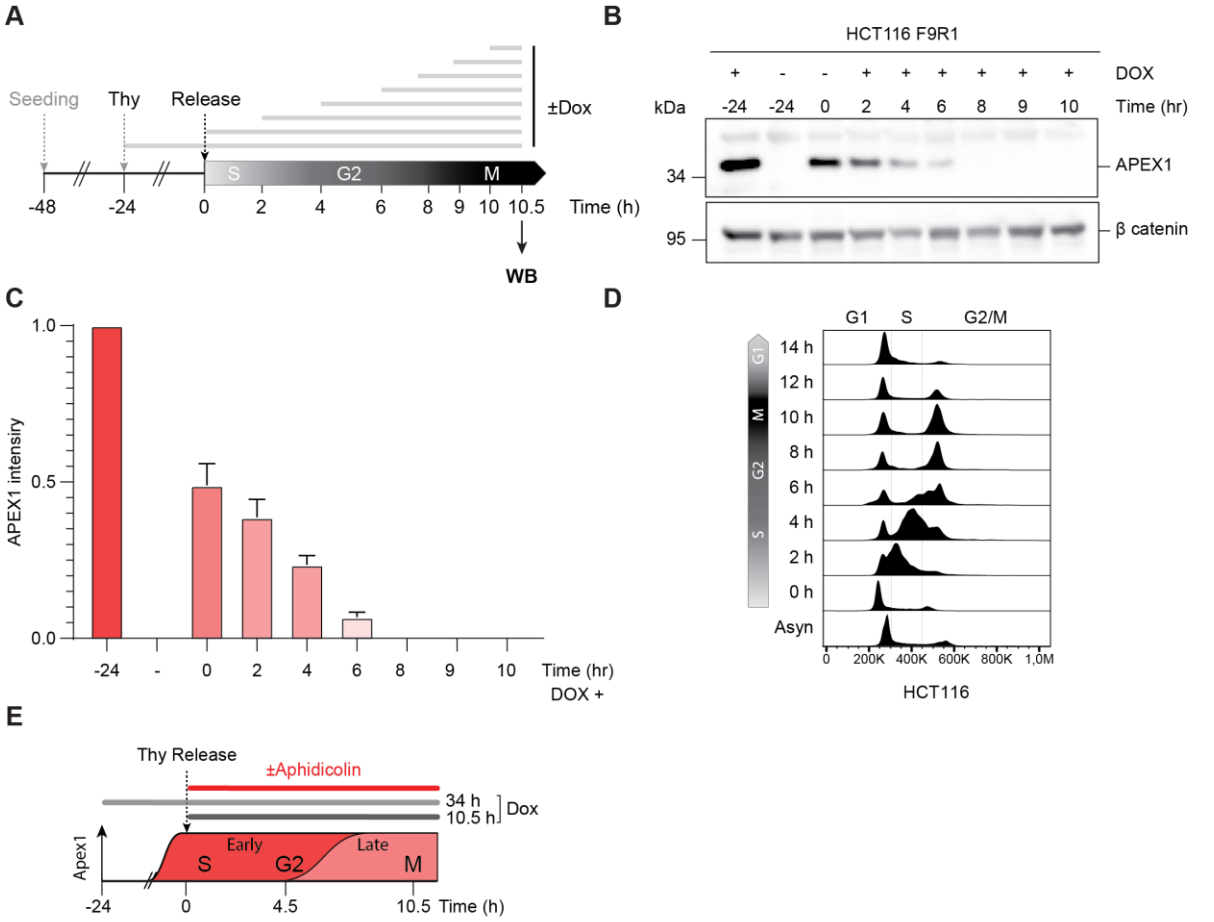


Figure 4.29 | Time-dependent induction of APEX1 following doxycycline treatment.
(A) Experimental schematic illustrating the timing of APEX1 re-expression at different stages of the cell cycle. (B) Western blot analysis showing APEX1 protein levels in cells progressing synchronously through the cell cycle. Cells were synchronized at the G1/S boundary using thymidine and treated with doxycycline (Dox) to induce APEX1 expression. (C) Quantification of APEX1 expression levels over time following Dox treatment. The x-axis indicates the duration of Dox treatment. (D) Flow cytometry analysis of propidium iodide (PI)-stained HCT116 cells synchronized at the G1/S boundary and released into S phase to monitor cell-cycle progression. A total of 10,000 events were recorded per sample (we used this figure from previous experiment). (E) Experimental design for assessing post-replicative APEX1 function based on cell synchronization and timing of Dox induction.

4.4.4 APEX1 re-expression after replication restores proper UFB resolution

To investigate the later functions of APEX1 in the cell cycle, particularly its role in DNA repair, genome stability during mitosis, and UFB formation and resolution, we examined the effects of APEX1 re-expression at later time points, as described above. F9R1 cells were synchronized at the G1/S boundary using thymidine. Two treatment conditions were established: (1) Early: a 34-hour Dox treatment, in which APEX1 was expressed continuously during the thymidine block and after release, representing early expression throughout the entire cell cycle; and (2) Late: a 10.5-hour Dox treatment, in which Dox was added only at the time of release from thymidine, thereby allowing APEX1 expression exclusively after S phase. Samples lacking Dox served as APEX1-knockout controls (Figure 4.30A). Western blot analysis confirmed that late APEX1 expression reached approximately half of the level observed under early expression conditions, whereas no APEX1 signal was detected in −Dox samples

(Figure 4.30B, D). To assess the impact of APEX1 on UFB formation, anaphase cells were analysed by fluorescence microscopy. FS-UFBs were distinguished from other UFBs based on FANCD2 localization at both ends of BLM- or PICH-positive bridges (Figure 4.30C).

Quantification of anaphase cells containing PICH-positive UFBs revealed that late APEX1 expression in APH-treated samples significantly reduced UFB frequency from approximately 42% in APEX1-knockout cells to 25%, comparable to the 26% observed following early expression (Figure 4.30E). These findings indicated that APEX1 activity during G2 and mitosis, even at approximately half the level observed under early expression conditions, was sufficient to restore normal UFB levels. When the data were combined to directly compare wild-type (WT) cells with cells expressing APEX1 only after replication, UFB frequency was restored to WT levels (Supplementary Figure 14), further supporting the conclusion that APEX1 activity during late G2 and mitosis is sufficient to suppress UFB formation.

Analysis of fragile-site–associated UFBs (FS-UFBs) further showed that under mild replication stress induced by APH, APEX1 knockout cells display a significant increase in FS-UFB frequency (≈40 %) compared to DMSO-treated controls (≈10 %, Figure 4.30F). While APH is known to elevate FS-UFB formation by stalling replication forks at common fragile sites during S-phase, APEX1 depletion exacerbated this effect, suggesting that APEX1 is required for efficient resolution of these structures. Re-expression of APEX1 after S phase reduced FS-UFB frequency to near–wild-type levels, highlighting a role for APEX1 in resolving fragile-site intermediates that persist into mitosis. Examination of the average number of anaphase cells with UFBs under mild replication stress revealed that the majority of UFBs correspond to FS-UFBs, and the increase in total UFBs observed under APH treatment is specifically due to FS-UFBs. APEX1 knockout had no significant effect on other types of UFBs (Figure 4.30G).

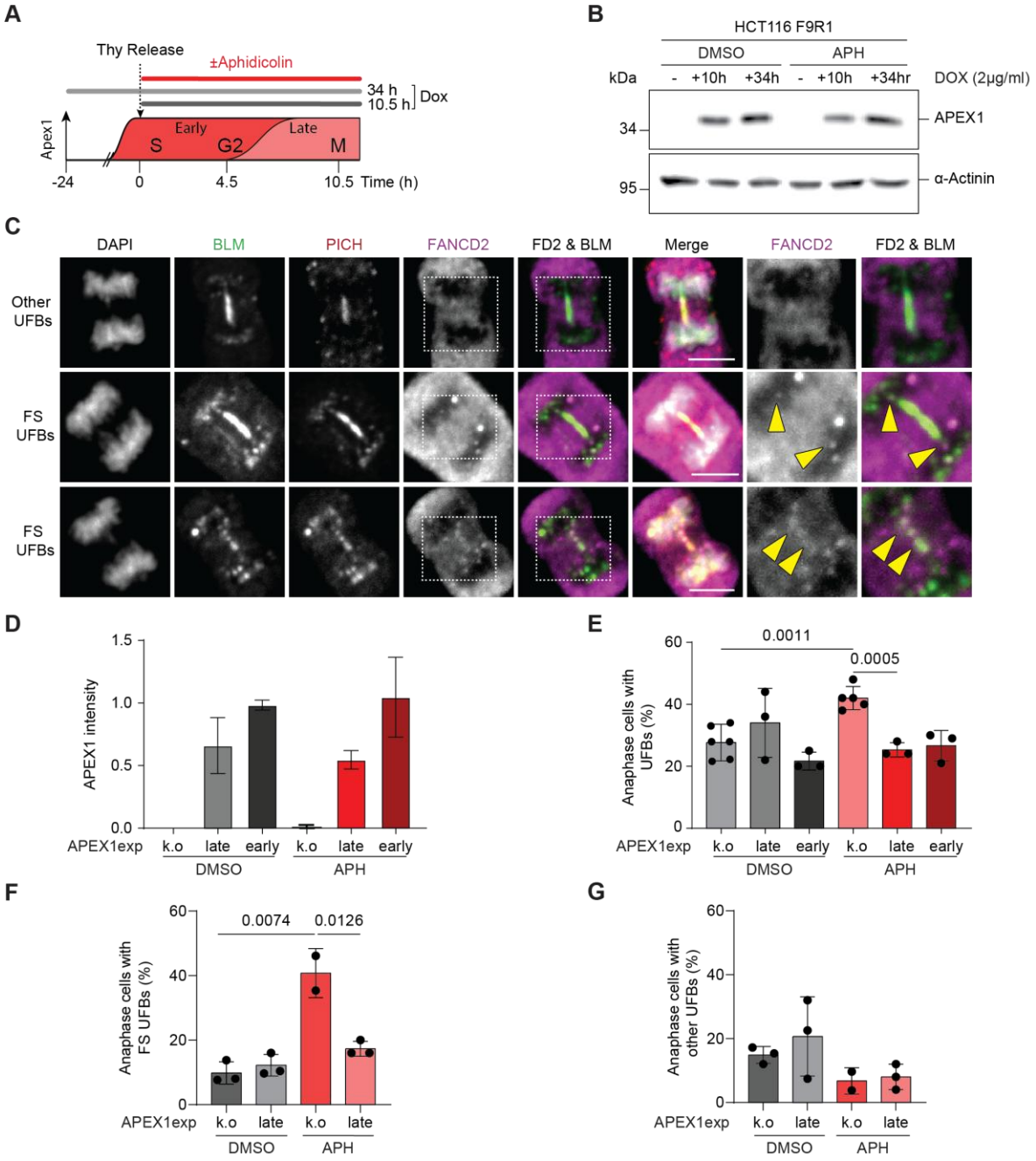


Figure 4.30 | APEX1 re-expression after replication restores proper UFB resolution.
(A) Experimental schematic illustrating the timing of APEX1 re-expression at different stages of the cell cycle. (B) Western blot analysis showing APEX1 protein levels in synchronized cells. Cells were arrested at the G1/S boundary using thymidine and treated with doxycycline (Dox) to induce APEX1 expression. (C) Representative fluorescence microscopy image of a fixed anaphase cell showing fragile site (FS) UFBs and other UFB types. BLM was visualized via GFP fluorescence (488 nm), PICH by mCherry (560 nm), FANCD2 by antibody staining (640 nm), and DNA by DAPI (402 nm). (D) Quantification of APEX1 expression levels for western blot after 0 h (no Dox), 10 h, and 34 h of Dox treatment. (E) Anaphase cells with PICH-positive UFBs following 10.5 h of aphidicolin treatment. (F) Fraction of anaphase cells with FANCD2-positive UFBs after 10.5 h of aphidicolin or DMSO treatment in APEX1 knockout (–Dox) and rescue (+Dox, 10 h) conditions. (G) Quantification of non–fragile site (other) UFBs under –Dox and +Dox (10 h) conditions in DMSO- or APH-treated samples. Data represent mean ± SD from three biological replicates (Student's t-test, n = 3), with at least 25 anaphase cells scored per replicate.

4.4.5 Catalytically active APEX1 is required for efficient resolution of fragile site ultrafine anaphase bridges (FS-UFBs)

To investigate whether the catalytic activity of APEX1 was required for UFB resolution, we examined the effect of re-expressing an APEX1 SO mutant in F9AK cells, which lack endogenous APEX1. The SO mutant contains the H309N point mutation, which allows APEX1 to recognize and bind AP sites but strongly impairs its catalytic activity. In addition, the construct carries the D238A and D308A point mutations, which delay the release of APEX1 from DNA[175]. This mutant provided a tool to test whether catalytic activity was required for APEX1 function during UFB resolution. Plasmids encoding wild-type APEX1 and the APEX1 SO mutant under the control of a doxycycline-inducible promoter were obtained as a kind gift from D. Pellman. Generating sustainable cell line was done as part of Katharina's master's thesis under my supervision. The doxycycline-inducible APEX1 SO construct was introduced into F9AK cells by lentiviral transduction. Doxycycline-inducible expression of the APEX1 SO mutant was successfully established, and this cell line was referred to as F9SO.

The experimental setup was identical to the original APEX1 rescue experiment (Figure 4.31A). F9R1 cells, which express wild-type APEX1 upon doxycycline treatment, and F9SO cells were seeded, synchronized with a single thymidine block, and released into fresh medium. Cells were treated with doxycycline throughout the thymidine block and after release, resulting in a total induction time of 34 h. A subset of F9SO cells was left untreated to serve as an APEX1-knockout control. Western blot analysis showed that doxycycline treatment successfully induced APEX1 expression in both F9R1 and F9SO cells, whereas untreated F9SO cells showed no detectable APEX1 signal (Figure 4.31B). Notably, APEX1 expression was considerably lower in F9R1 cells than in F9SO cells. We next analysed anaphase cells by fluorescence microscopy and quantified the frequency of UFB-positive anaphases. To further classify UFB subtypes, we performed FANCD2 staining, which allowed identification of fragile site-associated UFBs based on FANCD2 localization at the bridge ends (Figure 4.31C).

Under DMSO conditions, untreated F9SO cells, representing the APEX1-knockout state, showed UFBs in approximately 25% of anaphase cells. This level was similar to the UFB frequency previously observed in APEX1-knockout cells. Interestingly, doxycycline-induced expression of the APEX1 SO mutant further increased UFB frequency to approximately 35%, suggesting that expression of the catalytically impaired mutant may itself cause cellular stress even in the absence of replication stress. In contrast, doxycycline-treated F9R1 cells showed a UFB frequency comparable to the knockout control under DMSO conditions.

Under APH treatment, untreated F9SO cells showed a significant increase in UFB-positive anaphases compared with DMSO-treated knockout cells. Importantly, expression of the APEX1 SO mutant did not

reduce UFB frequency under replication stress, as approximately 40% of anaphase cells remained UFB-positive. In contrast, doxycycline-treated F9R1 cells again showed a marked reduction in UFB-positive anaphases to approximately 25% (Figure 4.31D). Together, these results suggested that wild-type APEX1, but not the catalytically impaired SO mutant, rescued the replication stress-induced UFB phenotype. This indicated that the catalytic activity of APEX1 was important for efficient UFB resolution.

Next, we distinguished between UFBs with FANCD2 foci at both ends and UFBs without FANCD2 signal on the bridge. This allowed us to analyse fragile site-associated UFBs (FS-UFBs) and other UFB types separately under the same experimental conditions. This analysis showed that the major changes observed in total UFB frequency were mainly driven by changes in FS-UFBs (Figure 4.31E). When FS-UFBs were analysed separately, untreated F9SO cells showed only low FS-UFB levels under DMSO conditions. Upon APH treatment, however, FS-UFB frequency increased significantly to approximately 25% in the knockout samples. Expression of the APEX1 SO mutant did not further increase FS-UFB frequency under APH treatment, but it also failed to reduce the elevated FS-UFB level. In contrast, and consistent with the previous rescue experiment (Figure 4.30F), re-expression of wild-type APEX1 reduced FS-UFB frequency (Figure 4.31F). In contrast, the frequency of other UFB types did not change significantly across the different samples, regardless of DMSO or APH treatment (Figure 4.31G). This suggested that the effect of APEX1 loss and rescue was specific to the FS-UFB fraction rather than affecting all UFB classes equally.

Together, these data supported two main conclusions. First, APEX1 catalytic activity was required for efficient UFB resolution. Second, the rescue effect of wild-type APEX1 mainly affected replication stress-induced FS-UFBs, indicating that APEX1 played a particularly important role in resolving fragile site-associated UFBs.

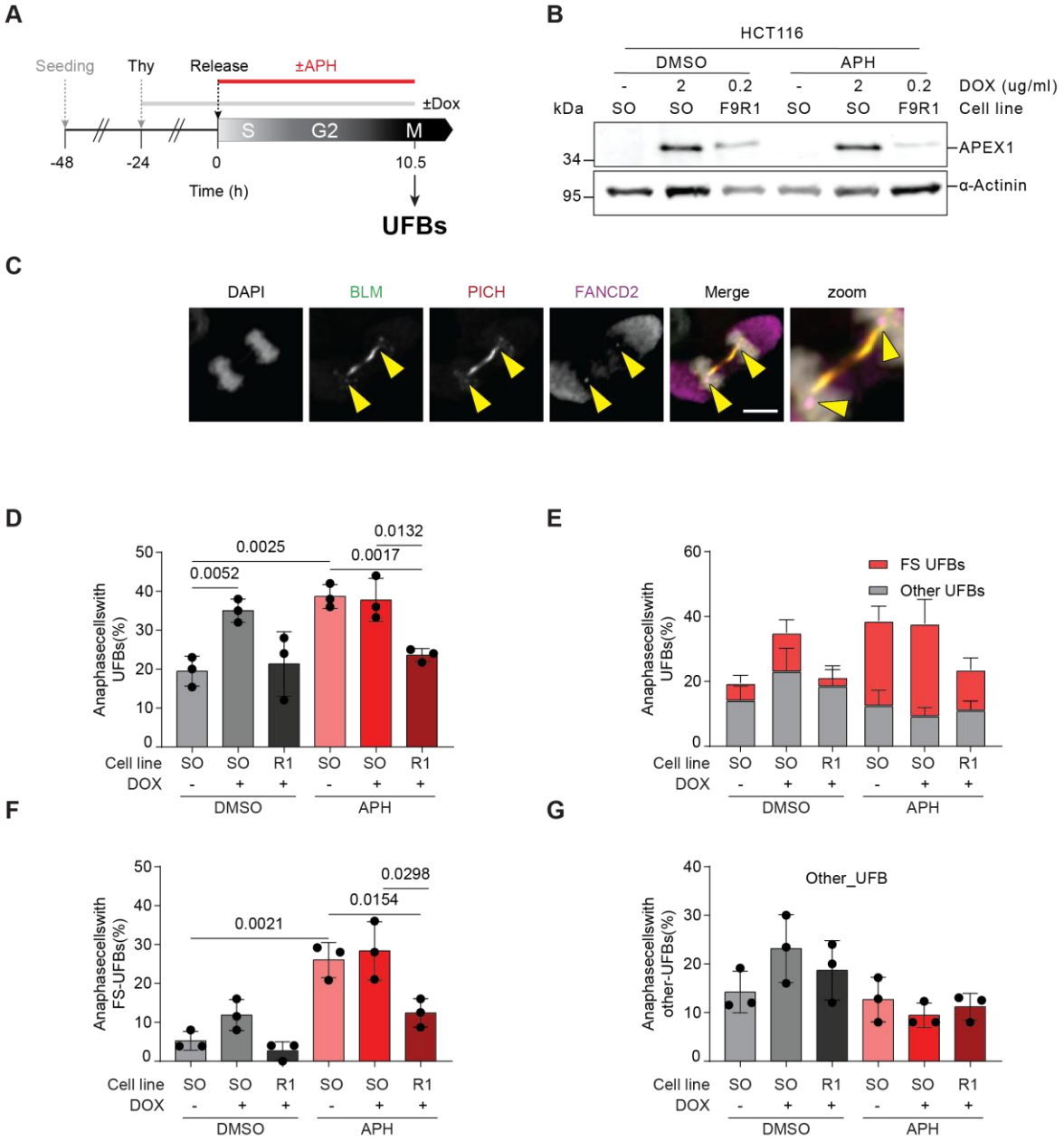


Figure 4.31 | Catalytically active APEX1 is required for efficient resolution of fragile site-derived ultrafine anaphase bridges (FS-UFBs).

(A) Schematic overview of the experimental workflow. (B) Western blot analysis of APEX1 expression in synchronized cells. Cells were arrested at the G1/S boundary using thymidine and treated with doxycycline (Dox) to induce expression of either wild-type APEX1 (R1) or the catalytically inactive mutant (SO). (C) Representative fluorescence microscopy image of a fixed anaphase cell showing fragile site-derived UFBs (FS-UFBs) and other UFB subtypes. BLM was visualized by GFP fluorescence (488 nm), PICH by mCherry fluorescence (560 nm), FANCD2 by immunofluorescence staining (640 nm), and DNA by DAPI (402 nm). (D) Average number of PICH-positive UFBs per anaphase cell following 10.5 h of aphidicolin treatment. Dox was added together with thymidine to induce APEX1 expression. Data represent mean ± SD from three biological replicates (Student's *t*-test, *n* = 3), with at least 25 anaphase cells analyzed per replicate. (E) Fraction of anaphase cells containing PICH-positive UFBs (other UFB subtypes) and FANCD2-positive UFBs (FS-UFBs). (F) Fraction of anaphase cells containing FANCD2-positive UFBs (FS-UFBs). (G) Fraction of anaphase cells containing PICH-positive UFBs (other UFB subtypes).

4.4.6 APEX1 is not required for the resolution of centromeric UFBs

So far, all experiments in this study were performed under mild replication stress induced by aphidicolin. Under these conditions, APEX1-knockout cells showed increased UFB formation compared with wild-type cells, indicating that APEX1 contributed to UFB resolution after replication stress. However, it remained unclear whether APEX1 function was specific to replication stress-induced UFBs or whether APEX1 also contributed to the resolution of other UFB classes.

To address this question, we designed an experiment that induced UFB formation independently of aphidicolin-induced replication stress. Cells were synchronized in prometaphase by treatment with nocodazole for 6 h and were then released into fresh medium for 1 h in the presence of ICRF-193, a TOP2A inhibitor (Figure 4.32A). TOP2A plays a key role in resolving DNA catenanes that remain between sister chromatids after DNA replication. Therefore, inhibition of TOP2A during mitotic release was expected to prevent proper decatenation and increase the formation of catenation-derived UFBs in early anaphase[90]. This experimental setup allowed us to test whether APEX1 also contributed to the resolution of UFBs that arise from unresolved DNA catenanes rather than from replication fork stalling or fragile site-associated replication intermediates. By comparing wild-type and APEX1-knockout cells under these conditions, we aimed to determine whether APEX1 had a broader role in UFB resolution or whether its function was mainly restricted to replication stress-induced UFBs.

Western blot analysis showed that doxycycline treatment successfully induced APEX1 expression in F9R1 cells, and it is worth mentioning that untreated F9 cells showed higher endogenous APEX1 levels compared with the rescue condition (Figure 4.32B). We next analysed anaphase cells by fluorescence microscopy and quantified the frequency of UFB-positive anaphases. To further classify UFB subtypes, we performed CENPB staining, which allowed identification of centromere-associated UFBs based on CENPB localization at the bridge ends (Figure 4.32C). Microscopy analysis showed that ICRF-193 treatment strongly affected anaphase cells, as individual mitotic cells displayed an increased number of UFBs after TOP2A inhibition. We focused on centromere-associated UFBs because most c-UFBs originate from unresolved DNA catenanes between sister chromatids, which require TOP2A-dependent decatenation for proper chromosome segregation[113].

Quantification of UFB-positive anaphase cells showed that, under DMSO conditions, approximately 20% of anaphase cells contained UFBs, consistent with our previous observations. Neither APEX1 knockout nor re-expression of wild-type APEX1 in APEX1-knockout cells significantly changed this frequency. Upon ICRF-193 treatment, the proportion of UFB-positive anaphase cells increased significantly to approximately 40% in wild-type cells. However, this increase was not further altered by

APEX1 knockout or by re-expression of wild-type APEX1 (Figure 4.32D). These results suggested that APEX1 did not affect the formation or resolution of catenation-origin UFBs in general.

We next analysed the relative contribution of centromere-associated UFBs and other UFB types. Two main observations emerged from this analysis. First, the majority of UFBs induced by ICRF-193 were centromere-associated UFBs, consistent with previous studies showing that TOP2A inhibition mainly promotes c-UFB formation. Second, APEX1 loss did not significantly affect the number of c-UFBs. Similarly, re-expression of wild-type APEX1 did not reduce c-UFB frequency. In contrast, the fraction of other UFB types remained comparatively low and did not show major changes across the different conditions (Figure 4.32E, F and G).

Together, these results indicated that ICRF-193 treatment mainly increased centromere-associated UFBs, most likely due to impaired TOP2A-dependent decatenation. In contrast to replication stress-induced FS-UFBs, APEX1 did not appear to play a major role in the resolution of catenation-derived UFBs.

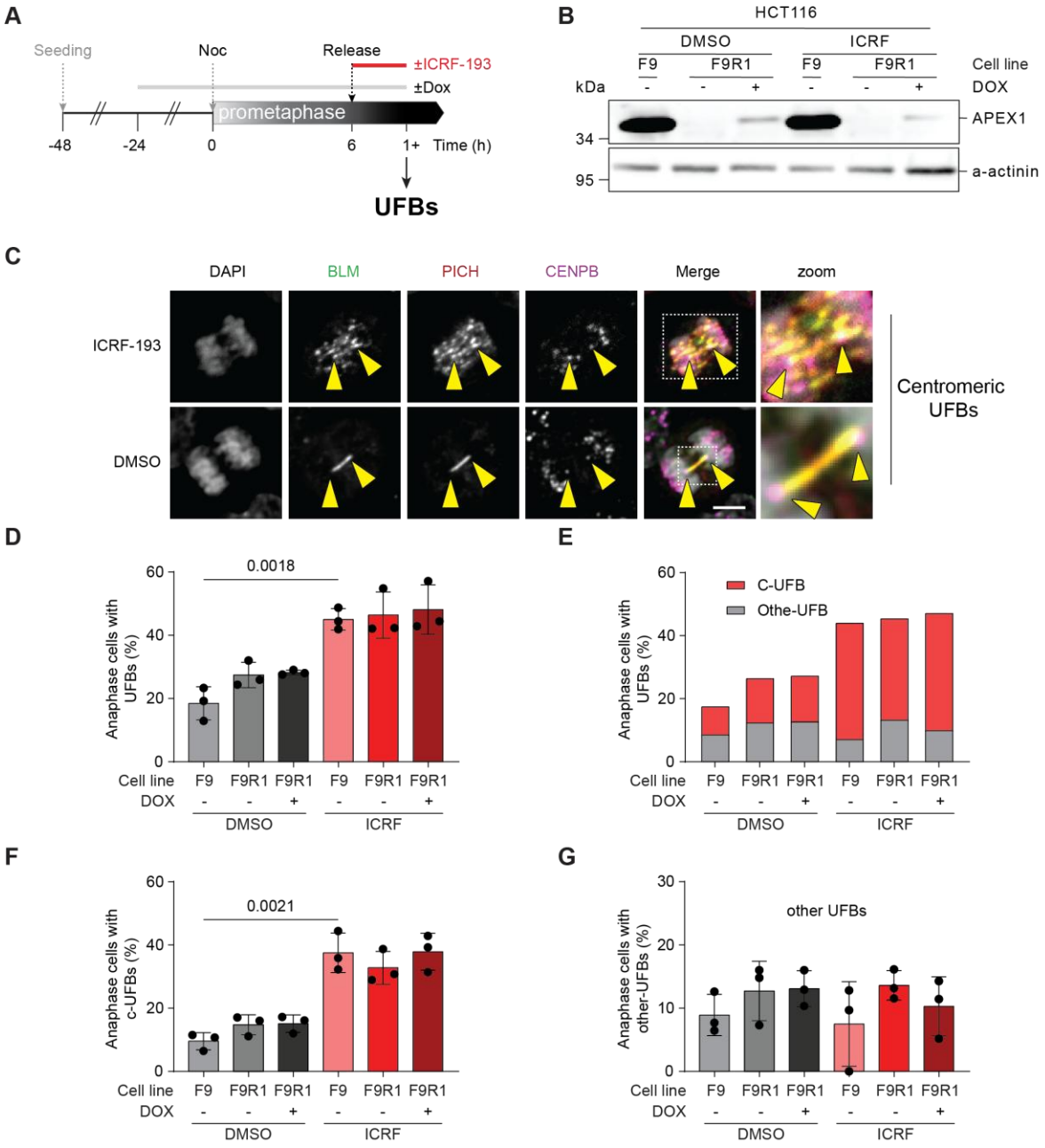


Figure 4.32 | APEX1 is not required for the resolution of centromeric UFBs.
(A) Experimental scheme. Cells were synchronized in prometaphase using nocodazole and subsequently released into fresh medium. Doxycycline (Dox) was added to induce APEX1 expression. (B) Western blot analysis confirming APEX1 expression in synchronized cells. Following nocodazole arrest, cells were released and treated with the topoisomerase II inhibitor ICRF-193 for 1 h to induce centromeric -UFBs. (C) Representative fluorescence microscopy image of a fixed anaphase cell containing centromeric and non-centromeric UFBs. BLM was visualized by eGFP fluorescence (488 nm), PICH by mCherry fluorescence (560 nm), CENP-B by immunofluorescence staining (640 nm), and DNA was counterstained with DAPI (402 nm). (D) Fraction of anaphase cells containing PICH-positive UFBs following DMSO or ICRF-193 treatment in APEX1 knockout (−Dox) and rescue (+Dox) conditions. Data represent mean ± SD from three biological replicates (Student's *t*-test, *n* = 3), with at least 25 anaphase cells analyzed per replicate. (E) Distribution of CENP-B-positive (centromeric) and CENP-B-negative UFBs in anaphase cells under the indicated conditions. (F) Fraction of anaphase cells containing CENP-B-positive UFBs following DMSO or ICRF-193 treatment in APEX1 knockout (−Dox) and rescue (+Dox) conditions. (G) Fraction of anaphase cells containing CENP-B-negative UFBs (other UFB subtypes) under the same conditions shown in (F).

4.4.7 Lagging chromatin after APEX1 loss primarily reflects acentric DNA fragments

In parallel with the analysis of centromeric UFBs and the effect of TOP2A inhibition on mitotic cells, we also evaluated lagging chromatin in anaphase and telophase cells. In previous experiments, we observed that APEX1 loss increased Chromosome breaks in metaphase under DMSO conditions (Figure 4.21D), suggesting that APEX1-deficient cells accumulated DNA repair defects during S/G2 phase. These DSBs likely persisted into mitosis as chromosome breaks in metaphase and subsequently appeared as lagging chromatin during anaphase.

In the present experiment, we used lagging chromatin analysis to address two questions. First, we asked whether mitotic stress induced by TOP2A inhibition affected lagging chromatin in a manner similar to replication stress. Second, we tested whether the lagging chromatin observed after APEX1 loss mainly reflected chromosome mis-segregation or broken chromatin fragments. CENPB staining allowed us to distinguish CENPB-positive lagging chromatin, which may reflect whole-chromosome mis-segregation, from CENPB-negative lagging chromatin, which more likely represents acentric chromatin fragments generated by DNA breaks (Figure 4.33A).

Under DMSO conditions, APEX1-knockout cells showed a significant increase in lagging chromatin compared with wild-type cells, consistent with our previous observations. Re-expression of wild-type APEX1 did not rescue this phenotype (Figure 4.33B). This may reflect the accumulation of DNA damage during the prolonged period of APEX1 loss before re-expression. Therefore, rescue of lagging chromatin may require APEX1 expression for more than one cell cycle to prevent damage accumulation before mitotic entry.

Under ICRF-193 treatment, wild-type cells did not show an increase in lagging chromatin compared with DMSO-treated controls. Similarly, APEX1 loss did not further alter the frequency of lagging chromatin under TOP2A inhibition (Figure 4.33B). This was consistent with the idea that ICRF-193 primarily induced mitotic decatenation defects rather than replication DNA damage. Therefore, TOP2A inhibition was expected to increase centromere UFBs, but not necessarily general lagging chromatin. Another possible explanation is that ICRF-193 reduced the number of cells reaching late anaphase or telophase, thereby limiting the detection of APEX1-dependent lagging chromatin phenotypes.

We next quantified the CENPB-positive fraction of lagging chromatin and found that only a small proportion of these events were CENPB-positive (Figure 4.33C), whereas most lagging chromatin was CENPB-negative (Figure 4.33D). These findings suggested that APEX1 loss primarily increased lagging

chromatin through DNA damage mechanisms rather than through increased whole-chromosome mis-segregation.

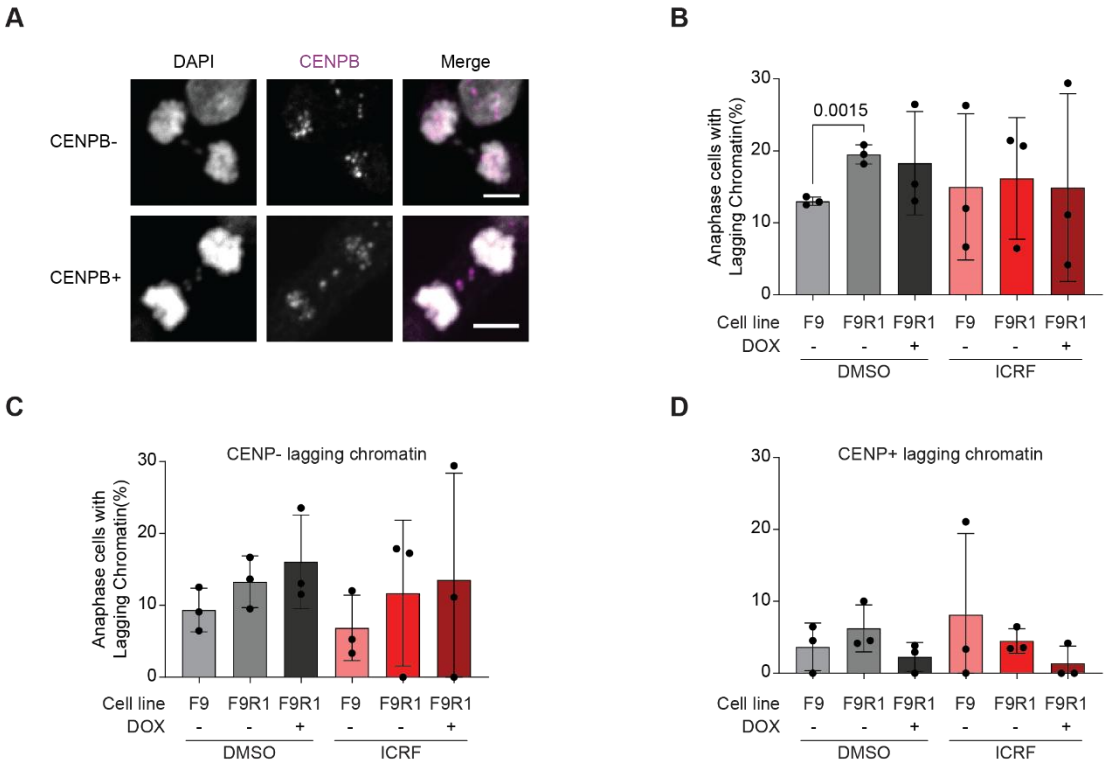


Figure 4.33 | APEX1 loss increases lagging chromatin under unperturbed conditions independently of chromosome mis-segregation.
(A) Representative fluorescence microscopy image of a fixed anaphase cell containing lagging chromatin. CENP-B was detected by immunofluorescence staining (640 nm), and DNA was counterstained with DAPI (402 nm). (B) Fraction of anaphase cells containing lagging chromatin following DMSO or ICRF-193 treatment in APEX1 knockout (−Dox) and rescue (+Dox) conditions. Doxycycline (Dox) was added 24 h before nocodazole treatment to induce APEX1 expression. Data represent mean ± SD from three biological replicates (Student's t-test, n = 3), with at least 25 anaphase cells analyzed per replicate. (C) Fraction of anaphase cells containing CENP-B-positive lagging chromatin under the indicated conditions. (D) Fraction of anaphase cells containing CENP-B-negative lagging chromatin under the same conditions shown in (C).

4.4.8 APEX1 is required for efficient resolution of fragile site- ultra fine bridges (FS-UFBs)

To summarize the role of APEX1 in UFB resolution, we integrated the results from several experiments assessing UFB formation in anaphase cells. As shown in Figure 4.34A, we compared cells under unperturbed replication conditions (DMSO) and mild replication stress (APH). This comparison allowed us to evaluate how APEX1 loss, re-expression of wild-type APEX1, and expression of the catalytically inactive APEX1 SO mutant affected UFB formation during anaphase.

F9SO and F9R1 cells without doxycycline treatment represented the APEX1-knockout state. In both cell lines, under DMSO conditions, APEX1 loss did not significantly increase the number of UFB-positive anaphase cells compared with F9 wild-type cells. In addition, re-expression of wild-type APEX1 in F9R1 cells did not alter UFB frequency under DMSO conditions. However, doxycycline-induced expression of the APEX1 SO mutant in F9SO cells significantly increased UFB frequency compared with F9 wild-

type cells. This suggested that expression of the catalytically impaired SO mutant may be more toxic to cells than APEX1 loss alone, even in the absence of exogenous replication stress (Figure 4.34A).

In contrast, APH treatment strongly increased UFB frequency in APEX1-knockout cells compared with F9 wild-type cells, reaching approximately 40% of anaphase cells. Re-expression of wild-type APEX1 in F9R1 cells reduced UFB frequency back to the level observed in F9 wild-type cells. However, expression of the APEX1 SO mutant in F9SO cells failed to reduce the number of UFB-positive anaphases. Together, these observations suggested that replication stress-induced UFBs required APEX1 for proper resolution and that the catalytic activity of APEX1 was important for this function (Figure 4.34A).

We next focused specifically on fragile site-associated UFBs under knockout and rescue conditions. This analysis revealed a clear pattern. Under replication stress, the frequency of FS-UFBs increased strongly in APEX1-knockout cells, reaching approximately 30–40%. Re-expression of wild-type APEX1 reduced FS-UFB frequency to approximately 10%, whereas expression of the APEX1 SO mutant failed to rescue this phenotype (Figure 4.34B). This provided the strongest evidence that catalytically active APEX1 was specifically required for the resolution of replication stress-induced FS-UFBs.

One remaining question was whether APEX1 acted before mitosis by repairing replication intermediates or reducing the accumulation of stalled replication forks under mild replication stress. If this were the case, APEX1 loss might increase the number of replication intermediates before anaphase, which could later give rise to FS-UFBs. To address this possibility, I quantified FANCD2 foci in prometaphase and metaphase cells under the same experimental conditions (Figure 4.34C). FANCD2 was used as a marker because it accumulates at under-replicated or unresolved DNA regions that persist into mitosis, particularly at common fragile sites[156].

Our results showed no clear difference in the number of FANCD2 foci between APEX1-knockout cells and cells re-expressing wild-type APEX1. In addition, expression of the APEX1 SO mutant did not increase FANCD2 foci (Figure 4.34D). These results indicated that APEX1 status did not strongly affect the number of FANCD2-marked replication intermediates before anaphase under these conditions. Together with the FS-UFB analysis, these findings suggested that wild-type APEX1 reduced FS-UFBs in anaphase without decreasing FANCD2 foci in prometaphase or metaphase. Thus, APEX1 did not appear to induce the formation of FANCD2-marked replication intermediates before mitosis but instead acted later to promote the resolution of replication stress-induced FS-UFBs. The failure of the SO mutant to rescue this phenotype further indicated that APEX1 catalytic activity was required for efficient FS-UFB resolution during mitosis.

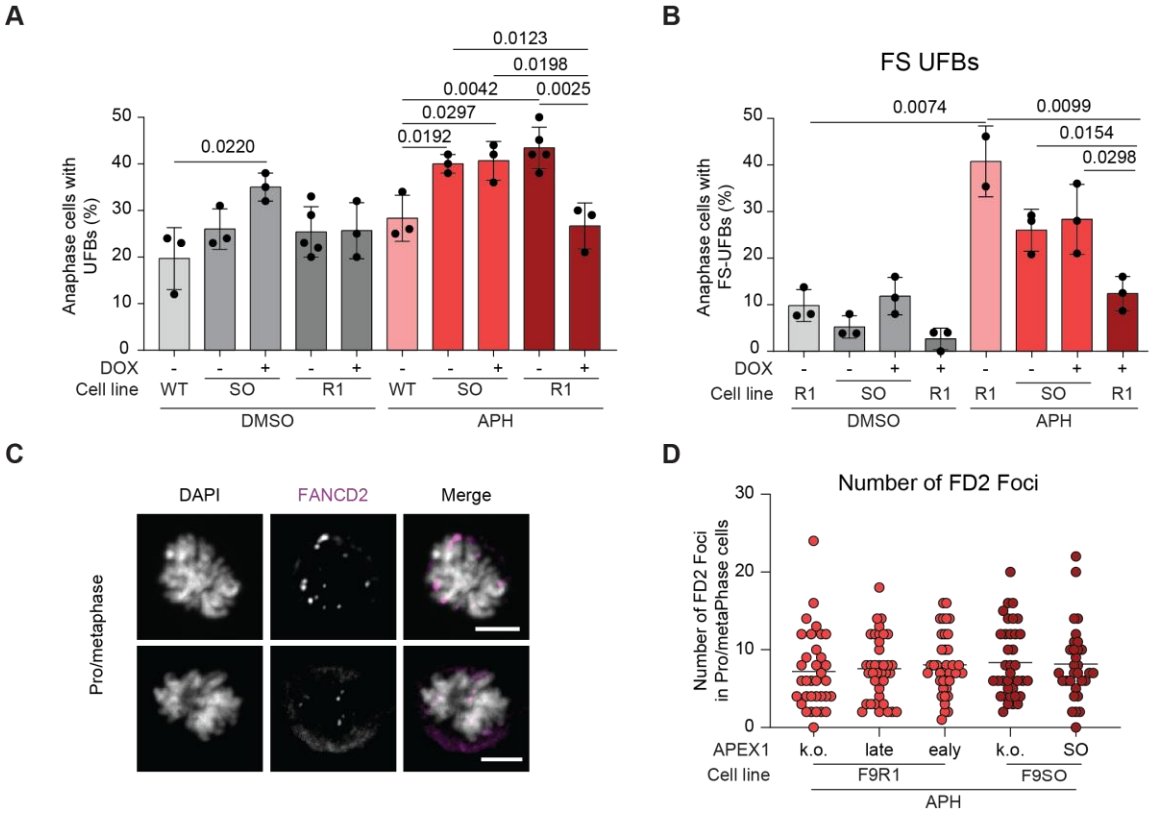


Figure 4.34 | APEX1 is required for efficient resolution of fragile site-derived ultrafine anaphase bridges (FS-UFBs).
(A) Fraction of anaphase cells containing PICH-positive UFBs following 10.5 h of aphidicolin (APH) or DMSO treatment. Doxycycline (Dox) was added together with thymidine to induce expression of either wild-type (WT) APEX1 or the catalytically inactive S0 mutant. (B) Fraction of anaphase cells containing FANCD2-positive UFBs (FS-UFBs) after 10.5 h of APH or DMSO treatment in APEX1 knockout (−Dox) and rescue (+Dox) conditions expressing either WT or S0 mutant APEX1. Data represent mean ± SD from three biological replicates (Student's t-test, n = 3). (C) Representative images of prometaphase/metaphase and anaphase cells used for FANCD2 foci analysis. DNA was visualized by DAPI staining, and FANCD2 foci were detected by immunofluorescence. (D) Quantification of FANCD2 foci per prometaphase/metaphase cell. Three independent biological replicates were analyzed, with 11–15 prometaphase/metaphase cells scored per replicate.

5 Discussion

5.1 Meta-analysis of mitotic chromatin interaction partners of UFB marker proteins

Ultrafine bridges (UFBs) are short-lived structures that are resolved within minutes to facilitate chromosome segregation. They are relatively rare and difficult to visualize, which makes them challenging to study. Their resolution depends on the coordinated action of several mitotic DNA-processing factors, including PICH, BLM, TOP3A–RMI1/2, FANCD2–FANCI, and RPA. Despite growing interest in UFB resolution, the protein interaction networks that act on DNA structures persisting into mitosis remain incompletely defined. Similarly, the mechanisms by which different UFB classes are resolved are still not fully understood[57].

To address these questions, we performed ChIP-MS to identify chromatin-bound proteins enriched in mitotic cells after replication stress and to determine whether these proteins may contribute to UFB processing. An important feature of this approach was the use of low dose aphidicolin, which induces mild replication stress while allowing cells to enter mitosis[148]. We hypothesized that this condition may better reflect endogenous replication stress, where incompletely replicated DNA regions can persist into mitosis and require processing during chromosome segregation[176,177]. However, because the mitotic population was not limited to anaphase cells, some detected associations may also reflect chromatin-bound complexes from other mitotic stages. This may also explain why some well-established UFB-associated interactions were not robustly detected in our dataset. For example, PICH and BLM have been reported to interact during mitosis. In addition, specific PICH domains required for BLM recruitment to UFBs have been identified previously[94]. Therefore, the weak recovery of the PICH–BLM interaction in our ChIP–MS analysis does not necessarily exclude a functional connection between these proteins during UFB resolution. Instead, this interaction may be transient, stage-specific, or sensitive to chromatin extraction and immunoprecipitation conditions.

Previous proteomic studies have provided important insight into replication stress and mitotic DNA repair, but they focused on different aspects of these pathways. Pladevall-Morera et al. used FANCD2 ChIP–MS to identify proteins associated with FANCD2-marked common fragile sites after mild replication stress[146]. Martin et al. analyzed TOPBP1 interaction networks across the cell cycle but did not specifically enrich chromatin-bound complexes[150]. More recently, proximity labelling was used to map proteins near the BLM–TOP3A–RMI1–RMI2 complex, and this approach was not focused on mitotic chromatin[151]. Our study extends these approaches by analyzing several UFB-associated bait proteins in mitotic chromatin under matched DMSO and APH conditions. This allowed us to compare

replication stress-dependent chromatin networks linked to different UFB markers and provided a broader strategy to identify candidate factors involved in UFB processing and resolution.

One important finding from the meta-analysis was the enrichment of proteins involved in DNA replication and repair. This is relevant because FS-UFBs are thought to arise from replication intermediates that remain unresolved and persist in mitosis[110]. Under mild APH treatment, such intermediates may accumulate at fragile sites and later appear as FS-UFBs. Consistent with this, FS-UFBs are typically flanked by sister FANCD2 foci, which mark stalled or incompletely replicated DNA regions[57,110]. Accordingly, PCNA, RPA1, FEN1, and PARP1 were enriched under aphidicolin treatment (Figure 4.6). These proteins are linked to DNA synthesis, ssDNA binding, flap processing, and PARP-dependent repair signaling, respectively[178,179]. Their enrichment supports the idea that APH-treated mitotic chromatin contains unresolved replication-associated DNA structures that require processing by replication and repair factors.

In parallel, the meta-analysis revealed enrichment of several RNA-processing factors, including DDX46, DDX39A, EIF4A3, DDX47, and ALYREF, under replication stress (Supplementary Figure 5). This is relevant because many common fragile sites overlap with large, actively transcribed genes, where delayed replication can promote transcription–replication conflicts and R-loop formation[160,180,181]. FANCD2 ChIP-seq studies have mapped these regions within large, highly transcribed genes. Thus, the enrichment of RNA-processing and R-loop-associated factors, including DDX47[78,182], may reflect the processing of transcription-associated replication intermediates at fragile genomic regions[78].

A key outcome of the meta-analysis was the identification of APEX1 and ALYREF as candidate proteins. APEX1 was repeatedly enriched with BLM and FANCD2 after APH treatment, whereas ALYREF was detected with several UFB marker proteins, suggesting a broader connection between UFB-associated chromatin and RNA-processing pathways. The APH-specific enrichment of both proteins suggested that their association was linked to mitotic DNA intermediates generated by replication stress.

Together, these findings suggest that mild replication stress promotes transcription-replication conflicts that can persist into mitosis. The resulting unresolved DNA intermediates are associated not only with replication and repair proteins, but also with RNA-processing factors.

5.2 Molecular characterization of candidate proteins

5.2.1 APEX1 associates with UFB under replication stress

Following the meta-analysis, APEX1 was selected for detailed molecular characterization. The APEX1 ChIP-MS showed that BER related proteins were enriched, including FEN1, PARP1, LIG1, LIG3, PCNA, NME1, ADAR, and RFC1–RFC5 (Figure 4.8). This indicated that, the detected protein pattern was more

consistent with a repair-synthesis-associated or long-patch BER module than with the complete canonical short-patch BER machinery[179,183], since key short-patch BER-associated factors such as POLB were not recovered. This does not exclude short-patch BER activity but suggests that the chromatin-bound APEX1 complexes enriched under these conditions may be biased toward PCNA/FEN1-dependent repair processing[179,184]. The absence of the DNA glycosylases OGG1, MPG, and UNG should be interpreted cautiously because these enzymes act upstream of APEX1 and may associate only transiently with damaged sites before APEX1-dependent processing[184]. Proteins of the hetero hexameric replicative helicase MCM2–7 were significantly enriched in the APEX1 ChIP-MS and were generally more enriched after APH treatment. This suggests that APEX1-associated chromatin complexes may become connected to replication intermediate DNA structures under mild replication stress[185,186]. APEX1 has also been detected in proteomic datasets of HU-stalled replication forks, although it was not functionally characterized in that study[187]. This provides additional support for a possible association of APEX1 with stalled replication-associated chromatin but does not by itself establish a direct role for APEX1 in fork processing.

APEX1 ChIP-MS showed increased enrichment of several UFB-associated proteins after APH treatment, including BLM, TOP2A, UBTF, RPA1, and RPA2. This stress-dependent enrichment supports the meta-analysis and suggests that during chromosome segregation, APEX1 associates with chromatin regions where replication stress, DNA repair, and UFB protein complex overlap. Although the ChIP-MS data do not demonstrate direct interactions between APEX1 and these UFB markers, they support a connection between APEX1 and BLM-associated repair sites on chromatin. In addition, the APEX1 ChIP-WB experiments showed that the APEX1 association with BLM and FANCD2 was not dependent on DNA or RNA (Figure 4.11), suggesting that this connection was not simply mediated by nucleic acids or RNA.

The enrichment pathway analysis from APEX1 ChIP MS reveals that, under replication stress, APEX1 may associate with highly transcribed or repetitive genomic regions where transcription replication conflicts and R-loops are more likely to form (Figure 4.8). This interpretation is consistent with previous APEX1 interactome studies showing that APEX1-associated networks extend beyond canonical BER and include factors involved in RNA metabolism, mRNA stability, RNA splicing, and miRNA processing[130]. In line with this broader RNA-associated role, Lin et al. classified APEX1 as a high-confidence R-loop-binding protein[152]. Together, these findings suggest that APEX1-associated mitotic chromatin complexes become more connected to RNA-associated genome maintenance pathways under replication stress.

The microscopy-based validation experiments support the idea that APEX1 is connected to replication stress-induced UFBs. APEX1 signal was detected on a subset of BLM-positive UFBs, and this fraction increased after APH treatment (Figure 4.13). Because conventional APEX1 immunofluorescence was limited by diffuse background staining, PLA provided an important validation step. The detection of APEX1–BLM and APEX1–FANCD2 PLA signals on BLM-positive UFBs, including at bridge ends and along the bridge axis, suggests that APEX1 is positioned close to staled replication fork with FANCD2 during anaphase (Figure 4.16). Although the PLA data was obtained from a single biological replicate and should be interpreted cautiously, they strengthen the possibility that APEX1 is not only biochemically enriched in replication stress-associated chromatin complexes but is an integral part of the UFB-associated structures. This interpretation is supported by previous studies showing that APEX1 can remain on mitotic chromatin and contribute to mitotic genome stability. Acetylated APEX1 was shown to localize condensed mitotic chromatin at H3K27Ac- and G4-enriched regions and to support post-mitotic transcriptional reactivation, indicating that APEX1 is not excluded from mitotic chromosomes and may act on DNA structures that persist in mitosis[188]. In addition, APEX1 acetylation promotes AP-site repair and coordination with downstream BER factors, providing a possible mechanism for its chromatin-associated repair function[189]. APEX1 depletion has also been linked to telomere dysfunction, anaphase bridges, micronuclei, and multinucleation[190]. Together with these studies, our IF and PLA data suggest that APEX1 may have a broader mitotic genome-stability function and may contribute to the processing or stabilization of replication stress-induced UFB intermediates during anaphase.

5.2.2 ALYREF associates with UFB markers without a clear role in UFB resolution

ALYREF was validated as a candidate linked to RNA processing and replication stress. Reciprocal ALYREF ChIP-MS efficiently recovered ALYREF as the bait protein and enriched several known RNA processing and export factors, including NXF1, NXT1, DDX39B, MAGOH, and EIF4A3 (Figure 4.9). This was consistent with the established role of ALYREF as an mRNA export adaptor connected to TREX, UAP56/DDX39B, and NXF1–NXT1-dependent RNA export[191–193]. The absence of several THO complex proteins suggested that the experiment did not recover the complete canonical TREX complex, but rather a selected ALYREF network associated with mitotic chromatin. Moreover, ALYREF showed stronger association with factors linked to R-loops, including RNA helicases such as DDX46 and DDX47 after APH treatment. Together with the reciprocal detection of BLM and FANCD2, this suggests that ALYREF may associate with chromatin regions where RNA processing, R-loop regulation, and transcription–replication conflicts overlap. This interpretation is consistent with studies showing that ALYREF contributes to R-loop regulation through UAP56/DDX39B[137,138].

However, functional validation did not support ALYREF as a UFB-resolution factor. In the IF microscopy data, antibody staining showed that ALYREF frequently colocalized with BLM-positive UFBs as discrete foci along the bridge, but this fraction of colocalization did not increase after APH treatment (Figure 4.14). Moreover, high background staining hampers the interpretation. To directly test whether ALYREF affect UFB resolution, ALYREF was partially depleted and the number of UFBs were quantified (Figure 4.15). Partial ALYREF depletion did not increase UFBs, suggesting that ALYREF was not required for preventing or resolving UFBs in this experimental system. One possible explanation is that the remaining ALYREF activity after partial depletion was sufficient to maintain its essential RNA-processing and R-loop-related functions. In addition, ALYREF depletion severely affected cell survival, suggesting that complete ALYREF knockout may not be feasible in this cell line.

In this context, ALYREF may represent a replication stress-associated RNA-processing/R-loop factor rather than a direct UFB resolution factor. Future experiments using acute ALYREF depletion, for example through an inducible degron, combined with transcription-associated stress, may clarify whether ALYREF contributes to transcription-replication conflicts that can persist into mitosis. Together, these validation experiments indicated that APEX1 showed a stronger and more consistent association with the BLM/FANCD2 replication stress response, making it a promising candidate for subsequent functional analysis.

5.3 APEX1 and BLM have overlapping and distinct roles in genome stability

APEX1 emerged as a functional contributor to UFB resolution under replication stress. The data suggest that APEX1 is not generally required for all UFB resolution events but becomes important when replication intermediates persist into mitosis.

Fixed-cell microscopy showed that APEX1 loss. Has no effect on formation of PICH-positive UFBs (Figure 4.18). In contrast, APH treatment caused a clear increase in UFB-positive anaphases in APEX1-deficient cells, supporting a replication stress-dependent role for APEX1. Live-cell imaging further refined this interpretation by showing that the increase was mainly caused by persistent wavy UFBs, whereas the straight UFBs were largely unaffected (Figure 4.25). This distinction is important because straight UFBs resolve rapidly, while wavy UFBs persist into late anaphase and telophase. Thus, APEX1 appears to be particularly important for the timely resolution of persistent replication stress-induced UFBs. A similar result with live-cell imaging was reported for TopBP1, where loss of TopBP1 delayed anaphase bridge resolution and allowed UFBs to persist into late telophase, supporting the idea that UFB-associated factors can influence the bridge persistence during late mitosis[69].

The non-additive phenotype after combined APEX1 loss and BLM depletion suggests that the two proteins act in overlapping processes that limit UFB persistence and binucleation (Figure 4.23). The

double-deficient cells largely resembled BLM-depleted cells, while APEX1 knockout alone show a weaker phenotype. This indicates that BLM has a broader role in UFB resolution, whereas APEX1 may contribute to the processing of a more specific subset of replication stress-induced intermediates. Two explanations may account for this difference. First, BLM may act during both the formation and resolution of replication-associated DNA intermediates, whereas APEX1 contributes mainly to their later processing during mitosis. Second, BLM may be required for the resolution of a wider range of UFB structures, while APEX1 acts only on a specific subset of replication stress-induced FS-UFB intermediates[140].

The analysis of RPA-coated UFBs provided further insight into this relationship. Previous work showed that PICH and BLM promote the conversion of unresolved sister chromatid linkages into RPA-coated ssDNA bridges, and that loss of BLM prevents efficient RPA coating of UFBs[89]. Consistent with these models, BLM depletion reduced RPA-coated UFBs. In contrast, APEX1 knockout increased RPA-coated UFBs under mild replication stress (Figure 4.18), suggesting that BLM-dependent ssDNA formation can still occur in the absence of APEX1, but that these RPA-coated intermediates persist or accumulate. Importantly, RPA-coated UFBs remained low in APEX1 knockout cells when BLM was depleted, supporting the idea that BLM activity is required upstream of RPA loading.

The phenotype correlation analysis further suggest that APEX1 loss and BLM depletion affect genome stability through two related but distinct routes (Figure 4.24). The first route is linked to unresolved mitotic bridge intermediates (Figure 5.1). In this group, UFBs correlates with chromatin bridges, while chromatin bridges are associated with binucleation, polyploidy, and reduced long-term survival. This supports the interpretation that unresolved UFB structures can persist through mitosis, interfere with cytokinesis, and contribute to post-mitotic genome instability. This model is consistent with studies showing that impaired PICH or BLM function disrupts late mitosis and cytokinesis[73,140]. It is also consistent with recent work showing that BLM-dependent conversion of PICH-coated bridges into RPA-coated ssDNA bridges activates RPA–ATR–CHK1 signalling during cytokinesis, linking unresolved UFBs to abscission checkpoint control[194].

The second route appear linked to chromosome breakage before anaphase (Figure 5.1). Double-strand DNA breaks and gaps observed in metaphase chromosome spreads are correlated strongly with lagging chromatin and micronucleation but showed little correlation with increased UFB formation (Figure 4.24). This suggests that micronuclei in APEX1-deficient or BLM-depleted cells are unlikely to arise mainly from persistent UFBs or chromatin bridges. Instead, they may reflect DNA breakage before mitosis, followed by mis-segregation of broken chromatin fragments during anaphase.

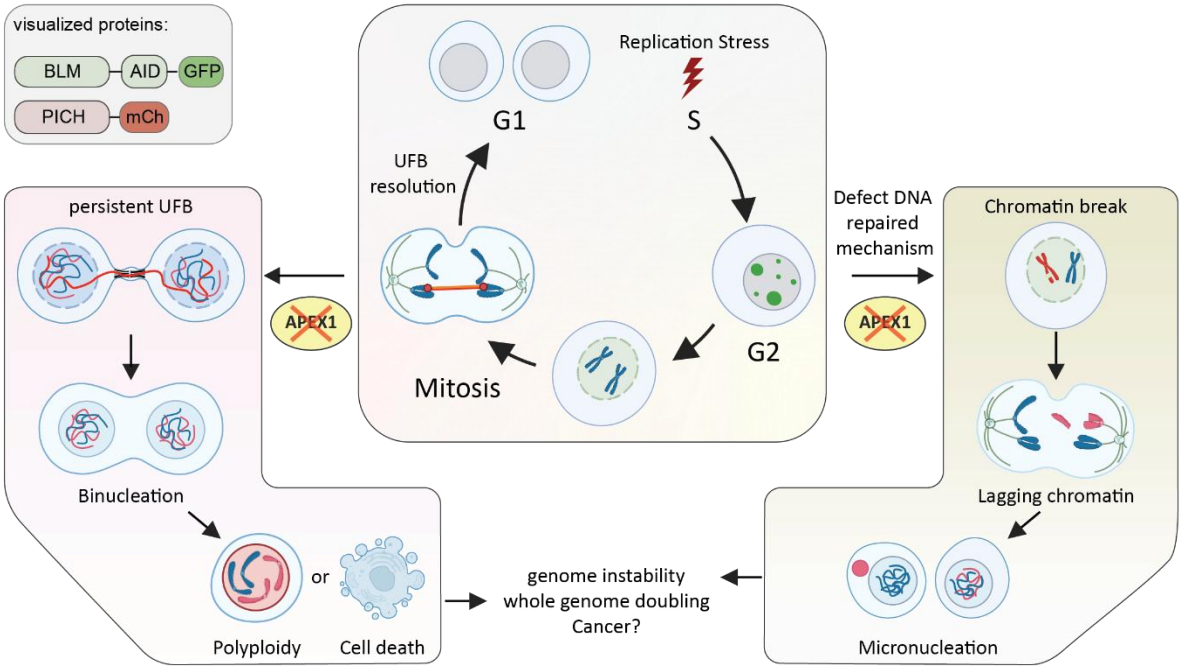


Figure 5.1 | Dual roles of APEX1 in maintaining genome stability throughout the cell cycle.
Schematic summary of the proposed functions of APEX1 during interphase and mitosis. During interphase, loss of APEX1 compromises DNA repair pathways, leading to the accumulation of double-strand DNA breaks and the formation of lagging chromatin and micronuclei in the subsequent cell cycle. In mitosis, APEX1 promotes the efficient resolution of fragile site-derived ultrafine anaphase bridges (FS-UFBs). Failure to resolve these structures results in persistent UFBs, which can give rise to binucleation (BN), polyploidy, or ultimately cell death. Together, these findings identify APEX1 as a novel factor involved in UFB resolution and establish it as a critical safeguard of genome stability through distinct functions in both interphase and mitosis.

5.4 Evidence for a specific role of APEX1 in the resolution of FS-UFBs

The functional analysis supports a stress-dependent role for APEX1 in the resolution of FS-UFBs. APEX1 appears to become important when replication intermediates persist into mitosis. The rescue experiments further support this interpretation. Re-expression of wild-type APEX1 reduced APH-induced UFBs to near wild-type levels (Figure 4.28), indicating that the increased UFB frequency was a direct consequence of APEX1 loss rather than an unrelated clonal effect. Importantly, APEX1 expression after S phase was sufficient to restore UFB numbers to wild type level (Figure 4.30).

FANCD2 and FANCI mark fragile site intermediates that persist into mitosis after replication stress and are associated with incompletely replicated DNA regions[110,195]. In this study, APEX1 loss did not increase prometaphase FANCD2 foci after APH treatment (Figure 4.34), although it increased FS-UFBs and RPA-coated bridges. This suggests that APEX1 deficiency does not primarily increase the formation or FANCD2 marking of fragile site intermediates. Instead, APEX1 may contribute to their later processing or resolution after they have entered mitosis. This interpretation is consistent with the generally mild phenotype of APEX1 loss in unstressed cells. If APEX1 loss mainly caused UFBs by increasing abasic sites during S phase, a stronger increase in replication-associated lesions might be

expected before mitosis. However, pre-existing abasic sites may be tolerated by Prim Pol-dependent repriming and post-replicative gap filling pathways[29,196].

APEX1 also does not appear to be required for the resolution of catenation-derived UFBs. This conclusion is supported by the c-UFB subtype analysis, where APEX1 loss did not significantly affect formation of centromeric UFBs induced by TOP2A inhibition (Figure 4.32). This suggests that APEX1 is more relevant for replication stress-associated DNA intermediates than for mitotic catenation stress. APEX1 could plausibly process damaged, nicked, or abasic-site-containing replication intermediates, but it would not be expected to directly resolve intact dsDNA catenanes[197].

Finally, catalytic mutant rescue experiments indicate that APEX1 catalytic activity is required for efficient UFB resolution. Whereas wild-type APEX1 restored UFB numbers to wild-type levels, the catalytically impaired SO mutant failed to rescue APH-induced UFBs and FS-UFBs (Figure 4.34). This indicates that APEX1 is not only present at replication stress-associated mitotic structures, but that its enzymatic activity is important for their efficient resolution.

5.5 Proposed models for APEX1-dependent FS-UFB resolution

5.5.1 Current model of FS-UFB resolution

FS-UFBs are thought to arise from incompletely replicated DNA regions that persist into mitosis. These structures are commonly marked by FANCD2 and FANCI. Recent work provides a possible explanation for this localization, as FANCD2–FANCI can slide on double-stranded DNA and stall at single-stranded/double-stranded DNA junctions[198]. Thus, FANCD2–FANCI mark fragile-site intermediates that persist into mitosis, whereas PICH, BLM, and BTRR mediate the physical processing of the stretched bridge during anaphase.

After cells enter mitosis, PICH binds stretched double-stranded bridge regions and recruits UFB processing factors, including BLM and the BTRR complex[101]. More recent work further showed that both PICH-mediated recruitment and PICH translocase activity contribute to efficient UFB resolution[199]. PICH-coated double-stranded UFBs are thought to be converted into RPA-coated single-stranded bridges through BLM-dependent unwinding. However, because BLM alone is a weak helicase, efficient bridge processing likely requires cooperation with BTRR and RPA[101,200]. Sarlós et al. proposed that BTRR may be recruited along PICH-coated UFBs but initiates productive processing mainly at high-affinity DNA structures, such as single-stranded/double-stranded DNA junctions or catenated regions[200]. In this model, RPA-coated ssDNA would restrict BTRR binding along single-stranded regions, making the ssDNA/dsDNA junction a likely nucleation point for unwinding and decatenation[89,101]. This provides a useful framework for interpreting basal FS-UFB resolution. The canonical PICH–BLM–

TOP3areRMI1/2 pathway may be sufficient when the number or complexity of fragile-site intermediates is low. BLM can promote ssDNA generation, RPA can stabilize the exposed ssDNA, and TOP3A within BTRR can mediate strand passage through an ssDNA gate, allowing disentanglement of replication or recombination intermediates[200].

This may explain why APEX1 loss did not strongly increase UFBs under DMSO conditions, where the number or complexity of fragile-site intermediates may remain low enough for the canonical PICH–BLM–TOP3A–RMI1/2 pathway to resolve them efficiently. In contrast, mild APH treatment increases fork slowing at common fragile sites and may also enhance TRCs at difficult-to-replicate regions, such as CFSs and rDNA. Under these conditions, BTRR may remain the primary resolution machinery, but APEX1 may become necessary as an additional processing factor for damaged, nicked, abasic-site-containing, or R-loop-associated intermediates that cannot be fully resolved by BTRR alone. The central unresolved question is which DNA structure within these persistent UFB intermediates is recognized and cleaved by APEX1.

5.5.2 Two possible sites of APEX1 incision during FS-UFB resolution

APEX1 may promote FS-UFB resolution by acting on distinct DNA substrates. These mechanisms are not mutually exclusive, since transcription-replication conflicts can themselves stall replication forks. However, they differ in the proposed site of APEX1 incision: either within the DNA strand of an RNA–DNA hybrid or at an abasic site near an ssDNA/dsDNA junction in a stalled fork-derived intermediate.

Model 1: APEX1 cleavage within the DNA strand of an R-loop-associated FS-UFB intermediate

One possibility is that APEX1 acts on an abasic site within the DNA strand of an RNA-DNA hybrid formed during a transcription-replication conflict. APEX1-mediated incision would generate a nick that could provide an entry point for BLM-mediated unwinding and destabilize the hybrid, facilitate removal of RNA and transcription proteins. In this model, the relevant APEX1 substrate is an abasic site within the DNA strand of the R-loop (Figure 5.2).

Studies on common fragile site replication support a connection between TRCs and RNA-DNA hybrids. Madireddy et al. showed that loss of FANCD2 increased replication stalling at common fragile sites through a mechanism involving RNaseH1-sensitive RNA-DNA hybrids[201]. Taken together, these findings provide indirect evidence that RNA-DNA hybrids can contribute to replication stress at common fragile sites. Tang et al. further showed that RNA-DNA hybrids can accumulate on micronuclear chromosomes and trigger ADAR dependent deoxyinosine formation in the DNA strand of the hybrid. Deoxyinosine is then removed by MPG, generating abasic sites that are cleaved by APEX1 and converted into single-

strand DNA nicks[175]. Although Tang et al. focused mainly on micronuclei, their findings suggest that persistent RNA-DNA hybrids can be converted into APEX1-dependent nicked DNA intermediates[175]. This interpretation is supported by our BLM and FANCD2 ChIP-MS data obtained after RNaseH1 overexpression. Since RNaseH1 removes RNA-DNA hybrids, the reduced APEX1 enrichment and decreased DNA repair/recombination pathway enrichment after RNaseH1 induction suggests that the APEX1-associated replication stress response depends on R-loop (Figure 4.7). APEX1-dependent incision may therefore be particularly important at TRC-associated FS-UFBs, where nick formation could facilitate BLM access to the DNA strand of the RNA-DNA hybrid and promote removal or displacement of transcription complex obstacles. Single-molecule studies showed that human RPA activates BLM-dependent bidirectional unwinding from a nick, indicating that nicked DNA can provide an entry point for productive BLM-mediated unwinding[202].

The increase in RPA-coated UFBs in APEX1-deficient cells suggests that BLM can still unwind the bridge and generate ssDNA. However, TRC- or R-loop-associated regions may remain unresolved in the absence of APEX1. The bridge is therefore only partially processed and persists as an RPA-coated UFB during anaphase. A direct way to test this model would be to combine mild replication stress with transcription inhibition in wild-type and APEX1-knockout cells. If the elevated UFB frequency in APEX1-deficient cells is mainly caused by TRC-associated intermediates, transcription inhibition should reduce or abolish the difference between wild-type and knockout cells. In contrast, if UFBs remain elevated after transcription inhibition, this would suggest that APEX1 also acts on transcription-independent replication intermediates generated by APH-induced fork slowing or under-replication.

Model 2: APEX1 cleavage at an ssDNA/dsDNA junction within a stalled fork-derived FS-UFB intermediate

A second possibility is that APEX1 acts at an abasic site located near an ssDNA/dsDNA junction within a stalled or under-replicated fork intermediate. Unlike the first model, this mechanism does not require an RNA-DNA hybrid or a transcription complex. Instead, APEX1 would process a damaged fork-like DNA structure generated directly by APH-induced stalled fork (Figure 5.2).

Persistent stalled fork intermediates may accumulate chemically modified bases that are converted into abasic sites. Kharat et al. showed that TET-dependent accumulation of 5hmC and related cytosine modifications at stalled replication forks promotes the formation of abasic sites and APE1-dependent fork degradation[175,203]. This suggests that APEX1 may process abasic-site-containing stalled fork structures that persist into mitosis as FS-UFB intermediates. Hoitsma et al. further showed that APEX1 can cleave abasic sites in stalled replication fork-like substrates, including in the presence of RPA, and that APEX1 acts more efficiently on primer-template junction-like substrates than on ssDNA alone[166].

Together, these findings suggest that APEX1 may process abasic sites at ssDNA/dsDNA junctions within persistent RPA-coated FS-UFB intermediates.

In this model, APEX1-dependent incision provides a late mitotic processing step that remodels the damaged junction and allows other UFB-resolution factors to complete bridge resolution. Whether APEX1 can access the lesion may depend on its protection status. HMCES can covalently bind abasic sites in ssDNA and protect them from incision and replication fork cleavage[204,205]. However, when an abasic site remains accessible, APEX1 may cleave the damaged fork-derived intermediate and facilitate its subsequent processing. Although these studies did not examine UFBs directly, they support the possibility that damaged or abasic-site-containing replication intermediates persist into mitosis and become substrates for APEX1 during FS-UFB resolution.

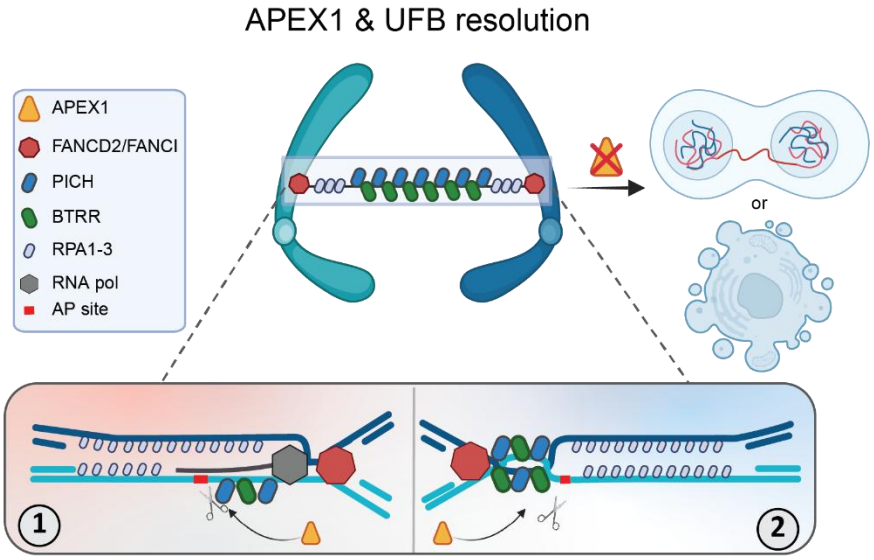


Figure 5.2 | Two possible sites of APEX1 incision during FS-UFB resolution.
Proposed model illustrating the role of APEX1 in FS-UFB resolution. Under replication stress, under-replicated DNA structures can persist at common fragile sites and enter mitosis as FANCD2-positive FS-UFBs. One possible source of these intermediates is a transcription–replication conflict (TRC), potentially involving an R-loop. In this model, APEX1 may help resolve the R-loop or associated DNA lesion, thereby facilitating removal of the transcription machinery, after which a helicase could unwind the DNA into single-stranded DNA (ssDNA). A second possible source is a replication intermediate generated directly by incomplete DNA replication. In this model, APEX1 may introduce or process a single-strand incision that helps separate the under-replicated sister DNA strands, allowing subsequent helicase-dependent unwinding into ssDNA. In both scenarios, APEX1 would promote the processing and resolution of replication stress-associated intermediates during anaphase, thereby preventing the persistence of FS-UFBs. The resulting ssDNA-containing structures may then be completed or repaired in the following G1 phase after the daughter cells have separated properly.

6 Conclusion

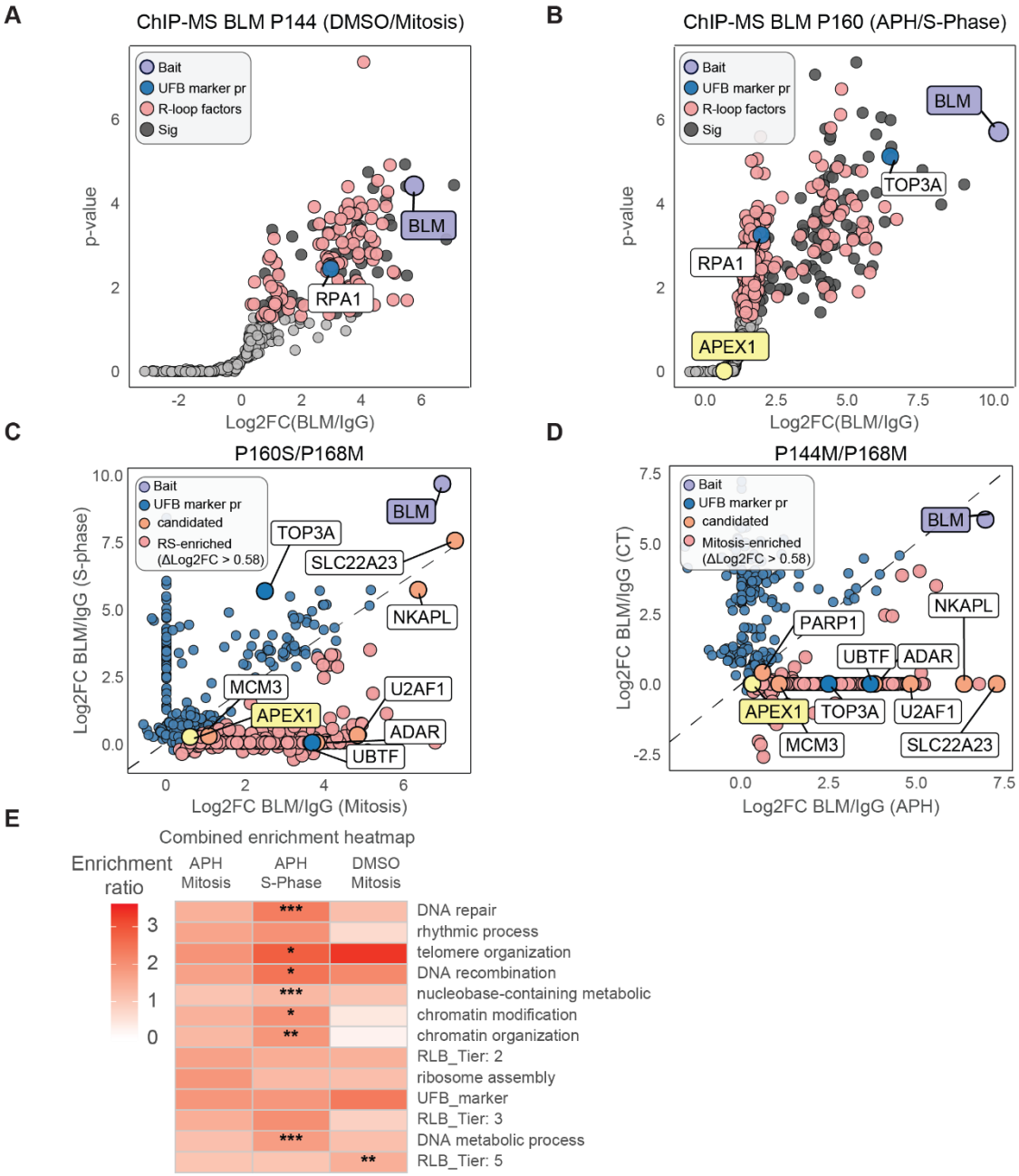
This study identified APEX1 as a replication stress-dependent factor that contributes to the resolution of fragile site ultrafine anaphase bridges. Proteomic and validation experiments linked APEX1 to BLM, FANCD2, RPA, and transcription–replication conflicts under mild replication stress.

Functional analyses showed that APEX1 loss mainly affected persistent FS-UFBs under replication stress and increased RPA-coated bridges. Our findings further demonstrated that APEX1 catalytic activity was required for efficient bridge resolution and that APEX1 function during mitosis was necessary for FS-UFB resolution. The non-additive effects of combined APEX1 loss and BLM depletion on several mitotic and post-mitotic phenotypes suggest that APEX1 and BLM act in overlapping processes during UFB resolution under replication stress. They also support a model in which BLM promotes ssDNA generation, while APEX1 contributes to the later processing of a specific subset of damaged or incompletely resolved bridge intermediates.

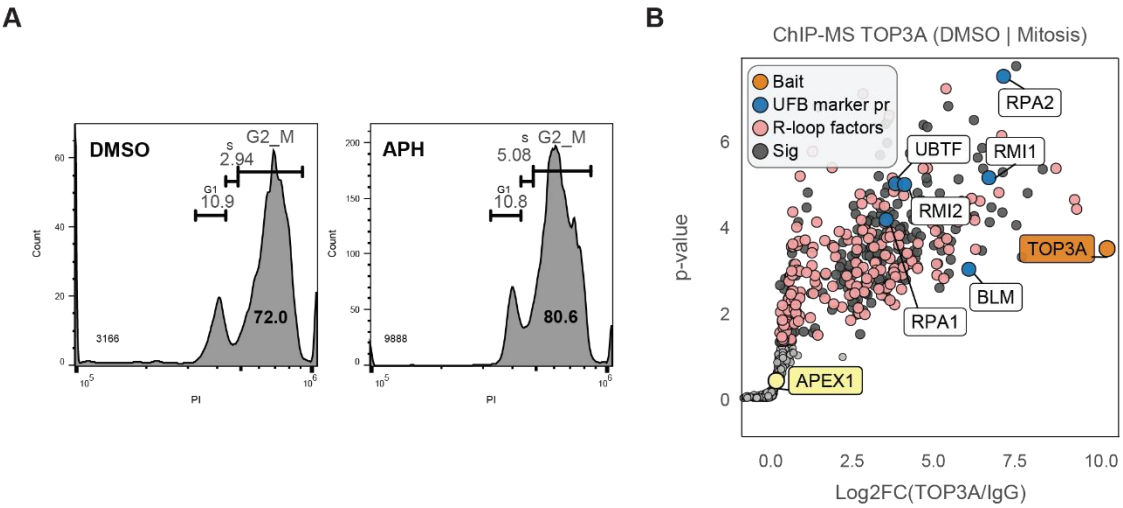
APEX1 may therefore act on abasic-site-containing DNA within R-loop structures or near ssDNA/dsDNA junctions in stalled fork-derived intermediates. Although the precise substrate remains unknown, the findings identify APEX1 as a previously unrecognized component of FS-UFB resolution and suggest that its catalytic activity helps limit genome instability through UFB resolution.

7 Supplementary information

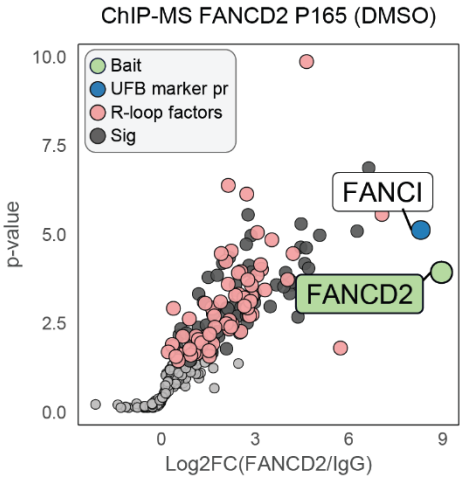
7.1 Supplementary Figure



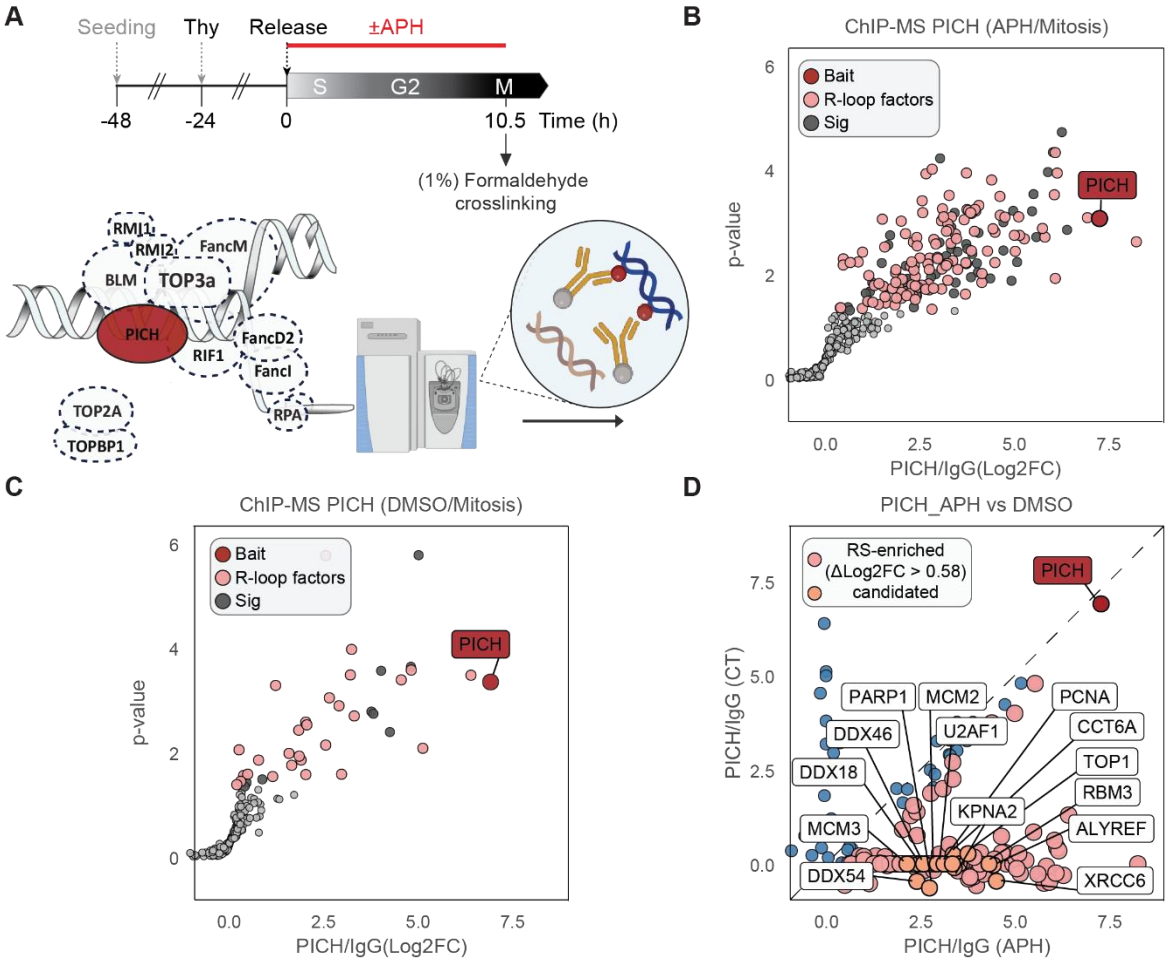
Supplementary Figure 1 | ChIP–MS analysis of BLM interactors under distinct cell-cycle and treatment conditions.
(A–B) Volcano plots of BLM helicase ChIP–MS datasets generated using a GFP nanobody as bait. Cells were synchronized with thymidine for 24 h, released into fresh medium, and crosslinked with formaldehyde at the indicated time points. (A) DMSO-treated cells harvested 10.5 h after release in mitosis. (B) aphidicolin (APH)-treated cells harvested 5 h after release in S phase. (C) Scatter plot comparing fold changes (FC) of BLM ChIP–MS interactors in mitotic cells (P168) versus S-phase cells. Proteins enriched by at least onefold in mitosis are highlighted. (D) Scatter plot comparing fold changes (FC) of BLM ChIP–MS interactors in mitotic cells treated with APH (P168) or DMSO. Proteins enriched by at least onefold in APH-treated cells are highlighted. (E) Enrichment analysis heatmap for the rest of significant pathways. (Gene Ontology Biological Process (GOBP) terms and R-loop–associated factors) across the three principal conditions: APH/S phase, APH/mitosis, and DMSO/mitosis.



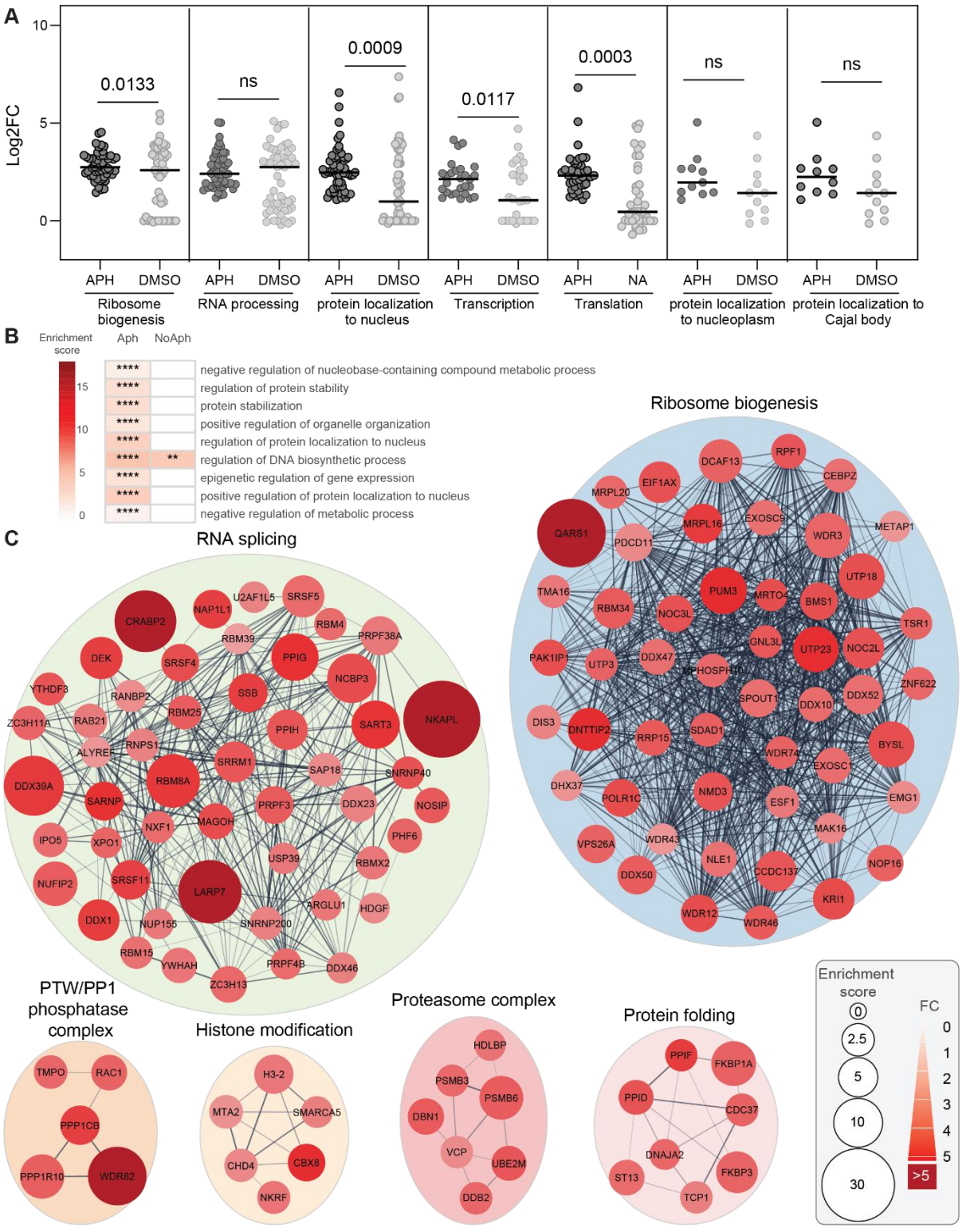
Supplementary Figure 2 | ChIP–MS analysis of TOP3A interactors under distinct treatment conditions.
(A) Flow cytometry analysis of aphidicolin (APH)- and DMSO-treated cells stained with propidium iodide (PI), confirming mitotic synchronization. (B) Volcano plot of the TOP3A ChIP–MS dataset generated using a TOP3A antibody as bait. Cells were synchronized with thymidine for 24 h, released into fresh medium, and crosslinked with formaldehyde 10.5 h after release in mitosis under DMSO-treated conditions.



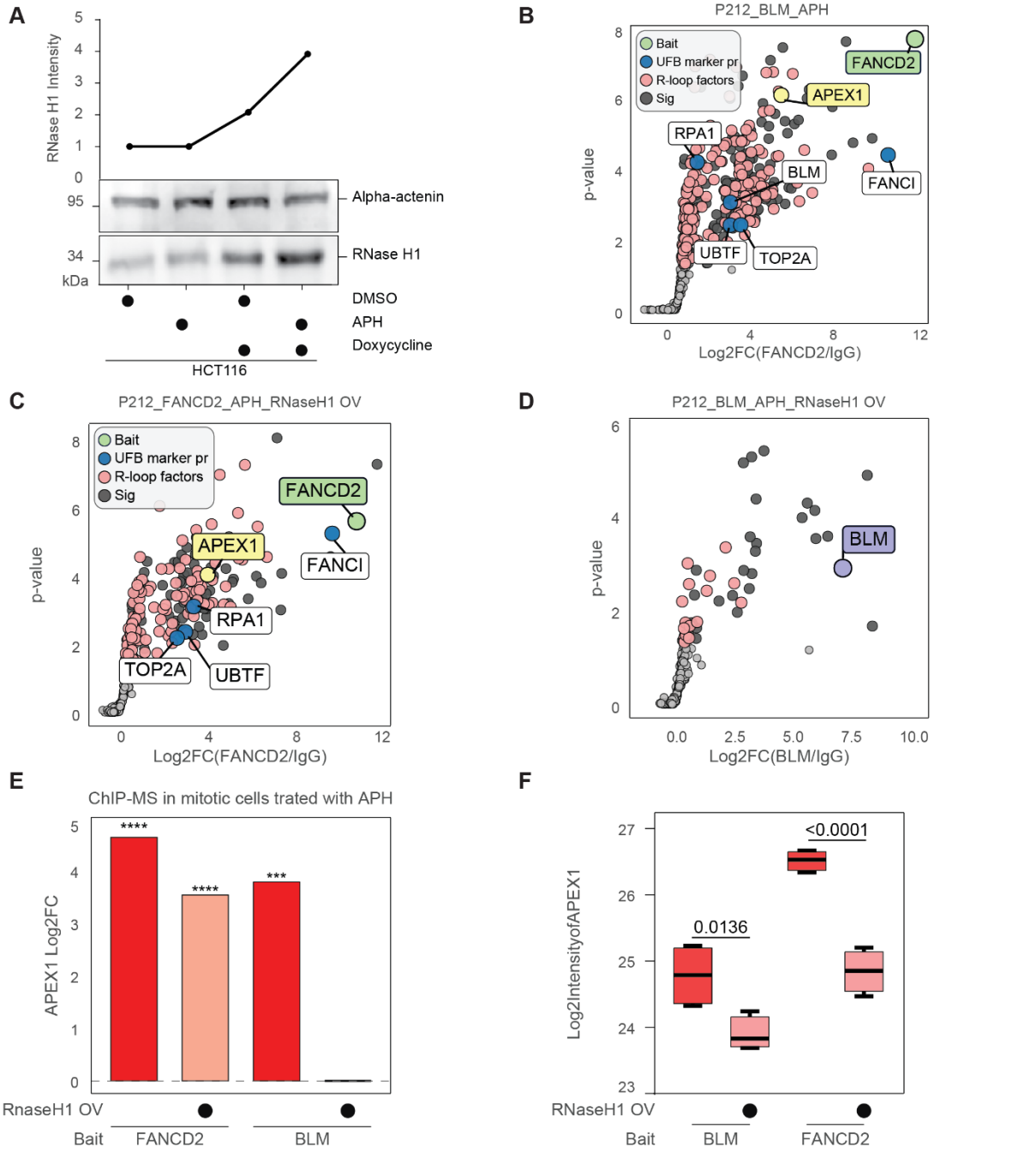
Supplementary Figure 3 | ChIP–MS analysis of FANCD2 interactors under distinct cell-cycle and treatment conditions.
Volcano plots of FANCD2 ChIP–MS datasets generated using a FANCD2 antibody as bait. Cells were synchronized with thymidine for 24 h, released into fresh medium, and crosslinked with formaldehyde 10.5 h after release in mitosis. DMSO-treated cells.



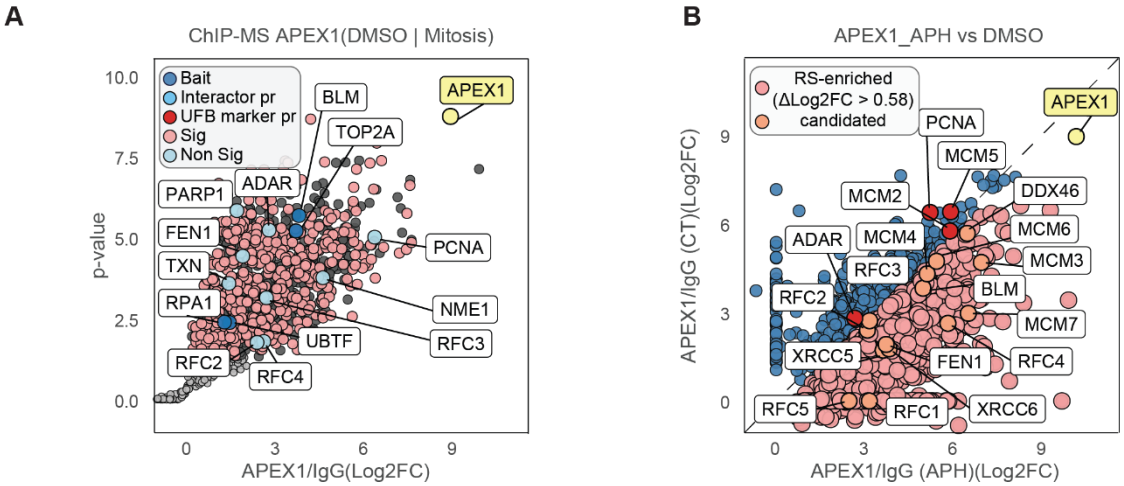
Supplementary Figure 4 | ChIP–MS analysis of PICH interactors.
(A) Schematic overview of the ChIP–MS experimental workflow. (B–C) Volcano plots of PICH ChIP–MS datasets generated using a PICH antibody as bait. Cells were synchronized with thymidine for 24 h, released into fresh medium, and crosslinked with formaldehyde 10.5 h after release in mitosis. (B) aphidicolin (APH)-treated cells. (C) DMSO-treated cells. (D) Scatter plot comparing fold changes (FC) of PICH ChIP–MS interactors in mitotic cells treated with APH or DMSO. All proteins shown were significantly enriched in at least one condition. Proteins enriched by at least onefold in APH-treated cells are highlighted.



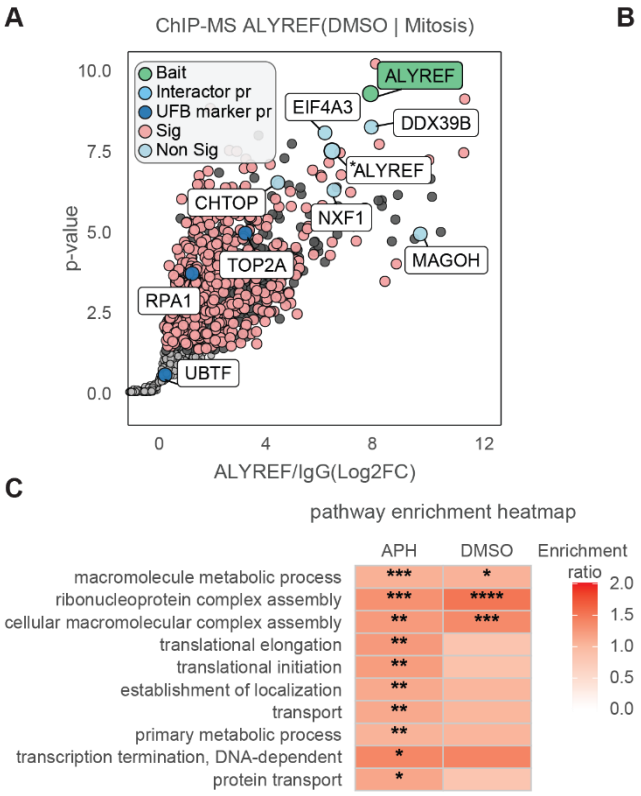
Supplementary Figure 5 | ChIP-MS meta-analysis of UFB-associated protein interactomes.
(A) Schematic overview of the ChIP–MS experimental workflow. (B) Volcano plot of the APEX1 ChIP–MS dataset generated using an APEX1 antibody as bait. Cells were synchronized with thymidine for 24 h, released into fresh medium containing aphidicolin (APH), and crosslinked with formaldehyde 10.5 h after release in mitosis. (C) Schematic overview of transcription and the proposed role of APEX1. (D) Protein interaction network of APEX1 generated using the STRING database. Proteins identified in the ChIP–MS dataset is highlighted in light blue. (E) Enrichment analysis of pathways, including Gene Ontology Biological Process (GOBP) terms and R-loop–associated factors, comparing APH/mitosis and DMSO/mitosis conditions. (F) Dot plot showing ultrafine bridge (UFB) marker proteins detected in the APEX1 ChIP–MS dataset under APH and DMSO conditions. (G) Fold-change analysis of rRNA-processing and R-loop–associated pathway proteins in APH versus DMSO APEX1 ChIP–MS conditions, showing increased enrichment under replication stress.



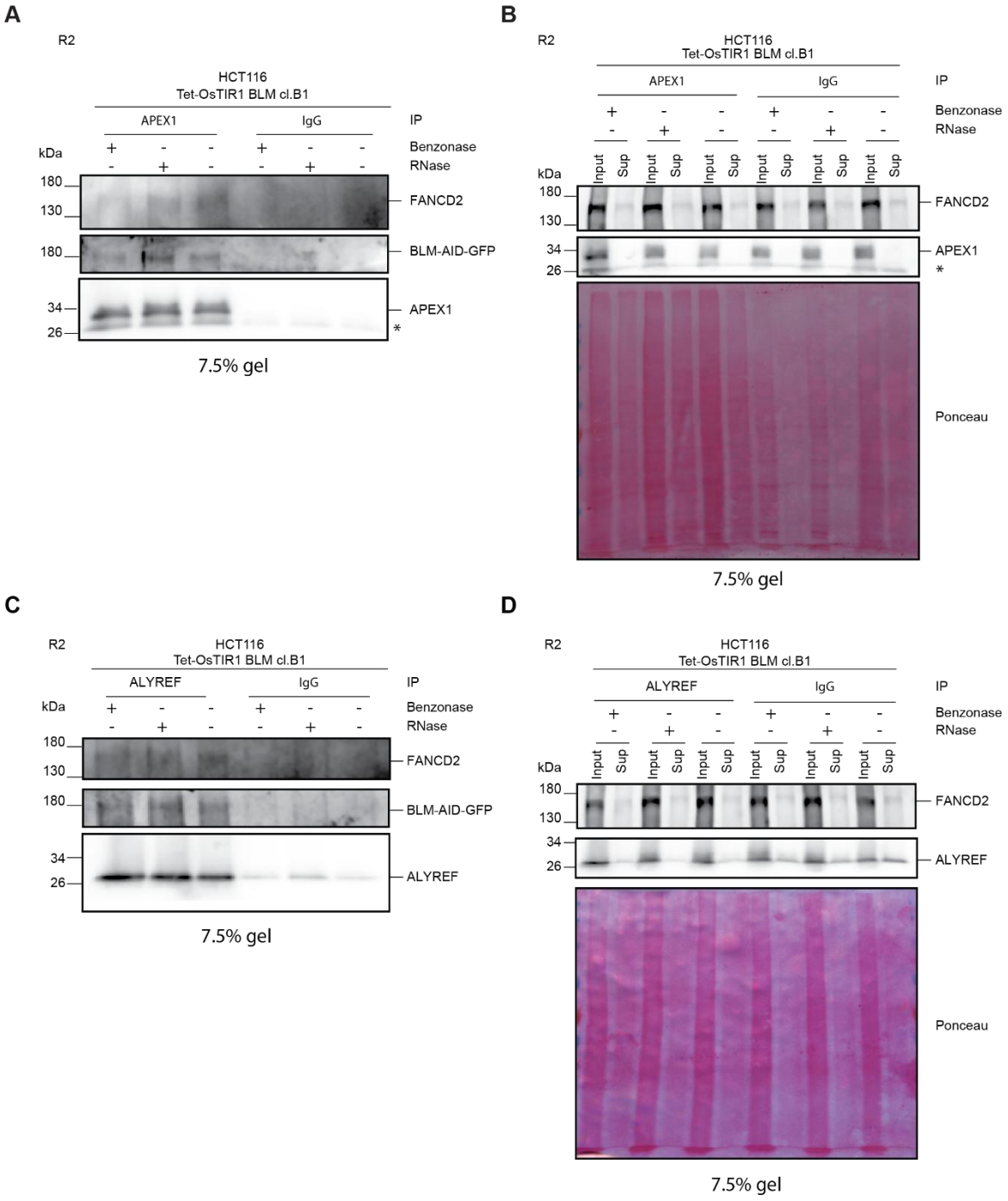
Supplementary Figure 6 | ChIP–MS analysis of FANCD2 and BLM helicase under RNase H1 overexpression.
(A) Western blot analysis of RNase H1 overexpression in HCT116 Tet-on cells treated with aphidicolin (APH) or DMSO, in the presence or absence of doxycycline (DOX; 200 ng/mL). (B–C) Volcano plots of FANCD2 helicase ChIP–MS datasets generated using a BLM antibody as bait. Cells were synchronized with thymidine for 24 h, released into fresh medium, and crosslinked with formaldehyde 10.5 h later. (B) DMSO-treated mitotic cells. (C) APH-treated cells with DOX-induced RNase H1 overexpression. (D) Volcano plot of BLM ChIP–MS from APH/DOX-treated cells. (E) Log2 fold-change of APEX1 across the four principal conditions.



Supplementary Figure 7 | ChIP–MS analysis of APEX1 interactors.
(A) Volcano plot of the APEX1 ChIP–MS dataset generated using an APEX1 antibody as bait. Cells were synchronized with thymidine for 24 h, released into fresh medium, and crosslinked with formaldehyde 10.5 h after release in mitosis under DMSO-treated conditions. (B) Scatter plot comparing fold changes (FC) of APEX1 ChIP–MS interactors in mitotic cells treated with aphidicolin (APH) or DMSO. All proteins shown were significantly enriched in at least one condition. Proteins enriched by at least onefold in APH-treated cells are highlighted.

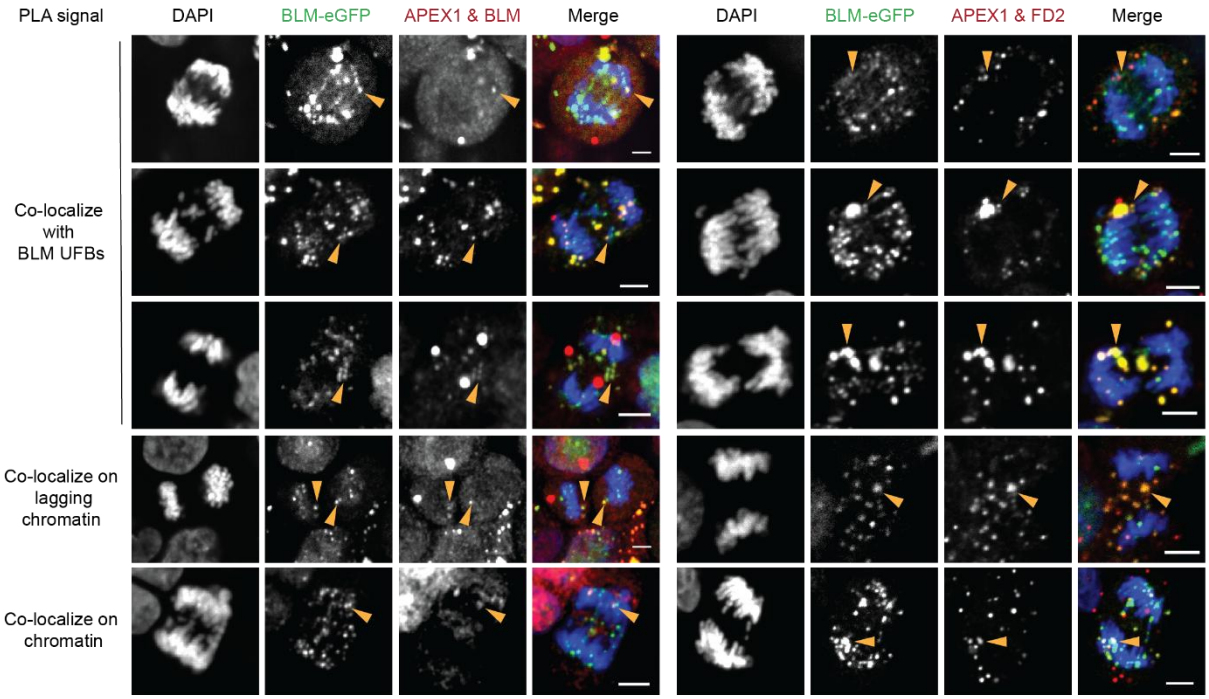


Supplementary Figure 8 | ChIP–MS analysis of ALYREF interactors.
(A) Volcano plot of the ALYREF ChIP–MS dataset generated using an ALYREF antibody as bait. Cells were synchronized with thymidine for 24 h, released into fresh medium, and crosslinked with formaldehyde 10.5 h after release in mitosis under DMSO-treated conditions. (B) Scatter plot comparing fold changes (FC) of ALYREF ChIP–MS interactors in mitotic cells treated with aphidicolin (APH) or DMSO. All proteins shown were significantly enriched in at least one condition. Proteins enriched by at least onefold in APH-treated cells are highlighted. (C) Extended enrichment analysis of pathways, including Gene Ontology Biological Process (GOBP) terms, comparing APH/mitosis and DMSO/mitosis conditions.

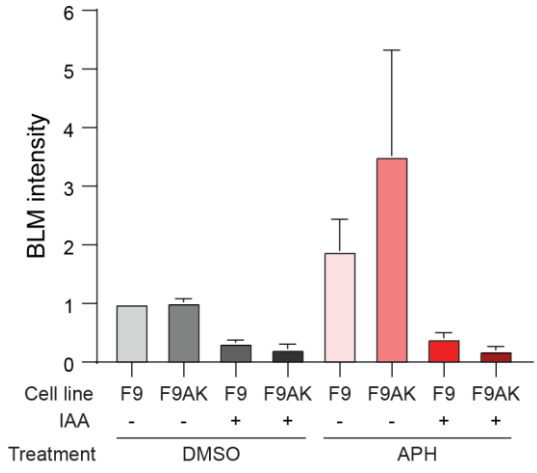


Supplementary Figure 9 | APEX1 and ALYREF ChIP–Western blot analysis following Benzonase and RNase A treatment second replicate.

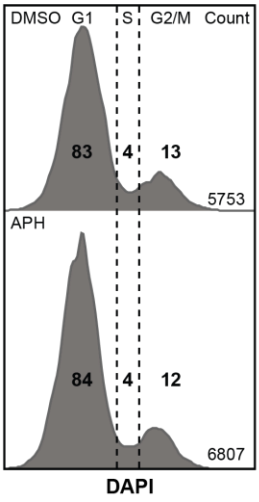
(A) Second biological replicate of the APEX1 ChIP–Western blot experiment following immunoprecipitation with an APEX1-specific antibody. Mouse IgG was used as a negative control. (B) Western blot analysis of the corresponding input and post-immunoprecipitation supernatant fractions under untreated, Benzonase-treated, and RNase A-treated conditions. (C) Second biological replicate of the ALYREF ChIP–Western blot experiment following immunoprecipitation with an ALYREF-specific antibody. Mouse IgG was used as a negative control. (D) Western blot analysis of the corresponding input and post-immunoprecipitation supernatant fractions under the same treatment conditions.



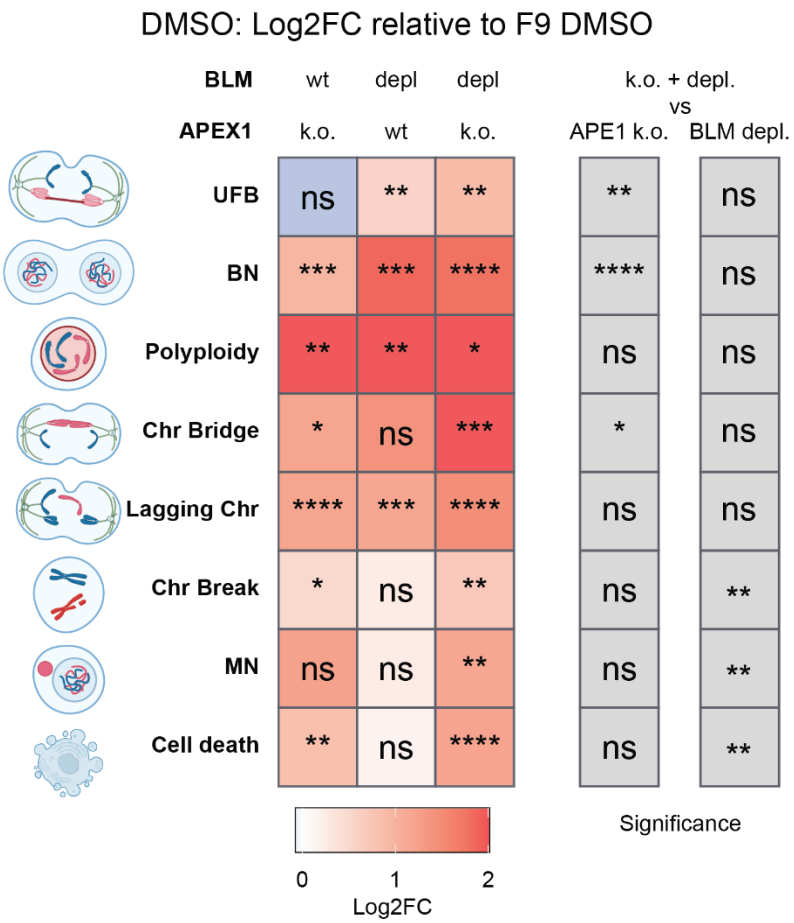
Supplementary Figure 10 | Proximity ligation assay reveals APEX1 co-localization with BLM and FANCD2 at ultra-fine anaphase bridges.
Representative immunofluorescence images from the PLA assay showing co-localization of APEX1 with BLM and FANCD2 at UFBs, lagging chromatin, and chromatin. UFBs were visualized by BLM–eGFP, PLA signals are shown in red (594 nm), and DNA was counterstained with DAPI. Scale bar: 5 µm.



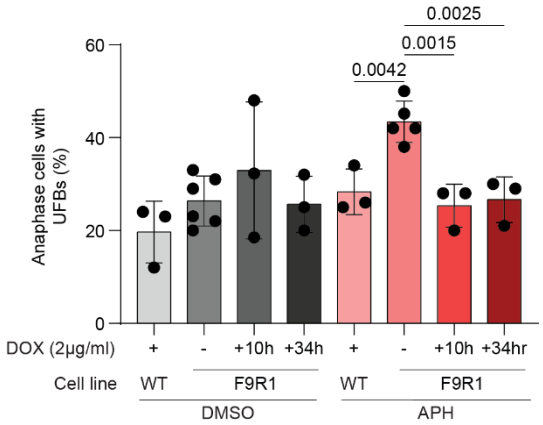
Supplementary Figure 11 | BLM intensity for Auxin and Aphidicolin treated samples.
BLM intensity for Auxin and Aphidicolin treated samples. cells treated for 10.5 h with aphidicolin or DMSO. IAA was added together with Thymidine (BLM depletion)



Supplementary Figure 12 | Flow cytometry analysis of cell cycle progression in HCT116 F9 wild-type cells.
Cells were synchronized at the G1/S boundary using a single thymidine block and subsequently released into medium containing either aphidicolin (APH) or DMSO. Four hours after release, Palbociclib was added to arrest cells in the G1 phase of the following cell cycle. Cells were maintained in the presence of Palbociclib and either APH or DMSO for an additional 18 hours. After treatment, cells were fixed and stained with DAPI for DNA content analysis by flow cytometry.



Supplementary Figure 13 | APEX1 loss and BLM depletion show non-additive effects on genome instability.
Heatmap showing the log2 fold change (log2FC) of genome instability phenotypes in DMSO-treated cells following APEX1 knockout, BLM depletion using the auxin-inducible degron (AID) system, combined APEX1 knockout and BLM depletion. Color intensity represents log2FC relative to wild-type (WT) DMSO-treated cells, and asterisks indicate statistically significant differences determined by unpaired t-tests. For the main heatmap, log2FC values and statistical comparisons were calculated relative to the WT DMSO condition. The two columns on the right show additional significance comparisons between the combined APEX1 knockout/BLM-depletion condition and either APEX1 knockout or BLM depletion alone. Data represents three independent biological replicates. Experiments were performed in collaboration with Amr Abdrbo and Katarina Gauch.



Supplementary Figure 14 | Early or Late Reintroduction of APEX1. Combined quantification of PICH-positive UFBs comparing early and late APEX1 re-expression, APEX1 knockout (–Dox), and wild-type (F9 WT) cells. Data are shown as mean ± SD from three biological replicates (Student's t-test, n = 3).

7.2 Supplementary Data

The complete meta-analysis tables for aphidicolin-treated and non-aphidicolin-treated samples, as well as the *t*-test results for each individual ChIP–MS experiment, are available on Seafile: https://seafile.rlp.net/d/dea389a9adb9462d87a7/

Supplementary Data 1 | Top 200 significantly enriched proteins identified under mild replication stress conditions.

Protein	Uniport id	score	log2fc mean	test count	Test count-sig
FANCI	Q9NVI1	33.9253648	9.099320482	3	3
SLC22A23	C9IZW5	23.7113132	8.016483249	2	2
IGHV3-7	P01780	23.03935863	6.866882901	4	3
NKAPL	Q5M9Q1	22.13048888	6.009867868	2	2
QARS	P47897-2	18.76300961	6.552216424	3	2
CDCA5	B5MBX0	18.10905904	9.002019714	2	2
LARP7	Q4G0J3	16.70333843	5.041008534	3	3
CRABP2	P29373	16.07401329	7.53661748	2	2
DDX39A	O00148	15.37737353	4.233744684	4	3
FANCD2	Q9BXW9	14.88597885	4.57215262	4	3
WDR82	Q6UXN9	14.80408645	6.512402137	2	2
CDK1	A0A024QZP7	14.2068932	4.21613581	2	2
BLM	P54132	13.56141199	6.178795612	5	5
ZBTB1	Q9Y2K1-2	12.92871948	5.044545897	2	2
RBM8A	Q9Y5S9	12.85341825	4.288509186	5	5
NCBP3	Q53F19	11.17777303	3.853872184	3	2
SART3	Q15020-4	10.70626946	4.362972997	4	4
TOP3A	Q13472-3	10.51431438	5.88375515	2	2
PPIG	C9JN15	10.33493318	4.450314462	3	3
RRP1B	Q14684-2	10.2237877	5.016622412	3	3
G3BP2	D6RBM9	10.1550033	4.221279861	5	5
PUM3	Q15397	10.10942696	4.539658494	3	3
BYSL	Q13895	9.820942684	3.81392272	3	3
UTP18	Q9Y5J1	9.762591023	3.761284178	6	5
UTP23	Q9BRU9	9.610889407	4.476180636	3	3
WDR3	Q9UNX4	9.521286868	3.223848016	3	3
FKBP1A	P62942	9.290509902	3.365792145	4	3
NUFIP2	Q7Z417	9.226813928	3.468322377	4	3
DPYSL2	A0A1C7CYX9	9.186406087	3.510055439	2	2
UHRF1	A0A087WVR3	9.136625885	3.33273322	4	4
PPP1R10	Q96QC0	9.106243406	3.427935599	2	2
PSMB6	P28072	8.915946122	3.463891541	3	3
DCAF13	A0A087WT20	8.816440157	3.350667334	3	3
PLRG1	O43660-2	8.695179485	3.300958187	3	3
DNTTIP2	Q5QJE6	8.623234478	4.528335394	3	3
STT3B	Q8TCJ2	8.433257323	3.38529095	3	3
DEK	P35659	8.322046575	4.1382836	4	4
SRSF5	Q13243-3	8.236839702	3.097479134	6	3

Protein	Uniport id	score	log2fc mean	test count	Test count-sig
APOBEC3B	B0QYD3	8.119051446	4.539067988	3	3
FKBP3	Q00688	8.0682104	3.311725187	3	3
DDX1	Q92499	8.035762225	4.201665018	5	5
CSDE1	E9PLT0	8.029547753	3.241856515	4	4
EIF1AX	X6RAC9	8.015408175	3.695276628	4	4
APEX1	G3V5Q1	8.013092532	3.206521469	8	6
KRI1	Q8N9T8	7.980494767	3.872895489	3	3
NOC2L	Q9Y3T9	7.895222003	3.715904519	4	4
SRRM1	Q8IYB3	7.821604139	3.598758498	4	3
U2SURP	E7ET15	7.752407763	4.085321364	5	5
CCDC137	I3L0U5	7.69212267	3.639477819	3	3
RBM34	A2A2V2	7.684898223	3.499126118	4	4
PPIH	O43447	7.606949912	3.629543515	5	5
MRPL16	Q9NX20	7.36417567	4.217385506	2	2
DDX52	Q9Y2R4	7.325304408	3.014941415	3	3
DDX56	F8WDT8	7.28926189	3.95614186	3	3
SRSF11	Q5T760	7.260188757	4.094888299	3	3
PPP1CB	P62140	7.160598728	4.135036951	3	3
PCLAF	Q15004	7.158016473	3.320073628	3	3
H3-7	Q5TEC6	7.083806366	2.816046647	7	2
SSB	P05455	7.027639466	4.158427094	4	4
PRPF38A	Q8NAV1	7.010006942	2.793489622	2	2
RUVBL1	Q9Y265	6.99993443	3.47764312	4	4
NAP1L1	P55209	6.966758566	4.133629406	3	3
NMD3	C9JA08	6.959072594	3.642209886	4	4
SARNP	P82979	6.944266801	4.460924472	5	3
DDX50	A0A087WVC1	6.930423504	3.467428536	4	4
VPS26A	O75436	6.804368864	3.334853649	3	3
PDCD11	Q14690	6.734805899	2.419988876	6	4
SPOUT1	Q5T280	6.656945453	3.008938624	3	3
NSUN5	Q96P11-2	6.639240086	3.104479962	3	3
PRPF3	O43395	6.582320357	3.493071219	4	4
POLR1C	E7EQB9	6.525371296	3.842805287	2	2
SRSF4	Q08170	6.516669082	3.809825071	5	5
BMS1	Q14692	6.421149136	3.775619708	4	4
CBX8	Q9HC52	6.389809022	4.498594412	2	2
WDR12	Q9GZL7	6.36239304	3.860987687	2	2
RRP12	Q5JTH9-2	6.253429063	3.800839194	3	3
NOC3L	Q8WTT2	6.201061101	3.720289244	3	3
DDX23	Q9BUQ8	6.176850373	2.583534025	3	3
KRR1	Q13601-2	6.116249719	3.49073815	5	4
ZC3H13	Q5T200-2	6.050950754	3.139918761	3	3
NOP16	Q9Y3C1	6.023904649	3.369095534	4	3

Protein	Uniport id	score	log2fc mean	test count	Test count-sig
PAK1IP1	Q9NWT1	6.012382007	3.790192825	3	3
S100A11	P31949	5.987205866	3.062805321	4	3
DBN1	Q16643	5.920432846	3.523774374	2	2
DNMT1	P26358	5.865787202	2.591475357	5	4
MAGOH	P61326	5.794456577	3.83263292	3	2
EXOSC1	Q9Y3B2	5.791991894	3.041118364	2	2
RRP15	Q9Y3B9	5.766008352	3.542288044	3	3
TOMM40	O96008-2	5.723754175	3.666937666	2	2
DDX47	Q9H0S4-2	5.719015572	3.003964772	5	4
RAC1	P63000	5.712538294	3.33479441	3	2
EXOSC9	Q06265	5.679008816	2.979275444	2	2
NOSIP	A0A075B6F9	5.663039111	3.525691257	5	5
ST13	H7C3I1	5.631368757	3.088585722	3	3
YWHAH	Q04917	5.617868625	2.847429546	2	2
NLE1	Q9NVX2	5.567295588	2.958594557	3	3
SAMM50	Q9Y512	5.519617861	3.33130751	2	2
DDX10	Q13206	5.426570267	3.073173945	3	3
UBE2M	P61081	5.418480163	3.619870748	2	2
RPF1	Q9H9Y2	5.362579465	3.618409339	3	2
PPID	Q08752	5.344324706	3.685846133	2	2
EDF1	O60869	5.336696787	3.586896492	3	3
CDSN	Q15517	5.332581704	3.124644784	4	2
IPO5	O00410	5.252073271	3.054881797	3	3
PHF6	A0A0D9SGE8	5.240829445	3.290047018	3	3
DIS3	Q9Y2L1	5.199070174	2.561958264	5	4
RBMXL1	Q96E39	5.191196234	3.509977476	3	2
RAB21	Q9UL25	5.146296914	2.770292341	2	2
RBM25	P49756	5.096005494	3.454466357	5	5
ZC3H11A	O75152	5.095513367	3.27352787	3	2
CEBPZ	Q03701	5.074452048	2.940535787	4	4
SAP18	X6RAL5	5.066647037	2.368705316	6	2
GLUD1	P00367-3	5.063203487	2.737389518	2	2
SET	A0A0C4DFV9	5.043124508	3.440902483	3	3
WDR46	O15213	5.027984422	3.54406044	3	3
SDAD1	E7EW05	5.007897335	3.400398299	3	3
MTA2	O94776	4.89401011	2.252118067	6	4
TMPO	P42166	4.854085541	3.211689901	7	6
NGDN	Q8NEJ9-2	4.787498887	2.828237225	3	3
RBMX2	Q9Y388	4.771539158	2.823494148	2	2
MPHOSPH10	O00566	4.76445073	3.179031589	2	2
MRPL20	Q9BYC9	4.743278212	3.164219359	2	2
CCDC124	Q96CT7	4.74101894	3.790756028	2	2
SNRNP200	O75643	4.728929226	2.57267285	7	6

Protein	Uniport id	score	log2fc mean	test count	Test count-sig
CHD4	A0A2R8Y5J0	4.717597032	2.439066505	3	2
DKC1	O60832	4.70601729	3.14675833	5	4
GNL3	Q9BVP2-2	4.6929422	2.614341297	6	5
RNPS1	Q15287	4.671197477	2.570745882	6	3
YTHDF3	A0A024R7W5	4.635649055	3.654912034	2	2
NKRF	O15226	4.634505456	2.884656235	4	4
RPA1	P27694	4.628324245	2.238151803	7	3
ZNF622	Q969S3	4.627240844	3.233588273	3	3
TMA16	H0Y9X1	4.590623507	2.795196032	2	2
EMG1	Q92979	4.582098455	2.355902002	5	3
WDR74	E9PS41	4.578211768	3.355718947	3	3
CDC37	Q16543	4.53179044	3.349643776	3	2
C11orf98	A0A0B4J220	4.498796509	3.052669496	3	2
GNL3L	Q9NVN8	4.477242809	3.570113459	2	2
ESF1	Q9H501	4.470295034	2.793534346	3	3
DDB2	Q92466	4.460524697	3.219024272	3	3
MRTO4	Q9UKD2	4.454412579	3.805786726	3	3
STRAP	Q9Y3F4-2	4.451849475	2.978236722	5	4
FUBP3	Q96I24	4.443159181	2.698000267	4	4
UTP3	Q9NQZ2	4.438422338	3.319158746	3	3
CPSF7	F5H669	4.430725427	3.374386479	6	6
VCP	P55072	4.415078412	2.37159266	6	4
SNRNP40	Q96DI7	4.404542252	3.710278559	2	2
TCP1	P17987	4.403976892	2.671597372	6	4
DNM1L	G8JLD5	4.3795578	2.943310367	2	2
RBM15	A0A087WWP4	4.379364639	2.969826524	5	5
NXF1	E9PIN3	4.363940076	3.090880504	4	4
RANBP2	P49792	4.356999932	2.336982227	4	2
RBM4	E9PB51	4.34949363	3.070394327	4	4
KPLCE	Q5T750	4.336607149	3.049039658	3	2
TSR1	Q2NL82	4.333052001	3.301075557	4	4
UTP14A	Q9BVJ6-3	4.321613211	3.311152429	3	3
PPIF	P30405	4.318176694	4.199667179	2	2
EXOSC10	Q01780	4.313804347	3.18269948	4	4
CAP1	Q01518	4.299418535	2.632396559	6	5
SRP9	P49458	4.296648011	2.569033166	5	4
NEMF	G3V5V3	4.292923835	2.473075473	3	3
PSMB3	A0A087WUL2	4.288516827	3.169904497	2	2
RPL37	P61927	4.269127054	2.900786807	3	2
PCNP	Q8WW12	4.26479611	3.202581414	2	2
ZNF638	Q14966-3	4.258341823	2.936078534	4	4
PCNA	P12004	4.248481286	2.916750075	8	5
ESD	P10768	4.225826472	3.012381727	4	3

Protein	Uniport id	score	log2fc mean	test count	Test count-sig
DNAJC7	Q99615-2	4.214442099	3.572775201	2	2
CLIC1	O00299	4.183730708	2.458133932	6	4
MTAP	Q13126	4.167018401	2.170513449	5	3
TES	Q9UGI8	4.162391717	2.124429554	4	3
ABCF1	Q8NE71-2	4.159824833	3.073197931	2	2
SMARCA5	O60264	4.112073162	2.638361169	5	4
KIFC1	Q9BW19	4.093684315	2.697853013	4	4
ATP1A1	P05023-3	4.093595947	2.049458555	2	2
U2AF1	Q01081	4.078086406	2.54836152	5	3
HACL2	M0R026	4.066040076	3.022775846	2	2
MYOF	Q9NZM1-5	4.041081995	2.955575079	4	3
WDR43	Q15061	4.003201268	2.132278951	3	2
CDC20	Q12834	3.980000731	2.827040208	3	2
HDLBP	Q00341	3.974324912	2.898269584	4	4
YBX3	P16989-2	3.96563584	2.580016579	5	3
DHX37	F5H3Y4	3.955935613	2.2289549	2	2
USP39	Q53GS9	3.953730543	2.811613138	4	4
S100A6	P06703	3.936743346	2.873921836	6	3
METAP1	P53582	3.936431328	2.182623284	3	2
ARGLU1	Q9NWB6	3.93362858	2.835409111	3	2
ACP1	G5E9R5	3.906121112	3.146476419	4	4
DDX46	Q7L014	3.882511131	2.628776916	7	6
CPNE3	O75131	3.876803354	2.178796344	6	3
PRP4K	Q13523	3.874921436	3.085277093	3	3
CDK11B	P21127	3.856642334	3.479749683	2	2
SRRT	Q9BXP5	3.850173587	2.465595411	6	3
RBM39	A0A0U1RQH7	3.82363722	1.912852771	5	3
XPO1	O14980	3.819291497	3.2531793	2	2
NUP155	E9PF10	3.808711611	2.775494577	2	2
MAK16	Q9BXY0	3.803142631	2.452570024	4	3
DNAJA2	O60884	3.80055082	3.23448656	3	3
ALYREF	Q86V81	3.771631227	2.138206059	9	4
HDGF	P51858	3.771082349	2.395861824	4	3

7.3 List of figures

Figure 1.1 | Overview of the eukaryotic cell cycle and mitotic progression. 14
Figure 1.2 | representation of the sequential activation of cyclin–CDK complexes that drive cell cycle transitions. 16
Figure 1.3 | Schematic overview of DNA replication during S phase. 17
Figure 1.4 | Major pathways and mediators of the replication stress response. 19
Figure 1.5 | Co-directional (CD) and head-on (HO) collisions between replisomes and co-transcriptional R-loops in eukaryotes. 21
Figure 1.6 | DNA damage types induced by replication stress and their corresponding repair pathways. 23
Figure 1.7 | Consequences of replication stress in mitosis and chromosome mis-segregation. 24
Figure 1.8 | DNA anaphase bridges and major classes of ultra-fine anaphase bridges (UFBs). 29
Figure 1.9 | Overview of BLM functions in genome maintenance. 31
Figure 1.10 | Structural and functional organization of APE1/Ref-1. 36
Figure 1.11 | Domain organization and proposed co-transcriptional function of ALYREF. 37
Figure 1.12 | Characterization of the HCT116 F9 cell line for visualization of ultrafine DNA bridges (UFBs). 39
Figure 1.13 | Cell cycle synchronization methods. 40
Figure 4.1 | ChIP-MS analysis of BLM interactors. 80
Figure 4.2 | ChIP-MS analysis of BLM interactors. 82
Figure 4.3 | ChIP–MS analysis of TOP3A interactors. 84
Figure 4.4 | ChIP–MS analysis of FANCD2 interactors. 86
Figure 4.5 | ChIP-MS analysis of FANCI interactors. 88
Figure 4.6 | ChIP-MS meta-analysis of UFB-associated protein interactomes. 91
Figure 4.7 | ChIP-MS analysis of FANCD2 and BLM helicase under RNase H1 overexpression. 94
Figure 4.8 | ChIP-MS analysis of APEX1 interactors. 97
Figure 4.9 | ChIP-MS analysis of ALYREF interactors. 100
Figure 4.10 | Reciprocal ChIP–western blot analysis of APEX1 and ALYREF. 101
Figure 4.11 | APEX1 association with BLM and FANCD2 is maintained after RNA and DNA digestion. 103
Figure 4.12 | ALYREF–BLM interactions occur independently of RNA or DNA. 104
Figure 4.13 | APEX1 co-localizes with BLM on ultra-fine anaphase bridges frequently under mild replication stress. 106
Figure 4.14 | ALYREF shows limited co-localization with BLM at ultra-fine anaphase bridges. 107
Figure 4.15 | ALYREF knockdown does not affect ultra-fine anaphase bridge formation. 108
Figure 4.16 | Proximity ligation assay reveals APEX1 co-localization with BLM and FANCD2 at ultra-fine anaphase bridges. 110
Figure 4.17 | CRISPR/Cas9-mediated knockout of APEX1 in HCT116 F9 cells. 111
Figure 4.18 | Effects of APEX1 loss and BLM depletion on anaphase defects. 114
Figure 4.19 | Depletion of BLM and APEX1 increases the frequency of mitotic aberrations. 116
Figure 4.20 | post-mitotic consequences of APEX1 and BLM depletion. 118
Figure 4.21 | Effects of APEX1 and BLM co-depletion on double-strand DNA breaks in metaphase. 121
Figure 4.22 | Effects of APEX1 and BLM co-depletion on long-term cell survival. 123
Figure 4.23 | APEX1 loss and BLM depletion show non-additive effects on genome instability. 125
Figure 4.24 | APEX1 and BLM loss reveal two correlated routes to genome instability. 127
Figure 4.25 | Visualization of replication stress-induced UFBs in APEX1 knockout cells reveals persistent sister chromatid linkages. 129
Figure 4.26 | Replication stress–induced mitotic aberrations in APEX1 knockout cells 130

Figure 4.27 | APEX1 rescue in the HCT116 F9AK cell line. 131
Figure 4.28 | APEX1 re-expression suppresses UFB formation. 133
Figure 4.29 | Time-dependent induction of APEX1 following doxycycline treatment. 135
Figure 4.30 | APEX1 re-expression after replication restores proper UFB resolution. 137
Figure 4.31 | Catalytically active APEX1 is required for efficient resolution of fragile site-derived ultrafine anaphase bridges (FS-UFBs). 140
Figure 4.32 | APEX1 is not required for the resolution of centromeric UFBs. 143
Figure 4.33 | APEX1 loss increases lagging chromatin under unperturbed conditions independently of chromosome mis-segregation. 145
Figure 4.34 | APEX1 is required for efficient resolution of fragile site-derived ultrafine anaphase bridges (FS-UFBs). 147
Figure 5.1 | Dual roles of APEX1 in maintaining genome stability throughout the cell cycle. 154
Figure 5.2 | Two possible sites of APEX1 incision during FS-UFB resolution. 158

7.4 List of supplementary figures

Supplementary Figure 1 | ChIP–MS analysis of BLM interactors under distinct cell-cycle and treatment conditions. 160
Supplementary Figure 2 | ChIP–MS analysis of TOP3A interactors under distinct treatment conditions. 161
Supplementary Figure 3 | ChIP–MS analysis of FANCD2 interactors under distinct cell-cycle and treatment conditions. 161
Supplementary Figure 4 | ChIP–MS analysis of PICH interactors. 162
Supplementary Figure 5 | ChIP–MS analysis of APEX1 interactors. 163
Supplementary Figure 6 | ChIP–MS analysis of FANCD2 and BLM helicase under RNase H1 overexpression. 164
Supplementary Figure 7 | ChIP–MS analysis of APEX1 interactors. 165
Supplementary Figure 8 | ChIP–MS analysis of ALYREF interactors. 165
Supplementary Figure 9 | APEX1 and ALYREF ChIP–Western blot analysis following Benzonase and RNase A treatment second replicate. 166
Supplementary Figure 10 | Proximity ligation assay reveals APEX1 co-localization with BLM and FANCD2 at ultra-fine anaphase bridges. 167
Supplementary Figure 11 | BLM intensity for Auxin and Aphidicolin treated samples. 167
Supplementary Figure 12 | Flow cytometry analysis of cell cycle progression in HCT116 F9 wild-type cells. 167
Supplementary Figure 13 | APEX1 loss and BLM depletion show non-additive effects on genome instability. 168
Supplementary Figure 14 | Early or Late Reintroduction of APEX1. Combined quantification of PICH-positive UFBs 168

7.5 List of supplementary Movies

The supplemental movies can be found on seafile: https://seafile.rlp.net/d/dea389a9adb9462d87a7/

Movie 1S | F9 cell showing straight UFB. Live Cell imaging of F9 cells treated with 100 nM aphidicolin for 10 hours before imaging started. UFB visualized by endogenous BLM-eGFP (green), PICH-mCherry (red). DNA staining (grey). Corresponding movie to stills shown in Figure 25A.

Movie S2 | F9 cell showing wavy UFB. Live Cell imaging of F9 cells treated with 100 nM aphidicolin for 10 hours before imaging started. UFB visualized by endogenous BLM-eGFP (green), PICH-mCherry (red). DNA staining (grey). Corresponding movie to stills shown in Figure 25A.

7.6 List of tables

Table 1 | List of equipment **44**
Table 2 | List of chemicals **47**
Table 3 | List of prepared buffers and solutions **49**
Table 4 | List of molecular biological reagents and cloning buffers **51**
Table 5 | List of general enzymes **52**
Table 6 | List of plasmids **52**
Table 7 | Target sequences and genomic positions of the APEX1 guide RNAs. **53**
Table 8 | List of Immunoprecipitation reagents specific reagents **53**
Table 9 | List of bacteria culture specific reagents **53**
Table 10 | List of human cell lines **53**
Table 11 | List of cell culture specific reagents **54**
Table 12 | List of immunoblotting reagents **55**
Table 13 | List of immunofluorescence specific reagents **56**
Table 14 | List of flow cytometry-specific reagents **56**
Table 15 | List of mass spectrometry specific chemicals and reagents **56**
Table 16 | List of primary antibodies **57**
Table 17 | List of secondary antibodies **58**
Table 18 | List of kits **59**
Table 19 | List of software **59**

7.7 List of abbreviations

Abbreviation	Full name
3’	3-prime
53BP1	p53-binding protein 1
5’	5-prime
AID	Auxin-inducible degron
ALYREF	Aly/REF export factor
APEX1	Apurinic/apyrimidinic endonuclease 1
ATM	Ataxia-telangiectasia mutated
ATR	Ataxia-telangiectasia and Rad3-related
BER	Base excision repair
BFB cycle	Breakage–fusion–bridge cycle
BIR	Break-induced replication
BLM	Bloom syndrome helicase
bp	Base pair(s)
BRCA2	Breast cancer type 2 susceptibility protein
BS	Bloom syndrome
BTRR	BLM–TOP3A–RMI1–RMI2 complex
C-UFB	Centromeric ultrafine anaphase bridge
Cas9	CRISPR-associated protein 9
CDK	Cyclin-dependent kinase
cDNA	Complementary DNA
CFS	Common fragile site
ChIP–WB	Chromatin immunoprecipitation followed by western blotting
ChIP–MS	Chromatin immunoprecipitation followed by Mass spectrometry
Chk1	Checkpoint kinase 1
Chk2	Checkpoint kinase 2
CIN	Chromosomal instability

CRISPR	Clustered regularly interspaced short palindromic repeats
D-loop	Displacement loop
DAPI	4’,6-Diamidino-2-phenylindole
DDR	DNA damage response
DDX39A	DExD-box helicase 39A
DDX39B	DExD-box helicase 39B
dHJ	Double Holliday junction
DMEM	Dulbecco’s modified Eagle medium
DMSO	Dimethyl sulfoxide
DNA	Deoxyribonucleic acid
Dox	Doxycycline
Doxo	Doxorubicin
DPC	DNA–protein crosslink
DSB	Double-strand break
DSBR	Double-strand break repair
dsDNA	Double-stranded DNA
DTT	Dithiothreitol
eGFP	Enhanced green fluorescent protein
EJC	Exon junction complex
EtOH	Ethanol
FA	Fanconi anemia
FANCD2	Fanconi anemia group D2 protein
FANCI	Fanconi anemia group I protein
FBS	Fetal bovine serum
FEN1	Flap endonuclease 1
FS-UFB	Fragile site-associated ultrafine anaphase bridge
G	Guanine
G1 phase	Gap phase 1
G2 phase	Gap phase 2
GFP	Green fluorescent protein
GG-NER	Global genome nucleotide excision repair
gRNA	Guide RNA
HCT116	Human colorectal carcinoma cell line HCT116
HR	Homologous recombination
HR-UFB	Homologous recombination-associated ultrafine anaphase bridge
Hygro	Hygromycin
IAA	Indole-3-acetic acid (auxin)
ICL	Interstrand crosslink
IF	Immunofluorescence
kb	Kilobase(s)
kDa	Kilodalton
KPNA2	Karyopherin subunit alpha 2
LFQ	Label-free quantification
M phase	Mitotic phase
MCM	Mini-chromosome maintenance protein
MEM	Minimum essential medium
MiDAS	Mitotic DNA synthesis
MMR	Mismatch repair
MN	Micronucleus
NB	Nuclear body
NEBD	Nuclear envelope breakdown
Neo	Neomycin
NER	Nucleotide excision repair
NHEJ	Non-homologous end joining

nt	Nucleotide(s)
OD	Optical density
PARP1	Poly (ADP-ribose) polymerase 1
PCC	Pearson correlation coefficient
PCNA	Proliferating cell nuclear antigen
PCR	Polymerase chain reaction
PEI	Polyethyleneimine
Pen/Strep	Penicillin/streptomycin
pH	Potential of hydrogen
PI	Propidium iodide
PICH	Polo-like kinase 1-interacting checkpoint helicase
Puro	Puromycin
r-UFB	Ribosomal ultrafine anaphase bridge
RB	Retinoblastoma protein
rDNA	Ribosomal DNA
Ref-1	Redox factor 1
RIPA	Radioimmunoprecipitation assay
RMI1	RecQ-mediated genome instability protein 1
RNA	Ribonucleic acid
RNase H1	Ribonuclease H1
RNP	Ribonucleoprotein
RPA	Replication protein A
rpm	Revolutions per minute
RRM	RNA recognition motif
RS	Replication stress
RT	Room temperature
S phase	Synthesis phase
SAC	Spindle assembly checkpoint
SCE	Sister chromatid exchange
SD	Standard deviation
SDS–PAGE	Sodium dodecyl sulfate–polyacrylamide gel electrophoresis
SEM	Standard error of the mean
sgRNA	Single-guide RNA
SSA	Single-strand annealing
SSB	Single-strand break
ssDNA	Single-stranded DNA
T-UFB	Telomeric ultrafine anaphase bridge
TIR1	Transport inhibitor response 1
TLS	Translesion synthesis
TOP1	DNA topoisomerase I
TOP2A	DNA topoisomerase II alpha
TOP3A	DNA topoisomerase III alpha
TOPBP1	DNA topoisomerase II-binding protein 1
TRIM28	Tripartite motif-containing protein 28
UBM	UAP56/DDX39B-binding motif
UBF	Upstream Binding Factor
UFB	Ultrafine anaphase bridge
UR-DNA	Under-replicated DNA
UV	Ultraviolet
WGD	Whole-genome doubling
WT	Wild type
XRCC5	X-ray repair cross-complementing protein 5
XRCC6	X-ray repair cross-complementing protein 6

7.8 Acknowledgement

First and foremost, I would like to express my deepest gratitude to Prof. Dr. Zuzana Storchová for giving me the opportunity to pursue my doctoral studies in her laboratory. I am sincerely thankful for your constant support in moving the project forward, your availability whenever I needed advice, and the many opportunities you gave me to develop professionally as a scientist.

I am also deeply grateful to Dr. Markus Räschle for his continuous and insightful guidance, particularly during the preparation of this thesis. Your suggestions and feedback played an important role in shaping this project and bringing it to its present stage. I am equally thankful for the many encouraging and motivating conversations we had throughout the course of the project.

I would also like to thank Prof. Dr. Jörg Fahrer for kindly agreeing to serve as the second examiner of this thesis.

Special thanks go to all my students, particularly Amr, Nikita, and Katharina. I am very grateful for your dedication, your interest in the progress of the project, and your valuable contributions. Working with you also helped me to grow as a supervisor. I am especially thankful that our collaboration developed into genuine friendship. It was a great pleasure to work with you, and the many late evenings we spent together in the laboratory will remain among my fondest memories of this time.

I would also like to thank all members of the lab. It was a pleasure to work with each of you in such a welcoming and supportive environment. You have been the best company I could have wished for, both scientifically and personally. Angi, you were there at the very beginning of my journey and played an important role in helping me find my way in the lab. You were, and remain, one of the best supervisors I could have hoped for. Thank you for making my start so easy and for all the wonderful moments we shared. I wish you all the best in life. Tamara, from the time you joined the lab for your master's thesis, through the revision of the BLM paper, and until the final days of my PhD, you were always there to discuss the work and help find the best solution to every problem we encountered. I am very grateful for your support, your friendship and for all the time we spent working together. Karen, thank you for our daily breaks and for the many conversations we shared. During the most difficult periods of my PhD, going to the gym with you was always one of the highlights of my day. Thanks to Toni, Stefan, Jan, Dastin, Basti, and Erik, I have many happy memories with all of you, including our game nights, lunches at the Mensa, and the many trips we took together. Thank you for making this time so enjoyable. I would like to thank Andrea, Prince, and Olha for their help and support whenever I needed it. Leah and Anna, thank you for being such wonderful office mates and for your continuous support. We began our master's studies together and continued side by side through our PhDs until the very end. I am very grateful that we shared this journey. Amelie and Celina, thank you for being such kind and supportive colleagues. I still remember when you first joined the laboratory for your bachelor's theses, and now you are pursuing your own PhDs here. Isabell, Robin, Luigina and Ingeborg, thank you for your help in managing the many administrative and lab-related tasks that kept everything running smoothly.

Pegah, even though you came into my life near the end of my PhD journey, you made its final days and the challenging writing period much easier and brighter. I am deeply grateful to have you by my side.

Finally, I would like to express my deepest gratitude to my entire family and to all my friends. I am especially grateful to my mother, my father, and my sister for their extraordinary encouragement, motivation, and unwavering belief in me at every stage of my life. Your support has been fundamental to everything I have achieved, and you have played an essential role in shaping the person I am today.

7.9 Curriculum Vitae

Personal Details

Name: Farbod Mohseni

Contact: fmohseni@rptu.de

Education

Ph.D. candidate at Dept. Molecular Genetics
RPTU Kaiserslautern-Landau, Kaiserslautern, Germany
01/2023 – present

- Project: Proteomic analysis of protein complexes involved in ultrafine anaphase bridge resolution and evaluation of novel proteins involved in UFB resolution.

10/2020 – 11/2022 **M.Sc. in Cell and Molecular Biology – Biology**
Technical University of Kaiserslautern (Kaiserslautern, Germany)

- Master's Thesis: "Proteomic analysis of protein complexes involved in ultrafine anaphase bridge resolution"

06/2014 – 07/2018 **B.Sc. in Cell and Molecular Biology – Genetics**
Shahid Bahonar University (Kerman, Iran)

- Bachelor's Thesis: "Evaluation of the cytotoxicity of methanol extracts of Zataria multiflora plants on P19 embryonic carcinoma cells"

09/2013 – 06/2014 **Pre-university education in Experimental Sciences**
Allameh Tabatabaei High School (College), Tehran, Iran

09/2010 – 06/2013 **High School Degree**
Tazkieh High School, Tehran, Iran

Practical Experience

01/2023 – 12/2025 **FOR2800 DFG-funded Research Unit "Chromosomal Instability:**
Crosstalk of DNA replication stress and mitotic dysfunction"

- regular progress reports, talks, retreats

07/2022 – 07/2025 **Teaching Assistant for Large Data Set Analysis Course, Dept. of Molecular Genetics**.
RPTU Kaiserslautern-Landau, Kaiserslautern, Germany

- Introduction to R programming and Perseus.
- Proteomics data analysis and data visualization.

03/2023 – 05/2025	**Member and founder of RPTU Student Group: "Iranian Freedom Advocates"** RPTU Kaiserslautern-Landau, Kaiserslautern, Germany • Provided guidance and support to first-semester students • Helped organize protests and public awareness events focused on equal rights for women and men, human rights, and freedom of expression in Iran.
09/2016 – 03/2018	**Member of the Biology Scientific Society.** Shahid Bahonar University, Kerman, Iran.

Academic awards:

2026	**Poster award: IMB/SFB 1361 Conference "The EVIL Within: Regulation and Repair of Endogenous DNA Damage"** Mainz, Germany
2024	**Poster award: 34th GUM meeting conference** Kaiserslautern, Germany
2023	**DAAD Prize winner of RPTU University** • The DAAD Prize - worth 1000 EUR - is a special distinction for international students who stand out from the crowd given their excellent academic achievements and remarkable social and intercultural commitment.

Conference presentations:

03/2026	Poster presentation at IMB/SFB 1361 Conference "The EVIL Within: Regulation and Repair of Endogenous DNA Damage" Institute of Molecular Biology, Mainz, Germany • AP endonuclease1: A new player in the resolution of DNA ultra-fine bridges?
03/2024	Poster presentation at 34th GUM meeting conference RPTU Kaiserslautern-Landau, Kaiserslautern, Germany • Identification of mitotic DNA-protein complexes formed after replication stress by ChIP-MS Analysis
09/2023	Poster presentation at 6th German–French DNA Repair Meeting University Medical Centre Campus, Mainz, Germany • Identification of mitotic DNA-protein complexes formed after replication stress by ChIP-MS Analysis
09/2023	Poster presentation at GBM Compact Conference: Focus on Proteomics University Hospital /Frankfurt am Main, Germany.

- Identification of mitotic DNA-protein complexes formed after replication stress by ChIP-MS Analysis

Publication:

2026 **Mitotic BLM functions are required to maintain genomic stability**
Nucleic Acids Research
Hamann, T.E.*, Wieland, A.*****, Tirincsi, A., Vukušić, K., Mohseni, F., Wardenaar, R., Losito, M., Gönenc, I.I., Wollnik, B., Foijer, F., Tolić, I.M., Storchová, Z., Räschle, M.

Supervised theses:

“Studying a potential role of APEX1 in maintaining genomic stability by the resolution of DNA ultra-fine anaphase bridges” Master thesis Amr Abdrbo, Rheinland-Pfälzische Technische Universität Kaiserslautern Landau, 2024

“Exploring the Role of ALYREF in Ultra-Fine Bridges Resolution and Genome Stability” Master thesis Nikita Kvasov, Rheinland-Pfälzische Technische Universität Kaiserslautern Landau, 2024

“The role of APEX1 in the resolution of fragile site ultrafine DNA bridges” Master thesis Katharina Gauch, Rheinland-Pfälzische Technische Universität Kaiserslautern Landau, 2026

8 References

1. Bell, S. P. & Dutta, A. DNA replication in eukaryotic cells. *Annual review of biochemistry* **71,** 333–374 (2002).
2. Bournaka, S., Badra-Fajardo, N., Arbi, M., Taraviras, S. & Lygerou, Z. The cell cycle revisited: DNA replication past S phase preserves genome integrity. *Seminars in cancer biology* **99,** 45–55 (2024).
3. Spegg, V. & Altmeyer, M. Genome maintenance meets mechanobiology. *Chromosoma* **133,** 15–36; 10.1007/s00412-023-00807-5 (2024).
4. Harashima, H., Dissmeyer, N. & Schnittger, A. Cell cycle control across the eukaryotic kingdom. *Trends in cell biology* **23,** 345–356; 10.1016/j.tcb.2013.03.002 (2013).
5. Takeda, D. Y. & Dutta, A. DNA replication and progression through S phase. *Oncogene* **24,** 2827–2843; 10.1038/sj.onc.1208616 (2005).
6. Walczak, C. E., Cai, S. & Khodjakov, A. Mechanisms of chromosome behaviour during mitosis. *Nature reviews. Molecular cell biology* **11,** 91–102; 10.1038/nrm2832 (2010).
7. Cooper, G. M. *The cell. A molecular approach.* 2nd ed. (ASM Press, Washington, D.C., Sunderland, Mass., 2000).
8. Asbury, C. L. Anaphase A: Disassembling Microtubules Move Chromosomes toward Spindle Poles. *Biology* **6**; 10.3390/biology6010015 (2017).
9. Kirichok, Y., Krapivinsky, G. & Clapham, D. E. The mitochondrial calcium uniporter is a highly selective ion channel. *Nature* **427,** 360–364; 10.1038/nature02246 (2004).
10. Nähse, V., Christ, L., Stenmark, H. & Campsteijn, C. The Abscission Checkpoint: Making It to the Final Cut. *Trends in cell biology* **27,** 1–11; 10.1016/j.tcb.2016.10.001 (2017).
11. Hayashi, M. T. & Karlseder, J. DNA damage associated with mitosis and cytokinesis failure. *Oncogene* **32,** 4593–4601; 10.1038/onc.2012.615 (2013).
12. Garribba, L. *et al.* Short-term molecular consequences of chromosome mis-segregation for genome stability. *Nature communications* **14,** 1353; 10.1038/s41467-023-37095-7 (2023).
13. Wei Xiao Yi. The cell cycle: a review of regulation, deregulation and therapeutic targets in cancer, 131–149; 10.1046/j.1365-2184.2003. 00266.x (2003).
14. Lara-Gonzalez, P. *et al.* The G2-to-M Transition Is Ensured by a Dual Mechanism that Protects Cyclin B from Degradation by Cdc20-Activated APC/C. *Developmental cell* **51,** 313-325.e10; 10.1016/j.devcel.2019.09.005 (2019).
15. Hume, S., Dianov, G. L. & Ramadan, K. A unified model for the G1/S cell cycle transition. *Nucleic acids research* **48,** 12483–12501; 10.1093/nar/gkaa1002 (2020).
16. Ding, L. *et al.* The Roles of Cyclin-Dependent Kinases in Cell-Cycle Progression and Therapeutic Strategies in Human Breast Cancer. *International journal of molecular sciences* **21**; 10.3390/ijms21061960 (2020).
17. Roskoski, R. Cyclin-dependent protein serine/threonine kinase inhibitors as anticancer drugs. *Pharmacological research* **139,** 471–488; 10.1016/j.phrs.2018.11.035 (2019).
18. Visconti, R., Della Monica, R. & Grieco, D. Cell cycle checkpoint in cancer: a therapeutically targetable double-edged sword. *Journal of experimental & clinical cancer research: CR* **35,** 153; 10.1186/s13046-016-0433-9 (2016).
19. Clay, D. E. & Fox, D. T. DNA Damage Responses during the Cell Cycle: Insights from Model Organisms and Beyond. *Genes* **12**; 10.3390/genes12121882 (2021).
20. Bailis, J. M., Luche, D. D., Hunter, T. & Forsburg, S. L. Minichromosome maintenance proteins interact with checkpoint and recombination proteins to promote s-phase genome stability. *Molecular and cellular biology* **28,** 1724–1738; 10.1128/MCB.01717-07 (2008).
21. Kang, S., Yoo, J. & Myung, K. PCNA cycling dynamics during DNA replication and repair in mammals. *Trends in genetics: TIG* **40,** 526–539; 10.1016/j.tig.2024.02.006 (2024).

22. Strauss, J. D. & Pursell, Z. F. Replication DNA polymerases, genome instability and cancer therapies. *NAR cancer* **5,** zcad033; 10.1093/narcan/zcad033 (2023).

23. Okazaki, T. Days weaving the lagging strand synthesis of DNA - A personal recollection of the discovery of Okazaki fragments and studies on discontinuous replication mechanism. *Proceedings of the Japan Academy. Series B, Physical and biological sciences* **93,** 322–338; 10.2183/pjab.93.020 (2017).

24. Saxena, S. & Zou, L. Hallmarks of DNA replication stress. *Molecular cell* **82,** 2298–2314; 10.1016/j.molcel.2022.05.004 (2022).

25. Zeman, M. K. & Cimprich, K. A. Causes and consequences of replication stress. *Nature cell biology* **16,** 2–9; 10.1038/ncb2897 (2014).

26. Williams, S. L. *et al.* Replication-induced DNA secondary structures drive fork uncoupling and breakage. *The EMBO journal* **42,** e114334; 10.15252/embj.2023114334 (2023).

27. Gan, W. *et al.* R-loop-mediated genomic instability is caused by impairment of replication fork progression. *Genes & development* **25,** 2041–2056; 10.1101/gad.17010011 (2011).

28. Hamperl, S., Bocek, M. J., Saldivar, J. C., Swigut, T. & Cimprich, K. A. Transcription-Replication Conflict Orientation Modulates R-Loop Levels and Activates Distinct DNA Damage Responses. *Cell* **170,** 774-786.e19; 10.1016/j.cell.2017.07.043 (2017).

29. Tirman, S. *et al.* Temporally distinct post-replicative repair mechanisms fill PRIMPOL-dependent ssDNA gaps in human cells. *Molecular cell* **81,** 4026-4040.e8; 10.1016/j.molcel.2021.09.013 (2021).

30. Duxin, J. P., Dewar, J. M., Yardimci, H. & Walter, J. C. Repair of a DNA-protein crosslink by replication-coupled proteolysis. *Cell* **159,** 346–357; 10.1016/j.cell.2014.09.024 (2014).

31. Yoshida, K. & Fujita, M. DNA damage responses that enhance resilience to replication stress. *Cellular and molecular life sciences: CMLS* **78,** 6763–6773; 10.1007/s00018-021-03926-3 (2021).

32. Räschle, M. *et al.* Mechanism of replication-coupled DNA interstrand crosslink repair. *Cell* **134,** 969–980; 10.1016/j.cell.2008.08.030 (2008).

33. Saldanha, J., Rageul, J., Patel, J. A. & Kim, H. The Adaptive Mechanisms and Checkpoint Responses to a Stressed DNA Replication Fork. *International journal of molecular sciences* **24**; 10.3390/ijms241310488 (2023).

34. Berti, M. *et al.* Sequential role of RAD51 paralog complexes in replication fork remodeling and restart. *Nature communications* **11,** 3531; 10.1038/s41467-020-17324-z (2020).

35. Jahjah, T., Singh, J. K., Gottifredi, V. & Quinet, A. Tolerating DNA damage by repriming: Gap filling in the spotlight. *DNA repair* **142,** 103758; 10.1016/j.dnarep.2024.103758 (2024).

36. Cybulla, E. & Vindigni, A. Leveraging the replication stress response to optimize cancer therapy. *Nature reviews. Cancer* **23,** 6–24; 10.1038/s41568-022-00518-6 (2023).

37. Niehrs, C. & Luke, B. Regulatory R-loops as facilitators of gene expression and genome stability. *Nature reviews. Molecular cell biology* **21,** 167–178; 10.1038/s41580-019-0206-3 (2020).

38. Hegazy, Y. A., Fernando, C. M. & Tran, E. J. The balancing act of R-loop biology: The good, the bad, and the ugly. *The Journal of biological chemistry* **295,** 905–913; 10.1074/jbc. REV119.011353 (2020).

39. García-Muse, T. & Aguilera, A. R Loops: From Physiological to Pathological Roles. *Cell* **179,** 604–618; 10.1016/j.cell.2019.08.055 (2019).

40. Hamperl, S., Bocek, M. J., Saldivar, J. C., Swigut, T. & Cimprich, K. A. Transcription-Replication Conflict Orientation Modulates R-Loop Levels and Activates Distinct DNA Damage Responses. *Cell* **170,** 774-786.e19; 10.1016/j.cell.2017.07.043 (2017).

41. LianaGoehring,1 TonyT.Huang,1. Transcription–Replication Conflicts as a Source of Genome Instability, 157–179; 10.1146/annurev-genet-080320 (2023).

42. Kumar, C. & Remus, D. Looping out of control: R-loops in transcription-replication conflict. *Chromosoma* **133,** 37–56; 10.1007/s00412-023-00804-8 (2024).

43. Sollier, J. *et al.* Transcription-coupled nucleotide excision repair factors promote R-loop-induced genome instability. *Molecular cell* **56,** 777–785; 10.1016/j.molcel.2014.10.020 (2014).

44. Luna, R., Gómez-González, B. & Aguilera, A. RNA biogenesis and RNA metabolism factors as R-loop suppressors: a hidden role in genome integrity. *Genes & development* **38,** 504–527; 10.1101/gad.351853.124 (2024).

45. Chang, E. Y.-C. *et al.* RECQ-like helicases Sgs1 and BLM regulate R-loop-associated genome instability. *The Journal of cell biology* **216,** 3991–4005; 10.1083/jcb.201703168 (2017).

46. Leung, W. *et al.* ATR protects ongoing and newly assembled DNA replication forks through distinct mechanisms. *Cell reports* **42,** 112792; 10.1016/j.celrep.2023.112792 (2023).

47. Adolph, M. B. & Cortez, D. Mechanisms and regulation of replication fork reversal. *DNA repair* **141,** 103731; 10.1016/j.dnarep.2024.103731 (2024).

48. Caldecott, K. W. Causes and consequences of DNA single-strand breaks. *Trends in biochemical sciences* **49,** 68–78; 10.1016/j.tibs.2023.11.001 (2024).

49. Ibrahim, M. *et al.* Replication-associated base excision repair/single-strand break repair regulates PARG inhibitor response via the PRMT1/PRMT5/ATR axis. *NAR cancer* **7,** zcaf057; 10.1093/narcan/zcaf057 (2025).

50. Audrey, A., Haan, L. de, van Vugt, M. A. T. M. & Boer, H. R. de. Processing DNA lesions during mitosis to prevent genomic instability. *Biochemical Society transactions* **50,** 1105–1118; 10.1042/BST20220049 (2022).

51. Ghosh, D. & Raghavan, S. C. Nonhomologous end joining new accessory factors fine tune the machinery. *Trends in genetics : TIG* **37,** 582–599; 10.1016/j.tig.2021.03.001 (2021).

52. Haan, L. de *et al.* CIP2A mediates mitotic recruitment of SLX4/MUS81/XPF to resolve replication stress-induced DNA lesions. *Nature communications* **17,** 13; 10.1038/s41467-025-66549-3 (2025).

53. Schmidt, T. T. *et al.* Alterations in cellular metabolism triggered by URA7 or GLN3 inactivation cause imbalanced dNTP pools and increased mutagenesis. *Proceedings of the National Academy of Sciences of the United States of America* **114,** E4442-E4451; 10.1073/pnas.1618714114 (2017).

54. Weickert, P. *et al.* SPRTN patient variants cause global-genome DNA-protein crosslink repair defects. *Nature communications* **14,** 352; 10.1038/s41467-023-35988-1 (2023).

55. Bertolin, A. P., Hoffmann, J.-S. & Gottifredi, V. Under-Replicated DNA: The Byproduct of Large Genomes? *Cancers* **12**; 10.3390/cancers12102764 (2020).

56. Messer, C. L. & Fox, D. T. Broken chromosomes heading into mitosis: More than one way to patch a flat tire. *The Journal of cell biology* **223**; 10.1083/jcb.202401085 (2024).

57. Chan, Y. W. & West, S. C. A new class of ultrafine anaphase bridges generated by homologous recombination. *Cell cycle (Georgetown, Tex.)* **17,** 2101–2109; 10.1080/15384101.2018.1515555 (2018).

58. Wilhelm, T., Said, M. & Naim, V. DNA Replication Stress and Chromosomal Instability: Dangerous Liaisons. *Genes* **11**; 10.3390/genes11060642 (2020).

59. Hengeveld, R. C. C. *et al.* Rif1 Is Required for Resolution of Ultrafine DNA Bridges in Anaphase to Ensure Genomic Stability. *Developmental cell* **34,** 466–474; 10.1016/j.devcel.2015.06.014 (2015).

60. Petsalaki, E., Balafouti, S., Kyriazi, A. A. & Zachos, G. The abscission checkpoint senses chromatin bridges through Top2α recruitment to DNA knots. *The Journal of cell biology* **222**; 10.1083/jcb.202303123 (2023).

61. Murnane, J. P. Telomere dysfunction and chromosome instability. *Mutation research* **730,** 28–36; 10.1016/j.mrfmmm.2011.04.008 (2012).

62. Pampalona, J., Frías, C., Genescà, A. & Tusell, L. Progressive telomere dysfunction causes cytokinesis failure and leads to the accumulation of polyploid cells. *PLoS genetics* **8,** e1002679; 10.1371/journal.pgen.1002679 (2012).

63. Lopez, V. *et al.* Cytokinesis breaks dicentric chromosomes preferentially at pericentromeric regions and telomere fusions. *Genes & development* **29,** 322–336; 10.1101/gad.254664.114 (2015).

64. Kok-Lung Chan, Phillip S North. BLM is required for faithful chromosome segregation, and its localization defines a class of ultrafine anaphase bridges_2007 **26,** 3397–3409; 10.1038/sj.emboj.7601777 (2007).

65. Chanboonyasitt, P. & Chan, Y. W. Regulation of mitotic chromosome architecture and resolution of ultrafine anaphase bridges by PICH. *Cell cycle (Georgetown, Tex.)* **20,** 2077–2090; 10.1080/15384101.2021.1970877 (2021).

66. Liu, Y., Nielsen, C. F., Yao, Q. & Hickson, I. D. The origins and processing of ultra-fine anaphase DNA bridges. *Current opinion in genetics & development* **26,** 1–5; 10.1016/j.gde.2014.03.003 (2014).

67. Broderick, R., Nieminuszczy, J., Blackford, A. N., Winczura, A. & Niedzwiedz, W. TOPBP1 recruits TOP2A to ultra-fine anaphase bridges to aid in their resolution. *Nature communications* **6,** 6572; 10.1038/ncomms7572 (2015).

68. Bou Samra, E. *et al.* A role for Tau protein in maintaining ribosomal DNA stability and cytidine deaminase-deficient cell survival. *Nature communications* **8,** 693; 10.1038/s41467-017-00633-1 (2017).

69. Germann, S. M. *et al.* TopBP1/Dpb11 binds DNA anaphase bridges to prevent genome instability. *The Journal of cell biology* **204,** 45–59; 10.1083/jcb.201305157 (2014).

70. Wang, L. H.-C., Schwarzbraun, T., Speicher, M. R. & Nigg, E. A. Persistence of DNA threads in human anaphase cells suggests late completion of sister chromatid decatenation. *Chromosoma* **117,** 123–135; 10.1007/s00412-007-0131-7 (2008).

71. Wilhelm, T., Said, M. & Naim, V. DNA Replication Stress and Chromosomal Instability: Dangerous Liaisons. *Genes* **11**; 10.3390/genes11060642 (2020).

72. Kong, N., Liu, Z. & Chan, Y. W. RIF1 suppresses the formation of single-stranded ultrafine anaphase bridges via protein phosphatase 1. *Cell reports* **42,** 112032; 10.1016/j.celrep.2023.112032 (2023).

73. Nielsen, C. F. *et al.* PICH promotes sister chromatid disjunction and co-operates with topoisomerase II in mitosis. *Nature communications* **6,** 8962; 10.1038/ncomms9962 (2015).

74. Li, S. & Wu, X. Common fragile sites: protection and repair. *Cell & bioscience* **10,** 29; 10.1186/s13578-020-00392-5 (2020).

75. Irony-Tur Sinai, M. & Kerem, B. Insights into common fragile site instability: DNA replication challenges at DNA repeat sequences. *Emerging topics in life sciences* **7,** 277–287; 10.1042/ETLS20230023 (2023).

76. Liew, L. P. *et al.* Hydroxyurea-Mediated Cytotoxicity Without Inhibition of Ribonucleotide Reductase. *Cell reports* **17,** 1657–1670; 10.1016/j.celrep.2016.10.024 (2016).

77. Enoiu, M., Jiricny, J. & Schärer, O. D. Repair of cisplatin-induced DNA interstrand crosslinks by a replication-independent pathway involving transcription-coupled repair and translesion synthesis. 12 p; 10.3929/ETHZ-B-000062403 (2012).

78. Okamoto, Y. *et al.* Replication stress induces accumulation of FANCD2 at central region of large fragile genes. *Nucleic acids research* **46,** 2932–2944; 10.1093/nar/gky058 (2018).

79. Okamoto, Y. *et al.* FANCD2 protects genome stability by recruiting RNA processing enzymes to resolve R-loops during mild replication stress. *The FEBS journal* **286,** 139–150; 10.1111/febs.14700 (2019).

80. Fragkos, M. & Naim, V. Rescue from replication stress during mitosis. *Cell cycle (Georgetown, Tex.)* **16,** 613–633; 10.1080/15384101.2017.1288322 (2017).

81. Titia de Lange. Shelterin the protein complex that shapes and safeguards human telomeres, 2100–2110; 10.1101/gad.1346005. (2005).

82. Palm, W. & Lange, T. de. How shelterin protects mammalian telomeres. *Annual review of genetics* **42,** 301–334; 10.1146/annurev.genet.41.110306.130350 (2008).

83. Sfeir, A. *et al.* Mammalian telomeres resemble fragile sites and require TRF1 for efficient replication. *Cell* **138,** 90–103; 10.1016/j.cell.2009.06.021 (2009).

84. Nera, B., Huang, H.-S., Lai, T. & Xu, L. Elevated levels of TRF2 induce telomeric ultrafine anaphase bridges and rapid telomere deletions. *Nature communications* **6,** 10132; 10.1038/ncomms10132 (2015).

85. Zimmermann, M., Kibe, T., Kabir, S. & Lange, T. de. TRF1 negotiates TTAGGG repeat-associated replication problems by recruiting the BLM helicase and the TPP1/POT1 repressor of ATR signaling. *Genes & development* **28,** 2477–2491; 10.1101/gad.251611.114 (2014).

86. d'Alcontres, M. S., Palacios, J. A., Mejias, D. & Blasco, M. A. TopoIIα prevents telomere fragility and formation of ultra-thin DNA bridges during mitosis through TRF1-dependent binding to telomeres. *Cell cycle (Georgetown, Tex.)* **13,** 1463–1481; 10.4161/cc.28419 (2014).

87. Xuan Li and Wolf-Dietrich Heyer. Homologous recombination in DNA repair and DNA damage tolerance_2008, 99–113; 10.1038/cr.2008.1 (2008).

88. Räschle, M. *et al.* Mechanism of replication-coupled DNA interstrand crosslink repair. *Cell* **134,** 969–980 (2008).

89. Chan, Y. W., Fugger, K. & West, S. C. Unresolved recombination intermediates lead to ultra-fine anaphase bridges, chromosome breaks and aberrations. *Nature cell biology* **20,** 92–103; 10.1038/s41556-017-0011-1 (2018).

90. Nielsen, C. F. & Hickson, I. D. PICH promotes mitotic chromosome segregation: Identification of a novel role in rDNA disjunction. *Cell cycle (Georgetown, Tex.)* **15,** 2704–2711; 10.1080/15384101.2016.1222336 (2016).

91. Fernández-Casañas, M. & Chan, K.-L. The Unresolved Problem of DNA Bridging. *Genes* **9**; 10.3390/genes9120623 (2018).

92. Potapova, T. A. *et al.* Superresolution microscopy reveals linkages between ribosomal DNA on heterologous chromosomes. *The Journal of cell biology* **218,** 2492–2513; 10.1083/jcb.201810166 (2019).

93. Uruci, S., Lo, C. S. Y., Wheeler, D. & Taneja, N. R-Loops and Its Chro-Mates: The Strange Case of Dr. Jekyll and Mr. Hyde. *International journal of molecular sciences* **22**; 10.3390/ijms22168850 (2021).

94. Ke, Y. *et al.* PICH and BLM limit histone association with anaphase centromeric DNA threads and promote their resolution. *The EMBO journal* **30,** 3309–3321; 10.1038/emboj.2011.226 (2011).

95. Spakman, D. *et al.* PICH acts as a force-dependent nucleosome remodeler. *Nature communications* **13,** 7277; 10.1038/s41467-022-35040-8 (2022).

96. Wu, L. Role of the BLM helicase in replication fork management. *DNA repair* **6,** 936–944; 10.1016/j.dnarep.2007.02.007 (2007).

97. Cunniff, C., Bassetti, J. A. & Ellis, N. A. Bloom's Syndrome: Clinical Spectrum, Molecular Pathogenesis, and Cancer Predisposition. *Molecular syndromology* **8,** 4–23; 10.1159/000452082 (2017).

98. Xue, X., Raynard, S., Busygina, V., Singh, A. K. & Sung, P. Role of replication protein A in double holliday junction dissolution mediated by the BLM-Topo IIIα-RMI1-RMI2 protein complex. *The Journal of biological chemistry* **288,** 14221–14227; 10.1074/jbc.M113.465609 (2013).

99. Sarbajna, S., Davies, D. & West, S. C. Roles of SLX1-SLX4, MUS81-EME1, and GEN1 in avoiding genome instability and mitotic catastrophe. *Genes & development* **28,** 1124–1136; 10.1101/gad.238303.114 (2014).

100. Norma F. Neff, Maria Proytcheva. The DNA Helicase Activity of BLM Is Necessary for the Correction of the Genomic Instability of Bloom Syndrome Cells_1999 **10,** 665–676; 10.1091/mbc.10.3.665 (1999).

101. Sarlós, K. *et al.* Reconstitution of anaphase DNA bridge recognition and disjunction. *Nature structural & molecular biology* **25,** 868–876; 10.1038/s41594-018-0123-8 (2018).

102. Sims, A. E. *et al.* FANCI is a second monoubiquitinated member of the Fanconi anemia pathway. *Nature structural & molecular biology* **14,** 564–567; 10.1038/nsmb1252 (2007).

103. Irene Garcia-Higuera, T. T. Interaction of the Fanconi Anemia Proteins and BRCA1 in a Common Pathway **7,** 249–262; 10.1016/s1097-2765(01)00173-3 (2001).

104. Woo Joo. Structure of the FANCI-FANCD2 Complex: Insights into the Fanconi Anemia DNA Repair Pathway. *Science (New York, N.Y.)* **333,** 308–312; 10.1126/science.1201512 (2011).

105. Alcón, P. *et al.* FANCD2-FANCI is a clamp stabilized on DNA by monoubiquitination of FANCD2 during DNA repair. *Nature structural & molecular biology* **27,** 240–248; 10.1038/s41594-020-0380-1 (2020).

106. Brison, O. *et al.* Mistimed origin licensing and activation stabilize common fragile sites under tight DNA-replication checkpoint activation. *Nature structural & molecular biology* **30,** 539–550; 10.1038/s41594-023-00949-1 (2023).

107. Lachaud, C. *et al.* Ubiquitinated Fancd2 recruits Fan1 to stalled replication forks to prevent genome instability. *Science (New York, N.Y.)* **351,** 846–849; 10.1126/science. aad5634 (2016).

108. Minocherhomji, S. *et al.* Replication stress activates DNA repair synthesis in mitosis. *Nature* **528,** 286–290; 10.1038/nature16139 (2015).

109. Wilson, T. E., Ahmed, S., Winningham, A. & Glover, T. W. Replication stress induces POLQ-mediated structural variant formation throughout common fragile sites after entry into mitosis. *Nature communications* **15,** 9582; 10.1038/s41467-024-53917-8 (2024).

110. Chan, K. L., Palmai-Pallag, T., Ying, S. & Hickson, I. D. Replication stress induces sister-chromatid bridging at fragile site loci in mitosis. *Nature cell biology* **11,** 753–760; 10.1038/ncb1882 (2009).

111. Baumann, C., Körner, R., Hofmann, K. & Nigg, E. A. PICH, a centromere-associated SNF2 family ATPase, is regulated by Plk1 and required for the spindle checkpoint. *Cell* **128,** 101–114; 10.1016/j.cell.2006.11.041 (2007).

112. Biebricher, A. *et al.* PICH: a DNA translocase specially adapted for processing anaphase bridge DNA. *Molecular cell* **51,** 691–701; 10.1016/j.molcel.2013.07.016 (2013).

113. Rouzeau, S. *et al.* Bloom's syndrome and PICH helicases cooperate with topoisomerase IIα in centromere disjunction before anaphase. *PloS one* **7,** e33905; 10.1371/journal.pone.0033905 (2012).

114. Sridharan, V., Park, H., Ryu, H. & Azuma, Y. SUMOylation regulates polo-like kinase 1-interacting checkpoint helicase (PICH) during mitosis. *The Journal of biological chemistry* **290,** 3269–3276; 10.1074/jbc.C114.601906 (2015).

115. Saha, L. K. & Pommier, Y. TOP3A coupling with replication forks and repair of TOP3A cleavage complexes. *Cell cycle (Georgetown, Tex.)* **23,** 115–130; 10.1080/15384101.2024.2314440 (2024).

116. Bocquet, N. *et al.* Structural and mechanistic insight into Holliday-junction dissolution by topoisomerase IIIα and RMI1. *Nature structural & molecular biology* **21,** 261–268; 10.1038/nsmb.2775 (2014).

117. Goulaouic, H. *et al.* Purification and characterization of human DNA topoisomerase IIIalpha. *Nucleic acids research* **27,** 2443–2450; 10.1093/nar/27.12.2443 (1999).

118. Bakx, J. A. M. *et al.* Duplex DNA and BLM regulate gate opening by the human TopoIIIα-RMI1-RMI2 complex. *Nature communications* **13,** 584; 10.1038/s41467-022-28082-5 (2022).

119. Shorrocks, A.-M. K. *et al.* The Bloom syndrome complex senses RPA-coated single-stranded DNA to restart stalled replication forks. *Nature communications* **12,** 585; 10.1038/s41467-020-20818-5 (2021).

120. Harami, G. M. *et al.* The toposiomerase IIIalpha-RMI1-RMI2 complex orients human Bloom's syndrome helicase for efficient disruption of D-loops. *Nat Commun* **13,** 654; 10.1038/s41467-022-28208-9 (2022).

121. Wold, M. S. Replication protein A: a heterotrimeric, single-stranded DNA-binding protein required for eukaryotic DNA metabolism. *Annual review of biochemistry* **66,** 61–92; 10.1146/annurev.biochem.66.1.61 (1997).

122. Gibb, B. *et al.* Concentration-dependent exchange of replication protein A on single-stranded DNA revealed by single-molecule imaging. *PloS one* **9,** e87922; 10.1371/journal.pone.0087922 (2014).

123. Zou, L. & Elledge, S. J. Sensing DNA damage through ATRIP recognition of RPA-ssDNA complexes. *Science (New York, N.Y.)* **300,** 1542–1548; 10.1126/science.1083430 (2003).

124. Choi, J.-H. *et al.* Reconstitution of RPA-covered single-stranded DNA-activated ATR-Chk1 signaling. *Proceedings of the National Academy of Sciences of the United States of America* **107,** 13660–13665; 10.1073/pnas.1007856107 (2010).

125. Bell, J. C., Dombrowski, C. C., Plank, J. L., Jensen, R. B. & Kowalczykowski, S. C. BRCA2 chaperones RAD51 to single molecules of RPA-coated ssDNA. *Proceedings of the National Academy of Sciences of the United States of America* **120,** e2221971120; 10.1073/pnas.2221971120 (2023).

126. Pangeni, S. *et al.* Rapid Long-distance Migration of RPA on Single Stranded DNA Occurs Through Intersegmental Transfer Utilizing Multivalent Interactions. *Journal of molecular biology* **436,** 168491; 10.1016/j.jmb.2024.168491 (2024).

127. Farbod Mohseni. Proteomic analysis of protein complexes Proteomic analysis of protein complexes involved in Ultrafine anaphase bridge resolution. Master thesis. Department of Biology, Molecular Genetics, 2022.

128. Caston, R. A. *et al.* The multifunctional APE1 DNA repair-redox signaling protein as a drug target in human disease. *Drug discovery today* **26,** 218–228; 10.1016/j.drudis.2020.10.015 (2021).

129. Kelley, M. R., Georgiadis, M. M. & Fishel, M. L. APE1/Ref-1 role in redox signaling: translational applications of targeting the redox function of the DNA repair/redox protein APE1/Ref-1. *Current molecular pharmacology* **5,** 36–53; 10.2174/1874467211205010036 (2012).

130. Antoniali, G. *et al.* Mammalian APE1 controls miRNA processing and its interactome is linked to cancer RNA metabolism. *Nature communications* **8,** 797; 10.1038/s41467-017-00842-8 (2017).

131. Li, J., Zhao, H., McMahon, A. & Yan, S. APE1 assembles biomolecular condensates to promote the ATR-Chk1 DNA damage response in nucleolus. *Nucleic acids research* **50,** 10503–10525; 10.1093/nar/gkac853 (2022).

132. Liu, Y. *et al.* RNA abasic sites in yeast and human cells. *Proceedings of the National Academy of Sciences of the United States of America* **117,** 20689–20695; 10.1073/pnas.2011511117 (2020).

133. Malfatti, M. C., Bellina, A., Antoniali, G. & Tell, G. Revisiting Two Decades of Research Focused on Targeting APE1 for Cancer Therapy: The Pros and Cons. *Cells* **12**; 10.3390/cells12141895 (2023).

134. Luo, M. L. *et al.* pre-mRNA splicing and mRNA export linked by direct interactions between UAP56 and Aly. *Nature* **413,** 644–647; 10.1038/35098106 (2001).

135. Palazzo, A. F. & Lee, E. S. Sequence Determinants for Nuclear Retention and Cytoplasmic Export of mRNAs and lncRNAs. *Frontiers in genetics* **9,** 440; 10.3389/fgene.2018.00440 (2018).

136. Gromadzka, A. M., Steckelberg, A.-L., Singh, K. K., Hofmann, K. & Gehring, N. H. A short, conserved motif in ALYREF directs cap- and EJC-dependent assembly of export complexes on spliced mRNAs. *Nucleic acids research* **44,** 2348–2361; 10.1093/nar/gkw009 (2016).

137. Bhandari, J. *et al.* The molecular chaperone ALYREF promotes R-loop resolution and maintains genome stability. *The Journal of biological chemistry* **300,** 107996; 10.1016/j.jbc.2024.107996 (2024).

138. Pérez-Calero, C. *et al.* UAP56/DDX39B is a major cotranscriptional RNA-DNA helicase that unwinds harmful R loops genome-wide. *Genes & development* **34,** 898–912; 10.1101/gad.336024.119 (2020).

139. Barber, T. D. *et al.* Chromatid cohesion defects may underlie chromosome instability in human colorectal cancers. *Proceedings of the National Academy of Sciences of the United States of America* **105,** 3443–3448; 10.1073/pnas.0712384105 (2008).

140. Hamann, T. E. *et al.* Mitotic BLM functions are required to maintain genomic stability. *Nucleic Acids Res* **54**; 10.1093/nar/gkag199 (2026).

141. Ligasová, A. & Koberna, K. Strengths and Weaknesses of Cell Synchronization Protocols Based on Inhibition of DNA Synthesis. *International journal of molecular sciences* **22**; 10.3390/ijms221910759 (2021).

142. Singh, A. & Xu, Y.-J. The Cell Killing Mechanisms of Hydroxyurea. *Genes* **7**; 10.3390/genes7110099 (2016).

143. Rihani, A., Vandesompele, J., Speleman, F. & van Maerken, T. Inhibition of CDK4/6 as a novel therapeutic option for neuroblastoma. *Cancer cell international* **15,** 76; 10.1186/s12935-015-0224-y (2015).

144. Hain, K. O., Colin, D. J., Rastogi, S., Allan, L. A. & Clarke, P. R. Prolonged mitotic arrest induces a caspase-dependent DNA damage response at telomeres that determines cell survival. *Scientific reports* **6,** 26766; 10.1038/srep26766 (2016).

145. Wierer, M. & Mann, M. Proteomics to study DNA-bound and chromatin-associated gene regulatory complexes. *Human molecular genetics* **25,** R106-R114; 10.1093/hmg/ddw208 (2016).

146. Pladevall-Morera, D. *et al.* Proteomic characterization of chromosomal common fragile site (CFS)-associated proteins uncovers ATRX as a regulator of CFS stability. *Nucleic acids research* **47,** 8004–8018; 10.1093/nar/gkz510 (2019).

147. Chen, G. & Deng, X. Cell Synchronization by Double Thymidine Block. *Bio-protocol* **8**; 10.21769/BioProtoc.2994 (2018).

148. Böhly, N., Kistner, M. & Bastians, H. Mild replication stress causes aneuploidy by deregulating microtubule dynamics in mitosis. *Cell cycle (Georgetown, Tex.)* **18,** 2770–2783; 10.1080/15384101.2019.1658477 (2019).

149. Apraiz, A., Mitxelena, J. & Zubiaga, A. Studying Cell Cycle-regulated Gene Expression by Two Complementary Cell Synchronization Protocols. *Journal of visualized experiments: JoVE*; 10.3791/55745 (2017).

150. Martin, P. R. *et al.* The CIP2A-TOPBP1 axis facilitates mitotic DNA repair via MiDAS and MMEJ. *Nat Commun* **16,** 10623; 10.1038/s41467-025-65594-2 (2025).

151. Ho, J. J. *et al.* The BLM-TOP3A-RMI1-RMI2 proximity map reveals that RAD54L2 suppresses sister chromatid exchanges. *EMBO reports* **26,** 1290–1314; 10.1038/s44319-025-00374-z (2025).

152. Lin, R. *et al.* R-loopBase: a knowledgebase for genome-wide R-loop formation and regulation. *Nucleic Acids Res* **50,** D303-D315; 10.1093/nar/gkab1103 (2022).

153. Tyanova, S. *et al.* The Perseus computational platform for comprehensive analysis of (prote)omics data. *Nature methods* **13,** 731–740; 10.1038/nmeth.3901 (2016).

154. Chaudhury, I., Sareen, A., Raghunandan, M. & Sobeck, A. FANCD2 regulates BLM complex functions independently of FANCI to promote replication fork recovery. *Nucleic Acids Res* **41,** 6444–6459; 10.1093/nar/gkt348 (2013).

155. Vinciguerra, P., Godinho, S. A., Parmar, K., Pellman, D. & D'Andrea, A. D. Cytokinesis failure occurs in Fanconi anemia pathway-deficient murine and human bone marrow hematopoietic cells. *The Journal of clinical investigation* **120,** 3834–3842; 10.1172/JCI43391 (2010).

156. Said, M. *et al.* FANCD2 promotes mitotic rescue from transcription-mediated replication stress in SETX-deficient cancer cells. *Communications biology* **5,** 1395; 10.1038/s42003-022-04360-2 (2022).

157. Liang, Z. *et al.* Binding of FANCI-FANCD2 Complex to RNA and R-Loops Stimulates Robust FANCD2 Monoubiquitination. *Cell reports* **26,** 564-572.e5 (2019).

158. García-Muse, T. & Aguilera, A. Transcription-replication conflicts: how they occur and how they are resolved. *Nature reviews. Molecular cell biology* **17,** 553–563; 10.1038/nrm.2016.88 (2016).

159. Crossley, M. P., Bocek, M. & Cimprich, K. A. R-Loops as Cellular Regulators and Genomic Threats. *Molecular cell* **73,** 398–411; 10.1016/j.molcel.2019.01.024 (2019).

160. Helmrich, A., Ballarino, M. & Tora, L. Collisions between replication and transcription complexes cause common fragile site instability at the longest human genes. *Molecular cell* **44,** 966–977; 10.1016/j.molcel.2011.10.013 (2011).

161. El Hage, A., French, S. L., Beyer, A. L. & Tollervey, D. Loss of Topoisomerase I leads to R-loop-mediated transcriptional blocks during ribosomal RNA synthesis. *Genes & development* **24,** 1546–1558; 10.1101/gad.573310 (2010).

162. Siqueira, P. B. *et al.* The APE1/REF-1 and the hallmarks of cancer. *Molecular biology reports* **51,** 47; 10.1007/s11033-023-08946-9 (2024).

163. García-Rubio, M. *et al.* Yra1-bound RNA-DNA hybrids cause orientation-independent transcription-replication collisions and telomere instability. *Genes & development* **32,** 965–977; 10.1101/gad.311274.117 (2018).

164. Niraj, J. *et al.* The identification of FANCD2 DNA binding domains reveals nuclear localization sequences. *Nucleic acids research* **45,** 8341–8357; 10.1093/nar/gkx543 (2017).

165. Budhathoki, J. B. *et al.* RecQ-core of BLM unfolds telomeric G-quadruplex in the absence of ATP. *Nucleic acids research* **42,** 11528–11545; 10.1093/nar/gku856 (2014).

166. Hoitsma, N. M. *et al.* Mechanistic insight into AP-endonuclease 1 cleavage of abasic sites at stalled replication fork mimics. *Nucleic acids research* **51,** 6738–6753; 10.1093/nar/gkad481 (2023).

167. Tang, S. *et al.* Proteomic characterization identifies clinically relevant subgroups of soft tissue sarcoma. *Nature communications* **15,** 1381; 10.1038/s41467-024-45306-y (2024).

168. Wilhelm, T. *et al.* Mild replication stress causes chromosome mis-segregation via premature centriole disengagement. *Nature communications* **10,** 3585; 10.1038/s41467-019-11584-0 (2019).

169. Thompson, S. L. & Compton, D. A. Chromosome missegregation in human cells arises through specific types of kinetochore-microtubule attachment errors. *Proceedings of the National Academy of Sciences of the United States of America* **108,** 17974–17978; 10.1073/pnas.1109720108 (2011).

170. Pampalona, J. *et al.* Chromosome Bridges Maintain Kinetochore-Microtubule Attachment throughout Mitosis and Rarely Break during Anaphase. *PloS one* **11,** e0147420; 10.1371/journal.pone.0147420 (2016).

171. Maciejowski, J., Li, Y., Bosco, N., Campbell, P. J. & Lange, T. de. Chromothripsis and Kataegis Induced by Telomere Crisis. *Cell* **163,** 1641–1654; 10.1016/j.cell.2015.11.054 (2015).

172. Gelot, C., Magdalou, I. & Lopez, B. S. Replication stress in Mammalian cells and its consequences for mitosis. *Genes* **6,** 267–298; 10.3390/genes6020267 (2015).

173. Kim, D. V. *et al.* Mild phenotype of knockouts of the major apurinic/apyrimidinic endonuclease APEX1 in a non-cancer human cell line. *PloS one* **16,** e0257473; 10.1371/journal.pone.0257473 (2021).

174. Cranford, M. T., Dahmen, S. N., Cortez, D. & Dewar, J. M. Leading and lagging strand abasic sites differentially affect vertebrate replisome progression but involve analogous bypass mechanisms. *Nucleic acids research* **53**; 10.1093/nar/gkaf975 (2025).

175. Tang, S., Stokasimov, E., Cui, Y. & Pellman, D. Breakage of cytoplasmic chromosomes by pathological DNA base excision repair. *Nature* **606,** 930–936; 10.1038/s41586-022-04767-1 (2022).

176. Macheret, M. *et al.* High-resolution mapping of mitotic DNA synthesis regions and common fragile sites in the human genome through direct sequencing. *Cell research* **30,** 997–1008; 10.1038/s41422-020-0358-x (2020).

177. Apraiz, A., Mitxelena, J. & Zubiaga, A. Studying Cell Cycle-regulated Gene Expression by Two Complementary Cell Synchronization Protocols. *Journal of visualized experiments: JoVE*; 10.3791/55745 (2017).

178. Gemble, S. *et al.* Pyrimidine Pool Disequilibrium Induced by a Cytidine Deaminase Deficiency Inhibits PARP-1 Activity, Leading to the Under Replication of DNA. *PLoS genetics* **11,** e1005384; 10.1371/journal.pgen.1005384 (2015).

179. Dianova, I. I., Bohr, V. A. & Dianov, G. L. Interaction of human AP endonuclease 1 with flap endonuclease 1 and proliferating cell nuclear antigen involved in long-patch base excision repair. *Biochemistry* **40,** 12639–12644; 10.1021/bi011117i (2001).

180. Michelle M. Le Beau. Replication of a common fragile site, FRA3B, occurs late in S phase and is delayed further upon induction implications for the mechanism of fragile site **7,** 755–761 (1998).

181. Brison, O. *et al.* Transcription-mediated organization of the replication initiation program across large genes sets common fragile sites genome-wide. *Nature communications* **10,** 5693; 10.1038/s41467-019-13674-5 (2019).

182. Marchena-Cruz, E. *et al.* DDX47, MeCP2, and other functionally heterogeneous factors protect cells from harmful R loops. *Cell reports* **42,** 112148; 10.1016/j.celrep.2023.112148 (2023).

183. Querol-Audí, J. *et al.* Repair complexes of FEN1 endonuclease, DNA, and Rad9-Hus1-Rad1 are distinguished from their PCNA counterparts by functionally important stability. *Proceedings of the National Academy of Sciences of the United States of America* **109,** 8528–8533; 10.1073/pnas.1121116109 (2012).

184. Krokan, H. E. & Bjørås, M. Base excision repair. *Cold Spring Harbor perspectives in biology* **5,** a012583; 10.1101/cshperspect. a012583 (2013).

185. Parlanti, E., Locatelli, G., Maga, G. & Dogliotti, E. Human base excision repair complex is physically associated to DNA replication and cell cycle regulatory proteins. *Nucleic acids research* **35,** 1569–1577; 10.1093/nar/gkl1159 (2007).

186. Simon, N. E. & Schwacha, A. The Mcm2-7 replicative helicase: a promising chemotherapeutic target. *BioMed research international* **2014,** 549719; 10.1155/2014/549719 (2014).

187. Lossaint, G. *et al.* FANCD2 binds MCM proteins and controls replisome function upon activation of s phase checkpoint signaling. *Molecular cell* **51,** 678–690; 10.1016/j.molcel.2013.07.023 (2013).

188. Pramanik, S., Chen, Y. & Bhakat, K. K. Base Excision Repair in Mitotic Cells and the Role of Apurinic/Apyrimidinic Endonuclease 1 (APE1) in Post-Mitotic Transcriptional Reactivation of Genes. *International journal of molecular sciences* **25**; 10.3390/ijms252312735 (2024).

189. Roychoudhury, S. *et al.* Human Apurinic/Apyrimidinic Endonuclease (APE1) Is Acetylated at DNA Damage Sites in Chromatin, and Acetylation Modulates Its DNA Repair Activity. *Molecular and cellular biology* **37**; 10.1128/MCB.00401-16 (2017).

190. Madlener, S. *et al.* Essential role for mammalian apurinic/apyrimidinic (AP) endonuclease Ape1/Ref-1 in telomere maintenance. *Proceedings of the National Academy of Sciences of the United States of America* **110,** 17844–17849; 10.1073/pnas.1304784110 (2013).

191. Gong, X. *et al.* Molecular insights into mRNA export regulation by the human TREX-2 complex. *Nature communications* **17**; 10.1038/s41467-026-70088-w (2026).

192. Strässer, K. *et al.* TREX is a conserved complex coupling transcription with messenger RNA export. *Nature* **417,** 304–308; 10.1038/nature746 (2002).

193. Pühringer, T. *et al.* Structure of the human core transcription-export complex reveals a hub for multivalent interactions. *eLife* **9**; 10.7554/eLife.61503 (2020).

194. Singh, M. I. *et al.* Mechanistic insight into anaphase bridge signaling to the abscission checkpoint. *EMBO J* **44,** 3824–3852; 10.1038/s44318-025-00453-w (2025).

195. Naim, V., Wilhelm, T., Debatisse, M. & Rosselli, F. ERCC1 and MUS81-EME1 promote sister chromatid separation by processing late replication intermediates at common fragile sites during mitosis. *Nature cell biology* **15,** 1008–1015; 10.1038/ncb2793 (2013).

196. Quinet, A., Tirman, S., Cybulla, E., Meroni, A. & Vindigni, A. To skip or not to skip: choosing repriming to tolerate DNA damage. *Molecular cell* **81,** 649–658; 10.1016/j.molcel.2021.01.012 (2021).

197. Marenstein, D. R., Wilson, D. M. & Teebor, G. W. Human AP endonuclease (APE1) demonstrates endonucleolytic activity against AP sites in single-stranded DNA. *DNA repair* **3,** 527–533; 10.1016/j.dnarep.2004.01.010 (2004).

198. Alcón, P. *et al.* FANCD2-FANCI surveys DNA and recognizes double- to single-stranded junctions. *Nature* **632,** 1165–1173; 10.1038/s41586-024-07770-w (2024).

199. Kong, N. *et al.* The interplay of the translocase activity and protein recruitment function of PICH in ultrafine anaphase bridge resolution and genomic stability. *Nucleic acids research* **53**; 10.1093/nar/gkae1249 (2025).

200. Bakx, J. A. M. *et al.* Duplex DNA and BLM regulate gate opening by the human TopoIIIα-RMI1-RMI2 complex. *Nature communications* **13,** 584; 10.1038/s41467-022-28082-5 (2022).

201. Madireddy, A. *et al.* FANCD2 Facilitates Replication through Common Fragile Sites. *Molecular cell* **64,** 388–404; 10.1016/j.molcel.2016.09.017 (2016).

202. Qin, Z. *et al.* Human RPA activates BLM's bidirectional DNA unwinding from a nick. *eLife* **9**; 10.7554/eLife.54098 (2020).

203. Kharat, S. S. *et al.* Degradation of 5hmC-marked stalled replication forks by APE1 causes genomic instability. *Science signaling* **13**; 10.1126/scisignal. aba8091 (2020).

204. Mehta, K. P. M., Lovejoy, C. A., Zhao, R., Heintzman, D. R. & Cortez, D. HMCES Maintains Replication Fork Progression and Prevents Double-Strand Breaks in Response to APOBEC Deamination and Abasic Site Formation. *Cell reports* **31,** 107705; 10.1016/j.celrep.2020.107705 (2020).

205. Hanthi, Y. W. *et al.* RAD51 protects abasic sites to prevent replication fork breakage. *Molecular cell* **84,** 3026-3043.e11; 10.1016/j.molcel.2024.07.004 (2024).